

Pollutant emission control in energy conversion process

Edited by

Zongliang Zuo, Siyi Luo, Huaqing Xie, Martin Van Sint Annaland and Zhanjun Cheng

Published in

Frontiers in Energy Research



FRONTIERS EBOOK COPYRIGHT STATEMENT

The copyright in the text of individual articles in this ebook is the property of their respective authors or their respective institutions or funders. The copyright in graphics and images within each article may be subject to copyright of other parties. In both cases this is subject to a license granted to Frontiers.

The compilation of articles constituting this ebook is the property of Frontiers.

Each article within this ebook, and the ebook itself, are published under the most recent version of the Creative Commons CC-BY licence. The version current at the date of publication of this ebook is CC-BY 4.0. If the CC-BY licence is updated, the licence granted by Frontiers is automatically updated to the new version.

When exercising any right under the CC-BY licence, Frontiers must be attributed as the original publisher of the article or ebook, as applicable.

Authors have the responsibility of ensuring that any graphics or other materials which are the property of others may be included in the CC-BY licence, but this should be checked before relying on the CC-BY licence to reproduce those materials. Any copyright notices relating to those materials must be complied with.

Copyright and source acknowledgement notices may not be removed and must be displayed in any copy, derivative work or partial copy which includes the elements in question.

All copyright, and all rights therein, are protected by national and international copyright laws. The above represents a summary only. For further information please read Frontiers' Conditions for Website Use and Copyright Statement, and the applicable CC-BY licence.

ISSN 1664-8714
ISBN 978-2-83251-771-0
DOI 10.3389/978-2-83251-771-0

About Frontiers

Frontiers is more than just an open access publisher of scholarly articles: it is a pioneering approach to the world of academia, radically improving the way scholarly research is managed. The grand vision of Frontiers is a world where all people have an equal opportunity to seek, share and generate knowledge. Frontiers provides immediate and permanent online open access to all its publications, but this alone is not enough to realize our grand goals.

Frontiers journal series

The Frontiers journal series is a multi-tier and interdisciplinary set of open-access, online journals, promising a paradigm shift from the current review, selection and dissemination processes in academic publishing. All Frontiers journals are driven by researchers for researchers; therefore, they constitute a service to the scholarly community. At the same time, the *Frontiers journal series* operates on a revolutionary invention, the tiered publishing system, initially addressing specific communities of scholars, and gradually climbing up to broader public understanding, thus serving the interests of the lay society, too.

Dedication to quality

Each Frontiers article is a landmark of the highest quality, thanks to genuinely collaborative interactions between authors and review editors, who include some of the world's best academicians. Research must be certified by peers before entering a stream of knowledge that may eventually reach the public - and shape society; therefore, Frontiers only applies the most rigorous and unbiased reviews. Frontiers revolutionizes research publishing by freely delivering the most outstanding research, evaluated with no bias from both the academic and social point of view. By applying the most advanced information technologies, Frontiers is catapulting scholarly publishing into a new generation.

What are Frontiers Research Topics?

Frontiers Research Topics are very popular trademarks of the *Frontiers journals series*: they are collections of at least ten articles, all centered on a particular subject. With their unique mix of varied contributions from Original Research to Review Articles, Frontiers Research Topics unify the most influential researchers, the latest key findings and historical advances in a hot research area.

Find out more on how to host your own Frontiers Research Topic or contribute to one as an author by contacting the Frontiers editorial office: frontiersin.org/about/contact

Pollutant emission control in energy conversion process

Topic editors

Zongliang Zuo — Qingdao University of Technology, China

Siyi Luo — Qingdao University of Technology, China

Huaqing Xie — Northeastern University, China

Martin Van Sint Annaland — Eindhoven University of Technology, Netherlands

Zhanjun Cheng — Tianjin University, China

Citation

Zuo, Z., Luo, S., Xie, H., Annaland, M. V. S., Cheng, Z., eds. (2023). *Pollutant emission control in energy conversion process*. Lausanne: Frontiers Media SA.
doi: 10.3389/978-2-83251-771-0

Table of contents

- 04 **Editorial: Pollutant emission control in energy conversion process**
Yan Feng, Zongliang Zuo, Zhanjun Cheng, Siyi Luo, Martin Van Sint Annaland and Huaqing Xie
- 06 **Selective Catalytic Reduction System Ammonia Injection Control Based on Deep Deterministic Policy Reinforcement Learning**
Peiran Xie, Guangming Zhang, Yuguang Niu and Tianshu Sun
- 19 **Quantifying Heat Transfer Characteristics of the Kroll Reactor in Titanium Sponge Production**
Wenhao Wang and Fuzhong Wu
- 26 **Enhanced Reforming of Tar Based on Double-Effect Ni/CaO–Ca₁₂Al₁₄O₃₃ Catalysts: Modified by Ce, Mg, and Fe**
Panlei Wang, Weidong Zhang, Zhenyu Yu, Huaqing Xie, Mi Zhou and Zhengyu Wang
- 37 **Advances in the Safe Disposal and Comprehensive Utilization of Spent Carbon Anode From Aluminum Electrolysis: Prospects for Extraction and Application of Carbon Resources From Hazardous Waste**
Bin Li, Jun Zhou, Zhen Yao, Qian Peng, Mengnan Liu, Xiaoqing Li and Wei Liu
- 47 **CO₂ Adsorption and Desorption by Waste Ion-Exchange Resin–Based Activated Carbon on Fixed Bed**
Mengqi Wei and Qiuyue Zhao
- 57 **Flow Regimes and Transitions for Two-Phase Flow of R152a During Condensation in a Circular Minichannel**
Na Liu, Qian Zhao and Zhixiang Lan
- 65 **Effect of Tube Expansion on Heat Transfer and Pressure Drop Characteristics During Condensation in Micro-Fin Tubes**
Na Liu, Qian Zhao and Zhixiang Lan
- 75 **Element Distribution and Migration Behavior in the Copper Slag Reduction and Separation Process**
Zongliang Zuo, Yan Feng, Siyi Luo, Xinjiang Dong, Xiaoteng Li, Dongdong Ren, Qingbo Yu and Jianxiang Guo
- 85 **Preparation of Adsorbents by Pyrolysis of Sludge Mixed With Steel Slag and Study on Adsorption of Chromium Ions in Water**
Xiaowen Qi, Enze Zhou, Xuefei Wu, Siyi Luo and Yanggang Song
- 95 **AHP-Based Evaluation of the Suitability of Shallow Geothermal Energy Utilization in GSHP System**
Jie Dong, Peng He, Honghua Liu, Yong Guan, Haisong Liu, Weiqiang Xia and Jierui Dong
- 104 **Heat Transfer Characteristics and Pressure Drop of U-type Channel in Vacuum Distillation Process for Titanium Sponge**
Kangquan Yang, Chengqi Zhang, Hui Yuan and Fuzhong Wu



OPEN ACCESS

EDITED AND REVIEWED BY
Bamidele Victor Ayodele,
University of Technology Petronas,
Malaysia

*CORRESPONDENCE
Zongliang Zuo,
✉ zuozongliangneu@163.com
Zhanjun Cheng,
✉ zjcheng@tju.edu.cn
Siyi Luo,
✉ Luosiyi666@126.com

SPECIALTY SECTION
This article was submitted to
Advanced Clean Fuel Technologies,
a section of the journal
Frontiers in Energy Research

RECEIVED 08 December 2022
ACCEPTED 07 February 2023
PUBLISHED 13 February 2023

CITATION
Feng Y, Zuo Z, Cheng Z, Luo S,
Annaland MVS and Xie H (2023), Editorial:
Pollutant emission control in energy
conversion process.
Front. Energy Res. 11:1118785.
doi: 10.3389/fenrg.2023.1118785

COPYRIGHT
© 2023 Feng, Zuo, Cheng, Luo, Annaland
and Xie. This is an open-access article
distributed under the terms of the
[Creative Commons Attribution License](#)
(CC BY). The use, distribution or
reproduction in other forums is
permitted, provided the original author(s)
and the copyright owner(s) are credited
and that the original publication in this
journal is cited, in accordance with
accepted academic practice. No use,
distribution or reproduction is permitted
which does not comply with these terms.

Editorial: Pollutant emission control in energy conversion process

Yan Feng¹, Zongliang Zuo^{1*}, Zhanjun Cheng^{2*}, Siyi Luo^{1*},
Martin Van Sint Annaland³ and Huaqing Xie⁴

¹School of Environmental and Municipal Engineering, Qingdao University of Technology, Qingdao, China, ²School of Environmental Science and Engineering, Tianjin University, Tianjin, China, ³Eindhoven University of Technology, Eindhoven, Netherlands, ⁴School of Metallurgy, Northeastern University, Shenyang, China

KEYWORDS

waste resource, waste energy, refrigeration, air conditioning, clean coal combustion

Editorial on the Research Topic

Pollutant emission control in energy conversion process

Copper slag is a solid contaminant with a high recovery rate. Reduction and separation are considered to be effective methods for the treatment of copper slag. How to control the formation of contaminants during this treatment process? Zuo et al. discussed the separation and migration behavior of elements in copper slag and used the obtained mechanistic results as a theoretical guide to optimize the operating parameters to reduce the formation of contaminants. Qi et al. prepared an adsorbent by mixing sludge and steel slag from a sewage plant. Subsequently, they investigated the adsorption of chromium ions using this adsorbent mixture. As part of the analysis, the authors performed various tests to study the physical properties of the pyrolysis products, among others. The article is significant in suggesting a viable method for the effective use of steel slag.

A recent review on this Research Topic is also available for the treatment of waste carbon cathode residues from aluminum electrolysis. Li et al. provide a comprehensive summary of the rationale and technical characteristics of safe disposal strategies for this hazardous waste and offer a unique perspective on the recovery and application of valuable components from waste carbon cathodes. They summarized and discussed the latest treatment methods for waste carbon cathodes, including physical activation, alkali melting, alkali leaching, and high-temperature graphitization. They also presented a balanced, comprehensive and critical view on the development direction of clean disposal and resource utilization of waste carbon cathode residues.

For non-metallic wastes, Wei et al. investigated the adsorption and desorption performance of waste ion exchange resin-based activated carbon on fixed-bed CO₂. The adsorption temperature, gas flow rate, CO₂ concentration and adsorbent filling amount during adsorption, and the desorption temperature, CO₂ concentration and purge gas flow rate during desorption were investigated. The successful completion of this work is of great significance to the industrial application of CO₂ adsorption on waste ion exchange resin-based activated carbon and the development of carbon capture technologies.

Titanium sponge is a main raw material for the industrial production of titanium alloys. In the production of titanium sponge, the production energy consumption can be reduced and the quality of titanium sponge can be improved by enhancing the heat transfer in the

reactor. Wang et al. used a waste heat energy recovery system with forced heat transfer design to enhance the surface heat dissipation of the Kroll reactor and thus reduce carbon emissions. Also based on experimental data, a new Nusselt correlation for the heat exchange between cooling air and the outer surface of the reactor or the inner surface of the heater was developed, taking into account the cooling air characteristics, equipment and operating parameters. Subsequently, the Nusselt correlation was innovatively used to evaluate the heat transfer characteristics of the Kroll reactor in titanium sponge production, which is expected to facilitate the commercialization of forced heat transfer design and optimize the titanium sponge production process efficiency. Meanwhile, Yang et al. experimentally investigated the channel heat transfer and the flow characteristics of the fluid in a channel, and obtained a Nusselt correlation to predict the heat transfer characteristics, thus proposing a solution to the blockage of the U-shaped channel in the decompression distillation process of titanium sponge, which helps to reduce the production energy consumption and improve the quality of titanium sponge.

Wang et al. synthesized dual-effect nickel-based catalysts modified by Ce, Mg and Fe, respectively, by the co-precipitation method for enhanced steam reforming of coal tar. The catalysts were investigated for the effect of different doping mass ratios on the syngas composition. How to effectively control the flue gas from coal combustion in thermal power plants has been a Research Topic of interest. Selective catalytic reduction has been widely used as an effective flue gas treatment technology. Xie et al. used reinforcement learning techniques to design an intelligent controller to precisely control the ammonia injection to achieve higher denitrification, effectively reducing the NO_x content, resulting in less secondary pollution.

Although a large number of studies have been devoted to the heat transfer and pressure drop characteristics of condensation in pristine micro-fin tubes. Liu et al. reported the first experimental study on the effect of tube expansion on the heat transfer and pressure drop characteristics during condensation in micro-fin tubes by comparing the performance of micro-fin tubes before and after expansion, which is a very important Research Topic in the field of HVAC. Meanwhile, Liu et al. reported the two-phase flow state and transition of refrigerant R152a throughout the condensation process in a circular glass microchannel, a study of great importance for energy saving and emission reduction in the refrigeration and air conditioning industry. Because of the favorable thermophysical and environmental properties of R152a, it is a potential alternative for R22 and R134a, and it is important to study the two-phase flow state of R152a for low carbon and environmental protection.

Shallow geothermal energy is one of the forms of cooling and heating sources for refrigeration and air conditioning, and energy is extracted through ground source heat pumps. Due to the high initial investment cost of ground source heat pump systems, the local geological environment needs to be evaluated before designing a ground source heat pump to ensure that the energy utilization efficiency of the system is improved. Dong et al. proposed for the ground: firstly, four attribute indices and 11 element indices of geological-hydrological-geological conditions, engineering-geological conditions, thermophysical conditions and environmental conditions of Qingdao area were detected, and then their weights were analyzed and calculated to obtain effective evaluation criteria. The method can provide guidance for the development of ground source heat pumps in specific areas, provide insight into the geothermal energy potential assessment methods, and is particularly valuable for understanding the role of geotechnical conditions in geothermal energy potential.

Thanks to the authors for their attention and support, as well as to the staff of the Research Topic for their careful guidance in this process.

Author contributions

YF provided the original draft preparation; ZZ, ZC and SL provided review and editing; MA and HX provided the conceptualization.

Conflict of interest

The authors declare that the research was conducted in the absence of any commercial or financial relationships that could be construed as a potential conflict of interest.

Publisher's note

All claims expressed in this article are solely those of the authors and do not necessarily represent those of their affiliated organizations, or those of the publisher, the editors and the reviewers. Any product that may be evaluated in this article, or claim that may be made by its manufacturer, is not guaranteed or endorsed by the publisher.



Selective Catalytic Reduction System Ammonia Injection Control Based on Deep Deterministic Policy Reinforcement Learning

Peiran Xie^{1*}, Guangming Zhang¹, Yuguang Niu¹ and Tianshu Sun²

¹State Key Laboratory of Alternate Electric Power System With Renewable Energy Sources, School of Control and Computer Engineering, North China Electric Power University, Beijing, China, ²School of Control and Computer Engineering, North China Electric Power University (Baoding), Baoding, China

OPEN ACCESS

Edited by:

Siyi Luo,
Qingdao University of Technology,
China

Reviewed by:

Safdar Hossain SK,
King Faisal University, Saudi Arabia
İsmail Altın,
Karadeniz Technical University, Turkey

*Correspondence:

Peiran Xie
peiranxiecpu@163.com

Specialty section:

This article was submitted to
Advanced Clean Fuel Technologies,
a section of the journal
Frontiers in Energy Research

Received: 15 June 2021

Accepted: 06 August 2021

Published: 16 August 2021

Citation:

Xie P, Zhang G, Niu Y and Sun T (2021)
Selective Catalytic Reduction System
Ammonia Injection Control Based on
Deep Deterministic Policy
Reinforcement Learning.
Front. Energy Res. 9:725353.
doi: 10.3389/fenrg.2021.725353

The control of flue gas emission in thermal power plants has been a topic of concern. Selective catalytic reduction technology has been widely used as an effective flue gas treatment technology. However, precisely controlling the amount of ammonia injected remains a challenge. Too much ammonia not only causes secondary pollution but also corrodes the reactor equipment, while too little ammonia does not effectively reduce the NOx content. In recent years, deep reinforcement learning has achieved better results than traditional methods in decision making and control, which provides new methods for better control of selective catalytic reduction systems. The purpose of this research is to design an intelligent controller using reinforcement learning technology, which can accurately control ammonia injection, and achieve higher denitrification effect and less secondary pollution. To train the deep reinforcement learning controller, a high-precision virtual denitration environment is first constructed. In order to make the virtual environment more realistic, this virtual environment was designed as a special structure with two decoders and a unique approach was used in fitting the virtual environment. A deep deterministic policy agent is used as an intelligent controller to control the amount of injected ammonia. To make the intelligent controller more stable, the actor-critic framework and the experience pool approach were adopted. The results show that the intelligent controller can control the emissions of nitrogen oxides and ammonia at the outlet of the reactor after training in virtual environment.

Keywords: selective catalytic reduction, deep reinforcement learning, deep deterministic policy, pollution control, nitrogen oxides

INTRODUCTION AND BACKGROUND

In China, thermal power generation is still the main way of generating electricity (Tang et al., 2018). In recent years, with the awakening of people's awareness of environmental protection and increasingly strict environmental protection policies and regulations, pollutant emission control has become an urgent issue for thermal power plants. Among the many pollutants, nitrogen oxides (NOx) have attracted the attention of many scholars because they are highly associated with many serious environmental threats, such as acid rain and photochemical smog. Selective catalytic reduction technology (SCR) is widely used as an efficient denitrification method. The basic

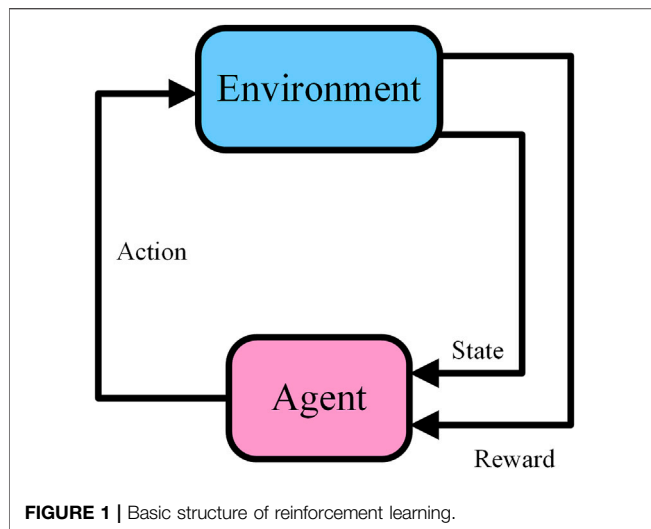
principle of SCR technology is to reduce nitrogen oxides to nitrogen and oxygen by spraying a reductant such as ammonia in the flue gas denitrification reactor. The key to SCR technology is to spray a proper amount of reductant. Ammonia is used as a reducing agent in the SCR reaction, which has some negative effects while eliminating nitrogen oxides. These negative effects include ammonia escape, corrosion of equipment and cost increase. Excess reductant, on the one hand, will enter the atmosphere with the flue gas to cause new pollution, and on the other hand, it will produce corrosive $(\text{NH}_4)_2\text{SO}_4$ and NH_4HSO_4 in the exhaust gas and corrode the equipment (Strege et al., 2008; Du et al., 2017). However, it is difficult to strike a delicate balance between denitrification and side reactions. This is mainly due to fluctuations in NOx concentrations caused by frequent load adjustments in power plants, where the adjustment of the ammonia quantity is significantly slower than the actual demand due to the delayed characteristics of the measurement control system.

In recent years, artificial intelligence technology is considered to provide a new solution to the problems faced by the electricity industry (Khargonekar and Dahleh, 2018; Mishra et al., 2020). The promise of artificial intelligence technology in power systems stems from the great results it has already achieved in other areas. Deep Q-networks (DQN) has achieved results that exceeded human levels in an Atari game environment (Mnih et al., 2015). Deep reinforcement learning techniques have also performed well in autonomous driving tasks. Direct perception (Chen et al., 2015) and end-to-end (Mnih et al., 2016) control were showcased in the open racing car simulator (TORCS) car racing game using deep reinforcement learning. Further, by using the more realistic virtual environment World Rally Championship 6 (WRC6), the deep reinforcement agent was able to learn to drift through the corners, an advanced professional driving technique (Jaritz et al., 2018). Those researches have revealed the superior decision control capability of deep reinforcement learning. By using multi-agents collaboration, deep reinforcement learning is able to cope with more complex environments, where StarCraft is a strategy game in which players need to maintain a clever balance between competition and cooperation in order to achieve victory (Vinyals et al., 2019). Deep reinforcement learning techniques have not only achieved satisfactory results in computer games, but also perform well in real physical systems. Hwangbo et al. designed a deep reinforcement learning controller to control a real quadcopter (Hwangbo et al., 2017). The controller can control the quadcopter to fly stably along a set path, and can also keep the quadcopter stable in response to disturbances. In another research, a deep reinforcement learning controller can make a legged robot move quickly and save battery power. Further, the deep reinforcement learning controller was able to enable the legged robot to recover from a fall, which is usually difficult for traditional control methods (Hwangbo et al., 2019). Because of the excellent performance of deep reinforcement learning, this method is expected to be used in the control of flue gas denitrification process in thermal power plants. The superior performance of deep reinforcement learning in decision

making is expected to determine the optimal amount of ammonia injection to balance the denitrification reaction and ammonia escape.

Reinforcement learning outperforms supervised learning in the control domain due to the “exploration-exploitation” style of learning that differs from supervised learning (Sutton and Barto, 1998). The virtual environment directly affects the performance of the intelligent controller, therefore building a compliant virtual environment is a very important part of this research. An inaccurate virtual environment can lead to bad results known as reality gap. A suitable virtual environment needs to meet both accuracy and responsiveness requirements. Some methods using numerical simulation perform well in terms of accuracy but are too time-consuming (Adamczyk et al., 2014; Stupar et al., 2015). In recent years, data-driven modeling method has been widely adopted by researchers. The main data-driven modeling approaches used in these studies include support vector machines and artificial neural networks (Zhou et al., 2012; Wei et al., 2013; Najafi et al., 2016; Lv et al., 2018). In this research, a model of the denitrification reaction needs to be constructed as an environment for the training of the agent. Since artificial neural networks have more advantages in nonlinear modeling, deep neural networks are used to construct NOx emission models. Details about the NOx model are elaborated in *Denitrification Environment Modeling*. Reinforcement learning agent is used as intelligent controller, which generates actions according to the state of the environment. There are three main approaches to realize reinforcement learning agents: value-based, policy-based and actor-critic algorithms (Sutton and Barto, 1998). Value-based reinforcement learning is not suitable for continuous action space, and policy-based reinforcement learning is more suitable for continuous action space tasks. Generally, the policy can be gaussian distribution or SoftMax policy. Policy-based reinforcement learning tends to be less stable during training and has higher sampling variance. The actor-critic algorithm is to introduce a value function on policy-based reinforcement learning to improve the stability of convergence. Since it combines the advantages of both value-based and policy-based reinforcement learning, the actor-critic algorithm has been intensively studied and several variants have been born. Details about the reinforcement learning intelligent controller are described in *Reinforcement learning intelligent controller*.

In order to reduce the emissions of nitrogen oxides and avoid new pollution caused by excessive ammonia escape, this research attempts to use intelligent controller based on deep reinforcement learning to control the injection of reductant. In this research, many analyses and improvements were used to improve the accuracy of the virtual environment due to the importance of a suitable virtual environment. A reinforcement learning agent with the actor-critic framework was used as an intelligent controller for the denitrification reactor. To make the training process more stable, target networks and soft update methods of parameter updating are used. The whole outline of the paper is presented as follows. The purpose and method of constructing a virtual environment is shown in *Denitrification Environment Modeling*. *Reinforcement learning intelligent controller* describes



the theory and methods for constructing deep deterministic policy reinforcement learning agent. *Experiments and results* describes the details of training the virtual environment and reinforcement learning intelligent controller, respectively. Conclusions and necessary discussions are presented in *Discussion and Conclusion*.

DENITRIFICATION ENVIRONMENT MODELING

This section will focus on the necessity and challenge of building a virtual environment. According to the characteristics of selective catalytic reduction systems, a high precision virtual environment is designed.

The “exploration-exploitation” learning approach is a distinct marker that distinguishes reinforcement learning from other machine learning methods. Deep learning relies on a lot of labeled data, which are the correct results. There is no correctly labeled data in reinforcement learning. The information for reinforcement learning comes from the feedback of an agent’s exploration of the environment. The basic principle of reinforcement learning is shown in **Figure 1**.

Because there are some dangerous results in the process of exploring the environment, and the low efficiency of acquiring experience, agents usually do not train in the real environment. The common research method is to train the agent to a satisfactory state in a virtual environment and deploy the agent in a real environment (Hwangbo et al., 2019). The advantage of using a virtual environment is not only to avoid some dangerous results, but also to improve learning efficiency. Although virtual environments have great advantages, the reality and responsiveness of virtual environments deserve special attention. Related researches indicate the importance of authenticity in virtual environments. The difference between virtual and real can lead to undesirable results known as reality gap (Zagal et al., 2004; Collins et al., 2019; Hwangbo et al., 2019), and a more realistic virtual environment helps agents

learn more specialized skills (Chen et al., 2015; Jaritz et al., 2018). These researches indicate that the virtual environment should reflect the characteristics of the real system as much as possible, and that reducing the reality gap is an effective way to improve the control effectiveness of reinforcement learning controllers. On the other hand, since the agent interacts with the virtual environment several times during the learning process, it requires a fast responsiveness of the virtual environment. This requires that the virtual environment should be as simple as possible, using fewer parameters and neural network units. In general, a good virtual environment needs to have high model accuracy and low computational resource consumption.

There are many challenges to building a good virtual environment. These difficulties are mainly caused by the characteristics of the denitrification reaction. SCR systems are multivariate, nonlinear, large lag systems. Several researches have analyzed the effect of different variables on NO_x emissions from various aspects such as secondary air, excess air coefficient (Díez et al., 2008; Ti et al., 2017; Stupar et al., 2019). The complex physical and chemical reactions that occur in SCR reactors also contain many nonlinear features. The complex physical and chemical reactions that occur in SCR systems make modeling the mechanism difficult and time-consuming. Some studies modeled SCR systems by numerical calculations and computational fluid dynamics methods (Díez et al., 2008; Adamczyk et al., 2014; Belošević et al., 2016; Wang et al., 2017; Mousavi et al., 2021). Although numerical calculations are highly accurate, their unsatisfactory responsiveness makes them unusable for building virtual environments. The data-driven modeling approach has received a lot of attention in recent years, and it usually has higher accuracy and better responsiveness.

Since the data stored in the distributed control system database of the power plant is time series data, Long Short-Term Memory (LSTM) neural networks, which are more suitable for processing time-series data, were chosen to construct the virtual environment (Tan et al., 2019; Yang et al., 2020). LSTM is a recurrent neural network. Different from other neural networks, recurrent neural network cells have connections with cells from previous time steps. Such a cell structure allows recurrent neural networks to have memory capabilities and to integrate information at different time steps. LSTM adds a gating control mechanism to the traditional recurrent neural network; the gating mechanism enables more efficient transfer of information from previous time steps. This improvement makes LSTM not suffer from “long-term dependency” problem. Specifically, the gate control mechanism consists of three gates, the forget gate input gate and the output gate. The forget gate is responsible for avoiding the over propagation of information from previous time steps. The input gate integrates the information from the current time step with the information from the previous time step and passes it to the output gate. The output gate finally combines the information from the previous and current time steps to produce a new message output. LSTM cell structure can be expressed in **Eq. 1**.

$$\begin{aligned}
\text{forget gate: } f(t) &= \sigma(W_{fx}x(t) + W_{fh}h(t-1) + b_f) \\
\text{input gate: } i(t) &= \sigma(W_{ix}x(t) + W_{ih}h(t-1) + b_i) \\
\hat{c}(t) &= \tanh(W_{cx}x(t) + W_{ch}h(t-1) + b_c) \\
c(t) &= f(t)c(t) + i(t)\hat{c}(t) \\
\text{output gate: } o(t) &= \sigma(W_{ox}x(t) + W_{oh}h(t-1) + b_o) \\
h(t) &= o(t)\tanh(c(t))
\end{aligned} \quad (1)$$

Where, x_t is the input at t moment. c_t is the cell state at t moment. h_t is the hidden state at t moment. f_t , i_t and o_t are forget gate, input gate and output gate, respectively. \hat{c}_t is new candidate cell state that could be added to the cell state. w and b are the corresponding weights and biases.

Similar to other neural networks, LSTM can improve nonlinear fitting ability by stacking multiple layers. Some scholars have used multilayer LSTM neural networks to study NOx emission (Tan et al., 2019; Yang et al., 2020), but another network structure with better performance is end-to-end network structure. End-to-end model (Cho et al., 2014; Sutskever et al., 2014) was developed by two Google teams. Although the details of the two are slightly different, the main encoder-decoder structure is the same. The encoder summarizes the information of the input sequence data to generate context information represented by a vector. The decoder generates an output sequence based on the context information. Such structures are widely used in areas such as natural language processing and video analysis, and offer better performance than traditional multilayer neural network structures. The denitrification model needs to provide the data of both NOx concentration and ammonia concentration at the SCR reactor outlet for the agent. In order to calculate the two data more accurately to avoid interfering with each other, two decoders are set up for NOx concentration and ammonia concentration respectively, based on using one decoder to extract the information.

Further considering the effect of multiple variables on the denitrification reaction, attention mechanism was introduced to improve the accuracy of the virtual environment model. Li et al. designed an ammonia injection control method for SCR systems based on leading factor analysis (Gang et al., 2016). In particular, the calculations of the dominant factor analysis indicated that the influence coefficients of different factors with NOx concentrations at different time intervals were dynamically varying. The calculation method of influence coefficient is expressed in Eq. 2.

$$E_m = \frac{1}{N} \sum_{t=1}^N \left\{ \frac{|u_t - u_0|}{u_0} - \frac{|p_{t+m} - p_0|}{p_0} \right\}^2 \quad (2)$$

Where, N is the number of historical samples; u_t is the parameter affecting the reactor inlet NOx concentration at time t ; p_{t+m} is the reactor inlet NOx concentration at time $t+m$; u_0 and p_0 are the average values of the parameters affecting the reactor inlet NOx concentration and the average values of the denitrification reactor inlet NOx concentration, respectively.

To be able to better cope with this dynamic change, the attention mechanism was introduced. Attention mechanisms appeared earlier in the field of computer vision, but have been

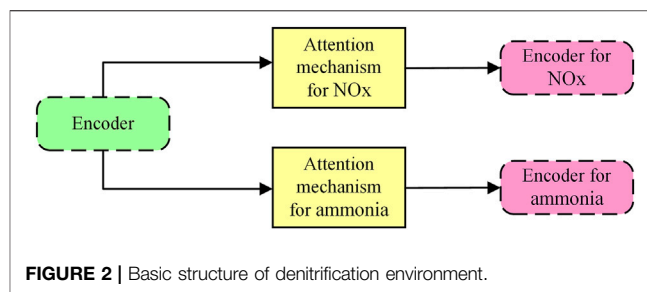


FIGURE 2 | Basic structure of denitrification environment.

more widely used in the field of natural language processing. There are two common attention mechanisms that have been widely used in sequence data, Bahdanau attention and Luong attention (Bahdanau et al., 2015; Luong et al., 2015). The core idea of both is the same, calculating additional weights for data at different time steps to highlight useful information. The two attention mechanisms differ only in the method of calculating attention weights. Similar to the reason for setting two decoders for the SCR reactor outlet NOx and ammonia concentrations separately, it is necessary to calculate the respective attention weights for NOx and ammonia concentrations. Basic structure of denitrification environment is shown in Figure 2.

In this section, the purpose and importance of the virtual environment is presented. By analyzing the characteristics of the SCR system, the requirements of the virtual environment are clarified. For accuracy and responsiveness, a single encoder dual decoder virtual environment with attention mechanism is proposed.

REINFORCEMENT LEARNING INTELLIGENT CONTROLLER

The objective of this research is to attempt to use artificial intelligence controllers to control ammonia injection in selective catalytic reduction systems to achieve a reduction in NOx emissions while reducing ammonia escape. In this research, the controller is the reinforcement learning agent. There are usually three ways to realize the agent, which are value-based, policy-based and actor-critic framework (Csáji and Monostori, 2008; Liu et al., 2020; Yu and Sun, 2020). As shown in Figure 1, the agent acts on the environment through actions and receives the immediate rewards (r) corresponding to the actions from the environment. The agent decides the action according to the state, and the mapping relationship between the state and the action is called a policy denoted by π .

$$\pi: S \rightarrow A \quad (3)$$

The goal of the agent is to find an optimal policy that allows the agent to obtain as many returns (R) from the environment as possible. Rewards and returns have the following relationship as shown in Eq. 4.

$$R_t = r_{t+1} + \gamma r_{t+2} + \gamma^2 r_{t+3} + \dots = \sum_{k=0}^{\infty} \gamma^k r_{t+k+1} \quad (4)$$

Where, R_t is the return at time step t . r_{t+1} is the immediate reward at time step $t+1$. γ is the discount factor.

Value-Based Intelligent Controller

To evaluate a policy, a value function needs to be defined. Such an evaluation is used to reflect how well the strategy is controlled. There are two kinds of value functions which are state value function and state-action value function. The state value function represents the expected return starting from state and then following policy, as shown in Eq. 5.

$$V^\pi(s) = E_\pi[R_t | s_t = s] = E_\pi \left[\sum_{k=0}^{\infty} \gamma^k r_{t+k+1} | s_t = s \right] \quad (5)$$

The state-action value function represents the expected return starting from state, taking action and then following policy, as shown in Eq. 6.

$$Q^\pi(s, a) = E_\pi[R_t | s_t = s, a_t = a] = E_\pi \left[\sum_{k=0}^{\infty} \gamma^k r_{t+k+1} | s_t = s, a_t = a \right] \quad (6)$$

The state value function and the state-action value function have the following relationship, as shown in Eq. 7.

$$\begin{aligned} Q^\pi(s, a) &= E[r_{t+1} + \gamma V^\pi(s_{t+1})] \\ V^\pi(s) &= E_{a \sim \pi(a|s)}[Q^\pi(s, a)] \end{aligned} \quad (7)$$

Solving the optimal policy is equivalent to solving the optimal value function. The method for solving the optimal value function is shown in Eq. 8 and Eq. 9.

$$Q(s_t, a_t) \leftarrow Q(s_t, a_t) + \alpha[r + Q(s_{t+1}, a_{t+1}) - Q(s_t, a_t)] \quad (8)$$

$$Q(s_t, a_t) \leftarrow Q(s_t, a_t) + \alpha \left[r + \max_a Q(s_{t+1}, a_{t+1}) - Q(s_t, a_t) \right] \quad (9)$$

The method of solving the optimal Q value using Eq. 8 is called SARSA (Chen et al., 2007), and the method of solving the optimal Q value using Eq. 9 is called Q-learning (Gomes and Kowalczyk, 2009). After the optimal Q value is obtained, this has two common policies for selecting actions based on the Q value, the greedy policy and the ϵ -greedy policy (Wang et al., 2019). The greedy policy is a deterministic strategy that always picks the largest value function. It is the use of known knowledge by the agent. The ϵ -greedy policy will probabilistically choose the non-maximal value function to represent the exploration of the unknown environment by the agent. As mentioned above, the reinforcement learning method that selects actions according to the value function is called value-based method.

The value-based reinforcement learning method requires that the state-action space is discrete and not too large. Usually, the value function is represented in the form of a table, so it is also called tabular reinforcement learning (Sutton and Barto, 1998). If the state-action space is too large, the table is difficult to converge. There are two main reasons. On the one hand, too large state-action space leads to too many elements in the table, so it is difficult to visit each element enough times to ensure convergence. On the other hand, from a practical point of view, it is very time-consuming to find an element in a very

large table. The method of value function approximation can cope with such a shortcoming (Korda et al., 2016; Wang et al., 2019). The state-action value function is fitted using a function containing the parameter θ . The state-action value function is made to approximate the optimal Q value function by updating the parameter θ , as shown in Eq. 10.

$$Q(s, a, \theta) \approx Q^\pi(s, a) \quad (10)$$

Using a deep neural network as an agent to solve a reinforcement learning problem is deep reinforcement learning. DQN is representative of this approach, which uses two layers of convolutional neural networks and two layers of fully connected layer neural networks (Mnih et al., 2015). DQN generates 18 discrete actions based on the input high-dimensional data. DQN can calculate Q value more accurately because of the good fitting ability of deep neural networks to nonlinear functions. Meanwhile, because neural network has good generalization ability, for unexplored states, neural network can also give reasonable q values according to similar states. The process of fitting the state-action value function by DQN is supervised learning. Label data is indispensable for supervised learning, and the method of making label data is shown in Eq. 11.

$$y = r + \max_a Q(s, a, \theta) \quad (11)$$

Neural network can fit the optimal value function as long as the loss function is minimized. Although function approximation methods using neural networks greatly alleviate the limitations of value-based reinforcement learning methods in high-dimensional state-action space, they are still difficult to solve for continuous action space problems. In this research, the amount of ammonia injection controlled by the intelligent controller is a continuous variable and the value-based method is not suitable for continuous variables. However, the critic in the actor-critic method is usually composed of value-based methods, so the value-based intelligent controller is introduced.

Policy-Based Intelligent Controller

The policy-based reinforcement learning methods can better solve the problem of continuous action space (Lillicrap et al., 2016). Policy-based reinforcement learning and value-based reinforcement learning have the same input, but the output is the probability distribution of actions being selected in the action space. The policy can be represented by the following Eq. 12, where, θ is the parameter to be trained (Sutton et al., 2000).

$$\pi_\theta(s, a) = P(a|s, \theta) \approx \pi(s, a) \quad (12)$$

The method of parameter updating is given by the policy gradient theorem (Peters and Schaal, 2008), as shown in Eq. 13.

$$\begin{aligned} \nabla R_\theta &= \sum_{\tau} R(\tau) \pi_\theta(\tau) \nabla \log \pi_\theta(\tau) \\ &= E_{\tau \sim \pi_\theta(\tau)} [R(\tau) \nabla \log \pi_\theta(\tau)] \end{aligned} \quad (13)$$

Where, τ is the trajectory of states and actions acquired by the agent as it explores the environment, $\tau = \{s_1, a_1, s_2, a_2, \dots, s_t, a_t\}$.

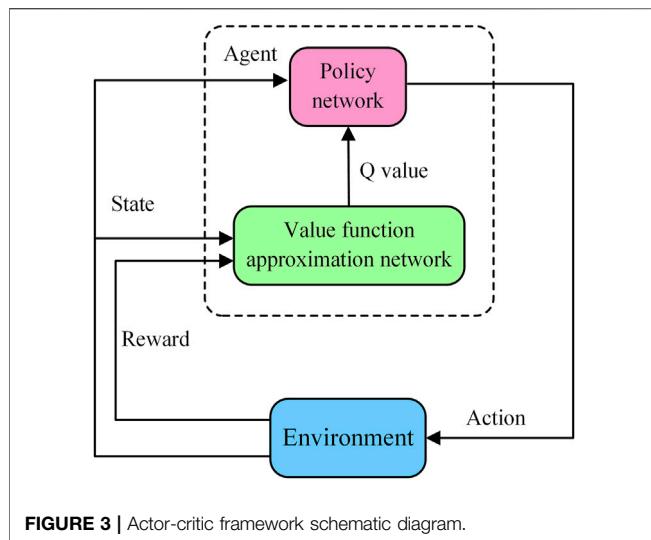


TABLE 1 | The results of MIC analysis.

Variables	MIC
Reactor inlet NOx concentration	0.579951
Reactor inlet oxygen concentration	0.543274
Ammonia injection volume	0.469567
Temperature near ammonia sprayer	0.469331
Temperature near reactor entrance	0.532343
Temperature near boiler outlet	0.556201
Total air volume	0.612232
Active Power of Generator	0.595234
Oxygen Content in Boiler Flue Gas	0.584735
Total fuel consumption	0.549589

Actor-Critic Intelligent Controller

The policy-based approach also has its own drawbacks, such as the tendency to converge to a local optimum rather than a global optimum. The actor-critic approach, a combination of value-based and policy-based reinforcement learning methods integrates the advantages of both. The Actor-Critic method is obtained by replacing the return R in Eq. 13 with the Q value. The new policy gradient is shown in Eq. 14.

$$\nabla R_{\theta} = \sum_{n=1}^N \sum_{t=1}^T Q^{\pi_{\theta}}(a_t^n, s_t^n) \nabla \log \pi_{\theta}(a_t^n | s_t^n) \quad (14)$$

Since Q value is an expectation, using Q value instead of the return R reduces the variance of the experience gained by the agent when exploring the environment, avoiding falling into a local optimum. When the Q value is larger, the gradient of the trainable parameter update is larger, which accelerates the convergence speed of the policy to the optimal direction. In the actor-critic method, the policy network that generates the actions is called the actor and the value function approximation network used to generate the Q value is called the critic. The framework of the actor-critic approach is shown in Figure 3.

This section focuses on the theoretical approach to constructing reinforcement learning intelligent controllers. Other details such as the structure of the intelligent controller will be elaborated in the next section.

EXPERIMENTS AND RESULTS

This section will elaborate on the experimental details of this study. The experiment consists of two main parts: building a virtual environment and training a reinforcement learning intelligent controller. As mentioned earlier, a high precision virtual environment is necessary and critical in order to train reinforcement learning intelligent controllers. In order to obtain a more accurate virtual environment, some effective measures are employed. These measures include data correlation analysis, hyperparameter optimization and unique step-by-step training. In the experiments to train the intelligent controllers, they were designed with different structures and a soft update approach in order to avoid coupling between the actor network and the critic network. Further, important details of the activation function and the reward function are elaborated.

Training Denitrification Environment

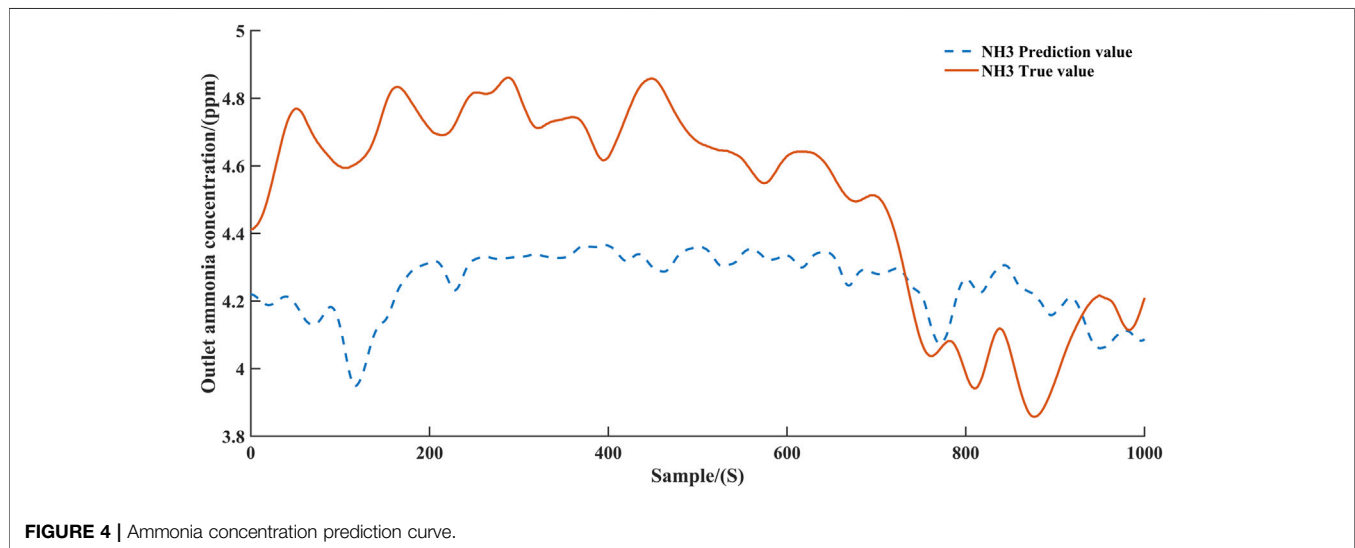
The learning process of reinforcement learning agent completely depends on the exploration of virtual environment, but there is inevitably a slight error between virtual environment and real environment. The error between the virtual environment and the real environment can cause a deterioration in the control of the agent, this phenomenon known as reality gap (Zagal et al., 2004; Collins et al., 2019; Hwangbo et al., 2019). It is important to build a high accuracy virtual environment for training intelligent controllers. In order to have a high accuracy of denitrification environment and reduce the reality gap, various measures including variable screening and validation of neural network models with various structures are taken.

Data-driven modeling approaches are usually data-sensitive, so it is necessary to filter the data to avoid irrelevant variables that reduce model accuracy. In this research, the maximum information coefficient (MIC), a statistical analysis tool, is used to analyze the correlation between variables and to select reasonable input variables to reduce the error caused by irrelevant variables (Reshef et al., 2011). The data used for modeling comes from the real historical data in the distributed control system of power plant, and is analyzed by MIC numerical value. Some variables with strong correlation were selected and the results of their MIC analysis are shown in Table 1.

Another factor that affects the accuracy of the neural network model is the structure and hyperparameters of the neural network. Although the properties of different neural networks are helpful to design models for the denitrification environment, designing the structure of the neural network and determining the hyperparameters need to be validated several times depending on the task. At first, in order to save computing resources and use more computing resources to train agents, a simple multilayer LSTM neural network was adopted. Although such a model consumes less computational resources, the accuracy is not satisfactory. Then, the end-to-end structure is used to replace

TABLE 2 | The raining errors for different models.

Network Structure	5 time steps (%)	10 time steps (%)	20 time steps (%)	
Multi-layer LSTM network	2 layers	7.9420	7.2094	7.0238
	4 layers	6.8226	6.5965	6.3765
	6 layers	6.2329	6.0883	6.1947
Single decoder with attention mechanism	2 layers	33384	3.0631	3.8497
	4 layers	2.9482	2.8395	2.6543
	6 layers	2.7389	2.3173	2.2879
Dual decoders with attention mechanism	2 layers	2.8274	2.4098	2.1062
	4 layers	1.9489	1.8159	1.7975
	6 layers	1.8037	1.7963	1.7498

**FIGURE 4 |** Ammonia concentration prediction curve.

the simple multilayer neural network structure, and attention mechanism is introduced to improve the accuracy of the denitrification environment. The end-to-end structure with an attention mechanism improves the accuracy of the denitrification environment, but considering the phenomenon of reality gap, higher accuracy is still needed. Further, the new structure uses two decoders with attention mechanisms to decode NO_x and ammonia separately, which avoids the coupling of ammonia and NO_x and improves the model accuracy. Finally, the output of the decoder is improved by multi-layer fully connected layer neural network to improve the nonlinear fitting ability. Suitable hyperparameters can improve the accuracy of neural networks. The common hyperparameters include the number of layers and time steps of neural networks. There is no clear theoretical method to determine the most suitable hyperparameters, which needs to be set according to researchers' experience and confirmed by multiple verifications. In this research, multiple validations were implemented to determine the structure and hyperparameters of a high precision denitrification environmental model. The training errors for different structural and hyperparametric models are shown in the table 2.

According to the verification of denitrification environment model structure and hyperparameters, considering the accuracy

of each model and the consumption of computing resources, the dual decoder structure with attention mechanism was selected. The time step is set to 20 and the number of neural network layers is set to 4. In order to make the virtual environment more realistic, a large amount of data was collected from the historical database of the power plant for training the virtual environment. These data include data under different load and operating conditions in order to give a more comprehensive description of the overall situation of the power plant.

To further improve the accuracy of the denitrification environment, a special approach is also taken in the training process of the model. In particular, the training of dual decoder model needs to be carried out step by step. Firstly, the whole model is trained to a relatively low error level. Secondly, the parameters of the encoder and the parameters of NO_x concentration decoders are frozen and only the parameters of ammonia concentration decoder are trained. Finally, only the NO_x concentration decoder parameters that were frozen in the second step are trained. The results of the denitrification environment model are shown in Figure 4, Figure 5, Figure 6 and Figure 7. In training the virtual environment, the first step is the most time-consuming and usually lasts for several days, while

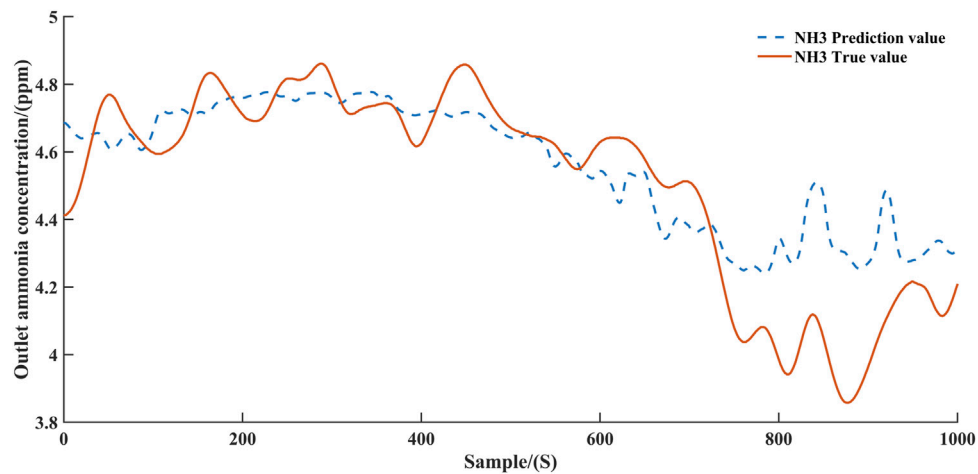


FIGURE 5 | Ammonia concentration prediction curve after parameter freezing training.

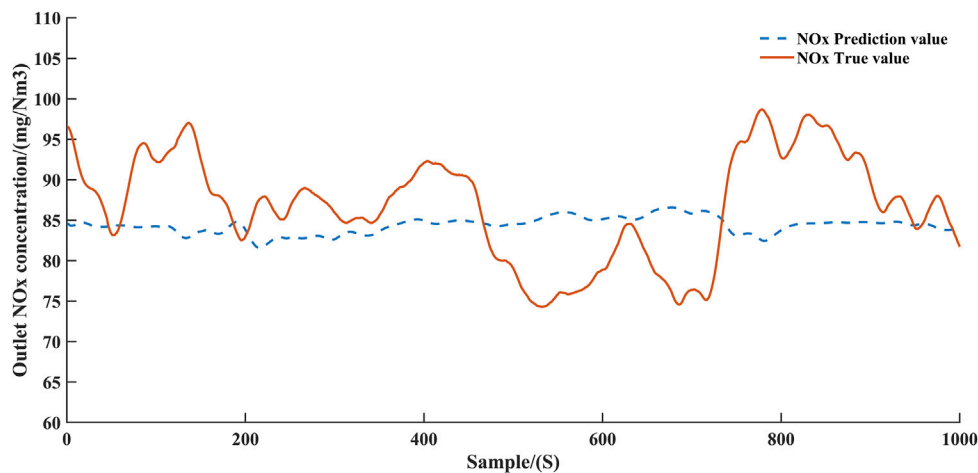


FIGURE 6 | NOx concentration prediction curve.

training the two decoders separately takes relatively less time. The reasons for this phenomenon will be discussed later.

Figure 4 and **Figure 6** demonstrate the predicted values of ammonia concentration and NOx concentration, respectively, after the first step of training. **Figure 5** and **Figure 7** demonstrate the predicted values of ammonia concentration and NOx concentration after parameter freezing training respectively. According to **Figure 4** and **Figure 5** **Figure 6** and **Figure 7**, it can be concluded that the accuracy of the model can be improved by training the model step by step. This can be explained as follows. Since the two decoders share a common encoder, the parameters of the encoder are optimized by the gradients returned by both decoders in the first training step. In this case, the information extracted by the encoder will bring more errors to the two decoders. When the encoder and one decoder are frozen, optimizing the other decoder can prevent the error

from propagating to the final predicted value. Obviously, separate models could be constructed for NOx and ammonia to improve accuracy, but this would increase the consumption of computational resources. The structure of single encoder and double decoder can balance the consumption of computing resources and the accuracy of the model, and devote more computational resources to training the agent.

Training Reinforcement Learning Intelligent Controller

In this research, the reinforcement learning agent is the controller that controls the spraying of ammonia into the SCR reactor. Since the amount of ammonia sprayed is a continuous action space, the deep deterministic policy gradient (DDPG) method is used as the reinforcement learning agent instead of other value-based

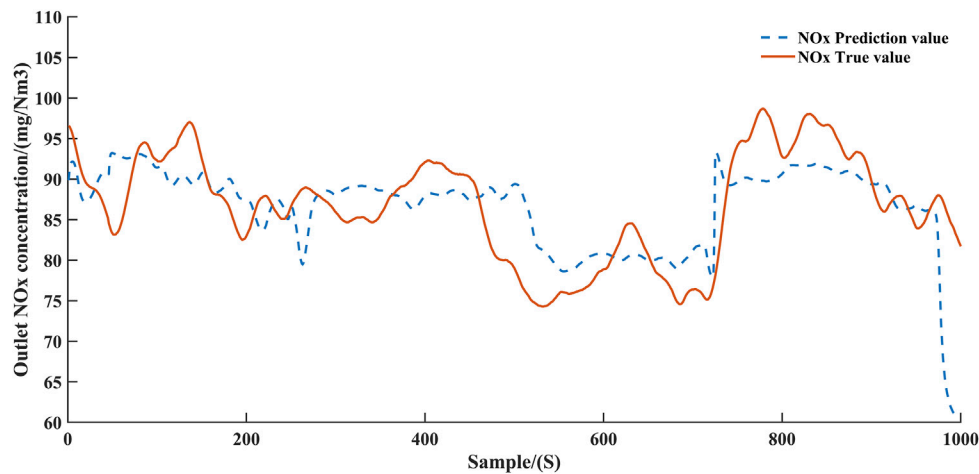


FIGURE 7 | NOx concentration prediction curve after parameter freezing training.

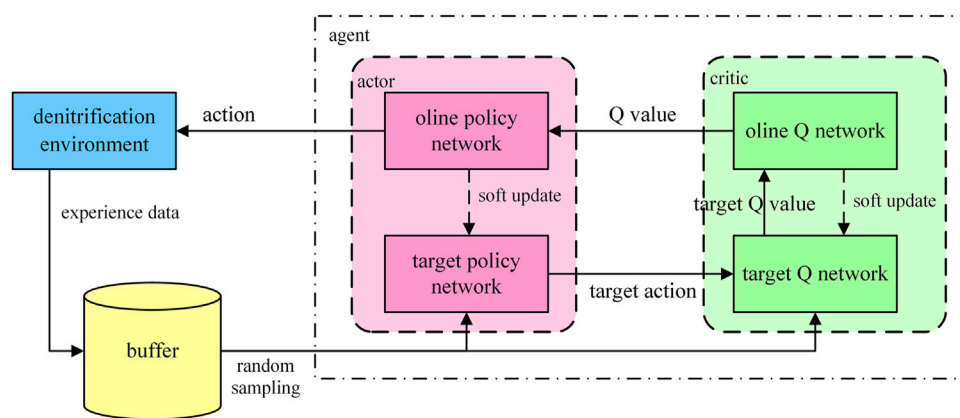


FIGURE 8 | DDPG algorithm flow chart.

reinforcement learning methods. The DDPG algorithm is based on the actor-critic framework, which contains a policy network as the actor and a Q network as the critic. The policy network generates action outputs and the Q network optimizes the parameters of the policy network by evaluating the actions generated by the policy network through Q values.

In order to improve the stability of the agent training, soft updating and buffering methods are adopted. DDPG creates two copies of the policy network and the Q network, called the target policy network and the target Q network, respectively. The target network parameters are updated using the soft update method as shown in Eq. 15.

$$\begin{aligned}\theta^{Q'} &\leftarrow \alpha \theta^Q + (1 - \alpha) \theta^{Q'} \\ \theta^{\mu'} &\leftarrow \alpha \theta^\mu + (1 - \alpha) \theta^{\mu'}\end{aligned}\quad (15)$$

Where, θ is the network parameter. Q' is the target Q network. μ' is the target policy network. α is update step. Different from other policy gradient methods that use random policies, deterministic

policies will only produce one action in one state, which is more suitable for industrial control requirement. Since a deterministic policy is used, the gradient of the policy network is shown in Eq. 16 (Silver et al., 2014).

$$\nabla R_{\theta^\mu} = \frac{1}{N} \sum_{n=1}^N \nabla_a Q(a, s | \theta^Q) \big|_{s=s_t, a=\mu(s_t)} \nabla_{\theta^\mu} \mu(s | \theta^\mu) \big|_{s=s_t} \quad (16)$$

The experience produced by agents in exploring the environment has sequence correlation. In order to avoid the agent falling into local optimum caused by sequence correlation, the delay buffering method is adopted in the research. The experience data obtained by the agent exploring the environment are not trained directly by the agent, but are stored in a buffer. The data of training agent is generated by random sampling in buffer. The structure of DDPG is shown in the Figure 8.

As shown in Figure 8, the agent and the environment contain five neural networks, which require a lot of computational

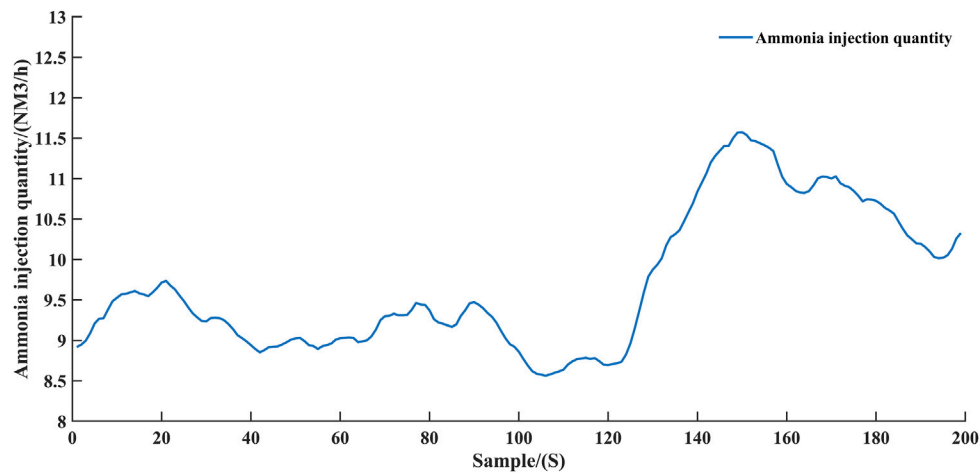


FIGURE 9 | Ammonia injection amount given by agent controller.

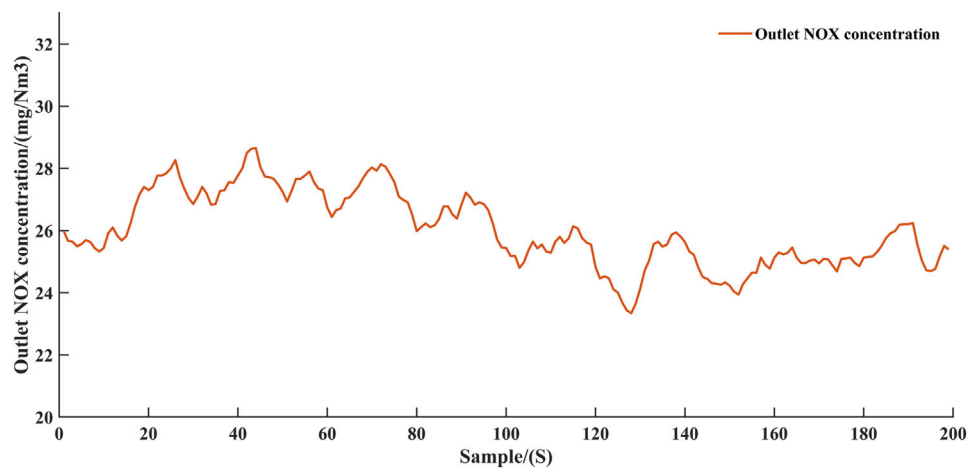


FIGURE 10 | NO_x concentration at the outlet of reactor controlled by agent controller.

resources to support. This is the reason that the structure of the denitrification environment model is designed as two decoders sharing one encoder. Compared with separately designing models for NO_x concentration and ammonia concentration at the outlet of denitrification reactor, this structure can save more computing resources. The computational resources need to be conserved for training the agent during the training agent phase.

After completing the overall architecture design of the reinforcement learning agent, there are still many details to be refined in the design of the actor network and the critic network inside the agent. The first concern is the network structure of the policy network and the value network. LSTM neural network is used as the policy network because the data processed are time series data. In particular, the policy network is designed as a three-layer LSTM neural network. To avoid the coupling caused by the same as the strategy network, the value network is designed as a three-layer one-dimensional convolutional neural network.

Convolution is a classical digital signal processing method. Usually, two-dimensional convolution neural network is used to process image data, and one-dimensional convolution is used to process time series data (Abdeljaber et al., 2017; Antoshchuk et al., 2020).

Another detail worth noting is the activation function of the neural network. Depending on the range of the activation function, the activation function can be divided into saturated and unsaturated activation functions (He et al., 2015; Krizhevsky et al., 2017). The action of the actor network output is the flow of ammonia injected into the denitrification reactor, which reaches a maximum value when the valve is fully open and reaches zero when the valve is fully closed. Such an action range is more suitable using the sigmoid activation function, which can avoid the actor network to produce some unreasonable actions, such as negative or too large flow values. The sigmoid function is a common saturation activation function, whose upper limit is one

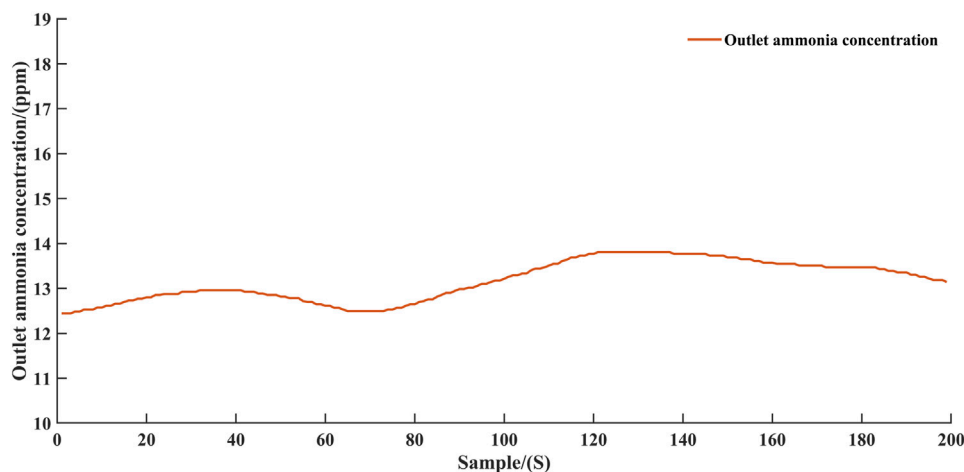


FIGURE 11 | Ammonia concentration at the outlet of reactor controlled by agent controller.

and lower limit is zero. However, the sigmoid activation function also has the drawback of causing the vanishing gradient. Therefore, the sigmoid function is only used as the activation function in the output layer of the actor network. The critic network outputs Q values and does not have upper and lower limits, thus using a non-saturating activation function.

In reinforcement learning, the goal of an agent is formally characterized as a special signal, called reward, which is usually a function of state. At each time step, the reward is a single scalar value. The role of reward is to guide the agent's policy toward the desired outcome. The goal of the controller in this research was to reduce both the NO_x and ammonia concentrations at the outlet of the denitrification reactor. Therefore, the reward function is designed as in the Eq. 17.

$$r = -\alpha C_{NOx} - (1 - \alpha) C_{NH3} \quad (17)$$

Where α is a number between 0 and 1 to tune the style of the reinforcement learning agent's policy. With the increase of α , the agent tends to inject more ammonia to reduce the nitrogen oxide content at the outlet of the reactor. After interactive training with virtual environment, the agent has learned to control ammonia injection to reduce the concentration of nitrogen oxides at the outlet of denitrification reactor. The ammonia injection quality of the agent controller and the concentration of nitrogen oxides and ammonia at the outlet of the reactor are shown in the Figure 9, Figure 10 and Figure 11, respectively. In this experiment, the parameter α in Eq. 17 is set to 0.5, which means that the agent regards the control of nitrogen oxide concentration and ammonia concentration as equally important. The results show a noticeable increase in ammonia injection after 120 steps, which corresponds to a slight overall decrease in NO_x concentration at the outlet of the SCR system. The ammonia escape from the system also tends to increase slightly after 120 steps. Such results are consistent with the empirical common sense that increasing ammonia injection would contribute to the reduction of NO_x emissions but would increase the extent of ammonia escape. On the other hand, such

results indicate that the virtual environment accurately reflects the dynamic characteristics of the system, and that the model structure of the virtual environment and the training methods to improve accuracy are successful and effective.

DISCUSSION AND CONCLUSION

The experiments of this study can be divided into two parts: training the virtual environment and training the intelligent controller. The method of freezing some parameters and setting up a double decoder during the training of the virtual environment significantly improves the accuracy of the virtual environment. In training the virtual environment, the first step is the most time-consuming and usually lasts for several days, while training the two decoders separately takes relatively less time. This is mainly due to the large number of model parameters that need to be optimized in the first training step, which contain the parameters of one encoder and two decoders, respectively. While in the stage of partial parameter freezing, the parameters of one encoder and one decoder are frozen and only the parameters of one decoder need to be optimized.

According to the experimental results, the intelligent controller was able to control the SCR system ammonia injection to reduce the nitrogen oxidation emissions while avoiding excessive ammonia escape. The experimental results validate the feasibility of reinforcement learning in the field of process control. In particular, as shown in Figure 9, the intelligent controller increases the ammonia injection after 120 time-steps. In response to this change, the NO_x concentration at the outlet decreased slightly from around 28 mg/Nm³ to around 26 mg/Nm³ as shown in Figure 10. Such a change also verifies that the intelligent controller is interacting correctly with the virtual environment.

The main contribution of this research consists of two aspects, which are the virtual environment and the intelligent

controller. As mentioned before, the accuracy of the virtual environment has a critical impact on the control effectiveness. The selective catalytic reduction system as the object of research has characteristics such as large latency and multiple inputs and outputs. The model structure designed in this research is well adapted to these characteristics, especially the parameter freezing and step-by-step training methods improve the accuracy of the virtual environment. Since other systems in thermal power plants have similar characteristics to SCR systems, the model structure and training methods in this study can be extended to other systems in thermal power plants. The methods used to construct and train the virtual environment in this research can support more in-depth studies. Another contribution of this research is its validation of the feasibility and effectiveness of using deep reinforcement learning intelligent controllers to control thermal power plant systems. The potential of artificial intelligence techniques in power systems has been noticed by many scholars, but little research has been reported in this area. This research takes a hot artificial intelligence technique, deep reinforcement learning, as an intelligent controller in the field of pollutant emission control, which is currently of wide interest. The experimental results demonstrate that the intelligent controller is able to keep both NO_x emissions and ammonia escaping at low levels. On

the one hand, such results validate the effectiveness of the reinforcement learning intelligent controller for selective catalytic reduction systems, and on the other hand, this study reveals the feasibility of applying deep reinforcement learning techniques to other systems in power plants.

DATA AVAILABILITY STATEMENT

The original contributions presented in the study are included in the article/Supplementary Material, further inquiries can be directed to the corresponding author.

AUTHOR CONTRIBUTIONS

PX: Conceptualization, Methodology, Software Data curation, Writing- Original draft. YN: Writing- Reviewing and Editing. GZ: Writing- Reviewing and Editing. TS: Writing- Reviewing and Editing.

FUNDING

This project was funded by the project supported by the National Key R&D Program of China (2016YFB0600205).

REFERENCES

- Abdeljaber, O., Avci, O., Kiranyaz, S., Gabbouj, M., and Inman, D. J. (2017). Real-time Vibration-Based Structural Damage Detection Using One-Dimensional Convolutional Neural Networks. *J. Sound Vibration* 388, 154–170. doi:10.1016/j.jsv.2016.10.043
- Adamczyk, W. P., Werle, S., and Ryfa, A. (2014). Application of the Computational Method for Predicting NO_x Reduction within Large Scale Coal-Fired Boiler. *Appl. Therm. Eng.* 73, 343–350. doi:10.1016/j.applthermaleng.2014.07.045
- Antoshchuk, S., Babilunha, O., Kim, T. T., Nikolenko, A., and Thi Khanh, T. N. (2020). Non-Stationary Time Series Prediction Using One-Dimensional Convolutional Neural Network Models. *Herald Adv. Inf. Techn.* 3, 362–372. doi:10.15276/hait01.2020.3
- Bahdanau, D., Cho, K. H., and Bengio, Y. (2015). “Neural Machine Translation by Jointly Learning to Align and Translate. arXiv preprint arXiv:1409.0473.
- Belošević, S., Tomanović, I., Crnomarković, N., Miličević, A., and Tucaković, D. (2016). Numerical Study of Pulverized Coal-Fired Utility Boiler over a Wide Range of Operating Conditions for In-Furnace SO₂/NO_x Reduction. *Appl. Therm. Eng.* 94, 657–669. doi:10.1016/j.applthermaleng.2015.10.162
- Chen, C., Seff, A., Kornhauser, A., and Xiao, J. (2015). “DeepDriving: Learning Affordance for Direct Perception in Autonomous Driving,” in Proceedings of the IEEE International Conference on Computer Vision, 2722–2730. doi:10.1109/ICCV.2015.312
- Chen, Y., Mabu, S., Hirasawa, K., and Hu, J. (2007). “Genetic Network Programming with Sarsa Learning and its Application to Creating Stock Trading Rules,” in 2007 IEEE Congress on Evolutionary Computation, 220–227. CEC 2007. doi:10.1109/CEC.2007.4424475
- Cho, K., Van Merriënboer, B., Gulcehre, C., Bahdanau, D., Bougares, F., Schwenk, H., and Bengio, Y. (2014). “Learning Phrase Representations Using RNN Encoder-Decoder for Statistical Machine Translation,” in EMNLP 2014 - 2014 Conference on Empirical Methods in Natural Language Processing, Proceedings of the Conference. doi:10.3115/v1/d14-1179
- Collins, J., Howard, D., and Leitner, J. (2019). “Quantifying the Reality gap in Robotic Manipulation Tasks,” in Proceedings - IEEE International Conference on Robotics and Automation (ICRA), 6706–6712. doi:10.1109/ICRA.2019.8793591
- Csáji, B. C., and Monostori, L. (2008). Value Function Based Reinforcement Learning in Changing Markovian Environments. *J. Machine Learn. Res.* 9 (8).
- Díez, L. I., Cortés, C., and Pallarés, J. (2008). Numerical Investigation of NO_x Emissions from a Tangentially-Fired Utility Boiler under Conventional and Overfire Air Operation. *Fuel* 87, 1259–1269. doi:10.1016/j.fuel.2007.07.025
- Du, X., Yang, G., Chen, Y., Ran, J., and Zhang, L. (2017). The Different Poisoning Behaviors of Various Alkali Metal Containing Compounds on SCR Catalyst. *Appl. Surf. Sci.* 392, 162–168. doi:10.1016/j.apsusc.2016.09.036
- Gang, L. I., Jia, X., Wu, B., Niu, G., and Xue, D. (2016). Spraying Ammonia Flow Control System of SCR Denitration System Based on Leading Factor Analysis. *Therm. Power Generation* 45, 99–102.
- Gomes, E. R., and Kowalczyk, R. (2009). “Modelling the Dynamics of Multiagent Q-Learning with ϵ -greedy Exploration,” in Proceedings of the International Joint Conference on Autonomous Agents and Multiagent Systems, 2, 1181–1182. (AAMAS).
- He, K., Zhang, X., Ren, S., and Sun, J. (2015). “Delving Deep into Rectifiers: Surpassing Human-Level Performance on Imagenet Classification,” in Proceedings of the IEEE International Conference on Computer Vision, 1026–1034. doi:10.1109/ICCV.2015.123
- Hwangbo, J., Lee, J., Dosovitskiy, A., Bellicoso, D., Tsounis, V., Koltun, V., et al. (2019). Learning Agile and Dynamic Motor Skills for Legged Robots. *Sci. Robot.* 4, eaau5872. doi:10.1126/scirobotics.aau5872
- Hwangbo, J., Sa, I., Siegwart, R., and Hutter, M. (2017). Control of a Quadrotor with Reinforcement Learning. *IEEE Robot. Autom. Lett.* 2, 2096–2103. doi:10.1109/LRA.2017.2720851
- Jaritz, M., De Charette, R., Toromanoff, M., Perot, E., and Nashashibi, F. (2018). “End-to-End Race Driving with Deep Reinforcement Learning,” in Proceedings - IEEE International Conference on Robotics and Automation, 2070–2075. doi:10.1109/ICRA.2018.8460934
- Khargonekar, P. P., and Dahleh, M. A. (2018). Advancing Systems and Control Research in the Era of ML and AI. *Annu. Rev. Control.* 45, 1–4. doi:10.1016/j.arcontrol.2018.04.001

- Korda, M., Henrion, D., and Jones, C. N. (2016). Controller Design and Value Function Approximation for Nonlinear Dynamical Systems. *Automatica* 67, 54–66. doi:10.1016/j.automatica.2016.01.022
- Krizhevsky, A., Sutskever, I., and Hinton, G. E. (2017). ImageNet Classification with Deep Convolutional Neural Networks. *Commun. ACM* 60, 84–90. doi:10.1145/3065386
- Lillicrap, T. P., Hunt, J. J., Pritzel, A., Heess, N., Erez, T., Tassa, Y., et al. (2016). “Continuous Control with Deep Reinforcement Learning,” in 4th International Conference on Learning Representations, ICLR 2016 - Conference Track Proceedings, arXiv:1509.02971.
- Liu, C.-L., Chang, C.-C., and Tseng, C.-J. (2020). Actor-critic Deep Reinforcement Learning for Solving Job Shop Scheduling Problems. *IEEE Access* 8, 71752–71762. doi:10.1109/ACCESS.2020.2987820
- Luong, T., Pham, H., and Manning, C. D. (2015). “Effective Approaches to Attention-Based Neural Machine Translation,” in Conference Proceedings - EMNLP 2015: Conference on Empirical Methods in Natural Language Processing, arXiv:1508.04025. doi:10.18653/v1/d15-1166
- Lv, Y., Romero, C. E., Yang, T., Fang, F., and Liu, J. (2018). Typical Condition Library Construction for the Development of Data-Driven Models in Power Plants. *Appl. Therm. Eng.* 143, 160–171. doi:10.1016/j.applthermaleng.2018.07.083
- Mishra, M., Nayak, J., Naik, B., and Abraham, A. (2020). Deep Learning in Electrical Utility Industry: A Comprehensive Review of a Decade of Research. *Eng. Appl. Artif. Intelligence* 96, 104000. doi:10.1016/j.engappai.2020.104000
- Mnih, V., Badia, A. P., Mirza, L., Graves, A., Harley, T., Lillicrap, T. P., et al. (2016). “Asynchronous Methods for Deep Reinforcement Learning,” in 33rd International Conference on Machine Learning, 1928–1937. (ICML 2016).
- Mnih, V., Kavukcuoglu, K., Silver, D., Rusu, A. A., Veness, J., Bellemare, M. G., et al. (2015). Human-level Control through Deep Reinforcement Learning. *Nature* 518, 529–533. doi:10.1038/nature14236
- Mousavi, S. M., Fatehi, H., and Bai, X.-S. (2021). Numerical Study of the Combustion and Application of SNCR for NO Reduction in a Lab-Scale Biomass Boiler. *Fuel* 293, 120154. doi:10.1016/j.fuel.2021.120154
- Najafi, G., Ghobadian, B., Moosavian, A., Yusaf, T., Mamat, R., Kettner, M., et al. (2016). SVM and ANFIS for Prediction of Performance and Exhaust Emissions of a SI Engine with Gasoline-Ethanol Blended Fuels. *Appl. Therm. Eng.* 95, 186–203. doi:10.1016/j.applthermaleng.2015.11.009
- Peters, J., and Schaal, S. (2008). Reinforcement Learning of Motor Skills with Policy Gradients. *Neural Networks* 21, 682–697. doi:10.1016/j.neunet.2008.02.003
- Reshef, D. N., Reshef, Y. A., Finucane, H. K., Grossman, S. R., McVean, G., Turnbaugh, P. J., et al. (2011). Detecting Novel Associations in Large Data Sets. *Science* 334, 1518–1524. doi:10.1126/science.1205438
- Silver, D., Lever, G., Heess, N., Degris, T., Wierstra, D., and Riedmiller, M. (2014). “Deterministic Policy Gradient Algorithms,” in 31st International Conference on Machine Learning, 387–395. (ICML 2014).
- Strege, J. R., Zygarlicke, C. J., Folkedahl, B. C., and McCollor, D. P. (2008). SCR Deactivation in a Full-Scale Cofired Utility Boiler. *Fuel* 87, 1341–1347. doi:10.1016/j.fuel.2007.06.017
- Stupar, G., Tucaković, D., Živanović, T., and Belošević, S. (2015). Assessing the Impact of Primary Measures for NOx Reduction on the thermal Power Plant Steam Boiler. *Appl. Therm. Eng.* 78, 397–409. doi:10.1016/j.applthermaleng.2014.12.074
- Stupar, G., Tucaković, D., Živanović, T., Stevanović, Ž., and Belošević, S. (2019). Predicting Effects of Air Staging Application on Existing Coal-Fired Power Steam Boiler. *Appl. Therm. Eng.* 149, 665–677. doi:10.1016/j.applthermaleng.2018.12.070
- Sutskever, I., Vinyals, O., and Le, Q. V. (2014). “Sequence to Sequence Learning with Neural Networks,” in Advances in Neural Information Processing Systems, 3104–3112.
- Sutton, R. S., and Barto, A. G. (1998). Reinforcement Learning: An Introduction. *IEEE Trans. Neural Netw.* 9, 1054. doi:10.1109/tnn.1998.712192
- Sutton, R. S., McAllester, D., Singh, S., and Mansour, Y. (2000). “Policy Gradient Methods for Reinforcement Learning with Function Approximation,” in Advances in Neural Information Processing Systems, 1057–1063.
- Tan, P., He, B., Zhang, C., Rao, D., Li, S., Fang, Q., et al. (2019). Dynamic Modeling of NOx Emission in a 660 MW Coal-Fired Boiler with Long Short-Term Memory. *Energy* 176, 429–436. doi:10.1016/j.energy.2019.04.020
- Tang, N., Zhang, Y., Niu, Y., and Du, X. (2018). Solar Energy Curtailment in China: Status Quo, Reasons and Solutions. *Renew. Sustain. Energy. Rev.* 97, 509–528. doi:10.1016/j.rser.2018.07.021
- Ti, S., Chen, Z., Li, Z., Min, K., Zhu, Q., Chen, L., et al. (2017). Effect of Outer Secondary Air Vane Angles on Combustion Characteristics and NO Emissions for Centrally Fuel Rich Swirl Burner in a 600-MWe wall-fired Pulverized-Coal Utility Boiler. *Appl. Therm. Eng.* 125, 951–962. doi:10.1016/j.applthermaleng.2017.05.180
- Vinyals, O., Babuschkin, I., Czarnecki, W. M., Mathieu, M., Dudzik, A., Chung, J., et al. (2019). Grandmaster Level in StarCraft II Using Multi-Agent Reinforcement Learning. *Nature* 575, 350–354. doi:10.1038/s41586-019-1724-z
- Wang, J., Zheng, K., Singh, R., Lou, H., Hao, J., Wang, B., et al. (2017). Numerical Simulation and Cold Experimental Research of a Low-NOx Combustion Technology for Pulverized Low-Volatile Coal. *Appl. Therm. Eng.* 114, 498–510. doi:10.1016/j.applthermaleng.2016.11.204
- Wang, Y., Zibaeenejad, A., Jing, Y., and Chen, J. (2019). “On the Optimality of the Greedy Policy for Battery Limited Energy Harvesting Communication,” in IEEE Workshop on Signal Processing Advances in Wireless Communications 2019 (SPAWC). doi:10.1109/SPAWC.2019.8815586
- Wei, Z., Li, X., Xu, L., and Cheng, Y. (2013). Comparative Study of Computational Intelligence Approaches for NOx Reduction of Coal-Fired Boiler. *Energy* 55, 683–692. doi:10.1016/j.energy.2013.04.007
- Yang, G., Wang, Y., and Li, X. (2020). Prediction of the NO Emissions from Thermal Power Plant Using Long-Short Term Memory Neural Network. *Energy* 192, 116597. doi:10.1016/j.energy.2019.116597
- Yu, M., and Sun, S. (2020). Policy-based Reinforcement Learning for Time Series Anomaly Detection. *Eng. Appl. Artif. Intelligence* 95, 103919. doi:10.1016/j.engappai.2020.103919
- Zagal, J. C., Ruiz-Del-Solar, J., and Vallejos, P. (2004). Back to Reality: Crossing the Reality gap in Evolutionary Robotics. *IFAC Proc. Volumes* 37, 834–839. doi:10.1016/s1474-6670(17)32084-0
- Zhou, H., Pei Zhao, J., Gang Zheng, L., Lin Wang, C., and Fa Cen, K. (2012). Modeling NOx Emissions from Coal-Fired Utility Boilers Using Support Vector Regression with Ant colony Optimization. *Eng. Appl. Artif. Intelligence* 25, 147–158. doi:10.1016/j.engappai.2011.08.005

Conflict of Interest: The authors declare that the research was conducted in the absence of any commercial or financial relationships that could be construed as a potential conflict of interest.

Publisher's Note: All claims expressed in this article are solely those of the authors and do not necessarily represent those of their affiliated organizations, or those of the publisher, the editors and the reviewers. Any product that may be evaluated in this article, or claim that may be made by its manufacturer, is not guaranteed or endorsed by the publisher.

Copyright © 2021 Xie, Zhang, Niu and Sun. This is an open-access article distributed under the terms of the Creative Commons Attribution License (CC BY). The use, distribution or reproduction in other forums is permitted, provided the original author(s) and the copyright owner(s) are credited and that the original publication in this journal is cited, in accordance with accepted academic practice. No use, distribution or reproduction is permitted which does not comply with these terms.



Quantifying Heat Transfer Characteristics of the Kroll Reactor in Titanium Sponge Production

Wenhao Wang* and Fuzhong Wu

School of Materials and Metallurgy, Guizhou University, Guiyang, China

OPEN ACCESS

Edited by:

Zongliang Zuo,
Qingdao University of Technology,
China

Reviewed by:

Kun Wang,
Northeastern University, China
Zhen Yao,
Guizhou Normal University, China
Mengqi Wei,
Jiangsu Provincial Academy of
Environmental Science, China

*Correspondence:

Wenhao Wang
whwang@gzu.edu.cn

Specialty section:

This article was submitted to
Advanced Clean Fuel Technologies,
a section of the journal
Frontiers in Energy Research

Received: 17 August 2021

Accepted: 16 September 2021

Published: 30 September 2021

Citation:

Wang W and Wu F (2021) Quantifying
Heat Transfer Characteristics of the
Kroll Reactor in Titanium
Sponge Production.
Front. Energy Res. 9:759781.
doi: 10.3389/fenrg.2021.759781

Various reactors with different sizes have been widely used for the production of titanium sponge in the Kroll process. But the further commercialization of the forced heat transfer design of the Kroll reactor is limited by lack of standard parameter to evaluate its convective heat transfer characteristics. This work proposes to evaluate and compare the Kroll reactor with the dimensionless Nusselt number. The results shown that the heat transfer coefficients for both surfaces increase with the volume flow rate of cooling air for each dimensionless temperature, and the heat transfer coefficients of the external surface of the reactor are higher than that of the internal surface of the heater. And new correlations regarding the Nusselt number between the cooling air and the external surface of the reactor or the internal surface of the heater are obtained based on experimental data, while the characteristics of the cooling air, equipment and operation parameters are considered.

Keywords: dimensionless temperature, heat transfer coefficient, nusselt number, convective heat transfer, titanium sponge

INTRODUCTION

The Kroll process is the most widely preferred industrial choice in titanium chain (Nakamura et al., 2017; Gao et al., 2018; Roux et al., 2019), even if it was of archaic, costly and energy-intensive (Wang et al., 2018b). Some of the major technological breakthroughs and equipment improvements in respect of titanium sponge production relating to the Kroll process have been achieved in the past decades (Gao et al., 2018), and the production cost has been significantly brought down (Zhang et al., 2016). However, further improvement is limited due to the insufficient theoretical understanding of the titanium sponge production (Wang et al., 2018a; Wang W. et al., 2020). For example, several efforts toward energy conservation were reported in the literature, but their commercial application is limited owing to technical or economic constraints (Wang and Wu, 2017). Currently, it's necessary to further decrease the energy consumption and improve energy efficiency of the Kroll process (Krauter et al., 2018).

In response to the problems of the titanium sponge production discussed above, we had exploited a waste thermal energy recovery system with forced heat transfer design to enhance the surface heat dissipation of the Kroll reactor (Figure 1A) (Wang et al., 2017a), and to reduce the carbon emission. The result showed that there was a growth rate of about only 5.00% in the heat transfer rate in a vertical annular duct of the Kroll reactor, while the feeding rate of titanium tetrachloride increases significantly of about 9.61%. Therefore, the forced convective heat transfer system as currently designed was hence expected to reduce the electrical power consumption by improving the production efficiency (shorten the production cycle), rather than by recycling waste thermal energy in the subsequent recovery system (Wang et al., 2017b). It is no doubt that the forced convective heat transfer design lowered the cost and improved the energy

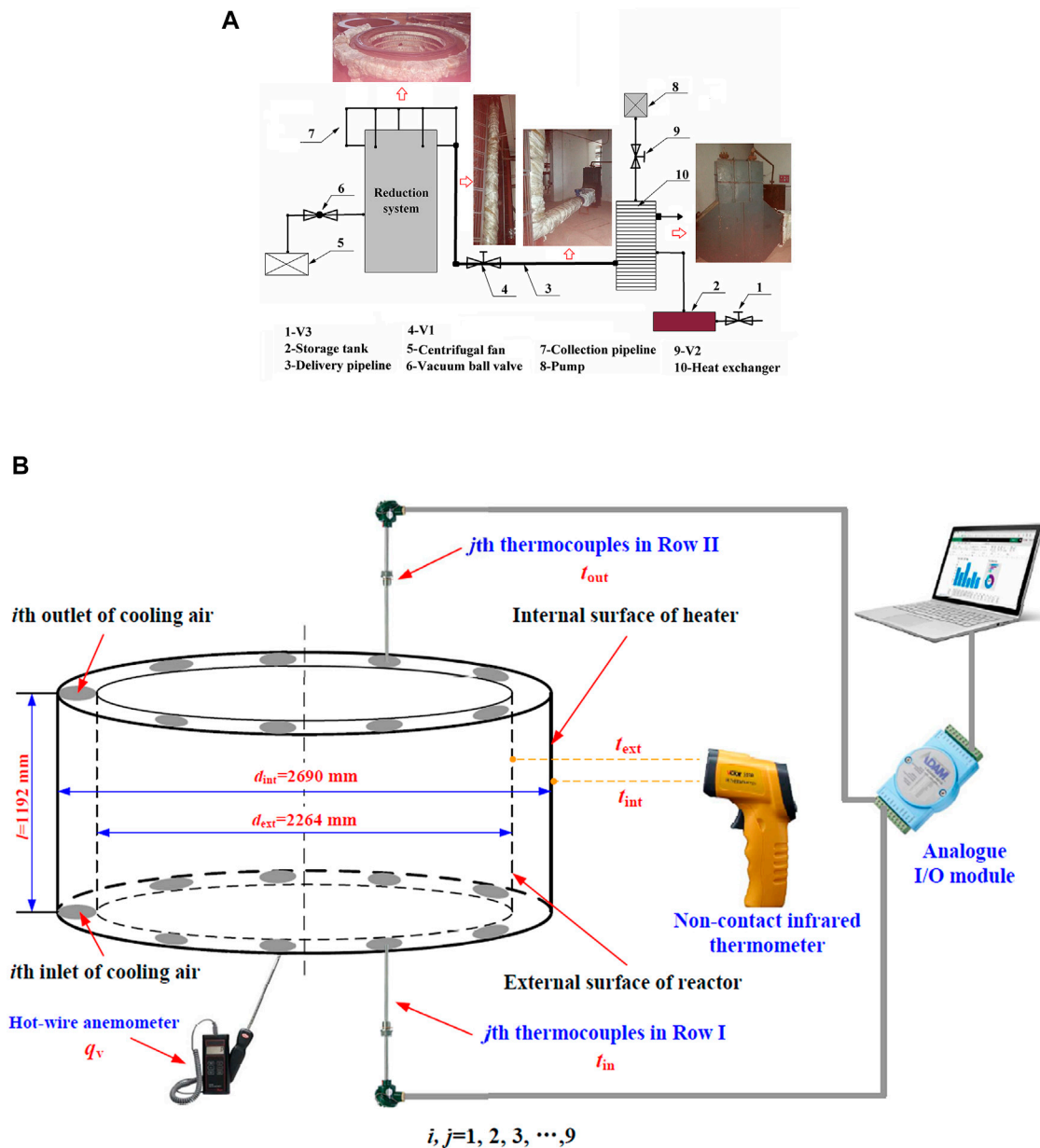


FIGURE 1 | System for: **(A)** enhancing heat transfer and recovering waste thermal energy for the Kroll equipment (Wang et al., 2017b) and **(B)** the experimental apparatus and measurements.

efficiency. However, the quantification and comparison of the heat transfer characteristics of the Kroll reactor with different sizes is difficult due to the lack of a standard method. For example, one previous work evaluated the heat transfer coefficient only based on the cooling air mass flow rate (Wang et al., 2017a). The result could not be compared with other works which study the Kroll reactor with a different size.

This work proposes a dimensionless Nusselt number as a general approach for quantifying and comparing the heat transfer characteristics of the vertical annular duct for the different Kroll reactor. And the Nusselt number has not been used for evaluating the heat transfer characteristics of the Kroll reactor in titanium

sponge production. The establishment of this standard is expected to push the commercialization of the forced heat transfer design and optimizing the efficiency of the titanium sponge production process.

EXPERIMENTAL APPARATUS AND PROCEDURE

The detailed structure of the Kroll equipment in titanium sponge production and the vertical annular duct named air-cooling zone

had been depicted in our previously published works (Wang et al., 2017a; Wang et al., 2017b), and the reducer unit capacity is 12 tons per batch. Therefore, the apparatus and measurements are only represented briefly in the present experiment. The external diameter of the Kroll reactor is $d_{\text{ext}} = 2264$ mm and the internal diameter of the heater is $d_{\text{int}} = 2690$ mm that would surround a concentric vertical annular duct for the Kroll equipment, which is outlined in **Figure 1B** with the present measurements. The thickness of the air-cooling zone is $D_h/2 = 213$ mm, and the length is $l = 1192$ mm. There are nine groups of the inlet and the outlet for the cooling air (Wang et al., 2017a). Both the roughness of the external surface and that of the internal surface are ignored.

The cooling air inlet temperatures, t_{in} , and outlet temperatures, t_{out} , are measured by standard thermocouples (type K, Class II) and collected by the analog I/O module (type ADAM-4018+, 16-channel, 0–1370.0°C). The thermocouples for measuring cooling air inlet temperatures are numbered Row I and that for measuring cooling air outlet temperatures are numbered Row II. The accuracy of the analog I/O module is better than $\pm 0.10\%$ full-scale. The temperature of the TiCl_4 -Mg system in the Kroll reactor, t_c , is extracted from the DCS control system with an accuracy of $\pm 2.0^\circ\text{C}$. The volume flow rate of cooling air, q_v , is measured by a hot-wire anemometer (0.0056 to $0.1405\text{ m}^3/\text{s}$, HHF-SD1) with an accuracy of $\pm 1.00\%$ full-scale stated by manufacturer. The measurements for the temperatures and the volume flow rate of cooling air are all installed near the center of the inlets or outlets. The external surface temperature of the reactor, t_{ext} , and internal surface temperature of the heater, t_{int} , are measured by a non-contact infrared thermometer (-50 – 1370°C , DT-8869H) with an accuracy of $\pm 1.50\%$ full-scale.

The air inlet temperature and the air outlet temperature are the average value of nine measurements, respectively. The air volume flow rate is the sum value of nine measurements. All available experimental data for the natural and the forced convective heat transfer are listed in the **Supplementary Tables S1, S2** in the Supplementary Material, respectively.

TECHNOLOGICAL NOTES

To determine the heat transfer characteristics of the cooling air in both the natural convection and forced convection in the vertical annular duct of the Kroll equipment, the complex heat transfer coefficient and the Nusselt number that due to convection and radiation are analyzed. Experiments and measurements are conducted with stable production process. We firstly analyzed the convective heat transfer characteristics of the cooling air in the vertical annular duct of the Kroll equipment, and a new set of the heat transfer correlations were established by considering the characteristics of cooling air, equipment and operation parameters. In the vertical annular duct, the cooling air absorbs thermal energy from the external surface of the reactor and the internal surface of the heater by convective and radiant heat transfer,

$$Q = Q_{\text{int}} + Q_{\text{ext}} \quad (1)$$

$$Q_{\text{int}} = h_{\text{int}} A_{\text{int}} \Delta t_{\text{int}} = \pi l d_{\text{int}} h_{\text{int}} \Delta t_{\text{int}} \quad (2a)$$

$$Q_{\text{ext}} = h_{\text{ext}} A_{\text{ext}} \Delta t_{\text{ext}} = \pi l d_{\text{ext}} h_{\text{ext}} \Delta t_{\text{ext}} \quad (2b)$$

Where Q is the heat transfer rate due to convection and radiation, h is the complex heat transfer coefficient, A is the heat transfer area, Δt is the logarithmic temperature difference (Wang et al., 2017a), and d is the internal diameter of the heater or the external diameter of the reactor. The subscripts, int and ext, represent the internal surface of the heater and the external surface of the reactor, respectively. The enthalpy energy change of cooling air is calculated by:

$$Q = \int_{t_{\text{in}}}^{t_{\text{out}}} \rho c_p q_v dt \quad (3)$$

Where t_{in} and t_{out} are the inlet and the outlet temperatures of cooling air, q_v is the volume flow rate, ρ and c_p are the density and the specific heat capacity of cooling air, respectively. Then, the Nusselt number is expressed as (Liu et al., 2019; Wang B. et al., 2020):

$$Nu = \frac{h D_h}{\lambda} \quad (4)$$

Where D_h is the characteristic length and λ is the thermal conductivity of cooling air. It could be expected that the Nusselt number is the function of the Rayleigh number for natural convective heat transfer or the function of the Reynolds number and the Prandtl number for forced convective heat transfer, while the physical and the geometrical characteristics would be summarized into dimensionless parameters as follows (Wang B. et al., 2020):

$$Nu = f(Ra, Ct) \text{ for natural convection} \quad (5)$$

$$Nu = g(Re, Pr, Ct) \text{ for forced convection} \quad (6)$$

Where Ra is the Rayleigh number, Re is the Reynolds number, Pr is the Prandtl number, and Ct is the dimensionless temperature. These dimensionless parameters are defined as (Cheng et al., 2019; Chai et al., 2020):

$$Ra = \frac{\rho^2 c_p g \Delta t D_h^3}{\lambda \mu T_s} \quad (7)$$

$$Pr = \frac{\mu c_p}{\lambda} \quad (8)$$

$$Re = \frac{4 \rho q_v}{\pi \mu (d_{\text{ext}} + d_{\text{int}})} \quad (9)$$

$$Ct = \frac{t_c + 273.15}{t_{\text{out}} + 273.15} - 1 \quad (10)$$

Where g is the gravitational acceleration, μ is the viscosity of cooling air, T_s is the temperature of the heat transfer surface in the Kelvin scale.

RESULTS AND DISCUSSIONS

The complex heat transfer coefficients of the natural convection and the forced convection for both heat transfer surfaces are

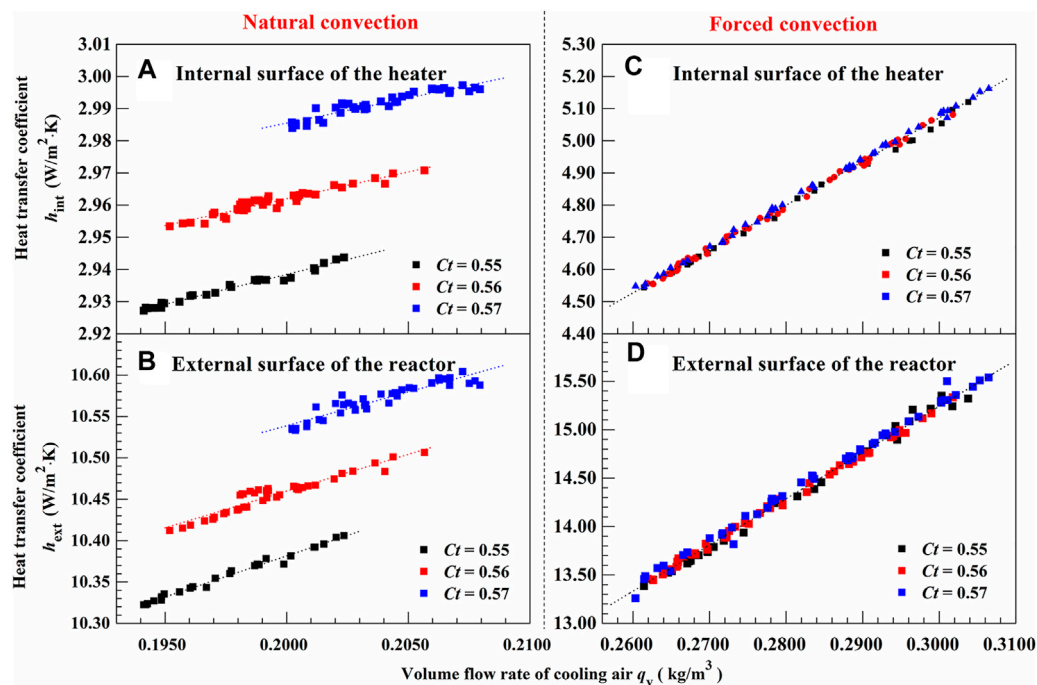


FIGURE 2 | Complex mean heat transfer coefficients of the natural convection and the forced convection.

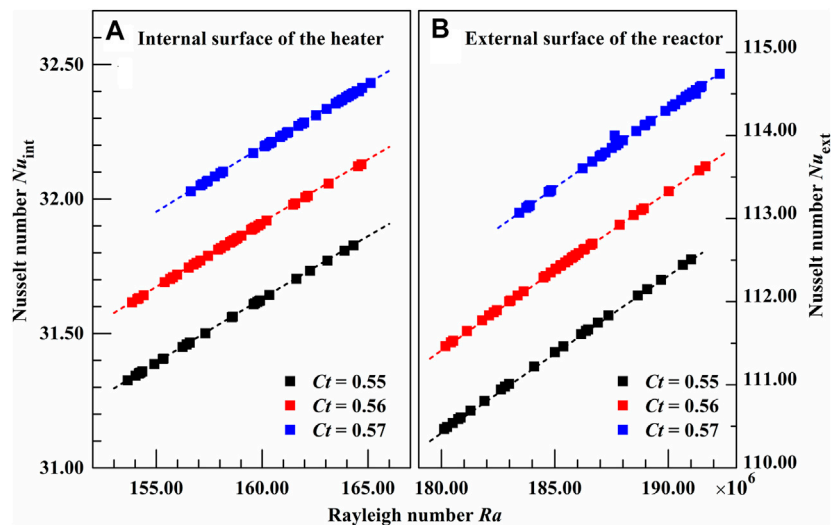


FIGURE 3 | Relationship between Nusselt number and relative dimensionless parameters of the natural convection.

illustrated in **Figure 2**, respectively. Measurements and calculations reveal that the heat transfer coefficients increase linearly with the volume flow rate of the cooling air for each dimensionless temperature. In the case of natural convective heat transfer, as shown in **Figures 2A,B**, higher temperature differences between the cooling air and heat transfer surfaces would lead to a higher volume flow rate of cooling air and higher heat transfer rate. It would be observed that a higher volume flow

rate of the cooling air is correlated with a greater heat transfer rate. Besides, the Rayleigh numbers have a positive correlation with the Nusselt numbers for both heat transfer surfaces, as shown in **Figure 3**. And the Nusselt number increased obviously with the Rayleigh number. Hence, it is possible to improve the heat transfer performance of the air-cooling zone by using a forced convection scheme. For natural convective heat transfer (**Figures 2A,B**), it is clear that the heat transfer coefficient of the

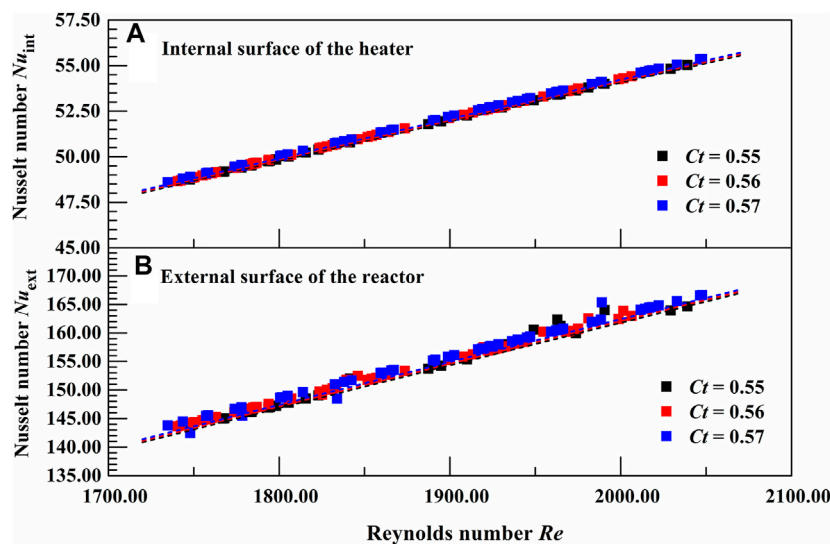


FIGURE 4 | Relationship between Nusselt number and relative dimensionless parameters of the forced convection.

external surface of the reactor is about 3.50 times that of the internal surface of the heater for each dimensionless temperature. Hence, the heat transfer rate of the external surface of the reactor maybe close to 80.00% of the total heat transfer rate. That is, the performance of the vertical annular air-cooling zone of the Kroll equipment is mainly determined by heat transfer between the cooling air and the external surface of the reactor in the case of natural convection.

Besides the air volume flow rate, a higher dimensionless temperature Ct results in a greater heat transfer coefficient for the natural convection, as shown in **Figures 2A,B**. It is understandable that the natural convection in the vertical annular air-cooling zone is driven by the temperature difference between the cooling air and the $\text{TiCl}_4\text{-Mg}$ system in the Kroll reactor. Thus, the Nusselt number also increases with the dimensionless temperature, as shown in **Figure 3**. The Rayleigh number and the dimensionless temperature show important effects on the heat transfer in the natural convection case. Thus, the physical and the geometrical characteristics could be summarized into dimensionless parameters as follows:

The external surface of the reactor:

$$Nu_{\text{ext}} = 0.333Ra_{\text{ext}}^{0.320} Ct^{0.488}, R^2 = 0.994 \quad (11a)$$

The internal surface of the heater:

$$Nu_{\text{int}} = 0.411Ra_{\text{int}}^{0.245} Ct^{0.488}, R^2 = 0.993 \quad (11b)$$

The **Eq. 11** could be used as the criteria for evaluating the performance of the natural convection in the vertical annular air-cooling zone of the Kroll equipment for titanium sponge production. The parameters used include the characteristics of the cooling air, equipment and operation parameters.

In the case of forced convective heat transfer, as shown in **Figures 2C,D**, the complex heat transfer coefficients for both the

external and internal surfaces are investigated. Note that the heat transfer coefficients increase linearly with volume flow rate of the cooling air for all dimensionless temperatures. It would be observed that a higher volume flow rate of the cooling air results in a greater heat transfer rate during forced convection. Thus, the Nusselt numbers for both heat transfer surfaces increase obviously with the Reynolds number, as shown in **Figure 4**.

However, the heat transfer coefficient of the external surface of the reactor is only about 3.00 times that of the internal surface of the heater for all dimensionless temperatures. The heat transfer rate of the external surface of the reactor accounts for about 76.00% of the total heat transfer rate. That is, the performance of the vertical annular air-cooling zone of the Kroll equipment is still mainly determined by the heat transfer between the cooling air and the external surface of the reactor in the case of forced convection.

The purpose of the forced convection in the vertical annular duct of the Kroll equipment is to enhance the heat transfer of the $\text{TiCl}_4\text{-Mg}$ system. The heat transfer coefficients for both heat transfer surfaces are nearly independent with the dimensionless temperature, and so do the Nusselt numbers. Thus, the physical and the geometrical characteristics would be summarized into dimensionless parameters as follows:

The external surface of the reactor:

$$Nu_{\text{ext}} = 0.157Re^{0.921} Ct^{0.104}, R^2 = 0.997 \quad (12a)$$

The internal surface of the heater:

$$Nu_{\text{int}} = 0.144Re^{0.786} Ct^{0.077}, R^2 = 0.996 \quad (12b)$$

The **Eq. 12** could be a design criterion of the forced convection in the vertical annular air-cooling zone of the Kroll equipment for titanium sponge production, while the characteristics of the cooling air, equipment and operation parameters are considered.

CONCLUSION

In summary for quantifying the heat transfer characteristics for the Kroll equipment used in titanium sponge production, this work proposes to calculate the Nusselt numbers based on parameters including the cooling air, equipment and operation. and the heat transfer coefficients for both the external surface of the reactor and the internal surface of the heater are also investigated. The main findings of this study can be listed as follows:

- 1) The heat transfer coefficients for both surfaces increase with the volume flow rate of cooling air for each dimensionless temperature.
- 2) The heat transfer coefficients of the external surface of the reactor are higher than that of the internal surface of the heater.
- 3) The dimensionless temperature has an important effect on the Nusselt number in the natural convective heat transfer, except for the forced convection.
- 4) New correlations regarding the Nusselt number between the cooling air and the external surface of the reactor or the internal surface of the heater are obtained based on experimental data, while the characteristics of the cooling air, equipment and operation parameters are considered.

DATA AVAILABILITY STATEMENT

The original contributions presented in the study are included in the article/**Supplementary Material**, further inquiries can be directed to the corresponding authors.

REFERENCES

- Chai, X., Liu, X., Xiong, J., and Cheng, X. (2020). Numerical Investigation of Turbulent Heat Transfer Properties at Low Prandtl Number. *Front. Energ. Res.* 8, 112. doi:10.3389/fenrg.2020.00112
- Cheng, H., Yanlin, A. B., Wang, J., and Zhao, J. (2019). Diameter Effect on the Wall Temperature Behaviors During Supercritical Water Heat Transfer Deterioration in Circular Tubes and Annular Channels. *Front. Energ. Res.* 7, 73. doi:10.3389/fenrg.2019.00073
- Gao, F., Nie, Z., Yang, D., Sun, B., Liu, Y., Gong, X., et al. (2018). Environmental Impacts Analysis of Titanium Sponge Production Using Kroll Process in China. *J. Clean. Prod.* 174, 771–779. doi:10.1016/j.jclepro.2017.09.240
- Krauter, N., Eckert, S., Gundrum, T., Stefani, F., Wondrak, T., Frick, P., et al. (2018). Inductive System for Reliable Magnesium Level Detection in a Titanium Reduction Reactor. *Metall. Materi Trans. B.* 49 (4), 2089–2096. doi:10.1007/s11663-018-1291-y
- Liu, Z., Yue, Y., She, L., and Fan, G. (2019). Numerical Analysis of Turbulent Flow and Heat Transfer in Internally Finned Tubes. *Front. Energ. Res.* 7, 64. doi:10.3389/fenrg.2019.00064
- Nakamura, K., Iida, T., Nakamura, N., and Arai, T. (2017). Titanium Sponge Production Method by Kroll Process at OTC. *Mater. Trans.* 58 (3), 319–321. doi:10.2320/matertrans.MK201634
- Roux, R. N., Van der Ling, E., and Botha, A. P. (2019). A Systematic Literature Review on the Titanium Metal Product Value Chain. *Sajie* 30 (3), 115–133. doi:10.7166/30-3-2233

AUTHOR CONTRIBUTIONS

WW: conceptualization; data curation; formal analysis; methodology; writing-original draft; project administration. FW: supervision; writing-review and editing.

FUNDING

The authors acknowledge the financial support received from the Science and Technology Foundation of Guizhou Province (grant number QKHJC-ZK 2021-YB261), the National Natural Science Foundation of China (grant number 51874108), and the Talent Projects of Guizhou University and the Education Department of Guizhou Province (grant number GDPY 2019-20, GDRJHZ 2019-14, and QJHKYZ 2021-097).

ACKNOWLEDGMENTS

The authors are grateful to Qiang Liang and Lvguo Zhang of Zunyi Titanium Co., Ltd. for their valuable discussions and experimental batches supply throughout this work. One of the authors, WW, is grateful to Professor Xiang Ge of Guizhou University for his valuable advice. And all co-authors thank the reviewers for the valuable comments and suggestions.

SUPPLEMENTARY MATERIAL

The Supplementary Material for this article can be found online at: <https://www.frontiersin.org/articles/10.3389/fenrg.2021.759781/full#supplementary-material>

- Wang, B., Chen, B., Ke, B., Wang, G., Li, R., Wen, J., et al. (2020a). Analysis of the Flow Characteristics of the Liquid Film on the Wall Surface of the Corrugated Plate Dryer Based on PSD Method: A Short Communication. *Front. Energ. Res.* 8, 215. doi:10.3389/fenrg.2020.00215
- Wang, W., and Wu, F. (2017). Exergy Destruction Analysis of Heat Exchanger in Waste Heat Recovery System in Kroll Process. *Ijex* 22 (1), 89–101. doi:10.1504/IJEX.2017.10001122
- Wang, W., Wu, F., and Jin, H. (2017a). Enhancement and Performance Evaluation for Heat Transfer of Air Cooling Zone for Reduction System of Sponge Titanium. *Heat Mass. Transfer* 53 (2), 465–473. doi:10.1007/s00231-016-1836-z
- Wang, W., Wu, F., and Jin, H. (2020b). Gaseous P-V-T Property Measurements for Titanium Tetrachloride from 873.0 to 1173.0 K and Low Pressure of 34.05 kPa. *ACS Omega* 5 (30), 18573–18578. doi:10.1021/acsomega.0c00667
- Wang, W., Wu, F., and Yu, Q. (2017b). Feasibility Study for Recovering Waste Heat in Reduction System of Kroll Process: Energy Analysis and Economic Valuation. *Russ. J. Non-ferrous Met.* 58 (3), 258–268. doi:10.3103/S1067821217030208
- Wang, W., Wu, F., Yu, Q., and Jin, H. (2018a). Experimental Investigation of Titanium Tetrachloride in Pool Boiling Heat Transfer. *Int. J. Heat Mass Transfer* 122, 1308–1312. doi:10.1016/j.ijheatmasstransfer.2018.02.051
- Wang, W., Wu, F., Yu, Q., and Jin, H. (2018b). Interfacial Liquid-Vapor Phase Change and Entropy Generation in Pool Boiling Experiment for Titanium Tetrachloride. *J. Therm. Anal. Calorim.* 133 (3), 1571–1578. doi:10.1007/s10973-018-7203-1

Zhang, Y., Fang, Z. Z., Xia, Y., Huang, Z., Lefler, H., Zhang, T., et al. (2016). A Novel Chemical Pathway for Energy Efficient Production of Ti Metal from Upgraded Titanium Slag. *Chem. Eng. J.* 286, 517–527. doi:10.1016/j.cej.2015.10.090

Conflict of Interest: The authors declare that the research was conducted in the absence of any commercial or financial relationships that could be construed as a potential conflict of interest.

Publisher's Note: All claims expressed in this article are solely those of the authors and do not necessarily represent those of their affiliated organizations, or those of

the publisher, the editors and the reviewers. Any product that may be evaluated in this article, or claim that may be made by its manufacturer, is not guaranteed or endorsed by the publisher.

Copyright © 2021 Wang and Wu. This is an open-access article distributed under the terms of the Creative Commons Attribution License (CC BY). The use, distribution or reproduction in other forums is permitted, provided the original author(s) and the copyright owner(s) are credited and that the original publication in this journal is cited, in accordance with accepted academic practice. No use, distribution or reproduction is permitted which does not comply with these terms.



Enhanced Reforming of Tar Based on Double-Effect Ni/CaO–Ca₁₂Al₁₄O₃₃ Catalysts: Modified by Ce, Mg, and Fe

Panlei Wang^{1,2}, Weidong Zhang², Zhenyu Yu², Huaqing Xie^{2*}, Mi Zhou^{1,2*} and Zhengyu Wang²

¹Key Laboratory of Metallurgical Emission Reduction and Resources Recycling, Ministry of Education (Anhui University of Technology), Maanshan, China, ²School of Metallurgy, Northeastern University, Shenyang, China

OPEN ACCESS

Edited by:

Akshat Tanksale,
Monash University, Australia

Reviewed by:

Ningbo Gao,
Xi'an Jiaotong University, China
Wenhao Wang,
Guizhou University, China

*Correspondence:

Huaqing Xie
huaqing_2008@163.com
Mi Zhou
zhoum@mail.neu.edu.cn

Specialty section:

This article was submitted to
Advanced Clean Fuel Technologies,
a section of the journal
Frontiers in Energy Research

Received: 24 June 2021

Accepted: 06 September 2021

Published: 06 October 2021

Citation:

Wang P, Zhang W, Yu Z, Xie H, Zhou M
and Wang Z (2021) Enhanced
Reforming of Tar Based on Double-
Effect Ni/CaO–Ca₁₂Al₁₄O₃₃ Catalysts:
Modified by Ce, Mg, and Fe.
Front. Energy Res. 9:729919.
doi: 10.3389/fenrg.2021.729919

The double-effect Ni-based catalysts, modified with Ce, Mg, and Fe and synthesized by the coprecipitation method, were applied into the enhanced steam reforming process of real tar. The effects of the catalysts with different doping mass proportions (3, 6, 9, and 12%) of Ce, Mg, and Fe on the H₂ yield, and H₂ and CO₂ concentrations were studied. The results revealed that the tar reforming efficiency was improved with appropriate proportions of the additives added. The Ce- or Mg-doped catalyst could change the distribution or morphology of the active component Ni. The modified catalyst with 6% Ce or 3% Mg doping showed the best catalytic activity in the reforming experiment, with the H₂ yield reaching 86.84% or 85.22%, respectively. The Fe-doped catalyst could form an Ni–Fe alloy and improve the stability of the catalyst, and the better catalytic activity can be obtained at 9 and 12% Fe doping, with the H₂ yield reaching 85.54 and 85.80%, respectively.

Keywords: tar, double-effect catalyst, CO₂ adsorption, enhanced reforming, hydrogen production

INTRODUCTION

Coal gasification plays an important role in the coal chemical industry, while tar is the main by-product of this process. In China, the total output of coke was 473.1 million tons in 2019, with about 19 million tons of tar as the by-product. The composition of tar is complex, and it is estimated to include more than ten thousand compounds. Distinguish by boiling point, tar includes light oil, phenol oil, naphthalene oil, washing oil, onion oil, and coal tar pitch (Li and Suzuki, 2010; Li et al., 2013; Duan et al., 2017). Tar is gaseous at high temperature and liquid at low temperature, which will easily corrode the pipeline equipment. In addition, it can cause harm to the ecology and the human body if discharged into the environment (Xie et al., 2016a; Zeng et al., 2018; Li et al., 2021; Zuo et al., 2021). The methods of tar removal include physical and chemical methods. The physical method is to remove the tar from the syngas through the principle of absorption and adsorption, such as water washing, oil washing to absorb tar, or using porous media to adsorb tar onto its surface. The physical method has the advantages of simple operation and a low equipment cost, but there are some disadvantages such as secondary pollution and low removal efficiency (Xie et al., 2016c). The chemical method mainly includes the pyrolysis method and reforming method (partial oxidation reforming and steam reforming). The pyrolysis method refers to the tar cracking at high temperature to produce non-condensable small molecules of gas, which increases the cost due to the need of adding additional heat sources (Torres et al., 2007). The partial oxidation reforming method

can effectively convert tar into small molecular gases such as H_2 and CO , but the process is mainly conducted at a higher temperature (about $1,200^\circ C$), by consuming a large amount of pure oxygen and additional fuel to supply heat (Onozaki et al., 2006). The steam reforming method prefers to obtain hydrogen-rich gas under the action of steam and catalyst. Compared with the partial oxidation reforming method, the temperature of this method is lower (about $800^\circ C$), with no additional O_2 and less heat. Thus, steam reforming of tar and its model compounds for hydrogen production has received extensive attention in recent years (Furusawa et al., 2013; Duan et al., 2015; Li et al., 2015; Dou et al., 2016; Duan et al., 2018; Xie et al., 2018).

Catalysts are key to steam reforming of tar, and many catalysts have been studied so far. The commonly used catalysts mainly include dolomite (Gusta et al., 2009; Sarioğlu, 2012), olivine (Virginie et al., 2012), alkali metal (Jiang et al., 2015), Ni-based catalysts (Richardson et al., 2010; Chan and Tanksale, 2014; Xie et al., 2015), and noble metal catalysts (Furusawa et al., 2013; Mei et al., 2013). Considering the catalyst efficiency and cost, the Ni-based catalyst is one of the most promising catalysts for tar reforming. However, inhibiting its carbon formation and improving its catalytic stability are the urgent problems to be solved (Yue et al., 2010; Gao et al., 2015). As a carrier, $Ca_{12}Al_{14}O_{33}$ can improve the reactivity and the anti-carbon property of the Ni-based catalyst. It itself can also be used as a catalyst for cracking tar, and the synergistic with Ni addition can further inhibit the carbon formation (Li et al., 2009). However, common steam reforming reactions yield only 70% (volume fraction) H_2 and more than 20% CO_2 , limiting the use of such a hydrogen-containing gas (Xie et al., 2016d). So, researchers try to add adsorption components to the original catalyst and combine the catalytic reforming process with the CO_2 adsorption process. The adsorbent components can break the balance of the original reforming reaction, improving the quality and concentration of H_2 , and the carbon deposition on the catalyst can be effectively reduced (Kinoshita and Turn, 2003; Dou et al., 2016; Xie, et al., 2016b; Zuo et al., 2020). In the adsorption-enhanced process, CaO is widely used as the CO_2 adsorbent due to its low cost and easy accessibility. However, CaO is easy to be sintered at high temperatures, resulting in a decrease in the adsorption capacity (Zamboni et al., 2011). As mentioned above, as a carrier, $Ca_{12}Al_{14}O_{33}$ has a special free oxygen storage structure, which can also effectively inhibit the sintering of CaO when carried within $Ca_{12}Al_{14}O_{33}$ (Li et al., 2009). Thus, the double-effect Ni/ CaO - $Ca_{12}Al_{14}O_{33}$ catalyst was prepared and applied to the steam reforming process of 1-methylnaphthalene ($C_{11}H_{10}$) as a tar model component in our previous study, showing a good catalytic activity and CO_2 adsorption capacity (Zhang et al., 2021a; Zhang et al., 2021b). However, the double-effect catalyst has not been applied in the reforming of real tar, and because of its component's complexity, the catalytic performance on the reforming process of real reforming

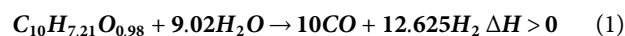
may be decreased compared to that on the model component. According to the literature, the catalytic activity and anti-carbon property of the Ni-based catalyst can be improved by adding additives such as precious metals (Pt, Rh, Ru, etc.) (Mei et al., 2013; Cai et al., 2014), rare earth metals (La, Ce, etc.) (Kimura et al., 2006; Tomishige et al., 2007; Mazumder and Lasa., 2015), alkali earth metals (Ca, Mg, etc.) (Wang et al., 2006; Ashok et al., 2015; Nakhaei and Mousavi, 2015), and transition metals (Fe, Co, etc.) (Wang et al., 2011; Koike et al., 2012; Wang et al., 2013). Considering the cost, Ce (rare earth metal), Mg (alkali earth metal), and Fe (transition metal) were studied in this article.

In this article, modified double-effect Ni-based catalysts were prepared and applied to the enhanced reforming process of real tar. The double-effect Ni-based catalysts with different additives (Ce, Mg, and Fe) of different doping mass proportions (3, 6, 9, and 12%) were synthesized by the coprecipitation method and were characterized by X-ray diffraction (XRD) and scanning electron microscopy (SEM). Then, the effects of different modified double-effect catalysts on the hydrogen production from the enhanced reforming of tar were studied, and the result was compared with that over the unmodified double-effect Ni-based catalyst.

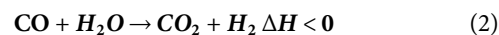
EXPERIMENTAL

Tar Sample

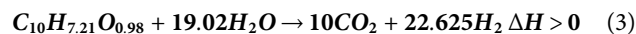
The raw tar sample came from a coking plant in Liaoning province, China. The sample was preheated by distillation to remove moisture and solid-phase impurities prior to the chemical composition analysis. Elementar (vario MACRO cube, Germany) was used for the elemental analysis of tar, and the results show that the molar content of C is 54.50%, H is 39.27%, O is 5.32%, N is 0.70%, and S is 0.21%. The chemical formula of the sample can be simplified to $C_{10}H_{7.21}O_{0.98}$, ignoring nitrogen and sulfur that were too low compared with other elements. Therefore, the steam reforming (SR) reaction of tar can be expressed by the following equation:



and following the water-gas shift (WGS) reaction, we obtain



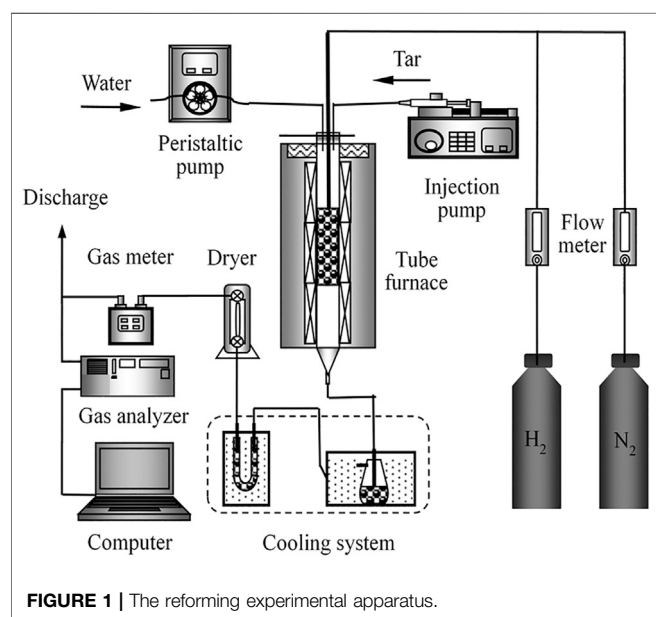
Thus, the total steam reforming reaction can be written as follows:



GC-MS (Agilent 5975-7890A, Shanghai Tianmei) was used for the composition analysis of tar. Specific operating conditions are as follows: 1) Chromatographic conditions: Hp-5 chromatographic column; oven temperature program was as follows: maintain 1 min at $60^\circ C$ as the starting temperature, heat to $280^\circ C$ with the heating rate of $15^\circ C/min$, and maintain for 5 min; and He as the carrier gas with the shunt ratio of 1:100. 2) Mass spectrometry conditions: solvent delay for 4 min; ionization source: EI; electron bombardment energy: 70 eV ;

TABLE 1 | Constituent analysis of tar.

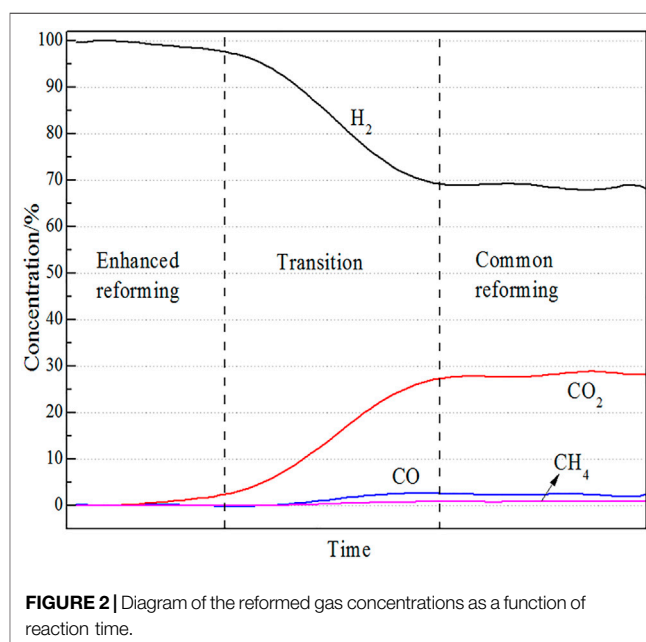
Number	Component	Molecular formula	Mole content/%
1	Indane	C_9H_8	1.753
2	Indene	C_9H_{10}	1.241
3	Naphthalene	$C_{10}H_8$	47.213
4	2-Benzothiophene	C_8H_6S	1.045
5	Naphthalene, 1-methyl-	$C_{11}H_{10}$	5.433
6	Naphthalene, 2-methyl-	$C_{11}H_{10}$	2.154
7	Biphenyl	$C_{12}H_{10}$	1.280
8	Naphthalene, 2,7-dimethyl-	$C_{12}H_{12}$	0.881
9	Naphthalene, 1,4-dimethyl-	$C_{12}H_{12}$	0.796
10	Naphthalene, 2,6-dimethyl-	$C_{12}H_{12}$	0.488
11	Acenaphthene	$C_{12}H_{10}$	7.059
12	Dibenzofuran	$C_{12}H_8O$	4.255
13	Fluorene	$C_{13}H_{10}$	5.991
14	[1,1'-Biphenyl]-4-carboxaldehyde	$C_{13}H_{10}O$	0.612
15	Dibenzofuran, 4-methyl-	$C_{13}H_{10}O$	0.671
16	Dibenzothiophene	$C_{12}H_8S$	1.247
17	Phenanthrene	$C_{14}H_{10}$	10.978
18	Anthracene	$C_{14}H_{10}$	1.655
19	Phenanthrene, 1-methyl-	$C_{15}H_{12}$	0.435
20	4H-Cyclopenta[def]phenanthrene	$C_{15}H_{10}$	0.594
21	Fluoranthene	$C_{16}H_{10}$	2.698
22	Pyrene	$C_{16}H_{10}$	1.521



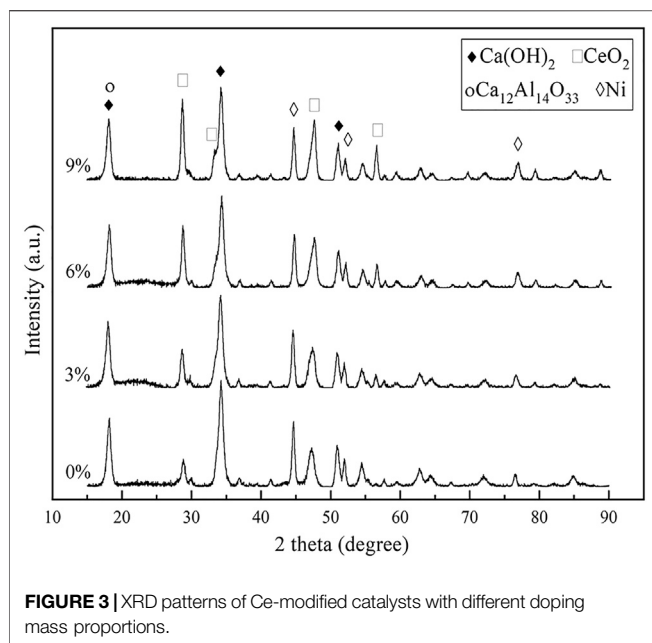
electronic multiplier voltage: 1200 V; and quality range: 30–600 amu, with the scanning interval of 0.5 s. Through the GC-MS analysis, a total of 22 major compounds were detected, among which the naphthalene content was the highest (given in **Table 1**).

Catalyst Preparation

The modified double-effect Ni-based catalysts were prepared by the coprecipitation method, with the mass proportion of Ni (catalytic component):CaO (adsorption component): $Ca_{12}Al_{14}O_{33}$ (carrier component) being 15:70:15. Meanwhile, Ce (Mg or Fe) was doped as the additive, with mass proportions of 3, 6,



9, or 12%. The catalyst preparation process needed to undergo a series of dissolving, stirring, drying, and calcination processes as follows: First, $Ca(CH_3COO)_2$ was calcined at 900°C for 2 h, to obtain high-activity CaO. Second, a certain quality of CaO, $Al(NO_3)_3 \cdot 9H_2O$, $Ni(NO_3)_2 \cdot 6H_2O$, and Ce (or Mg, Fe) were mixed with deionized water to form a suspension. Then, the suspension was stirred for 3 h, dried for 12 h at 120°C, and then calcined at 500°C for 3 h. Afterward, the calcined solid was cooled and formed into a suspension by adding deionized water again, followed by stirring and drying. Finally, the dried solid was calcined at 1,000°C for 4 h to obtain a catalyst.



Experimental Apparatus

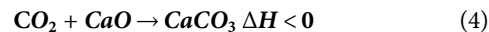
The experimental apparatus for the reforming experiment is shown in **Figure 1**. The modified double-effect catalyst was kept in a three-stage temperature control tube furnace. The tar and deionized water were pumped into the stainless-steel downstream reactor drop by dropping through an injection pump and a peristaltic pump with 600 ml/min N_2 carrier gas. To ensure the good fluidity of tar, the syringe was wrapped with a

heating belt, keeping the wall temperature above 50°C. The product gas in the reactor was cooled and dried successively, and finally detected by a gas meter and a gas analyzer.

Experimental Design and Assessment

In this article, the catalytic performances of the modified double-effect catalysts were assessed under the optimal experimental condition based on the previously enhanced reforming experiment result with the unmodified catalyst (temperature = 740°C, S/C (the mole ratio of steam to carbon in tar) = 15, and WHSV (weight hourly space velocity) = 0.0447 h⁻¹).

The experimental process of the tar reforming can be divided into two stages: enhanced reforming stage and common reforming stage (shown in **Figure 2**). For the enhanced reforming stage, CO_2 generated via the WGS reaction (**Eq. 2**) was adsorbed by CaO in the double-effect catalyst (adsorption reaction, **Eq. 4**). Then, the equilibriums of the steam reforming reactions of tar were transferred to the direction of hydrogen production, with the CH_4 and CO concentrations being very low and the H_2 concentration being quite high. As the time went by, the concentration of CO_2 was increased and that of H_2 was decreased because the CO_2 adsorption capacity of the double-effect catalyst tended to be saturated. Finally, the H_2 and CO_2 concentrations tended to be stable, about 70 and 25%, respectively, which were similar with those of the dry reformed gas without adding any CO_2 adsorbent, and thus, such a stage was considered as a common reforming stage (Xie et al., 2018; Zhang et al., 2021b),



The main indicators in this article were as follows.

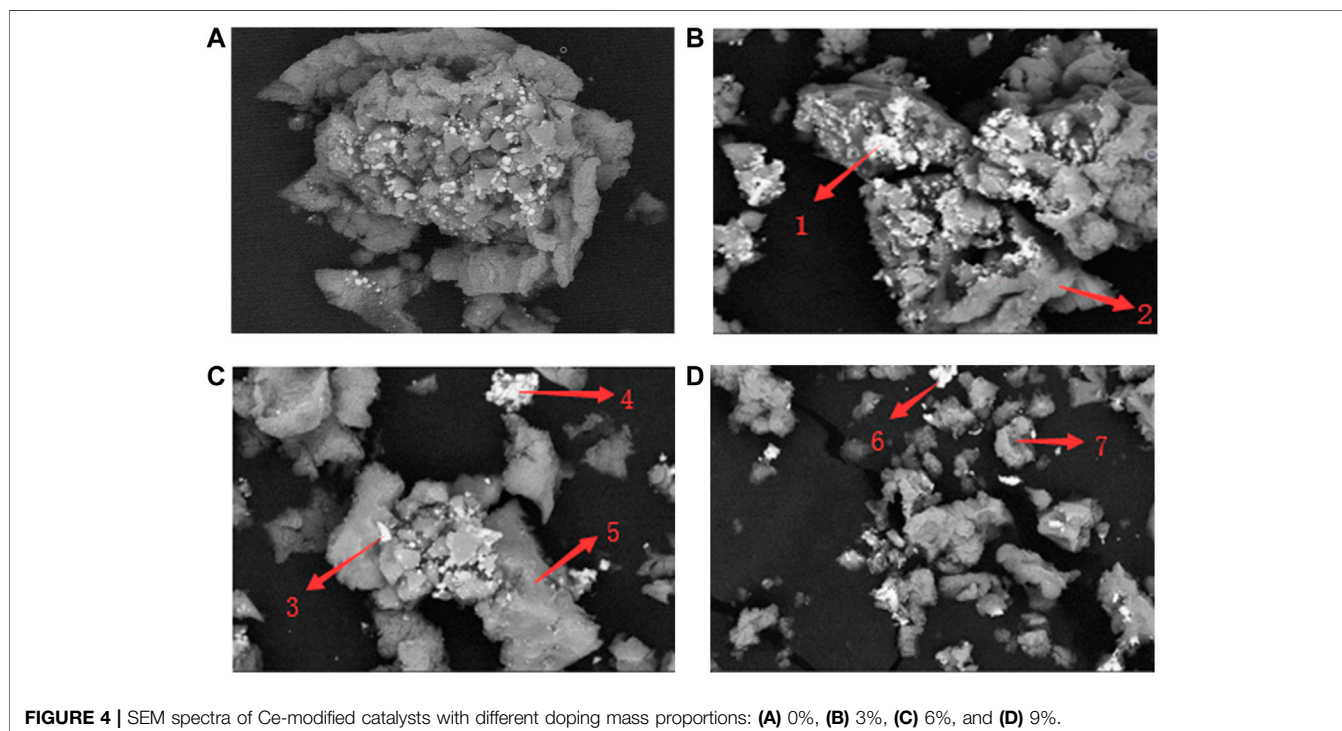


TABLE 2 | EDS table of Ce doped catalysts.

Element/%	O	Al	Ca	Ni	Ce
1	10.9	1.7	7.21	55.84	24.36
2	53.71	3.48	40.62	0.99	1.2
3	23.23	4.06	13.82	47.87	11.03
4	11	3.16	5.19	76.24	4.38
5	50.78	2.47	42.42	3.47	0.86
6	11.03	0.71	4.67	75.08	8.5
7	50.17	0.31	48.71	0.81	0

H_2 yield (Y_{H_2}) was defined as the ratio of the output of H_2 ($Q_{H_2, out}$) in the reformed gas to the theoretical output of H_2 (Q_{H_2}) when all the input tar is converted completely via Eq. 3.

$$Y_{H_2} = \frac{Q_{H_2, out}}{Q_{H_2}} \times 100\% \quad (5)$$

The dry reformed gas ($Q_{total, out}$) was considered to be composed of H_2 , CO , CO_2 , and CH_4 . The concentration of the reformed gas (C_i , i was H_2 , CO , CO_2 , or CH_4) was defined as the ratio of the output of i ($Q_{i, out}$) to the total output of the reformed gas ($Q_{total, out}$). In this article, only the concentrations of H_2 and CO_2 were studied in consideration of the extremely low concentrations of CO and CH_4 .

$$C_i = \frac{Q_{i, out}}{Q_{total, out}} \times 100\% \quad (6)$$

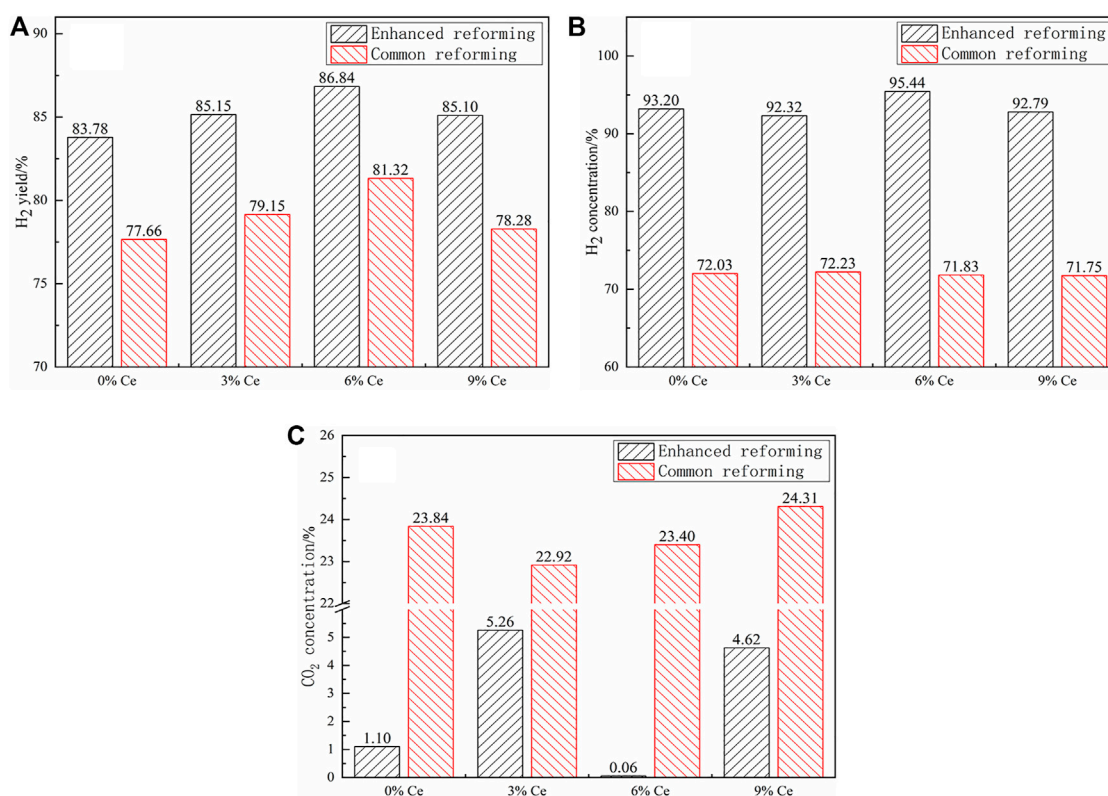
RESULTS AND DISCUSSION

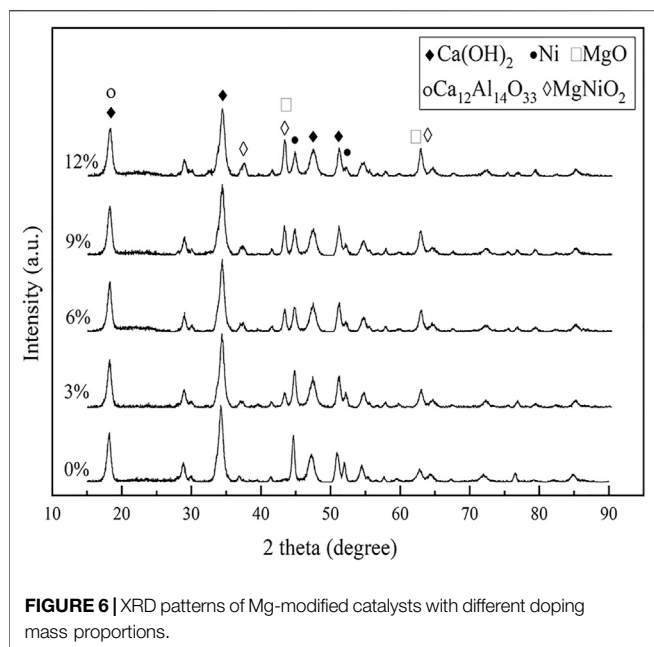
Effect of the Ce-Modified Double-Effect Ni-Based Catalyst

Catalyst Characterization Results

Prior to characterization, the prepared catalysts were activated at 800°C with 10% mol H_2/N_2 stream for 3 h. The structure of the catalysts was characterized by XRD (Shimazu, Japan, XRD-7000) using Cu K α radiation operated at 30 kV and 40 mA, with the scanning angle of $10\text{--}80$ rad and the scanning speed of 2 rad/min. The morphology of the catalysts was observed by SEM with the aid of a Hitachi su-8010 microscope.

Figure 3 shows the XRD patterns of Ce-modified catalysts with different doping mass proportions. As shown in the figure, the Ce-modified catalysts include the active components, Ni and CeO_2 ; adsorption component, $Ca(OH)_2$ (formed by CaO absorbing water in the air); and carrier component, $Ca_{12}Al_{14}O_{33}$. As the doping proportion increases, the peak value of CeO_2 significantly increased. **Figure 4** shows the SEM spectra of Ce-modified catalysts as well as the undoped sample

**FIGURE 5** | Effect of the Ce-modified catalysts: (A) H_2 yield, (B) H_2 concentration, and (C) CO_2 concentration.



(shown in **Figure 4A**). In the spectra, the bright part is mainly the active component Ni (shown by arrows 1, 3, 4, and 6), and the gray part is the adsorption component CaO and the carrier component $\text{Ca}_{12}\text{Al}_{14}\text{O}_{33}$ (shown by arrows 2, 5, and 7); the element contents of the different parts are

shown in **Table 2**. The different particles were based on a $\text{CaO}-\text{Ca}_{12}\text{Al}_{14}\text{O}_{33}$ matrix, with Ni and CeO_2 dotting on the surface of the matrix by small spherical particles. Proper addition of Ce can improve the distribution of Ni, which showed that part of Ni no longer relied on or just relied on a small amount of the $\text{CaO}-\text{Ca}_{12}\text{Al}_{14}\text{O}_{33}$ matrix after Ce doping, with the small particles of Ni- CeO_2 also slightly increased.

Reformation Result

CeO_2 generally has a strong oxygen storage capacity due to its face-centered cubic structure. CeO_2 can provide oxygen atoms to the adjacent nickel metal and promote the oxidation reaction of carbon intermediate products on nickel metal, thus improving the catalyst reactivity and reducing the formation of carbon deposition (Kimura et al., 2006; Tomishige et al., 2007).

Figure 5A shows the H_2 yields of tar reforming over the catalysts with different Ce doping mass proportions. Overall, the catalysts, H_2 yields, and concentrations at the enhanced reforming stage were higher than those at the common reforming stage. It could also be seen that Ce doped in the catalyst could improve the H_2 yield at both the stages. As the doping proportion rose, the H_2 yields in the two stages first increased, then decreased, and finally reached the highest at the doping proportion of 6% (86.84% for the enhanced reforming). It was corroborated that a small amount of Ce doping made the active component no longer completely rely on the $\text{CaO}-\text{Ca}_{12}\text{Al}_{14}\text{O}_{33}$ matrix, and the active component distribution was more uniform,

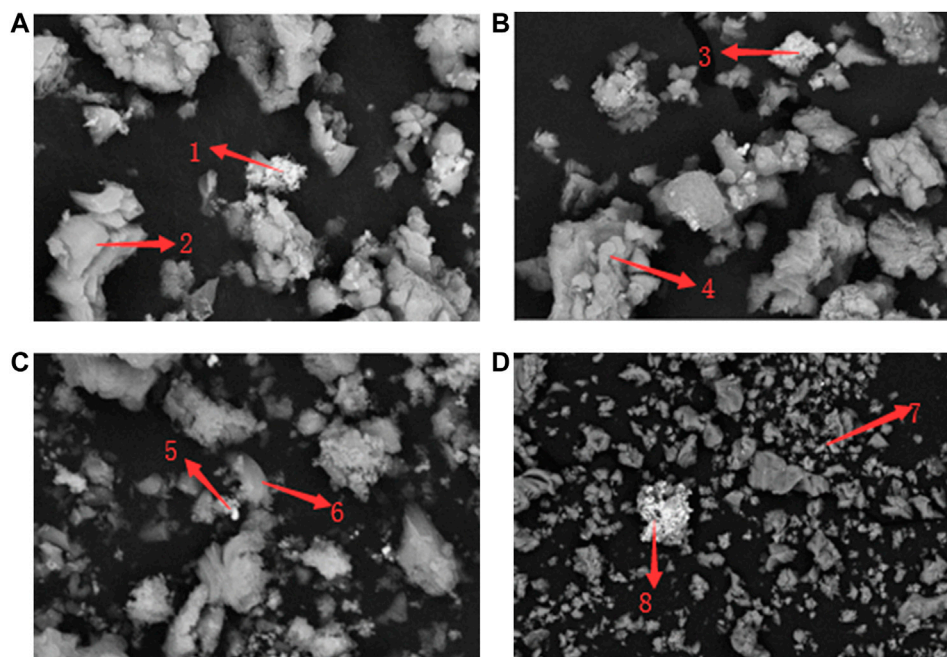


FIGURE 7 | SEM spectra of Mg-modified catalysts with different doping mass proportions: (A) 3%, (B) 6%, (C) 9%, and (D) 12%.

TABLE 3 | EDS of Mg doped catalysts.

Element/%	O	Mg	Al	Ca	Ni
1	23.6	10.57	5.13	9.5	51.2
2	41.5	0.28	0.58	56.89	0.75
3	19.27	17.46	2.25	4.88	56.15
4	68.58	1.23	1.98	19.08	9.12
5	12.03	3.64	3.22	7.43	73.68
6	41.74	10.22	10.54	17.71	19.78
7	21.75	20.23	2.54	12.08	43.4
8	29.44	24.61	3.17	6.54	36.24

thus promoting the SR reaction (Eq. 1), with the increase in the H_2 yield. However, the excessive Ce (>6%) doping produced more Ni and CeO_2 aggregated particles, which reduced the effective catalytic activity area, with the decrease in the H_2 yield. **Figures 5B,C** show the H_2 and CO_2 concentrations obtained over the catalysts with different Ce doping proportions. Due to the *in-situ* CO_2 adsorption, the H_2 concentrations of the enhanced reforming all over the catalysts with Ce doping were >90%, and among them, the sample with 6% Ce had the highest H_2 concentration (95.44%) and a very little CO_2 concentration, on some extent indicating that proper Ce addition can also improve the dispersion of CaO. After the adsorption saturation, i.e., at the common reforming stage, the H_2 concentrations were all about 72% and CO_2 concentrations were about 23–24%.

Effect of the Mg-Modified Double-Effect Ni-Based Catalyst

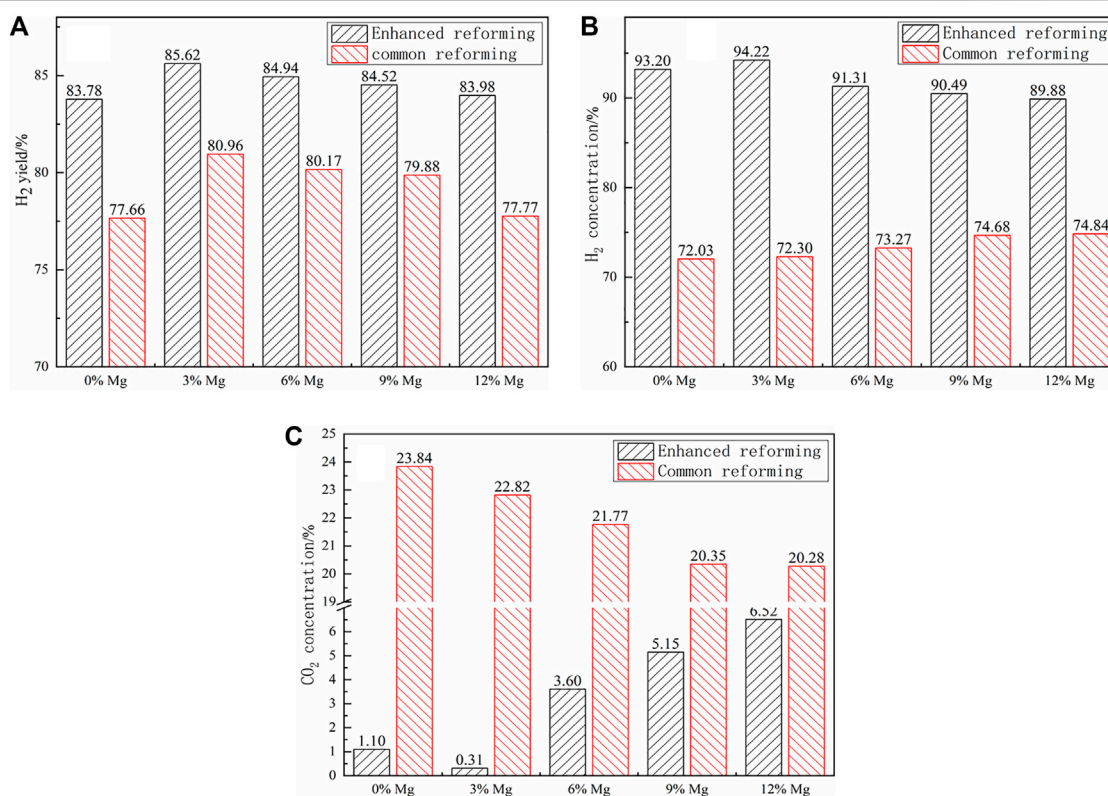
Catalyst Characterization Results

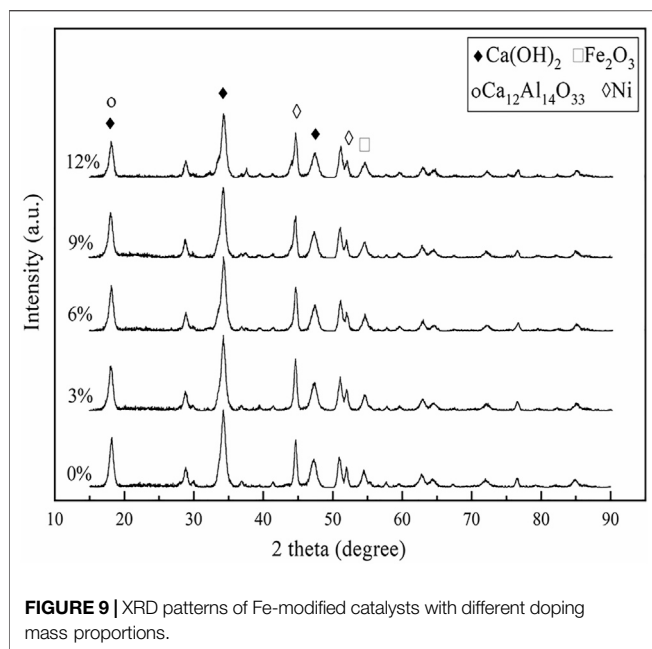
Figure 6 shows the XRD patterns of Mg-modified catalysts with different doping mass proportions. With the rise of the doping proportion, the peak value of Ni decreased, while those of MgO and $MgNiO_2$ spinels increased significantly. From **Figure 7** and **Table 3**, we can see that the $CaO-Ca_{12}Al_{14}O_{33}$ matrix was still the main composition in the catalyst (shown by arrows 2, 4, and 6), and the active components (shown by arrows 1, 3, 5, 7, and 8) on the matrix were changed from the original globular particles to spiny pellets, caused by the formation of $MgNiO_2$. With the rise of the doping proportions, the Mg-modified catalysts also showed the phenomenon that the active components detached from the $CaO-Ca_{12}Al_{14}O_{33}$ matrix and then aggregated alone, resulting in the decrease in the catalytic area (shown by arrows 7 and 8).

Reformation Result

Mg is a common additive in the process of steam reforming. MgO has a certain catalytic property and can also promote the oxidation of CO. For the Ni-based catalyst, the doping of Mg enables the catalyst to form one Ni-Mg-O solid solution, which has good stability and resistance to carbon deposition (Wang et al., 2006).

Figure 8 shows the H_2 yield and concentrations over the catalysts at different Mg doping proportions. For the two reforming stages, the

**FIGURE 8** | Effect of the Mg-modified catalyst: (A) H_2 yield, (B) H_2 concentration, and (C) CO_2 concentration.



addition of Mg can improve the SR reactions, with the increase in the H_2 yield. However, for the Mg-doped samples, the H_2 yield gradually decreased with the increase in the doping proportion. For the enhanced reforming, the H_2 yield reached the highest, 85.62%, at the doping proportion of 3%, and the H_2 concentration also decreased gradually with the rise of the Mg doping proportion in the enhanced

reforming stage, and reached 93.20% at the doping proportion of 3%. Compared with the undoped catalyst, the increase in the H_2 yield and concentration corroborated that the increase in the catalytic area, causing the active components to change from the original globular particles to spiny pellets, promoted the SR reaction. Then, the decrease in the H_2 yield and concentration was because too much of the Mg-doped catalyst caused the active components to detach and aggregate, reducing the catalytic area. In the enhanced reforming stage, the CO_2 concentration gradually increased with the rise of the Mg doping proportion, to some extent corroborating the result found in the literature that doping Mg in the catalyst could promote the oxidation of CO (Wang et al., 2006). For the common reforming, Mg addition showed a slight increase in the H_2 concentration and a slight decrease in the CO_2 concentration with the increase in the doping proportion, which almost had no effect.

Effect of the Fe-Modified Double-Effect Ni-Based Catalyst Catalyst Characterization Results

Figure 9 shows the XRD patterns of Fe-modified catalysts with different doping mass proportions. The XRD spectra of Fe-modified catalysts were similar to those of unmodified catalysts, and the peak value of Fe_2O_3 was weak and nearly did not change with the rise of the doping proportion. The SEM spectra and EDS results of Fe-modified catalysts are shown in **Figure 10** and **Table 4**. It could be seen that Ni (shown by arrows 1, 3, 5, 7, and 8) adhered to the surface of the $CaO-Ca_{12}Al_{14}O_{33}$ matrix (shown by arrows 2, 4, 6, and 8) in a

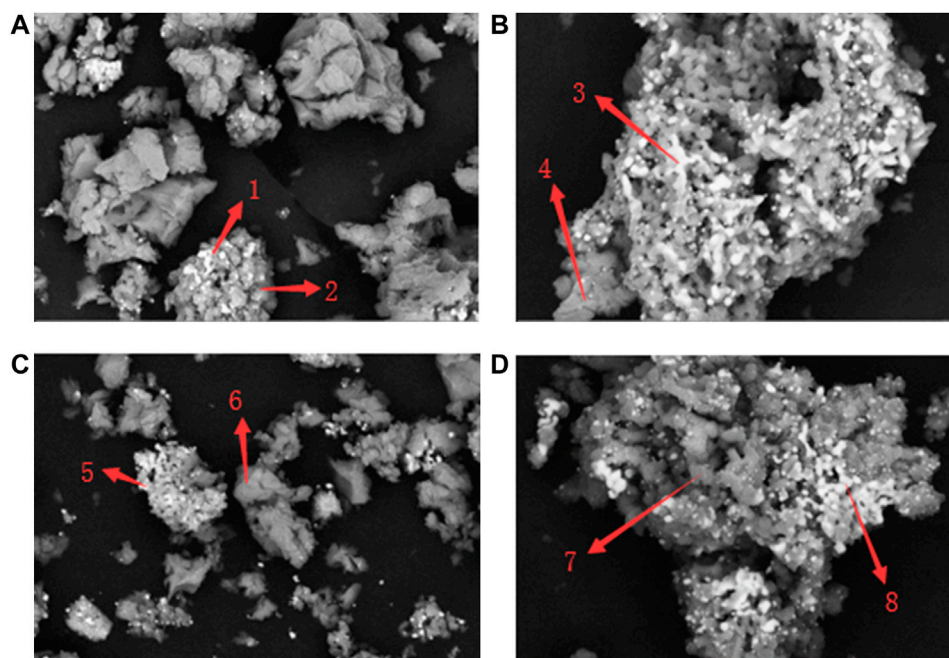


FIGURE 10 | SEM spectra of Fe-modified catalysts with different doping mass proportions: (A) 3%, (B) 6%, (C) 9%, and (D) 12%.

TABLE 4 | EDS of Fe doped catalysts.

Element/%	O	Al	Ca	Fe	Ni
1	14.01	2.5	14.36	1.7	67.43
2	41.49	2.46	52.32	0.38	3.35
3	5.48	2.59	3.55	5.29	83.09
4	45.43	1.83	39.6	1.64	11.5
5	6.89	1.57	4.71	1.5	85.33
6	33.67	8.94	30.59	19.37	7.43
7	15.3	1.14	5.41	50.42	27.74
8	31.08	6.41	28.12	4.49	29.9

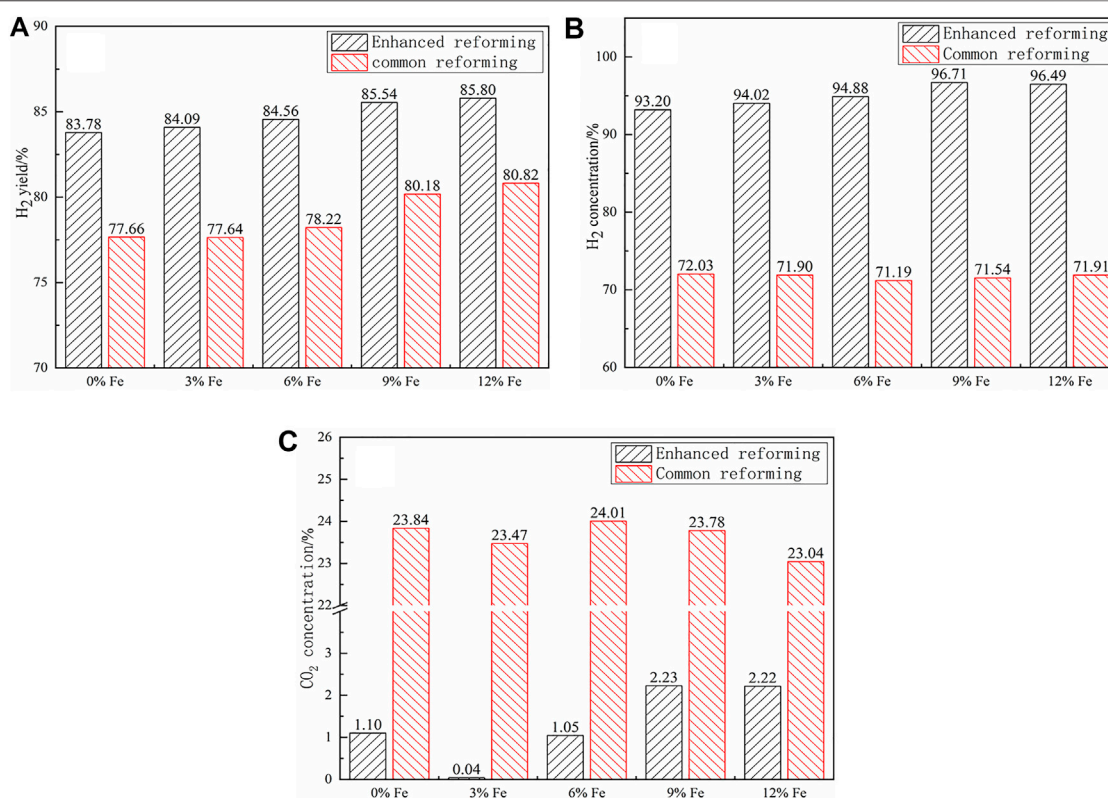
granular form. Fe was uniformly distributed in the CaO–Ca₁₂Al₁₄O₃₃ matrix (shown by arrows 6 and 7), and different doping mass proportions of Fe had little effect on the distribution of the active component Ni.

Reformation Result

The oxide of Fe can be used as a catalyst for the reforming reaction, and its catalytic activity is lower than that of the Ni-based catalyst. For example, the active component of olivine is mainly Fe₂O₃. Ni and Fe can closely combine to form a Ni–Fe alloy and improve the stability of the catalyst. In

addition, Fe doping in the catalyst can provide oxygen to neighboring nickel species and promote the oxidation of carbon, reducing the amount of carbon formation (Wang et al., 2011).

The effects of the modified catalysts on the H₂ yield and concentration are shown in **Figures 11A,B**. From the figure, it is clear that the H₂ yield and concentration gradually increased with the rise of the Fe doping proportion and then flattened out when the Fe doping proportion was over 9%. The H₂ yield of the enhanced reforming can reach 85.54 and 85.80% at the doping proportions of 9 and 12%, respectively. The result corroborated that Fe doping in the catalyst (forming a Ni–Fe alloy) could improve the catalyst stability, which promoted the SR reaction for the hydrogen production. For the common reforming, the concentrations of the products were relatively stable over the catalysts with different Fe loads, around 73% for H₂ and around 24% for CO₂. However, for the enhanced reforming, the CO₂ concentration showed an increasing trend with the increase in the Fe load, like the H₂ yield, to some extent corroborating that doping Fe in the catalyst could promote the oxidation of CO.

**FIGURE 11** | Effect of the Fe-modified catalysts: **(A)** H₂ yield, **(B)** H₂ concentration, and **(C)** CO₂ concentration.

CONCLUSION

In this article, the double-effect Ni-based catalysts, modified with Ce, Mg, and Fe and synthesized by the coprecipitation method, were applied into the enhanced steam reforming process of real tar. The effects of the catalysts with different doping mass proportions (3, 6, 9, and 12%) of Ce, Mg, and Fe on the H₂ yield, and H₂ and CO₂ concentrations contrasted with those of the unmodified catalyst. The results revealed that the tar reforming efficiency was improved with appropriate proportion of the additives added. The Ce-doped catalyst, existing in the form of CeO₂, could change the distribution of the active component Ni and promote the thermal cracking and SR reactions. The modified catalyst with 6% Ce doping The Mg-doped catalyst, existing in the form of MgO and MgNiO₂, could change the morphology of Ni, increasing the catalytic area, which promoted the SR reaction. The best catalytic activity was obtained at 3% Mg doping, with the H₂ yield reaching 85.22%. The Fe-doped catalyst, existing in the form of Fe₂O₃, could form a Ni-Fe alloy and improve the stability of the catalyst, and the modified catalyst with 9 and 12% Fe doping showed the better catalytic activity, with the H₂ yield reaching 85.54 and 85.80%, respectively.

REFERENCES

- Ashok, J., Kathiraser, Y., Ang, M. L., and Kawi, S. (2015). Bi-functional Hydrotalcite-Derived NiO-CaO-Al₂O₃ Catalysts for Steam Reforming of Biomass And/or Tar Model Compound at Low Steam-To-Carbon Conditions. *Appl. Catal. B: Environ.* 172–173, 116–128. doi:10.1016/j.apcatb.2015.02.017
- Cai, W.-J., Qian, L.-P., Yue, B., and He, H.-Y. (2014). Rh Doping Effect on Coking Resistance of Ni/SBA-15 Catalysts in Dry Reforming of Methane. *Chin. Chem. Lett.* 25, 1411–1415. doi:10.1016/j.ccl.2014.06.016
- Chan, F. L., and Tanksale, A. (2014). Review of Recent Developments in Ni-Based Catalysts for Biomass Gasification. *Renew. Sust. Energ. Rev.* 38, 428–438. doi:10.1016/j.rser.2014.06.011
- Dou, B., Wang, C., Song, Y., Chen, H., Jiang, B., Yang, M., et al. (2016). Solid Sorbents for *In-Situ* CO₂ Removal during Sorption-Enhanced Steam Reforming Process: A Review. *Renew. Sust. Energ. Rev.* 53, 536–546. doi:10.1016/j.rser.2015.08.068
- Duan, W., Yu, Q., Wang, K., Qin, Q., Hou, L., Yao, X., et al. (2015). ASPEN Plus Simulation of Coal Integrated Gasification Combined Blast Furnace Slag Waste Heat Recovery System. *Energ. Convers. Manage.* 100, 30–36. doi:10.1016/j.enconman.2015.04.066
- Duan, W., Yu, Q., Wang, Z., Liu, J., and Qin, Q. (2018). Life Cycle and Economic Assessment of Multi-Stage Blast Furnace Slag Waste Heat Recovery System. *Energy* 142, 486–495. doi:10.1016/j.energy.2017.10.048
- Duan, W., Yu, Q., Xie, H., and Qin, Q. (2017). Pyrolysis of Coal by Solid Heat Carrier-Experimental Study and Kinetic Modeling. *Energy* 135, 317–326. doi:10.1016/j.energy.2017.06.132
- Furusawa, T., Saito, K., Kori, Y., Miura, Y., Sato, M., and Suzuki, N. (2013). Steam Reforming of Naphthalene/benzene with Various Types of Pt- and Ni-Based Catalysts for Hydrogen Production. *Fuel* 103, 111–121. doi:10.1016/j.fuel.2011.09.026
- Gao, N., Liu, S., Han, Y., Xing, C., and Li, A. (2015). Steam Reforming of Biomass Tar for Hydrogen Production over NiO/ceramic Foam Catalyst. *Int. J. Hydrogen Energ.* 40, 7983–7990. doi:10.1016/j.ijhydene.2015.04.050
- Gusta, E., Dalai, A. K., Uddin, M. A., and Sasaoka, E. (2009). Catalytic Decomposition of Biomass Tars with Dolomites. *Energy Fuels* 23, 2264–2272. doi:10.1021/ef8009958
- Jiang, L., Hu, S., Wang, Y., Su, S., Sun, L., Xu, B., et al. (2015). Catalytic Effects of Inherent Alkali and Alkaline Earth Metallic Species on Steam Gasification of

DATA AVAILABILITY STATEMENT

The original contributions presented in the study are included in the article/Supplementary Material; further inquiries can be directed to the corresponding authors.

AUTHOR CONTRIBUTIONS

PW and WZ conducted the experiments and wrote the manuscript. HX and ZY have corrected and edited the manuscript. MZ and ZW supported the project technically.

FUNDING

This research was financially supported by the Fundamental Research Funds for the Central Universities (N2025029), the National Natural Science Foundation of Liaoning Province (2019-MS-133), and the Open Project Program of Key Laboratory of Metallurgical Emission Reduction and Resources Recycling, Ministry of Education (Anhui University of Technology) (JKF19-06).

- Biomass. *Int. J. Hydrogen Energ.* 40, 15460–15469. doi:10.1016/j.ijhydene.2015.08.111
- Kimura, T., Miyazawa, T., Nishikawa, J., Kado, S., Okumura, K., Miyao, T., et al. (2006). Development of Ni Catalysts for Tar Removal by Steam Gasification of Biomass. *Appl. Catal. B: Environ.* 68, 160–170. doi:10.1016/j.apcatb.2006.08.007
- Kinoshita, C. M., and Turn, S. Q. (2003). Production of Hydrogen from Bio-Oil Using CaO as a CO Sorbent. *Int. J. Hydrogen Energ.* 28 (10), 1065–1071. doi:10.1016/s0360-3199(02)00203-3
- Koike, M., Li, D., Nakagawa, Y., and Tomishige, K. (2012). A Highly Active and Coke-Resistant Steam Reforming Catalyst Comprising Uniform Nickel-Iron alloy Nanoparticles. *ChemSusChem* 5, 2312–2314. doi:10.1002/cssc.201200507
- Li, C., Hirabayashi, D., and Suzuki, K. (2009). A Crucial Role of O₂- and O₂₂- on Mayenite Structure for Biomass Tar Steam Reforming over Ni/Ca₁₂Al₁₄O₃₃. *Appl. Catal. B: Environ.* 88, 351–360. doi:10.1016/j.apcatb.2008.11.004
- Li, C., and Suzuki, K. (2010). Resources, Properties and Utilization of Tar. *Resour. Conservation Recycling/Conservation Recycling* 54, 905–915. doi:10.1016/j.resconrec.2010.01.009
- Li, D., Ishikawa, C., Koike, M., Wang, L., Nakagawa, Y., and Tomishige, K. (2013). Production of Renewable Hydrogen by Steam Reforming of Tar from Biomass Pyrolysis over Supported Co Catalysts. *Int. J. Hydrogen Energ.* 38, 3572–3581. doi:10.1016/j.ijhydene.2013.01.057
- Li, D., Tamura, M., Nakagawa, Y., and Tomishige, K. (2015). Metal Catalysts for Steam Reforming of Tar Derived from the Gasification of Lignocellulosic Biomass. *Bioresour. Technol.* 178, 53–64. doi:10.1016/j.biortech.2014.10.010
- Li, J., Tao, J., Yan, B., Jiao, L., Chen, G., and Hu, J. (2021). Review of Microwave-Based Treatments of Biomass Gasification Tar. *Renew. Sust. Energ. Rev.* 150, 111510. doi:10.1016/j.rser.2021.111510
- Mazumder, J., and de Lasa, H. I. (2015). Fluidizable La₂O₃ Promoted Ni/γ-Al₂O₃ Catalyst for Steam Gasification of Biomass: Effect of Catalyst Preparation Conditions. *Appl. Catal. B: Environ.* 168–169, 250–265. doi:10.1016/j.apcatb.2014.12.009
- Mei, D., Lebarbier, V. M., Rousseau, R., Glezakou, V.-A., Albrecht, K. O., Kovarik, L., et al. (2013). Comparative Investigation of Benzene Steam Reforming over Spinel Supported Rh and Ir Catalysts. *ACS Catal.* 3, 1133–1143. doi:10.1021/cs4000427
- Nakhaei Pour, A., and Mousavi, M. (2015). Combined Reforming of Methane by Carbon Dioxide and Water: Particle Size Effect of Ni-Mg Nanoparticles. *Int. J. Hydrogen Energ.* 40, 12985–12992. doi:10.1016/j.ijhydene.2015.08.011

- Onozaki, M., Watanabe, K., Hashimoto, T., Saegusa, H., and Katayama, Y. (2006). Hydrogen Production by the Partial Oxidation and Steam Reforming of Tar from Hot Coke Oven Gas. *Fuel* 85, 143–149. doi:10.1016/j.fuel.2005.02.028
- Richardson, Y., Blin, J., Volle, G., Motuzas, J., and Julbe, A. (2010). *In Situ* generation of Ni Metal Nanoparticles as Catalyst for H₂-Rich Syngas Production from Biomass Gasification. *Appl. Catal. A: Gen.* 382, 220–230. doi:10.1016/j.apcata.2010.04.047
- Sarioğlu, A. (2012). Tar Removal on Dolomite and Steam Reforming Catalyst: Benzene, Toluene and Xylene Reforming. *Int. J. Hydrogen Energ.* 37, 8133–8142. doi:10.1016/j.ijhydene.2012.02.045
- Tomishige, K., Kimura, T., Nishikawa, J., Miyazawa, T., and Kunimori, K. (2007). Promoting Effect of the Interaction between Ni and CeO₂ on Steam Gasification of Biomass. *Catal. Commun.* 8, 1074–1079. doi:10.1016/j.catcom.2006.05.051
- Torres, W., Pansare, S. S., and Goodwin, J. G. (2007). Hot Gas Removal of Tars, Ammonia, and Hydrogen Sulfide from Biomass Gasification Gas. *Catal. Rev.* 49, 407–456. doi:10.1080/01614940701375134
- Virginie, M., Adánez, J., Courson, C., De Diego, L. F., García-Labiano, F., Niznansky, D., et al. (2012). Effect of Fe-Olivine on the Tar Content during Biomass Gasification in a Dual Fluidized Bed. *Appl. Catal. B: Environ.* 121–122, 214–222. doi:10.1016/j.apcatb.2012.04.005
- Wang, L., Li, D., Koike, M., Koso, S., Nakagawa, Y., Xu, Y., et al. (2011). Catalytic Performance and Characterization of Ni-Fe Catalysts for the Steam Reforming of Tar from Biomass Pyrolysis to Synthesis Gas. *Appl. Catal. A: Gen.* 392, 248–255. doi:10.1016/j.apcata.2010.11.013
- Wang, L., Li, D., Koike, M., Watanabe, H., Xu, Y., Nakagawa, Y., et al. (2013). Catalytic Performance and Characterization of Ni-Co Catalysts for the Steam Reforming of Biomass Tar to Synthesis Gas. *Fuel* 112, 654–661. doi:10.1016/j.fuel.2012.01.073
- Wang, T., Chang, J., Cui, X., Zhang, Q., and Fu, Y. (2006). Reforming of Raw Fuel Gas from Biomass Gasification to Syngas over Highly Stable Nickel-Magnesium Solid Solution Catalysts. *Fuel Process. Technol.* 87, 421–428. doi:10.1016/j.fuproc.2005.10.006
- Xie, H., Yu, Q., Yao, X., Duan, W., Zuo, Z., and Qin, Q. (2015). Hydrogen Production via Steam Reforming of Bio-Oil Model Compounds over Supported Nickel Catalysts. *J. Energ. Chem.* 24, 299–308. doi:10.1016/S2095-4956(15)60315-1
- Xie, H., Yu, Q., Zhang, J., Liu, J., Zuo, Z., and Qin, Q. (2016a). Preparation and Performance of Ni-Based Catalysts Supported on Ca₁₂ Al₁₄ O₃₃ for Steam Reforming of Tar in Coke Oven Gas. *Environ. Prog. Sust. Energ.* 36, 729–735. doi:10.1002/ep.12509
- Xie, H., Yu, Q., Zuo, Z., Han, Z., Yao, X., and Qin, Q. (2016b). Hydrogen Production via Sorption-Enhanced Catalytic Steam Reforming of Bio-Oil. *Int. J. Hydrogen Energ.* 41, 2345–2353. doi:10.1016/j.ijhydene.2015.12.156
- Xie, H., Yu, Q., Zuo, Z., Zhang, J., Han, Z., and Qin, Q. (2016c). Thermodynamic Analysis of Hydrogen Production from Raw Coke Oven Gas via Steam Reforming. *J. Therm. Anal. Calorim.* 126, 1621–1631. doi:10.1007/s10973-016-5638-9
- Xie, H., Zhang, J., Yu, Q., Zuo, Z., Liu, J., and Qin, Q. (2016d). Study on Steam Reforming of Tar in Hot Coke Oven Gas for Hydrogen Production. *Energy Fuels* 30, 2336–2344. doi:10.1021/acs.energyfuels.5b02551
- Xie, H., Zhang, W., Zhao, X., Chen, H., Yu, Q., and Qin, Q. (2018). Sorption-enhanced Reforming of Tar: Influence of the Preparation Method of CO₂ Absorbent. *Korean J. Chem. Eng.* 35, 2191–2197. doi:10.1007/s11814-018-0136-3
- Yue, B., Wang, X., Ai, X., Yang, J., Li, L., Lu, X., et al. (2010). Catalytic Reforming of Model Tar Compounds from Hot Coke Oven Gas with Low Steam/carbon Ratio over Ni/MgO-Al₂O₃ Catalysts. *Fuel Process. Technol.* 91, 1098–1104. doi:10.1016/j.fuproc.2010.03.020
- Zamboni, I., Courson, C., and Kiennemann, A. (2011). Synthesis of Fe/CaO Active Sorbent for CO₂ Absorption and Tars Removal in Biomass Gasification. *Catal. Today* 176, 197–201. doi:10.1016/j.cattod.2011.01.014
- Zeng, X., Wang, F., Sun, Y., Zhang, J., Tang, S., and Xu, G. (2018). Characteristics of Tar Abatement by thermal Cracking and Char Catalytic Reforming in a Fluidized Bed Two-Stage Reactor. *Fuel* 231, 18–25. doi:10.1016/j.fuel.2018.05.043
- Zhang, W., Xie, H., Wang, P., Li, R., Yu, Z., and Yu, Q. (2021a). Steam Reforming of Tar from Raw Coke Oven Gas over Bifunctional Catalysts: Effects of Preparation Parameters on CO₂ Adsorption Performance. *Environ. Prog. Sust. Energ.* 40, e13506. doi:10.1002/ep.13506
- Zhang, W., Xie, H., Yu, Z., Wang, P., Wang, Z., and Yu, Q. (2021b). Steam Reforming of Tar from Raw Coke Oven Gas over Bifunctional Catalysts: Reforming Performance for H₂ Production. *Environ. Prog. Sust. Energ.* 40, e13501. doi:10.1002/ep.13501
- Zuo, Z., Luo, S., Liu, S., Zhang, J., Yu, Q., and Bi, X. (2021). Thermokinetics of Mass-Loss Behavior on Direct Reduction of Copper Slag by Waste Plastic Char. *Chem. Eng. J.* 405, 126671. doi:10.1016/j.cej.2020.126671
- Zuo, Z., Yu, Q., Luo, S., Zhang, J., and Zhou, E. (2020). Effects of CaO on Two-step Reduction Characteristics of Copper Slag Using Biochar as Reducer: Thermodynamic and Kinetics. *Energy Fuels* 34, 491–500. doi:10.1021/acs.energyfuels.9b03274

Conflict of Interest: The authors declare that the research was conducted in the absence of any commercial or financial relationships that could be construed as a potential conflict of interest.

Publisher's Note: All claims expressed in this article are solely those of the authors and do not necessarily represent those of their affiliated organizations, or those of the publisher, the editors and the reviewers. Any product that may be evaluated in this article, or claim that may be made by its manufacturer, is not guaranteed or endorsed by the publisher.

Copyright © 2021 Wang, Zhang, Yu, Xie, Zhou and Wang. This is an open-access article distributed under the terms of the Creative Commons Attribution License (CC BY). The use, distribution or reproduction in other forums is permitted, provided the original author(s) and the copyright owner(s) are credited and that the original publication in this journal is cited, in accordance with accepted academic practice. No use, distribution or reproduction is permitted which does not comply with these terms.



Advances in the Safe Disposal and Comprehensive Utilization of Spent Carbon Anode From Aluminum Electrolysis: Prospects for Extraction and Application of Carbon Resources From Hazardous Waste

Bin Li¹, Jun Zhou^{1,2}, Zhen Yao^{1,2*}, Qian Peng^{1,2}, Mengnan Liu¹, Xiaoqing Li¹ and Wei Liu^{1,2*}

¹School of Materials and Architectural Engineering, Guizhou Normal University, Guiyang, China, ²Guizhou Engineering Research Center for Carbon Materials of Aluminum Electrolysis, Guiyang, China

OPEN ACCESS

Edited by:

Zongliang Zuo,
Qingdao University of Technology,
China

Reviewed by:

Jindi Huang,
Jiangxi University of Science and
Technology, China
Yike Liu,
Guizhou Institute of Technology, China

*Correspondence:

Zhen Yao
yaozhen@gznu.edu.cn
Wei Liu
cjlw@gznu.edu.cn

Specialty section:

This article was submitted to
Advanced Clean Fuel Technologies,
a section of the journal
Frontiers in Energy Research

Received: 18 September 2021

Accepted: 18 October 2021

Published: 01 November 2021

Citation:

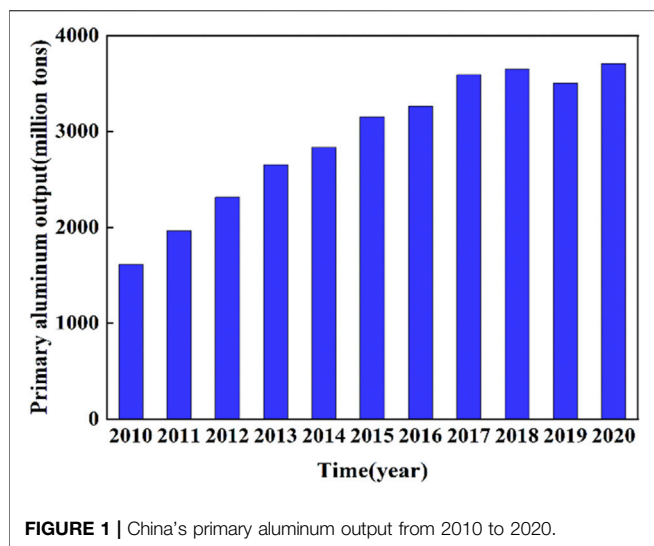
Li B, Zhou J, Yao Z, Peng Q, Liu M, Li X
and Liu W (2021) Advances in the Safe
Disposal and Comprehensive
Utilization of Spent Carbon Anode
From Aluminum Electrolysis:
Prospects for Extraction and
Application of Carbon Resources From
Hazardous Waste.
Front. Energy Res. 9:779476.
doi: 10.3389/fenrg.2021.779476

Spent carbon anode (SCA) is a dangerous solid waste that is continuously discharged from the aluminum electrolysis industry and has a large number of valuable resources and a high risk of environmental pollution. Its safe disposal and resource utilization have become a resource and environmental problem that must be solved urgently. Current methods for SCA disposal include flotation, vacuum metallurgy, physical activation, roasting, bubbling fluidized bed combustion, alkali fusion, alkali leaching, and chemical leaching combined with high temperature graphitization. In this paper, the material composition, resource properties, and environmental risks of SCA are discussed. Working principle, treatment process, advantages and disadvantages of the above methods are also briefly described and compared. Results showed that flotation is the safest disposal and comprehensive utilization technology that is suitable for characteristics of SCA raw materials and has the most large-scale application potential. In addition, characteristics of SCA recovery products are correlated to the recycling of aluminum reduction cells. This technology can alleviate the shortage of high-quality petroleum coke resources in China's carbon material industry and the high cost of raw materials in aluminum electrolysis industry.

Keywords: aluminum electrolysis, hazardous waste, spent carbon anode, safe disposal, comprehensive utilization

INTRODUCTION

Hall-Heroult method is currently used to produce aluminum. High-purity primary aluminum is produced by electrolysis with aluminum electrolysis cell as the carrier, cryolite (Na_3AlF_6) as the reaction solvent, and alumina (Al_2O_3) as the raw material. As a core component, prebaked anode drives the electric current into the electrolytic cell and participates in electrochemical reaction (Yang et al., 2016). However, reactivity differs between aggregate (calcined petroleum coke) and binder coking product (pitch coke), thus leading to the selective oxidation and uneven combustion of prebaked anode during production. In addition, the prebaked anode is washed and eroded by high temperature aluminum liquid and molten electrolytes. Hence, some carbon particles fall off from the prebaked anode, enter the electrolyte, and form spent carbon anode (SCA) (Li et al., 2015; TU, 2017; Hou et al., 2020). When excessive SCA accumulates on the surface of molten electrolytes, the



resistance of aluminum reduction cell increases, and the electric energy is excessively consumed (Zhang, 2013; Bai, 2020). SCA can also hinder Al_2O_3 dissolution and induce the anode effect (GuoHou et al., 2019; GuoHou et al., 2020) and therefore must be salvaged regularly to ensure the normal operation of the aluminum reduction cell. As a result, SCA has become an unavoidable solid waste that is continuously discharged from the aluminum electrolysis industry.

Calcined petroleum coke has a remarkable porous structure and can be used as the prebaked anode aggregate. This material can provide sufficient adsorption and permeation channels for molten electrolytes, resulting in a large amount of electrolytes in the SCA (Zhao and Yang, 2013; Liu and Wu, 2020). When SCA piles up in the open air or is buried unprotected, soluble fluoride with strong solubility and permeability gradually migrates to nearby soil and water sources along with rainwater, thus seriously threatening the ecological balance. Therefore, the SCA produced during electrolytic aluminum production has been classified as toxic hazardous waste (code: 321-025-48, hazardous characteristics: T) in the National List of Hazardous Wastes (2021 Edition). This waste is strictly prohibited to be discarded or stored in the open air and must be harmlessly disposed within the enterprise or by entrusting a third-party institution with hazardous waste treatment qualification.

With the continuous development of electrolytic aluminum industry, the discharge of SCA and the scale of harmless disposal have increased annually. As shown in **Figure 1**, the growth rate of China's primary aluminum output was approximately 129.80% from 2010 to 2020 (Wang, 2021). For every 5–15 kg of SCA (Liu et al., 2021) produced per ton of aluminum, its discharge amount exceeded 35,000 tons in 2020. SCA is composed of a large number of high-quality carbon materials and high-value electrolyte components and therefore has high recycling value (Zhang et al., 2018). The safe disposal and comprehensive utilization of SCA is conducive to promoting the green and sustainable development of the aluminum electrolysis industry.

COMPOSITION AND HARM OF SPENT CARBON ANODE

SCA usually comprises 60–70% electrolyte components and 30–40% carbon materials (Zhao et al., 2015; Wei, 2018; Liu, 2020). **Table 1** shows the main material components, resource attributes, and environmental risks of SCA.

SAFE DISPOSAL AND COMPREHENSIVE UTILIZATION TECHNOLOGY OF SPENT CARBON ANODE

The safe disposal and comprehensive utilization of SCA has been a major concern of the aluminum electrolysis industry. According to their principle of action, existing technologies for the safe disposal and comprehensive utilization of SCA can be grouped into physical separation and chemical treatment. Physical separation methods include flotation, vacuum metallurgy, and physical activation. Chemical treatment processes involve roasting, bubbling fluidized bed combustion, alkali fusion, and alkali leaching. The co-treatment involving chemical treatment and physical separation includes alkali-acid leaching and high temperature graphitization.

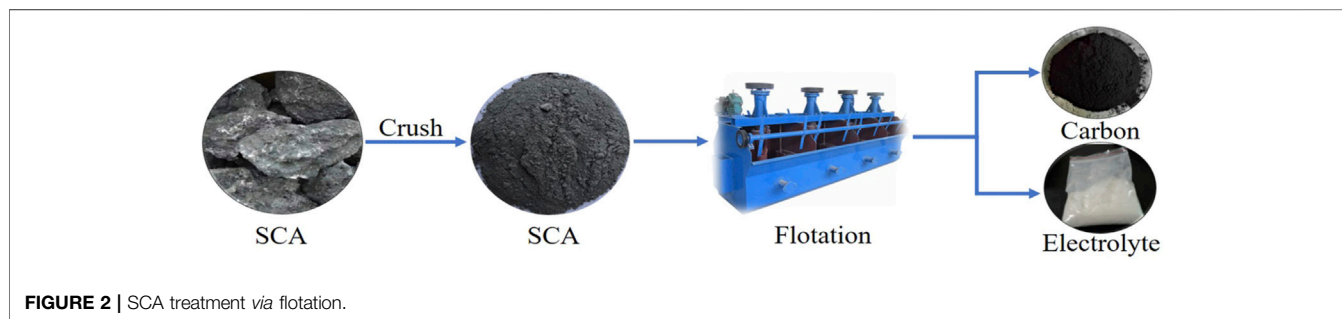
Physical Separation Flotation

Flotation is currently the most mature and widely used disposal technology of SCA. Its working principle is based on the hydrophobic difference between carbon materials (hydrophobic) and electrolyte components (hydrophilic). With the assistance of flotation reagents, carbon materials floating up with bubbles are collected, and electrolytes are discharged from the bottom of the flotation machine. Thus, the preliminary separation of carbon and electrolyte in SCA is realized. The main processes of this method include crushing, grinding, classification, flotation, and drying (Wang et al., 2019) as shown in **Figure 2**.

Mei et al. (2016) conducted an experimental study on recovering SCA through flotation. Under the optimized parameters of pulp concentration of 25–33%, SCA size of <200 mesh (<74 μm) accounting for 90%, and flotation machine speed of 1800 r/min, carbon materials with a carbon content of 94.59% were recovered, and the carbon content of electrolyte concentrate decreased from 4.10 to 1.01%. In addition, the flotation effect of SCA was improved through process optimization. Zhou et al. (2019) investigated the effect of flotation conditions on the separation of carbon and electrolytes in SCA. The optimal experimental conditions were obtained by single factor experiment. Carbon materials with a carbon content of 85.23% were retrieved with recovery rate of 81.55% under the optimal flotation parameters of SCA size of 120–140 mesh (106–125 μm), pulp concentration of 30%, stirring speed of 1,600 r/min, and aeration rate of 0.30 m^3/h (Li et al., 2021). explored the influence of conventional process conditions (size of SCA, stirring speed, and pulp concentration) on the flotation effect of SCA and studied the effect of pH regulator and

TABLE 1 | Material composition, resource attributes, and environmental risk of SCA.

Component	Material composition	Resource properties	Environmental risk
Carbon materials	Petroleum coke, pitch coke	Aluminum electrolysis carbon material raw materials, reductants and fuels	Combustion treatment produces harmful gases (SO ₂ and H ₂ S) and greenhouse gas (CO ₂)
Electrolyte components	Na ₃ AlF ₆ , Al ₂ O ₃ , NaF, Na ₅ Al ₃ F ₁₄ , CaF ₂ , LiF	Electrolytes and chemical raw materials in aluminum electrolysis industry	Solubility, permeability and corrosivity, causing soil and water pollution

**TABLE 2** | Summary of optimal parameters for SCA treatment with different flotation conditions.

Size (μm)	Pip concentration (%)	Stirring speed (r/min)	Aeration rate (m ³ /h)	Flotation reagents	Flotation process	Carbon content of recovered carbon (%)
<74 μm accounting for 90%	25–33%	1,800	—	Kerosene and water glass	One roughing, one cleaning and twice scavenging	94.59
106–125 μm	30%	1,600	0.30	Kerosene, water glass, 2# oil	—	85.23
<74 μm accounting for 70%	25%	1,700	—	Kerosene, water glass, 2# oil	One roughing, twice cleanings and twice scavengings	75.60

collector adding mode. The results showed that pH regulator has minimal influence on SCA flotation, and the flotation effect was remarkably improved through the batch addition of flotation reagents. Finally, the following optimal flotation parameters were obtained: particle size of <200 mesh (<74 μm) accounting for 70%, stirring speed of 1700 r/min, pulp concentration of 25%, collectors added in five batches, and mixing time of 5 min. The carbon content of SCA was increased from 23.30 to 75.60%, and the carbon recovery rate reached 86.90%.

Flotation has the advantages of large treatment capacity per unit time, low cost, simple operation, good working environment, and stable quality of recycled products. However, SCA is usually composed of many components and is infiltrated by electrolytes for a long time, resulting in the complex distribution state among the components. This method also has some disadvantages such as poor separation effect of valuable components, low purity of recovered products (carbon materials and electrolytes), and a large amount of produced fluorine-containing wastewater. Most of the above studies reported that the flotation effect of SCA can be enhanced by optimizing the flotation parameters as shown in Table 2. However, the recycling of recycled products and the safe disposal of flotation wastewater are rarely discussed. Given the

characteristics of SCA, raw materials should be pretreated in advance to realize the enhanced separation between carbon materials and electrolytes. New flotation reagent systems such as reagent emulsification and reagent compounding should also be constructed.

Vacuum Metallurgy

Vacuum metallurgy utilizes the volatility difference of valuable components in SCA. The volatile electrolytes are removed from the SCA under high temperature and vacuum conditions to separate the carbon materials and electrolyte components (Luo et al., 2020). The process of SCA treatment via vacuum metallurgy is shown in Figure 3.

Chai et al. (2016) explored the effect of vacuum degree, reaction temperature, SCA particle size, and reaction time on the separation of carbon materials and electrolytes in SCA. Under the optimal parameters of vacuum degree of 5 Pa, reaction temperature of 950°C, raw material size of 0.50 mm, and reaction time of 4 h, the separation rate of electrolytes reached 83%, and the carbon content of SCA was improved from 36 to 74%.

Vacuum metallurgy is used to directly recover high purity electrolyte components (such as Na₃AlF₆, AlF₃, LiF, and KF).

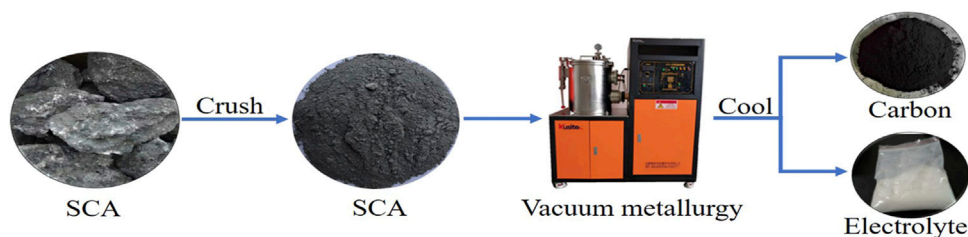


FIGURE 3 | SCA treatment via vacuum metallurgy.

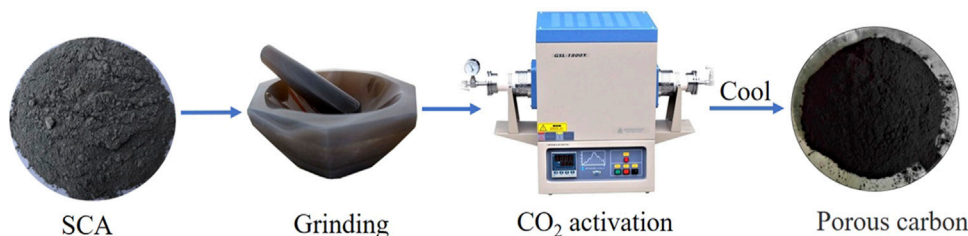


FIGURE 4 | SCA treatment via CO₂ activation.

However, only carbon materials with low carbon content are recovered because SCA has abundant Al₂O₃ (boiling point: 2,980°C) and CaF₂ (boiling point: 2,500°C), which are stable and difficult to volatilize. In addition, the high treatment temperature and long reaction time for this method are accompanied by high energy consumption and equipment loss, which hinder its industrial application.

Physical Activation

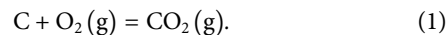
Physical activation is used to treat carbon-rich materials by activating media (such as water vapor and CO₂) to form porous carbon materials (Geng et al., 2014; Yi et al., 2008). The process of SCA treatment via CO₂ activation is shown in **Figure 4**.

(Liu et al., 2021) used SCA as raw material and CO₂ as activation medium to prepare porous carbon materials. The effects of CO₂ flow rate, activation temperature, and activation time on the properties of porous carbon were investigated through single factor experiments. The results showed the best adsorption performance of the porous carbon materials (79.75 mg/g) at CO₂ flow rate of 200 cc, activation temperature of 650°C, and activation time of 2 h. TEM, Raman, XRD and other analysis results showed that the porous carbon materials are mostly composed of mesopores and macropores. Their crystallization and graphitization degree were remarkably improved.

CO₂ activation for SCA treatment is a simple process, and the prepared porous carbon materials show pore structure and good adsorption performance. The application channels and utilization value of SCA are broadened. However, this method has high requirements for the carbon content of raw carbon; hence, the SCA must be deeply pretreated.

Chemical Treatment Roasting

Roasting completely burns the carbon materials in SCA at high temperature while keeping the electrolyte components stable (non-volatile and non-decomposed). Only the electrolytes with high purity are recovered (Chen, 2011). The main reaction in roasting is shown in **Eq. 1**. Its process mainly includes grinding, roasting, and cooling as shown in **Figure 5**.



Chen et al. (2009) employed roasting for SCA treatment and analyzed the influence of process parameters on roasting reaction efficiency. Electrolytes with content above 99% were recovered under the optimal parameters of roasting temperature of 760°C, addition of combustion improver of 12%, addition of dispersant of 15%, and rotary kiln rotating speed of 1 rpm. Meanwhile, the roasting reaction efficiency of SCA is as high as 95.31%.

Roasting is used to recover high-purity electrolytes that can be directly returned to the aluminum reduction cell for recycling. However, research and demonstration on the suitability of the characteristics of the recovered electrolytes for reuse in aluminum electrolysis are lacking. During this treatment, a large number of high-quality petroleum cokes are burned, and CO₂ is released. These problems bring pressure to environmental protection. In addition, its high energy consumption does not meet the requirements of energy conservation and emission reduction.

Bubbling Fluidized Bed Combustion

Bubbling fluidized bed combustion is used to roast SCA in suspension. The electrolyte components in SCA are effectively recovered by burning the carbon materials (Luo et al., 2019).

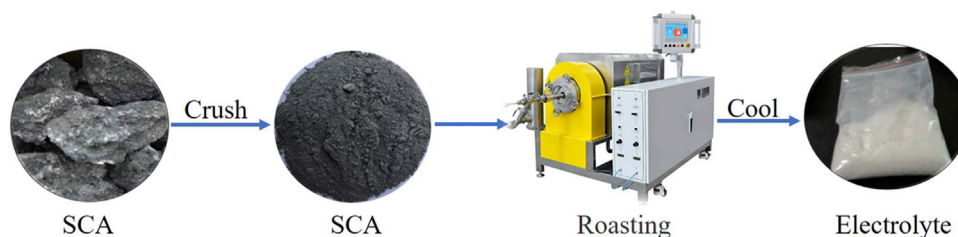


FIGURE 5 | SCA treatment via roasting.

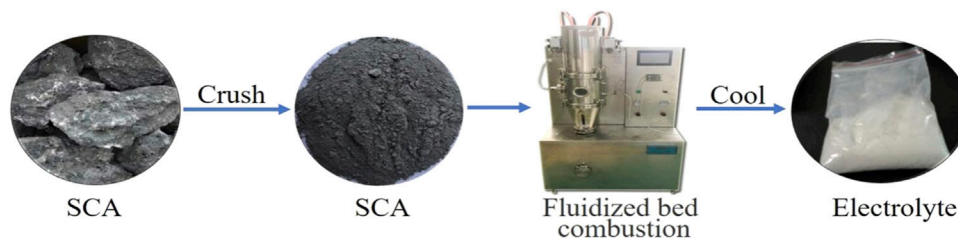


FIGURE 6 | SCA treatment via bubbling fluidized bed combustion.

The process of SCA treatment via bubbling fluidized bed is shown in **Figure 6**.

Zhou et al. (2014) investigated the combustion characteristics of SCA through differential thermal analysis and the influences of technical parameters such as particle size of SCA, initial bed height, air distribution plate structure, and fluidization velocity on the fluidization of SCA. SCA samples were roasted under the optimal parameters of bed diameter of 100 mm, opening rate of air distribution plate of 1.80%, fluidization velocity of 0.40 mm/s, SCA size of 0.40 mm, and roasting temperature of 565–734°C. However, the expected effect was not achieved, and only 66.30% of the carbon materials were removed.

In theory, bubbling fluidized bed combustion has better gas–solid contact effect and higher combustion efficiency and intensity than conventional roasting. However, the melting of $\text{Na}_5\text{Al}_3\text{F}_{14}$ with low melting point may lead to the sintering of SCA. As a result, its distribution in the fluidized bed is worsened, thereby reducing the reaction rate and limiting the removal efficiency of carbon materials.

Alkali Fusion

Alkali fusion removes electrolyte components by molten alkaline reagents such as NaOH and Na_2CO_3 . Carbon materials with high content are recovered after water leaching (Wang et al., 2016; Li et al., 2015). The alkaline substance changes from solid state to molten state when the roasting temperature is higher than its melting point. Therefore, the reaction activity and mass transfer conditions with the electrolyte components in the SCA are remarkably improved (Shoppert et al., 2019).

Yang et al. (2020) treated SCA by using NaOH as an additive. The effects of alkali fusion temperature, reaction time, and alkali–material mass ratio on the carbon content of recovered

carbon materials were investigated through single factor experiments. Parameters were optimized through orthogonal experiment. Carbon materials with a carbon content of 99.10% were recovered under the optimized parameters of alkali fusion temperature of 600°C, reaction time of 6.50 h, mass ratio of alkali to material of 5.5:1, and acid leaching. The recovered carbon materials had a large reversible capacity ($286.80 \text{ mAh}\cdot\text{g}^{-1}$) at 1 C and have a good capacity attenuation rate (the attenuation rate of each cycle in 500 cycles is 0.03%) and thus can be used as anode material of lithium-ion batteries. This finding provides a theoretical basis for the high-value utilization of SCA. The process of SCA treatment via NaOH alkali fusion is shown in **Figure 7**. Tian et al. (2021) used recovered SCA (carbon content >99.00%) and nano-silicon powder as raw materials to prepare Si/C composite materials by mechanical ball milling for lithium-ion battery anode. The Si/C composites exhibited good electrochemical properties under the ball milling speed of 500 r/min, mass ratio of ball to material of 5:1, and ball milling time of 25 h. The specific discharge capacity of Si/C composites reached $382.40 \text{ mAh}\cdot\text{g}^{-1}$ after 100 cycles at current density of $120 \text{ mA}\cdot\text{g}^{-1}$. This work provides a new idea for the high-value utilization of valuable components in SCA.

Liang et al. (2021) treated SCA with Na_2CO_3 as an additive. Na_2CO_3 almost completely reacted with Al_2O_3 , Na_3AlF_6 , and $\text{Na}_5\text{Al}_3\text{F}_{14}$ in SCA under the parameters of mass ratio of alkali to SCC of 2.5:1, alkali fusion temperature of 950°C, and reaction time of 2 h. Carbon materials with a carbon content of 89.00% were recovered after repeated water leaching, and Na_3AlF_6 was prepared by introducing CO_2 into the leachate. The process of SCA treatment via Na_2CO_3 alkali fusion is shown in **Figure 8**.

Alkali fusion can realize the efficient separation of carbon materials and electrolyte components in SCA. Combined with

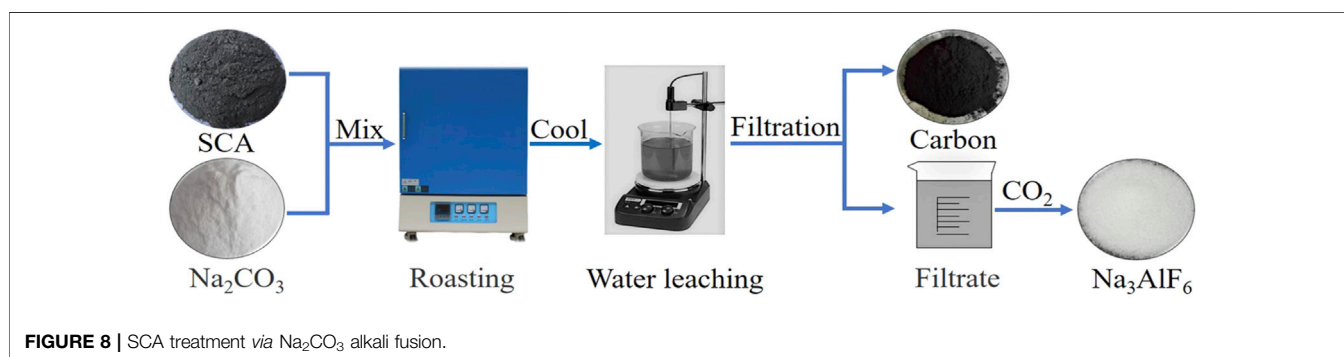
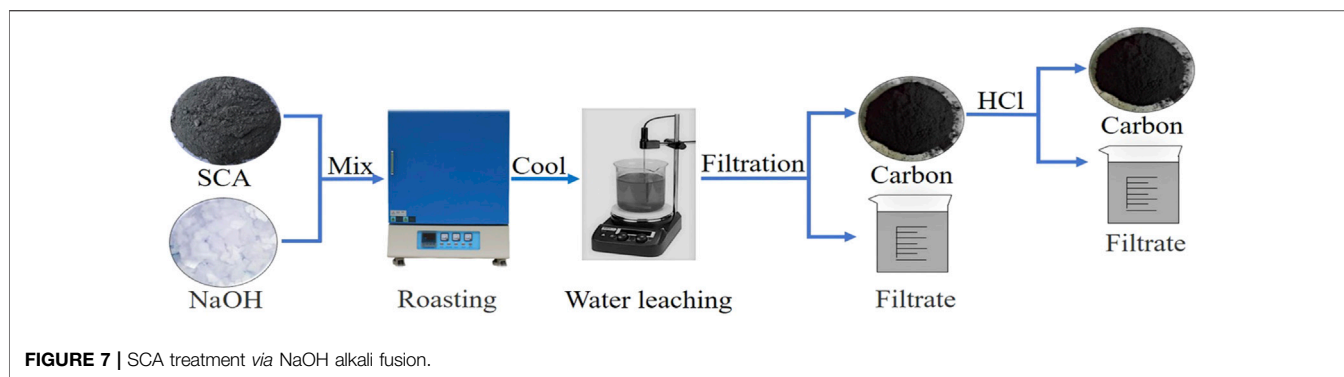


TABLE 3 | Optimum parameters for SCA treatment with different alkaline reagents.

Alkaline agent	Temperature (°C)	Time (h)	Mass ratio	Main reaction equations
NaOH	600	6.5	5.5:1	$\text{Na}_3\text{AlF}_6 + 4\text{NaOH} = \text{NaAlO}_2 + 6\text{NaF} + 2\text{H}_2(\text{g})$ (2) $\text{Al}_2\text{O}_3 + 2\text{NaOH} + 3\text{H}_2\text{O} = 2\text{NaAl}(\text{OH})_4$ (3) $\text{CaF}_2 + 2\text{NaOH} = \text{Ca}(\text{OH})_2 + \text{NaF}$ (4)
Na ₂ CO ₃	950	2	2.5:1	$\text{NaAl}_{11}\text{O}_{17} + 10\text{NaOH} = 11\text{NaAlO}_2 + 5\text{H}_2\text{O}$ (5) $\text{Na}_3\text{AlF}_6 + 1.5\text{Na}_2\text{CO}_3 = 1.5\text{CO}_2(\text{g}) + 0.5\text{Al}_2\text{O}_3 + 6\text{NaF}$ (6) $\text{Na}_3\text{AlF}_6 + 2\text{Na}_2\text{CO}_3 = 2\text{CO}_2(\text{g}) + \text{NaAlO}_2 + 6\text{NaF}$ (7) $\text{Al}_2\text{O}_3 + \text{Na}_2\text{CO}_3 = 2\text{NaAlO}_2 + \text{CO}_2(\text{g})$ (8) $\text{Na}_5\text{Al}_3\text{F}_{14} + 4.5\text{Na}_2\text{CO}_3 = 4.5\text{CO}_2(\text{g}) + 1.5\text{Al}_2\text{O}_3 + 14\text{NaF}$ (9)

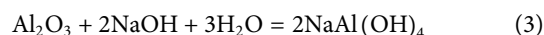
acid leaching, carbon materials with a carbon content >99.00% and high-value application potential can be recovered. However, given that SCA is composed of a large amount of electrolyte components, this process consumes a large amount of alkaline reagents with extremely high economic cost. A summary of the optimal parameters for SCA treatment with different alkaline agents is shown in **Table 3**.

Alkali Leaching

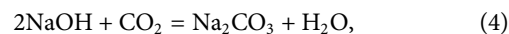
Alkali leaching removes the electrolyte components reacting with alkaline solution to recover carbon materials (Yuan et al., 2018; Yuan et al., 2018; Yuan et al., 2018). The specific process is shown in **Figure 9**.

Li et al. (2021) used NaOH solution to treat SCA and recover the carbon materials. Carbon materials with a carbon content of

98.00% were recovered under the parameters of leaching temperature of 110°C, NaOH solution concentration of 15%, solvent-to-solid ratio of 10:1, leaching time of 120 min, and the NaOH solution dissolved the Na₃AlF₆ and Al₂O₃ in SCA. The main chemical reaction equations are shown in Formulas **Eqs 2–3**.



According to the composition of alkali leaching filtrate (Na⁺, F⁻, and AlO₂⁻), Na₃AlF₆ and Na₂CO₃ were prepared by introducing CO₂ into leachate. The related chemical reaction equations are shown in Formulas **Eqs 4–5**.



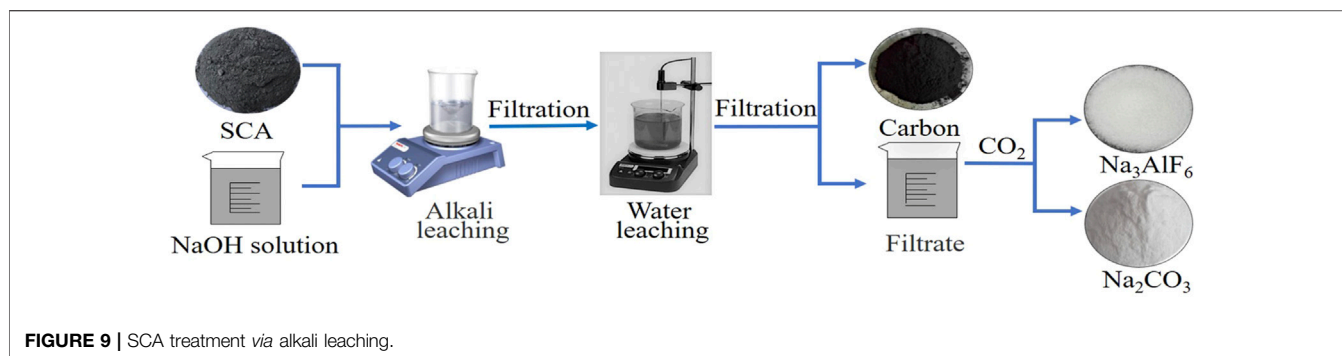


FIGURE 9 | SCA treatment via alkali leaching.

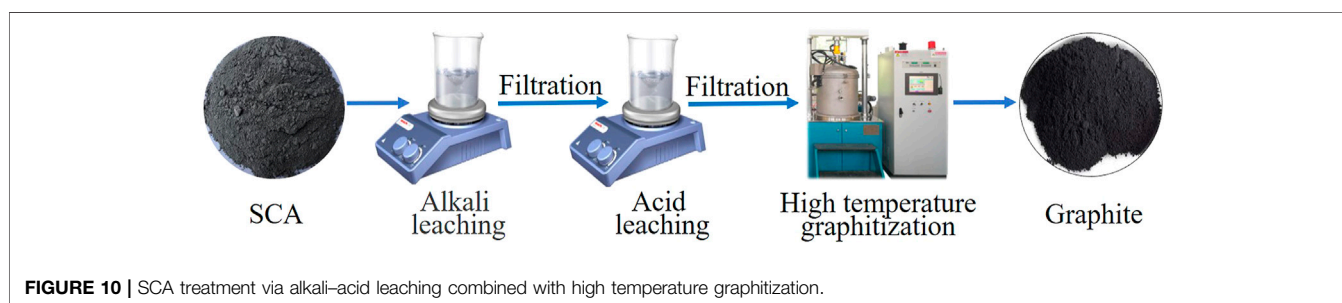
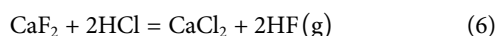


FIGURE 10 | SCA treatment via alkali-acid leaching combined with high temperature graphitization.

Alkali leaching can realize the complete quantitative recovery of valuable components (carbon materials and electrolyte components) in SCA. When combined with carbonation, this method can generate Na₂CO₃ and Na₃AlF₆. Alkali leaching is similar to a closed-loop treatment and has the technical advantages of low energy consumption and high product yield. However, the process is complex and consumes a large amount of alkaline reagents. In addition, CaF₂ not be removed by alkali leaching, thus limiting the high-value utilization of recycled carbon materials.

Chemical Treatment Combined With Physical Separation

Wang (2021) conducted a co-treatment involving alkali-acid leaching and high temperature graphitization to treat SCA. Na₃AlF₆ and Al₂O₃ in SCA were dissolved into the leachate by NaOH solution. The carbon content of SCA was further increased by acid leaching, aiming at removing CaF₂ from SCA. The main reaction in acid leaching is shown in formula Eq. 6. Accordingly, Carbon materials with a carbon content of 93.15% were recovered by alkali-acid leaching.



Afterwards, the carbon content of carbon materials was increased from 93.15 to 99.90% by high temperature graphitization (2,800°C). In the process of graphitization, the carbon in SCA undoubtedly converted from disordered structure to graphite crystal structure by thermal activation. The process of SCA treatment via alkali-acid leaching and high temperature graphitization is shown in Figure 10.

Chemical leaching combined with high temperature graphitization can produce carbon materials with high purity and graphitization degree. The application channels and utilization value of carbon materials in SCA are broadened. Nonetheless, the process is complex and consumes a large amount of chemical reagents. In addition, the high treatment temperature is accompanied by high energy consumption and equipment loss.

Summary

Physical separation and chemical treatment technologies for SCA can realize the separate/complete quantitative recovery of valuable components (carbon materials and electrolytes). The feasibility of utilizing recycled carbon materials to prepare porous carbon materials and lithium-ion batteries has been widely explored. The principle, advantages, and disadvantages of existing methods for the safe disposal and comprehensive utilization of SCA are shown in Table 4.

CONCLUSION AND PROSPECT

SCA is a hazardous solid waste that is inevitably and continuously produced in the aluminum electrolysis industry. Owing to its large number of high-quality carbon materials and high-value electrolyte components, this material has extremely high recycling value. Therefore, the safe disposal and comprehensive utilization of SCA is essential.

- 1) Roasting and vacuum metallurgy can be used to recover electrolyte components that have high purity and could be

TABLE 4 | Principle, advantages, and disadvantages of existing methods for the safe disposal and comprehensive utilization of SCA.

Method	Schematic diagram	Advantages	Disadvantages
Flotation	<p>SCA → Flotation → Carbon, Electrolyte</p>	Large treatment capacity per unit time, low cost, simple operation	A large amount of produced fluoride-containing wastewater
Vacuum metallurgy	<p>SCA → Vacuum smelting → Carbon, Electrolyte</p>	The recovered electrolytes have high purity and recycling property	High energy consumption and equipment loss
CO ₂ activation	<p>SCA → CO₂ activation → Porous carbon</p>	Broaden the utilization channel of SCA	High requirements for the carbon content of raw carbon
Roasting	<p>SCA, Dispersing agent, Combustion improver → Roasting → CO₂, Electrolyte</p>	The recovered electrolytes have high purity and recycling property	Waste a lot of high-quality carbon materials and discharge CO ₂ gas
Bubbling fluidized bed combustion	<p>SCA → Blast air & roasting → CO₂, Electrolyte</p>	High combustion efficiency and combustion intensity	Waste a lot of high-quality carbon materials and discharge CO ₂ gas
Alkali fusion	<p>SCA, Alkaline reagent → Alkali fusion → Carbon, Filtrate (F⁻, Na⁺, AlO₂⁻)</p>	The recovered carbon materials have high purity and high utilization potential	The treatment process is complex and consumes a large amount of alkaline reagents
Alkali leaching	<p>SCA, NaOH solution → Alkali leaching → Carbon, Filtrate (F⁻, Na⁺, AlO₂⁻)</p>	Closed-loop treatment, high product yield and treatment efficiency	The treatment process is complex and consumes a large amount of alkaline reagents
Alkali-acid leaching combined with graphitization	<p>SCA → Alkali-acid leaching → Carbon → Graphitization → Graphite, Graphite structure</p>	The recovered carbon materials with high purity and graphitization degree	High energy consumption and equipment loss

directly returned to the aluminum electrolysis cell for recycling. However, these processes are accompanied by a large amount of CO₂ emission and energy consumption, which do not meet the strategic needs of “carbon

neutrality” and “peak carbon dioxide emissions” promoted by the state. Compared with physical separation, chemical treatment has the advantages of high separation efficiency and high product yield. However, some problems such as large

consumption of chemical reagents and high production cost must be addressed.

- 2) Given the raw material characteristics of SCA, flotation is the most promising technology for the safe disposal and comprehensive utilization of SCA. In future research work, raw materials must be pretreated to further realize the enhanced separation of carbon materials and electrolyte components. Flotation should be combined with chemical treatment to develop a technology with high efficiency, low consumption, and environmental protection.
- 3) Recycling of valuable resources in SCA should be actively explored. For example, carbon materials can be used as raw materials to prepare carbon anode for aluminum electrolysis. The pressure of low-sulfur petroleum coke resource shortage is alleviated, and the production cost is reduced. The high-value utilization of recycled products in catalysis, adsorption, and new energy should be expanded to build a common key

technical system for the safe disposal and comprehensive utilization of SCA.

AUTHOR CONTRIBUTIONS

BL: Methodology, Writing-Original draft preparation. JZ: Conceptualization. ZY: Visualization, Writing-Review and Editing. QP: Investigation, Software. ML: Data Curation. XL: Validation, Formal analysis. WL: Resources, Supervision.

FUNDING

This work was supported by Guizhou Provincial Science and Technology (No. (2020)1Y224, No. (2020)4Y036)).

REFERENCES

- Bai, Qiong. (2020). Causes and Countermeasures of Carbon Slag in Aluminum Electrolysis Production. *Metallurgical Management* 17, 158–159. (in Chinese). doi:10.3969/j.issn.1007-1865.2020.17.002
- Chai, D. P., Hou, G. H., and Huang, H. B. (2016). Experimental Study on the Treatment of Aluminum Reduction Carbon Residue by Vacuum Metallurgy. *Light Met.* 4, 25–27. (in Chinese). doi:10.13662/j.cnki.qjs.2016.04.006
- Chen, X. P. (2011). Latest Status of Processing Technologies for Spent Potlining from Aluminum Smelters. *Light Met.* 12, 21–24. (in Chinese). doi:10.13662/j.cnki.qjs.2011.12.011
- Chen, X. P., Zhao, L., and Luo, Z. S. (2009). Study on Recycling Process for Electrolyte in Carbon Dust from Reduction Cells. *Light Met.* 12, 21–25. (in Chinese). doi:10.13662/j.cnki.qjs.2009.12.006
- Geng, L. L., Zhang, H. X., Li, X. Q., Liao, S., and Wu, Y. (2014). Research Progress in the Preparation of Biomaterial Activated Carbon. *Guangdong Chem. Industry* 41, 102–103. (in Chinese). doi:10.3969/j.issn.1007-1865.2014.12.052
- Guo, Z. H. (2020). Causes and Countermeasures of Carbon Slag in Aluminum Electrolysis Production. *Low Carbon World* 10, 16–17. (in Chinese). doi:10.3969/j.issn.2095-2066.2020.05.010
- Hou, W., Li, H., Feng, Y., Wang, J., Li, M., Cheng, B., et al. (2020). Effects of the Application of a Perforated Anode in an Aluminum Electrolysis Cell on the Gas-Liquid Two-phase Flow and Bubble Distribution Characteristics. *Ind. Eng. Chem. Res.* 59, 14522–14530. doi:10.1021/acs.iecr.0c02478
- Hou, W., Li, H., Li, M., Zhang, B., Wang, Y., and Gao, Y. (2019). Multi-physical Field Coupling Numerical Investigation of Alumina Dissolution. *Appl. Math. Model.* 67, 588–604. doi:10.1016/j.apm.2018.11.041
- Li, C. L., Ou, Y. J., Xie, G. H., Wang, H. Y., Wang, J. Y., Zhao, L. L., et al. (2021). Cultivating Students' Engineering Awareness and Innovation Ability Based on Internet+College Students' Innovation and Entrepreneurship Competition—Taking Carbon Recovery Process Design of Carbon Powder after Aluminum Electrolysis Carbon Residue Flotation as an Example. *Guangdong Chem. Industry* 48, 248–250. (in Chinese). doi:10.3969/j.issn.1007-1865.2021.02.115
- Li, D., Guo, X., Xu, Z., Tian, Q., and Feng, Q. (2015). Leaching Behavior of Metals from Copper Anode Slime Using an Alkali Fusion-Leaching Process. *Hydrometallurgy* 157, 9–12. doi:10.1016/j.hydromet.2015.07.008
- Li, H., Wang, J., Hou, W., Li, M., Cheng, B., Feng, Y., et al. (2021). The Study of Carbon Recovery from Electrolysis Aluminum Carbon Dust by Froth Flotation. *Metals* 11, 145. doi:10.3390/met11010145
- Li, Q., Cui, X. D., and Gao, W. Y. (2015). Countermeasures and Origins of Carbon Residue in Aluminum Electrolysis Production. *Light Met.* 11, 36–38. (in Chinese). doi:10.13662/j.cnki.qjs.2015.11.008
- Liang, C., Zhao, R. M., Peng, J. P., Di, Y. Z., and Wang, Y. W. (2021). Treatment of Carbon Slag from Aluminum Electrolysis Cell Using Na_2CO_3 . *Chin. J. Eng.* 7, 1–12. (in Chinese). doi:10.13374/j.issn2095-9389.2020.11.30.007
- Liu, C. S., and Wu, S. W. (2020). Discussion on Causes and Treatment for Carbon Residue during Aluminum Reduction Pot Production. *World Nonferrous Met.* 14, 19–20. (in Chinese). doi:10.3969/j.issn.1002-5065.2020.14.008
- Liu, K. (2020). Practice of Recovering Electrolyte in Aluminum Electrolysis Carbon Slag Flotation Process. *Resource Regen.* 10, 54–56. (in Chinese). doi:10.3390/min10090820
- Liu, S. X., Gao, B. F., and Zeng, Z. H. (2021). Preparation of Aluminum Electrolytic Cell Porous Carbon by CO_2 Activation and Performance for Adsorption. *Guangzhou Chem. Industry* 49, 75–77. (in Chinese). doi:10.3969/j.issn.1001-9677.2021.07.025
- Liu, Y., Hu, G. Y., Sun, W., Zhang, Y., and Wang, L. (2021). Progress in Comprehensive Utilization of Carbon Solid Waste in Aluminum Electrolytic Cell. *Conservation Utilization Mineral. Resour.* 41, 166–171. (in Chinese). doi:10.13779/j.cnki.issn1001-0076.2021.01.024
- Luo, M. Y., Gu, X. P., Qu, T., Shi, L., and Dai, Y. N. (2020). Separation of Carbon and Electrolyte from Electrolytic Aluminum Spent Cathode Carbon Block by Vacuum Distillation. *Nonferrous Met. Eng.* 10, 47–52. (in Chinese). doi:10.3969/j.issn.2095-1744.2020.07.08
- Luo, Z., Zhao, Y., Lv, B., Fu, Y., Xu, X., and Chen, C. (2019). Dry Coal Beneficiation Technique in the Gas-Solid Fluidized Bed: a Review. *Int. J. Coal Preparation Utilization* 10, 1–29. doi:10.1080/19392699.2019.1678469
- Mei, X. Y., Li, J., and Yu, Z. L. (2016). The Research on Recycling Carbon Residue by Flotation Process. *Light Met.* 4, 28–30. (in Chinese). doi:10.13662/j.cnki.qjs.2016.04.007
- Shoppert, A., Loginova, I., Rogozhnikov, D., Karimov, K., and Chaikin, L. (2019). Increased as Adsorption on Maghemite-Containing Red Mud Prepared by the Alkali Fusion-Leaching Method. *Minerals* 9, 60. doi:10.3390/min9010060
- Tian, Z. L., Gong, Y. P., Xin, X., Yang, K., Deng, C. Y., and Yin, G. (2021). Electrochemical Properties of Si/C Composite Materials Prepared from Discarded Carbon Anode Residue from Aluminum Electrolysis by ball Milling Method. *Mining Metallurgical Eng.* 41, 110–113. doi:10.3969/j.issn.0253-6099.2021.03.027
- Tu, X. C. (2017). Analysis on the Causes and Preventive Measures of Carbon Residue in Aluminum Electrolysis Production. *Shanxi Metall.* 40, 126–128. (in Chinese). doi:10.16525/j.cnki.cn14-1167/tf.2017.04.46
- Wang, H., Feng, Q., Tang, X., and Liu, K. (2016). Preparation of High-Purity Graphite from a fine Microcrystalline Graphite Concentrate: Effect of Alkali Roasting Pre-treatment and Acid Leaching Process. *Separation Sci. Technology* 51, 2465–2472. doi:10.1080/01496395.2016.1206933
- Wang, Y. R. (2021). *Preparation and Electrochemical Performance of Anode Materials for Lithium-Ion Batteries by Spent Carbon Anode from Electrolytic Aluminum*. [master's thesis] (Lanzhou: Lanzhou University of Technology) (in Chinese).
- Wang, Z. Q., Wen, T. J., and Zhang, H. T. (2019). Analysis and Research on Resource Utilization Technology of Anode Carbon Slag Disposal in Aluminum Electrolysis Production. *World Nonferrous Met.* 22, 8–9. (in Chinese). doi:10.3969/j.issn.1002-5065.2019.22.004

- Wei, Y. H. (2018). Improvement and Application of Cryolite Regeneration Technology by Carbon Residue Flotation. *Light Met.* 10, 29–31. (in Chinese). doi:10.13662/j.cnki.qjs.2018.10.007
- Yang, K., Gong, P., Xin, X., Tian, Z., and Lai, Y. (2020). Purifying Spent Carbon Anode (SCA) from Aluminum Reduction Industry by Alkali Fusion Method to Apply for Li-Ion Batteries Anodes: from Waste to Resource. *J. Taiwan Inst. Chem. Eng.* 116, 121–127. doi:10.1016/j.jtice.2020.10.034
- Yang, Y., Gao, B., Wang, Z., Shi, Z., and Hu, X. (2016). Study on the Inter-electrode Process of Aluminum Electrolysis. *Metall. Materi Trans. B* 47, 621–629. doi:10.1007/s11663-015-0508-6
- Yi, S. Y., Wang, X. Y., Li, N., Wei, J. L., and Dai, C. L. (2008). Research Progress in Activation Treatment Technology of Activated Carbon. *Mater. Guide* 3, 72–75. (in Chinese). doi:10.3321/j.issn:1005-023x.2008.03.018
- Yuan, J., Xiao, J., Li, F., Wang, B., Yao, Z., Yu, B., et al. (2018). Co-treatment of Spent Cathode Carbon in Caustic and Acid Leaching Process under Ultrasonic Assisted for Preparation of SiC. *Ultrason. Sonochem.* 41, 608–618. doi:10.1016/j.ultsonch.2017.10.027
- Yuan, J., Xiao, J., Tian, Z., Yang, K., and Yao, Z. (2018). Optimization of Spent Cathode Carbon Purification Process under Ultrasonic Action Using Taguchi Method. *Ind. Eng. Chem. Res.* 57, 7700–7710. doi:10.1021/acs.iecr.7b05351
- Yuan, J., Xiao, J., Tian, Z., Yang, K., Yao, Z., Yu, B., et al. (2018). Optimization of Purification Treatment of Spent Cathode Carbon from Aluminum Electrolysis Using Response Surface Methodology (RSM). *Asia-pac. J. Chem. Eng.* 13, e2164. doi:10.1002/apj.2164
- Zhang, B. S. (2013). Harm of Carbon Slag in Aluminum Electrolysis Production. *Xinjiang Nonferrous Met.* 36, 70–72. (in Chinese). doi:10.16206/j.cnki.65-1136/tg.2013.01.046
- Zhang, Y. N., Chai, D. P., Zhou, Y. F., Wang, Y. Fang., Bai, W. G., and Hou, G. H. (2018). Research Progress on Resource Comprehensive Utilization Technology of Carbon Dust in Aluminum Electrolysis. *World Nonferrous Met.* 7, 1–3. (in Chinese). doi:10.3969/j.issn.1002-5065.2018.07.001
- Zhao, D. F., and Yang, Y. Z. (2013). Analysis on the Harmfulness of Carbon Residue in Aluminum Electrolysis Production. *Introduction Scientific Technol. Innovation* 10, 154, 2013 (in Chinese). doi:10.16660/j.cnki.1674-098x.2013.10.028
- Zhao, R. M., Yu, Z. L., and Li, S. H. (2015). The Recycling Experimental Study on Aluminum Electrolysis Carbon Residues. *Yunnan Metall.* 44, 15–18. (in Chinese). doi:10.3969/j.issn.1006-0308.2015.01.004
- Zhou, J., Yao, Z., Liu, W., Luo, J., and Xie, Y. S. (2019). Effects of Flotation Conditions on the Separation Efficiency of Carbon in Carbon Residue in Aluminum Electrolysis. *Carbon Technology* 38, 58–61. (in Chinese). doi:10.14078/j.cnki.1001-3741.2019.05.012
- Zhou, J. Y., Wu, C. B., Zhang, J. B., and Wu, Q. J. (2014). Study of Characteristic of Carbon Residue from Electrolytic Aluminum and its Filidization Recovery. *Nonferrous Met. (Smelting Part)* 12, 16–18. (in Chinese). doi:10.3969/j.issn.1007-7545.2014.12.005

Conflict of Interest: The authors declare that the research was conducted in the absence of any commercial or financial relationships that could be construed as a potential conflict of interest.

Publisher's Note: All claims expressed in this article are solely those of the authors and do not necessarily represent those of their affiliated organizations, or those of the publisher, the editors and the reviewers. Any product that may be evaluated in this article, or claim that may be made by its manufacturer, is not guaranteed or endorsed by the publisher.

Copyright © 2021 Li, Zhou, Yao, Peng, Liu, Li and Liu. This is an open-access article distributed under the terms of the Creative Commons Attribution License (CC BY). The use, distribution or reproduction in other forums is permitted, provided the original author(s) and the copyright owner(s) are credited and that the original publication in this journal is cited, in accordance with accepted academic practice. No use, distribution or reproduction is permitted which does not comply with these terms.



CO₂ Adsorption and Desorption by Waste Ion-Exchange Resin-Based Activated Carbon on Fixed Bed

Mengqi Wei^{1,2*} and Qiuyue Zhao¹

¹Jiangsu Key Laboratory of Environmental Engineering, Jiangsu Provincial Academy of Environmental Science, Nanjing, China,

²State Key Laboratory of Materials-Oriented Chemical Engineering, National Engineering Research Center for Special Separation Membrane, Nanjing Tech University, Nanjing, China

OPEN ACCESS

Edited by:

Siyi Luo,
Qingdao University of Technology,
China

Reviewed by:

Lu Chen,
Dalian University of Technology, China
Xiangmin Wang,
Chongqing Normal University, China
Ye Zhao,
Inner Mongolia University of Science
and Technology, China

*Correspondence:

Mengqi Wei
mengqi_wei@163.com

Specialty section:

This article was submitted to
Advanced Clean Fuel Technologies,
a section of the journal
Frontiers in Energy Research

Received: 08 September 2021

Accepted: 28 September 2021

Published: 02 November 2021

Citation:

Wei M and Zhao Q (2021) CO₂
Adsorption and Desorption by Waste
Ion-Exchange Resin-Based Activated
Carbon on Fixed Bed.
Front. Energy Res. 9:772710.
doi: 10.3389/fenrg.2021.772710

The waste ion-exchange resin-based activated carbon (WIRAC) was utilized for CO₂ adsorption. The effect of adsorption temperature, gas flow, CO₂ concentration, and adsorbent filling content on CO₂ adsorption properties of WIRAC and the effect of desorption temperature and sweep gas flow on CO₂ desorption performances of WIRAC were researched. In the adsorption process, with the increase of adsorption temperature, the CO₂ adsorption capacity and adsorption rate decrease; as the gas flow increases, the CO₂ adsorption capacity decreases, but the adsorption rate increases; with the increase of CO₂ concentration and adsorbent filling content, the CO₂ adsorption capacity and adsorption rate both increase. In the desorption process, the higher the desorption temperature and the smaller the sweep gas flow, the higher the CO₂ purity of product gas and the longer the desorption time. In order to make sure the adsorbent be used efficiently and the higher CO₂ concentration of product gas, the adsorption and desorption conditions selected should be a suitable choice.

Keywords: CO₂ adsorption, waste ion-exchange resin-based activated carbon, fixed bed, breakthrough curve, desorption

INTRODUCTION

Since the 20th century, the rising required energy and ecological and environmental problems caused by the pollution and overuse of resources have significantly threatened the existence and development of human beings with the rapid development of the global economy. The emission of large amounts of CO₂ with a lot of energy consumption leads to global warming. In order to slow down global warming, carbon capture and storage (CCS) technology has been conceived to reduce the emission of CO₂. Among all CO₂ capture technologies, because of lots of adsorbents, low cost of equipment and operation, convenient automatic operation, and high-purity product, adsorption has been judged to be a good carbon capture technology (Wang et al., 2011; Wei et al., 2016). High cost is the biggest obstacle to promote CCS technology better and faster. The capture cost of CCS is approximately 75% of the total cost (Plasynski et al., 2009; Wei et al., 2018); hence, the important thing is reducing the cost of CO₂ capture. There are three methods to reduce the cost in the adsorption process: reduce the adsorbent cost, increase the adsorption capacity of the adsorbent, and improve the adsorption-desorption process cycle (Wei et al., 2018). Wang (Wang et al., 2011) and Samanta (Samanta et al., 2012) reviewed different adsorbents in CO₂ capture and discussed their new trends. Adsorbents utilized for CO₂ adsorption are porous

carbonaceous materials (Wang et al., 2012; Wang et al., 2016; Botomé et al., 2017; Álvarez-Gutiérrez et al., 2017), mesoporous silicon (Watabe and Yogo, 2013; Jiao et al., 2016; Kishor and Ghoshal, 2016; Sanz-Pérez et al., 2017), zeolite (Krishna and van Baten, 2012; Cheung et al., 2013; Zhang et al., 2016), metal-organic frameworks (MOFs) (Bao et al., 2011; Krishna and van Baten, 2012; Chen et al., 2017; Delgado et al., 2017), metallic oxide (Kierzkowska et al., 2013; Ozcan et al., 2013), and so on.

In order to reduce the cost of adsorbent, using the wastes as a raw material to produce adsorbents is one of the research hotspots (Hoseinzadeh Hesas et al., 2013; Wee, 2013). Because of the higher carbon content and less ash content, waste ion-exchange resin has been found to be a suitable precursor to produce activated carbon (Wei et al., 2016). And the waste ion-exchange resin-based activated carbon (WIRAC) has been produced to be utilized for sewage treatment (Bratek et al., 2002; Gun'ko et al., 2005), naphthalene adsorption (Shi et al., 2013), and high-performance supercapacitors (Zhang et al., 2013), but to the best of our knowledge, there is no one using the WIRAC to separate CO₂ from flue gas. In our previous work (Wei et al., 2016), we have researched the effect of preparation parameters on the pore structure of WIRAC and the preliminary adsorption properties of WIRAC by TGA. But the CO₂ adsorption by TGA is only a preliminary research, which is far from industrial application.

Hence, in this paper, the CO₂ adsorption and desorption properties on a fixed bed have been further studied. In the adsorption process, the effect of adsorption temperature, gas flow, CO₂ concentration, and adsorbent filling content on CO₂ breakthrough and adsorption capacity of WIRAC was researched. In the desorption process, the effect of desorption temperature and sweep gas flow on CO₂ desorption properties of WIRAC was studied.

EXPERIMENTAL

Materials

The waste ion-exchange resin (a kind of cation exchange resin named "D001" according to the ministerial standard of petroleum chemical industry of the People's Republic of China (1978)) has been used to produce activated carbon (AC) in our previous research (Wei et al., 2016). And the preparation parameters of WIRAC are that the activation agent is KOH, the activation temperature is 900°C, the activation time is 2 h, the impregnation ration (the mass ratio of KOH and char) is 1.5, and the atmosphere is inert (N₂).

The Characterization of WIRAC

The N₂ adsorption-desorption isotherm of WIRAC was tested by TriStar II 3020. The BET equation was used to calculate the specific surface area (S_{BET}). The micropore area (S_{mic}) and micropore volume (V_{mic}) were calculated by the D-R equation. The external surface area (S_{ext}) was obtained by subtracting S_{mic} from S_{BET} .

CO₂ Adsorption and Desorption on Fixed Bed

The CO₂ adsorption and desorption performances of WIRAC were tested by a fixed bed, and the experimental system can be seen in **Figure 1**. The experimental system includes three sections: gas distribution system, reaction system, and detection system. The gas distribution system is mainly composed of N₂, CO₂, mass flow meters, valves, and a mixing tank. The reaction system is mainly composed of a tubular furnace, adsorber, and temperature controller. The detection system is mainly composed of a CO₂ analysis instrument and data recording system. The exhaust gas generated from the experiment is expelled from the exhaust system.

The Calculation of CO₂ Adsorption Capacity

The CO₂ adsorption capacity on a fixed bed can be calculated by

$$q = \frac{1}{M} \left[\int_0^t Q \frac{c_0 - c}{1 - c} dt \right] \frac{T_0}{T} \frac{1}{V_m}, \quad (1)$$

where q is the CO₂ adsorption capacity of per gram adsorbent, mmol/g; M is the mass of the adsorbent, g; Q is the flow of the inlet gas, cm³/min; c_0 and c are the CO₂ concentrations of the inlet gas and outlet gas, respectively, vol%; t is the adsorption time, min; T_0 is 273 K; T is the adsorption temperature, K; and V_m is the molar volume of the gas, 22.4 ml/mmol.

The regeneration degree is defined as follows:

$$D_{\text{reg}} = \frac{m_{\text{reg}}}{m_1}, \quad (2)$$

where m_{reg} is the CO₂ adsorption capacity of the regenerated WIRAC and m_1 is the CO₂ adsorption capacity of the fresh WIRAC.

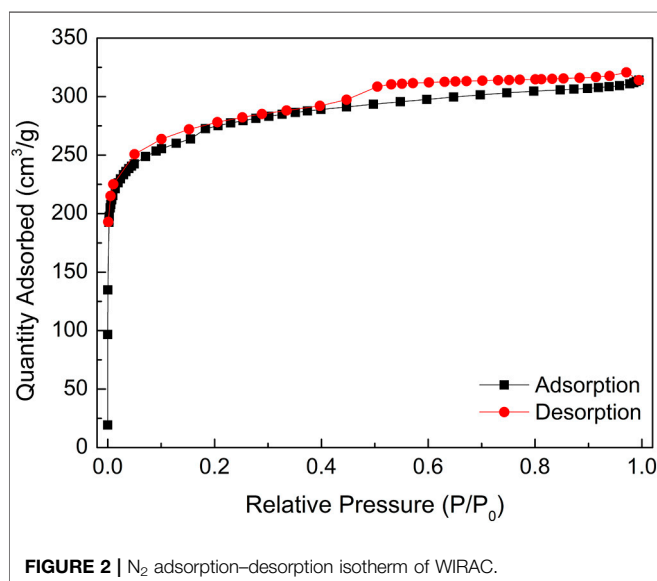
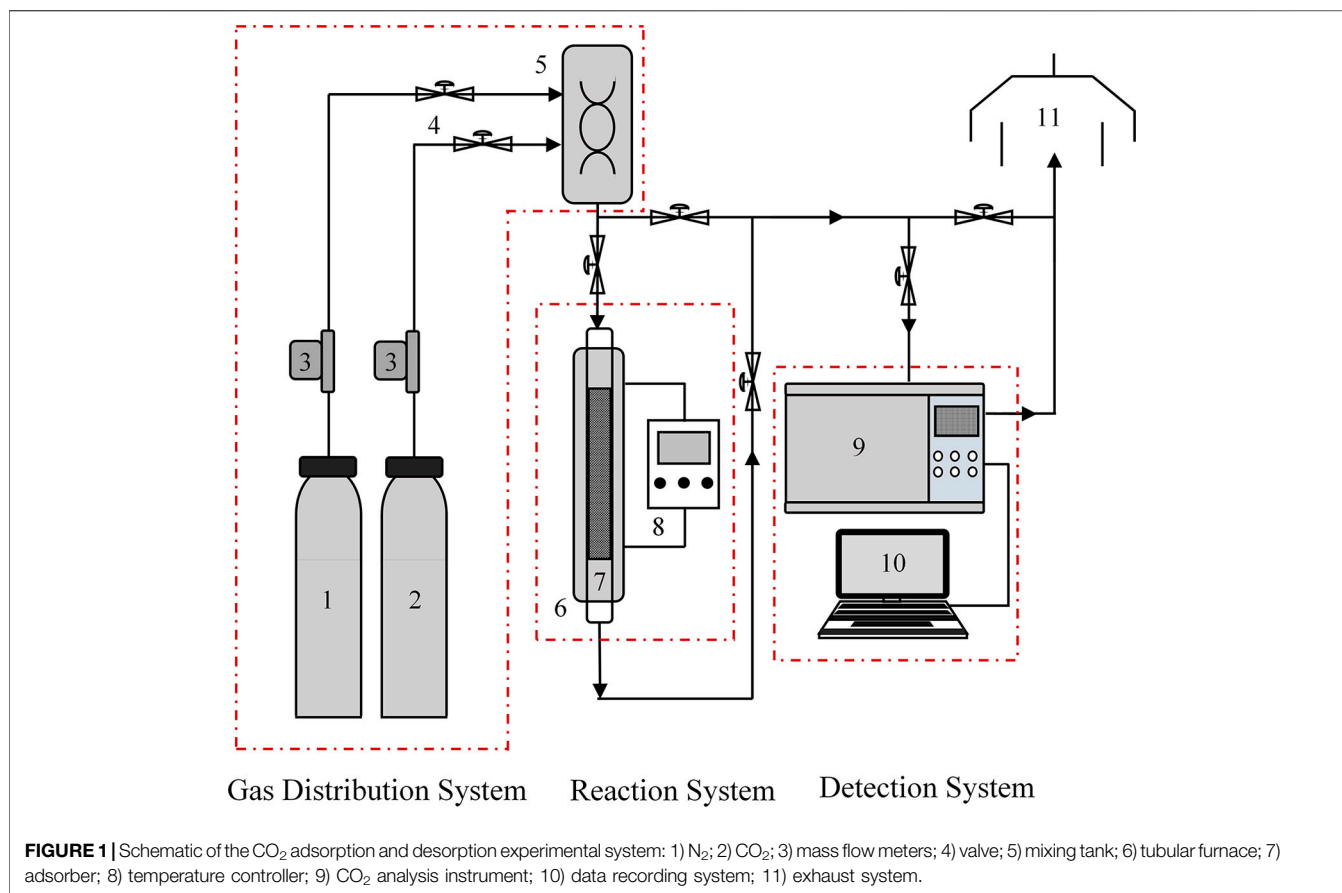
RESULTS AND DISCUSSION

The Characterization of WIRAC

Figure 2 shows the N₂ adsorption-desorption isotherm of WIRAC at -196 °C. On the basis of adsorption isotherm classification and adsorption hysteresis loops of the IUPAC (International Union of Pure and Applied Chemistry) (Brunauer et al., 1940; Sing et al., 1985), WIRAC presents a type I adsorption isotherm and H4 hysteresis loop. The pore structure parameters can be calculated by the N₂ adsorption-desorption isotherm. **Table 1** shows the pore structure parameters of WIRAC, and **Figure 3** shows the pore size distributions of WIRAC by the DFT model. As shown in **Figure 3**, the pore sizes are in the range of 0.9–3.6 nm, especially 0.9–1.25 nm, which is suitable for CO₂ adsorption (the dynamic diameter of CO₂ is 0.33 nm).

CO₂ Adsorption Performances of WIRAC

In the research of adsorption bed experiments, the breakthrough curve is very important. The so-called breakthrough curve shows that the mixture gas enters into the adsorption bed continuously



and the strong adsorbate gas can be detected in the outlet, and until the concentration of the strong adsorbate gas in the outlet is the same as the concentration of the gas in the inlet. In the following experiments, the effects of different operating

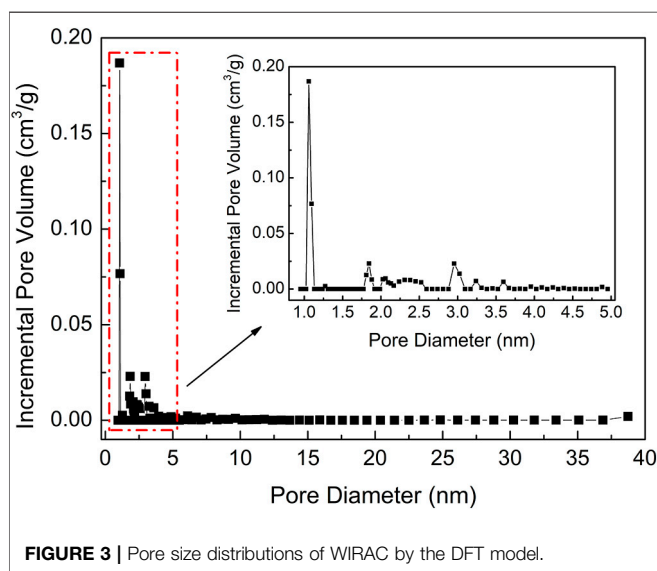
parameters on CO₂ adsorption performance of WIRAC were researched.

The Effect of Adsorption Temperature on CO₂ Adsorption

Figure 4 shows CO₂ adsorption properties at different adsorption temperatures. As shown in **Figures 4A,B**, as the adsorption temperature increases, the breakthrough curves move to the left and the breakthrough time reduces. The two points of the breakthrough curve are important, and they are 5% (the concentration of the strong adsorbate gas in the outlet divided by the concentration of the gas in the inlet) and 95%, respectively. The point of 5% expresses the adsorption bed begins to be broken through, and the point of 95% expresses the adsorption bed is almost broken through completely. The CO₂ adsorption capacity reduces with the increasing adsorption temperature. There are two reasons leading to the situation. One is that the adsorption process is an exothermal reaction. For an exothermal reaction, the reaction will move toward the reverse direction with the increase of temperature. Thus, adsorption can be inhibited, which is not conducive to the adsorption process. The other is that as the temperature increases, CO₂ molecules can get more energy. This will lead to more adsorbed CO₂ molecules removed from the surface of WIRAC. The two reasons lead to the reduction of CO₂ adsorption capacity with the increase of adsorption temperature. **Figure 4B** demonstrates the CO₂ adsorption capacity of different

TABLE 1 | Pore structure parameters of WIRAC.

Sample	S_{BET} m ² /g	S_{mic} m ² /g	S_{ext} m ² /g	V_{mic} cm ³ /g	V_{total} cm ³ /g	D_{ave} nm	$V_{\text{mic}}/V_{\text{total}}$ %
WIRAC	987.20	553.88	433.32	0.2595	0.4858	1.9684	53.42

**FIGURE 3** | Pore size distributions of WIRAC by the DFT model.

situations. The adsorption capacity of 5% is named q_b ($q_{\text{breakthrough}}$), adsorption capacity of 95% is named q_s ($q_{\text{saturation}}$), and adsorption capacity of 100% is named q_e ($q_{\text{equilibrium}}$). q_b is over 85% of q_e , except for 80°C (about 80% of q_e). q_s is over 97% of q_e .

As revealed in **Figures 4C,D**, with the increase of temperature, the CO₂ adsorption equilibrium time reduces, which is the same as the result of breakthrough curves. And as the temperature increases, the CO₂ adsorption rate reduces. Theoretically, the adsorption rate should increase with the increase of temperature. However, the result was contrary to the theoretical result. As the temperature increases, the rates of adsorption and desorption both increase, but the desorption rate can be affected more than the adsorption rate. This leads to the CO₂ adsorption rate reducing with the increase of adsorption temperature.

CO₂ adsorption in the lower temperature not only makes the time of breakthrough be longer but also makes the CO₂ adsorption capacity and adsorption rate be higher. Hence, CO₂ can be adsorbed consecutively for a long time without changing the pipeline frequently to switch adsorption and desorption processes. And in this situation, the CO₂ adsorption capacity and adsorption rate are both higher. The temperature of flue gas is about 50–80°C, which is dependent on the difference of desulfurization and denitrification processes. In this range, it is not conducive to CO₂ adsorption. Therefore, the temperature of flue gas should be properly reduced, or development a kind of adsorbent which has a good adsorption capacity at the temperature of 50–80°C.

The Effect of Gas Flow on CO₂ Adsorption

Figure 5 shows CO₂ adsorption properties at different gas flows. In **Figures 5A,B**, with the increase of gas flow, the breakthrough curves move to the left and the breakthrough time and CO₂ adsorption capacity reduce. With the increase of gas flow, the total amounts of gas flowing and CO₂ molecules through the adsorbent increase per unit time and breakthrough time shortens. However, the larger gas flow can sweep the adsorbed CO₂ molecules and make some adsorbed CO₂ molecules desorb. Hence, the CO₂ adsorption capacity reduces with the increase of gas flow. **Figure 5B** shows the CO₂ adsorption capacity of different situations. q_b is over 86% of q_e , and q_s is over 98% of q_e .

From the results of **Figures 5C,D**, it can be seen that as the gas flow increases, the CO₂ adsorption equilibrium time reduces, which is the same as the result of breakthrough curves. And with the increase of flow gas, the adsorption rate increases. With the increase of gas flow, the total amounts of gas flow and CO₂ molecules through the adsorbent increase per unit time, which makes the total gas pressure increase and the reaction move toward the direction of decrease of pressure reduction (the direction of CO₂ adsorption). Hence, the adsorption rate increases, as the gas flow increases.

Although the larger gas flow can make the adsorption rate increase, the CO₂ adsorption capacity per unit mass of adsorbent and breakthrough time reduce. The reduction of breakthrough time leads to the change of pipeline frequently to switch adsorption and desorption processes, and the reduction of adsorption capacity cannot make the adsorbent be utilized better. In the actual production, the total amount of flue gas is unchanged generally. In order to reduce the flue gas flow, the flue gas can be bypassed to enter into parallel adsorption beds. In this way, not only switching pipes frequently can be reduced, but also WIRAC can be utilized better.

The Effect of CO₂ Concentration on CO₂ Adsorption

Figure 6 shows CO₂ adsorption properties at different CO₂ concentrations. As shown in **Figures 6A,B**, as the CO₂ concentration increases, the breakthrough curves move to the left and the breakthrough time reduces, but the CO₂ adsorption capacity increases. With the increase of CO₂ concentration, the total amount of CO₂ molecules through the adsorbent increases per unit time and breakthrough time shortens. The larger reactant concentration (CO₂ concentration) promotes the adsorption reaction to move toward the direction of positive reaction (the direction of CO₂ adsorption), so the CO₂ adsorption capacity increases. **Figure 6B** shows the CO₂ adsorption capacity of different situations. q_b is over 86% of q_e , and q_s is over 98% of q_e .

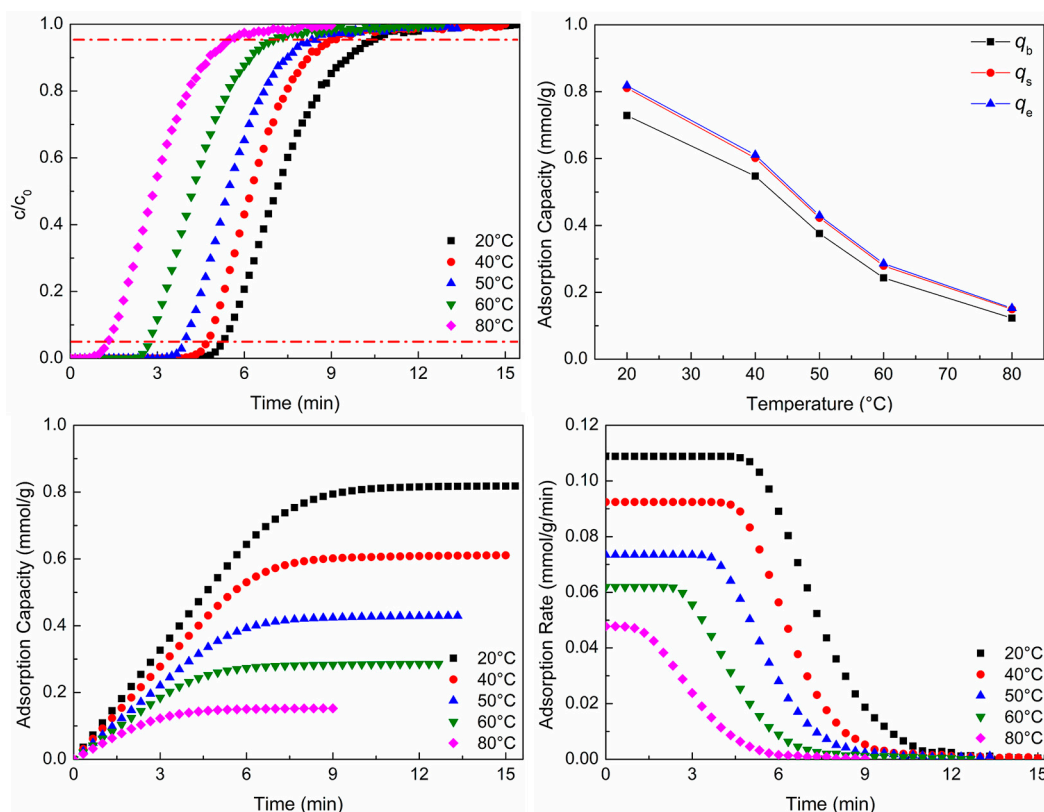


FIGURE 4 | CO₂ adsorption properties at different adsorption temperatures: **(A)** breakthrough curves; **(B)** adsorption capacity; **(C)** adsorption process; **(D)** adsorption rate.

As revealed in **Figures 6C,D**, as the CO₂ concentration increases, the CO₂ adsorption equilibrium time reduces, which is the same as the result of breakthrough curves, and the CO₂ adsorption capacity and adsorption rate increase with the increase of CO₂ concentration. As the CO₂ concentration increases, the total amount of CO₂ molecules through the adsorbent increases per unit time, which is advantageous to moving toward the direction of positive reaction (the direction of CO₂ adsorption). Hence, the CO₂ adsorption rate increases. The increase of adsorption rate makes the adsorption equilibrium time reduce.

The larger CO₂ concentration not only increases the adsorption capacity but also promotes the adsorption rate, which is advantageous to CO₂ adsorption. However, the larger CO₂ concentration can reduce the breakthrough time and make the adsorbent be regenerated frequently, which is disadvantageous to the utilization of adsorbent. The CO₂ concentration of flue gas is dependent on the kind of fuel, the process, and the status of combustion. When the fuel, process, and status of combustion are determined, the CO₂ concentration of flue gas is almost unchanged. In general, the high purity of product gas (CO₂ gas) cannot be obtained by only one adsorption-desorption cycle. That is, the adsorption

of low CO₂ concentration needs more time to obtain high purity of product gas, while the high CO₂ concentration needs less time. So, the number of adsorption beds of high CO₂ concentration should be more than that of low CO₂ concentration in order to make sure CO₂ adsorption be carried out continuously.

The Effect of Adsorbent Filling Content on CO₂ Adsorption

Figure 7 shows CO₂ adsorption properties at different adsorbent filling contents. In **Figures 7A,B**, with the increase of adsorbent filling content, the breakthrough curves move to the right and the breakthrough time and the total CO₂ adsorption capacity increase, but the adsorption capacity per mass of adsorbent reduces. As the adsorbent filling content increases, that is, with the increase of the height of adsorbent, the time of gas flowing through the adsorbent bed increases, so the breakthrough time increases. The more adsorbent makes some adsorbent could not contact with CO₂ gas. Although the total adsorption capacity increases, the adsorption capacity per mass of adsorbent reduces. **Figure 7B** shows the CO₂ adsorption capacity of different situations. q_b is over 86% of q_e , and q_s is over 97% of q_e .

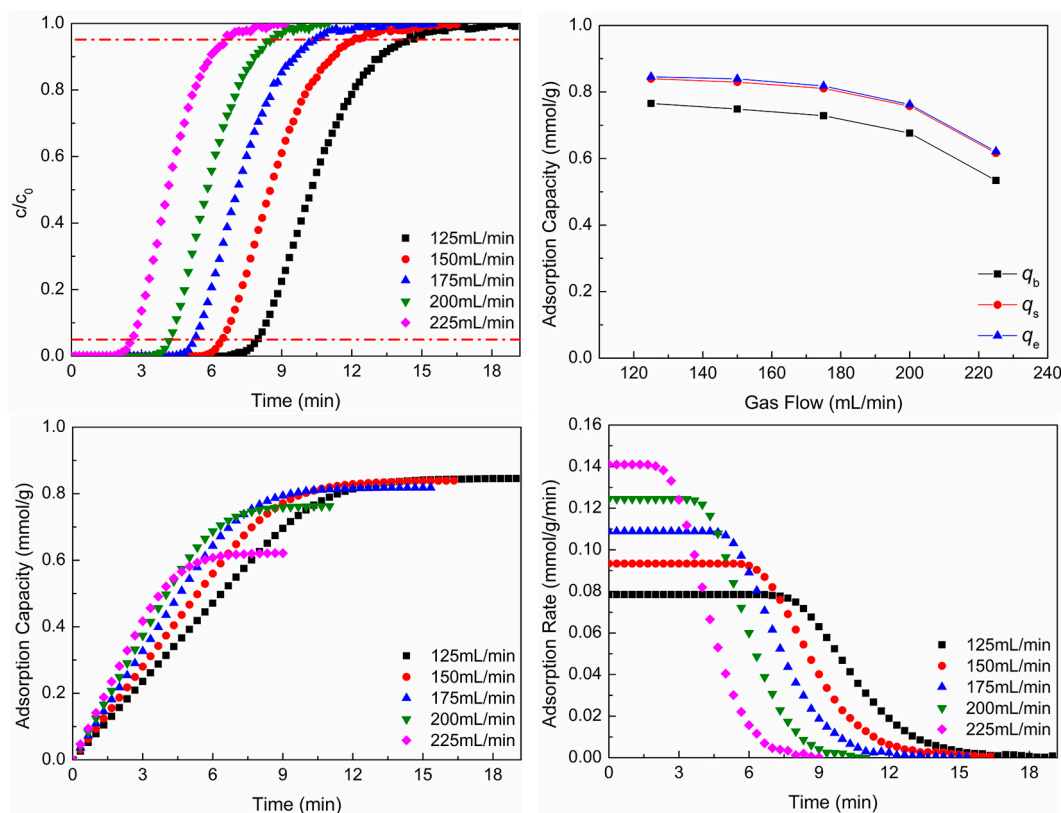


FIGURE 5 | CO₂ adsorption properties at different gas flows: (A) breakthrough curves; (B) adsorption capacity; (C) adsorption process; (D) adsorption rate.

As revealed in Figures 7C,D, as the adsorbent filling content increases, the CO₂ adsorption equilibrium time increases, which is the same as the result of breakthrough curves, but the CO₂ adsorption capacity per mass of adsorbent and adsorption rate reduce with the increase of adsorbent filling content.

The larger amount of adsorbent makes the breakthrough time increase, but the CO₂ adsorption capacity per mass of adsorbent and adsorption rate reduce. The larger amount of adsorbent also leads to the further decrease of pressure drop of gas, and the adsorbent cannot be utilized effectively, which is disadvantageous to CO₂ adsorption. However, the smaller amount of adsorbent makes the CO₂ adsorption capacity per mass of adsorbent and adsorption rate be bigger, and the breakthrough time is small, which is disadvantageous to the cycle of adsorbent. Hence, the amount of adsorbent should be chosen according to the actual situation. In this way, the breakthrough time is enough, and the adsorbent can be utilized well.

The CO₂ adsorption capacity of WIRAC has been compared with that of some other ACs. And the comparison results can be seen in Table 2. As shown in Table 2, the adsorption capacity of WIRAC is just at a middle level. And in consideration of the precursor of WIRAC, WIRAC shows great potential as an adsorbent for post-combustion CO₂ capture.

CO₂ Desorption Performance of WIRAC

After the CO₂ adsorption process, the WIRAC is regenerated and can be recycled. The different operation parameters can affect the desorption properties of WIRAC. In the following experiments, the effect of different desorption temperatures and sweep gas flows on CO₂ desorption performance of WIRAC was researched. And the sweep gas in the CO₂ desorption process is pure N₂.

The Effect of Desorption Temperature on CO₂ Desorption

Figure 8 shows CO₂ desorption properties at different desorption temperatures. As shown in Figure 8A, at the chosen experimental desorption temperature, as the desorption temperature increases, the CO₂ concentration of desorption gas increases. Although CO₂ concentration increases to a certain extent, the magnitude of increase is not significant, and the time of desorption increases. The higher CO₂ concentration of desorption gas dependent on a higher desorption temperature makes the time of CO₂ concentration reduction be longer than the lower CO₂ concentration in a certain condition of sweep gas flow. So, the higher the desorption temperature is, the longer the desorption time will be. As revealed in Figure 8B, at the chosen experimental desorption temperature, the second CO₂ adsorption capacity is almost the same as the first adsorption capacity, and the regeneration degree of WIRAC remains at about 1.0. It

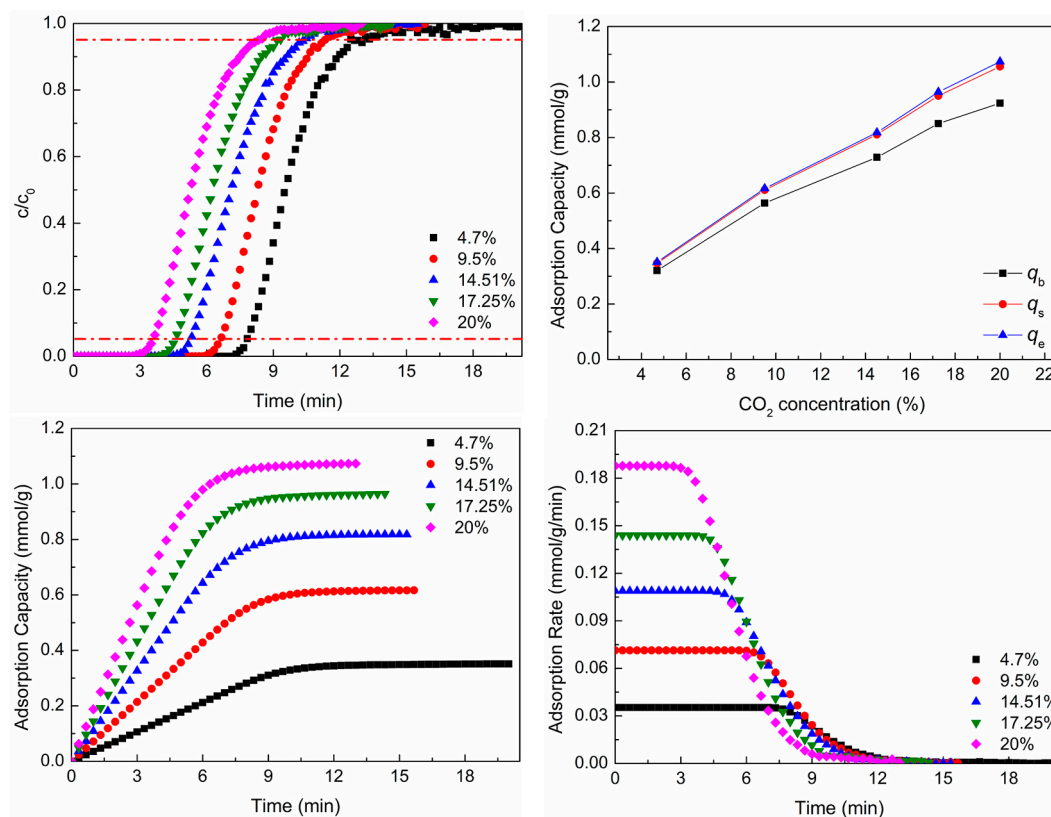


FIGURE 6 | CO₂ adsorption properties at different CO₂ concentrations: **(A)** breakthrough curves; **(B)** adsorption capacity; **(C)** adsorption process; **(D)** adsorption rate.

indicates that, at the chosen experimental desorption temperature, the WIRAC can be regenerated well and the CO₂ adsorption capacity of regenerated WIRAC is not affected by the desorption temperature.

From the results of **Figure 8**, it can be seen that, at the chosen experimental desorption temperature, the WIRAC can be regenerated well and the higher purity of CO₂ depends on the higher desorption temperature. With the increase of desorption temperature, the energy required for regeneration increases, while the increased scope of the purity of CO₂ in product gas is not big. In order to obtain the higher purity CO₂ product gas, increasing the desorption temperature simply makes the input more than the output and lost than gained. Hence, a suitable desorption temperature not only makes the WIRAC be regenerated well but also makes the input energy be not too much and the purity of CO₂ in product gas be relatively high.

The Effect of Sweep Gas Flow on CO₂ Desorption

Figure 9 shows CO₂ desorption properties at different sweep gas flows. As shown in **Figure 9A**, with the increase of sweep gas flow, the CO₂ concentration in desorption gas and desorption time reduce. When the adsorption process and desorption condition are unchanged, the amount of CO₂ in desorption gas is unchanged, too. As the sweep gas flow increases, the CO₂ in

desorption gas is diluted. Hence, the CO₂ concentration in desorption gas and desorption time reduce with the increase of sweep gas flow. As revealed in **Figure 9B**, the second CO₂ adsorption capacity is almost the same as the first adsorption capacity, and the regeneration degree of WIRAC remains at about 1.0 at different sweep gas flows. This indicates that the WIRAC can be regenerated well and the CO₂ adsorption capacity of regenerated WIRAC is not affected by the sweep gas flow.

From the results of **Figure 9**, it can be seen that no matter what the sweep gas flow is, the WIRAC can be regenerated completely at the chosen regeneration condition. The regeneration of WIRAC is almost not affected by the sweep gas flow, while the CO₂ concentration in product gas is affected by the sweep gas flow. The bigger the sweep gas flow, the lower the CO₂ purity in product gas. And the shorter the desorption time is, the faster the desorption process will be. In the actual production, the suitable sweep gas flow should be chosen, so not only the higher CO₂ purity in product gas can be obtained, but also the faster regeneration of WIRAC can be got.

CONCLUSION

In this paper, WIRAC is utilized as an adsorbent for CO₂ adsorption. The adsorption and desorption properties of

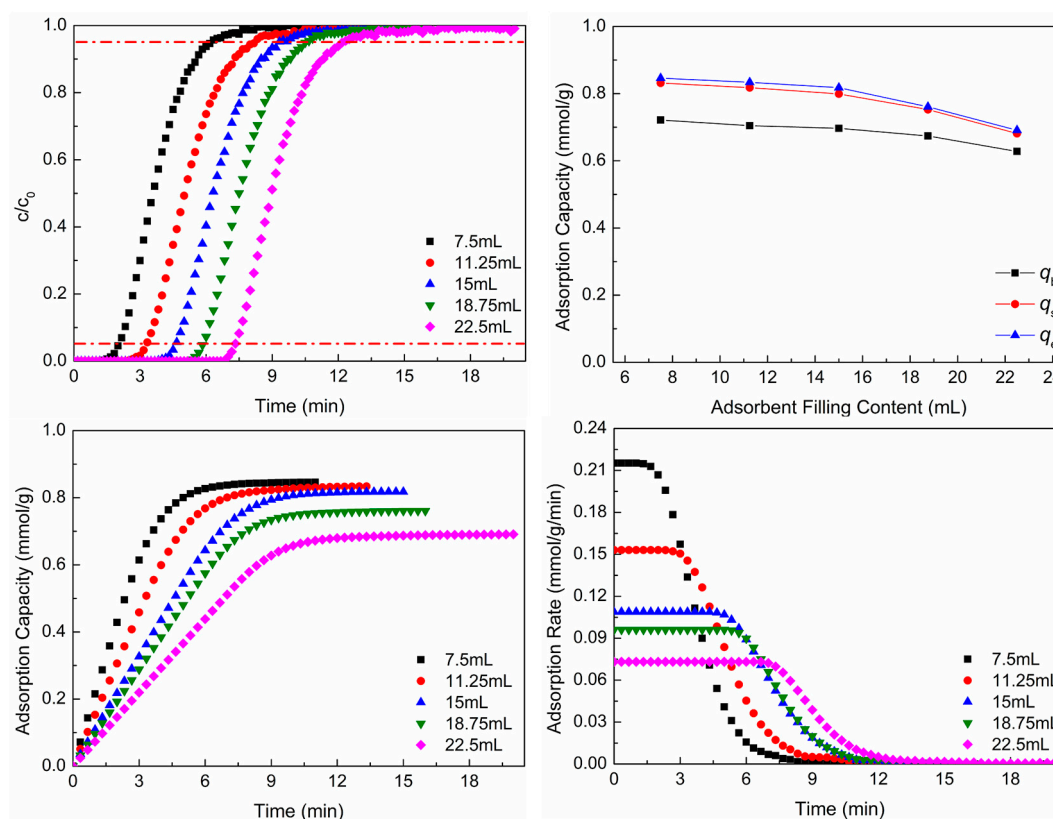


FIGURE 7 | CO₂ adsorption properties at different adsorbent filling contents: **(A)** breakthrough curves; **(B)** adsorption capacity; **(C)** adsorption process; **(D)** adsorption rate.

TABLE 2 | Adsorption capacity of CO₂ by ACs in different literature studies.

Sample	Adsorption capacity	Experimental conditions and equipment	References
WIRAC	0.729 mmol/g	20°C, 14.51%, 175 ml/min, adsorption bed	This paper
A	6.9 wt% (1.568 mmol/g)	25°C, 100% CO ₂ , 1 bar, TGA	Plaza et al. (2010)
AA750	11.7 wt% (2.659 mmol/g)		
C-700	0.8 mmol/g	30°C, 100% CO ₂ , TGA	Goel et al. (2016)
C@MF-x	3.4–4.3 mmol/g	20°C, 100% CO ₂ , 760 mmHg, Quantachrome Autosorb 1MP	Liu et al. (2017)
AC	2.1 mmol/g	298 K, 1 bar, IGA	Yang et al. (2012)
NPC10	3.2 mmol/g	298 K, 1 bar, IGA	
AC1	0.75 wt% (0.170 mmol/g)	RT, 1 bar, IGA	Caglayan and Aksoylu (2013)
	3.30 wt% (0.75 mmol/g)	RT, 20 bar, IGA	
AC4-200-400He	8.19 wt% (1.861 mmol/g)	RT, 1 bar, IGA	
	22.38 wt% (5.086 mmol/g)	RT, 20 bar, IGA	
MF-700	1.29 mmol/g	30°C, 100% CO ₂ , ASAP 2010	Goel et al. (2017)

WIRAC on a fixed bed were researched. In the adsorption process, with the increase of adsorption temperature, the CO₂ adsorption capacity and adsorption rate decrease; as the gas flow increases, the CO₂ adsorption capacity decreases, but the adsorption rate increases; with the increase of CO₂ concentration, the CO₂ adsorption capacity and adsorption rate increase; as the adsorbent filling content increases, the

CO₂ adsorption capacity and adsorption rate increase. In order to make the CO₂ adsorption capacity and adsorption rate of WIRAC be higher, the adsorption temperature should be low; the flue gas should be bypassed to enter into parallel adsorption beds; the amount of adsorbent should be chosen according to the actual situation. In the desorption process, the higher the desorption temperature and the smaller the

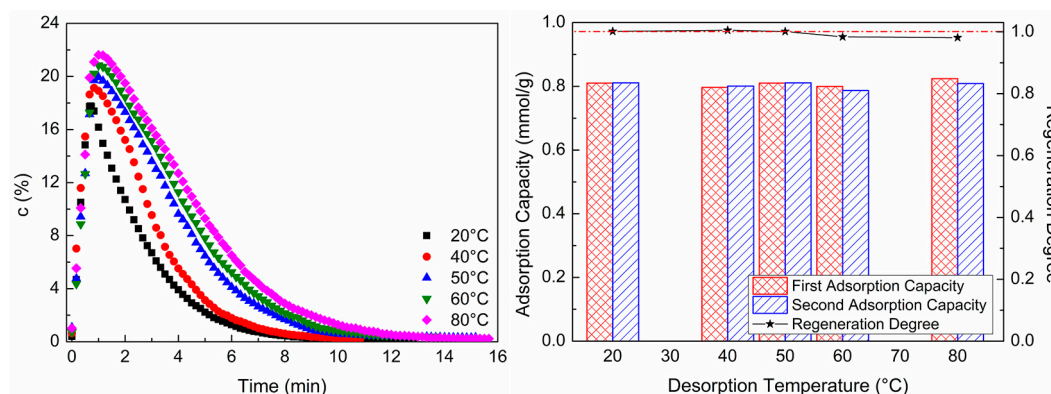


FIGURE 8 | CO₂ desorption properties at different desorption temperatures: **(A)** CO₂ desorption concentration; **(B)** adsorption capacity and regeneration degree.

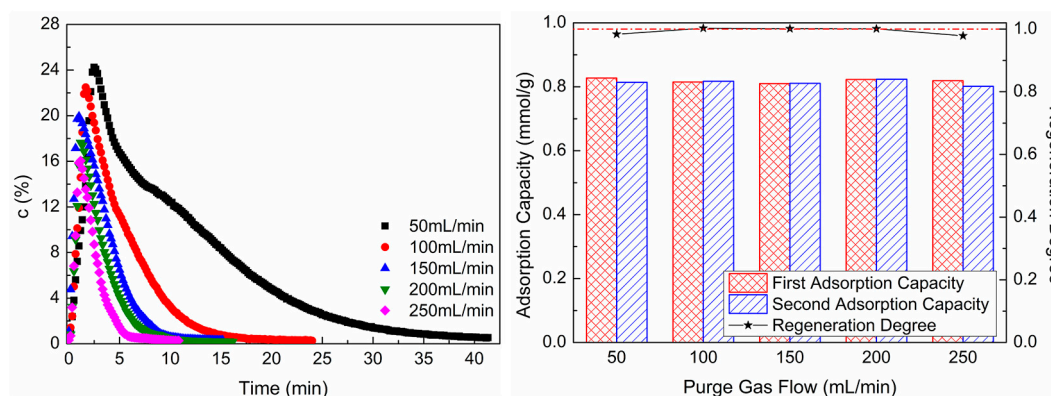


FIGURE 9 | CO₂ desorption properties at different sweep gas flows: **(A)** CO₂ desorption concentration; **(B)** adsorption capacity and regeneration degree.

sweep gas flow, the higher the CO₂ purity of product gas and the longer the desorption time. Due to obtaining high CO₂ purity of product gas in a short time, the desorption temperature and sweep gas flow should be chosen with suitable values.

DATA AVAILABILITY STATEMENT

The original contributions presented in the study are included in the article/Supplementary Material, and further inquiries can be directed to the corresponding author.

REFERENCES

Álvarez-Gutiérrez, N., Gil, M. V., Rubiera, F., and Pevida, C. (2017). Kinetics of CO₂ Adsorption on Cherry Stone-Based Carbons in CO₂/CH₄ Separations. *Chem. Eng. J.* 307, 249–257. doi:10.1016/j.cej.2016.08.077

AUTHOR CONTRIBUTIONS

All authors listed have made a substantial, direct, and intellectual contribution to the work and approved it for publication.

FUNDING

This research was supported by the Jiangsu Planned Projects for Postdoctoral Research Funds (2019K119), Jiangsu Planned Projects for Postdoctoral Daily Funds (2019Z003), and Open Research Fund of Jiangsu Province Key Laboratory of Environmental Engineering (ZZ2020003).

Bao, Z., Alnemrat, S., Yu, L., Vasiliev, I., Ren, Q., Lu, X., et al. (2011). Kinetic Separation of Carbon Dioxide and Methane on a Copper Metal-Organic Framework. *J. Colloid Interf. Sci.* 357 (2), 504–509. doi:10.1016/j.jcis.2011.01.103

Botomé, M. L., Poletto, P., Junges, J., Perondi, D., Dettmer, A., and Godinho, M. (2017). Preparation and Characterization of a Metal-Rich Activated Carbon from CCA-Treated wood for CO₂ Capture. *Chem. Eng. J.* 321, 614–621. doi:10.1016/j.cej.2017.04.004

- Bratek, K., Bratek, W., and Kulażyński, M. (2002). Carbon Adsorbents from Waste Ion-Exchange Resin. *Carbon* 40 (12), 2213–2220. doi:10.1016/s0008-6223(02)00091-x
- Brunauer, S., Deming, L. S., Deming, W. E., and Teller, E. (1940). On a Theory of the van der Waals Adsorption of Gases. *J. Am. Chem. Soc.* 62, 1723–1732. doi:10.1021/ja01864a025
- Caglayan, B. S., and Aksoylu, A. E. (2013). CO₂ Adsorption on Chemically Modified Activated Carbon. *J. Hazard. Mater.* 252–253, 19–28. doi:10.1016/j.jhazmat.2013.02.028
- Chen, Y., Lv, D., Wu, J., Xiao, J., Xi, H., Xia, Q., et al. (2017). A New MOF-505@GO Composite with High Selectivity for CO₂/CH₄ and CO₂/N₂ Separation. *Chem. Eng. J.* 308, 1065–1072. doi:10.1016/j.cej.2016.09.138
- Cheung, O., Bacsik, Z., Liu, Q., Mace, A., and Hedin, N. (2013). Adsorption Kinetics for CO₂ on Highly Selective Zeolites NaKA and Nano-NaKA. *Appl. Energ.* 112, 1326–1336. doi:10.1016/j.apenergy.2013.01.017
- Delgado, J. A., Águeda, V. I., Uguina, M. A., Brea, P., and Grande, C. A. (2017). Comparison and Evaluation of Agglomerated MOFs in Biohydrogen Purification by Means of Pressure Swing Adsorption (PSA). *Chem. Eng. J.* 326, 117–129. doi:10.1016/j.cej.2017.05.144
- Goel, C., Bhunia, H., and Bajpai, P. K. (2017). Prediction of Binary Gas Adsorption of CO₂/N₂ and Thermodynamic Studies on Nitrogen Enriched Nanostructured Carbon Adsorbents. *J. Chem. Eng. Data* 62, 214–225. doi:10.1021/acs.jced.6b00604
- Goel, C., Kaur, H., Bhunia, H., and Bajpai, P. K. (2016). Carbon Dioxide Adsorption on Nitrogen Enriched Carbon Adsorbents: Experimental, Kinetics, Isothermal and Thermodynamic Studies. *J. CO₂ Utilization* 16, 50–63. doi:10.1016/j.jcou.2016.06.002
- Gun'ko, V. M., Leboda, R., Skubiszewska-Zięba, J., Charnas, B., and Oleszczuk, P. (2005). Carbon Adsorbents from Waste Ion-Exchange Resins. *Carbon* 43 (6), 1143–1150. doi:10.1016/j.carbon.2004.09.032
- Hoseinzadeh Hesas, R., Wan Daud, W. M. A., Sahu, J. N., and Arami-Niya, A. (2013). The Effects of a Microwave Heating Method on the Production of Activated Carbon from Agricultural Waste: A Review. *J. Anal. Appl. Pyrolysis* 100, 1–11. doi:10.1016/j.jaap.2012.12.019
- Jiao, J., Cao, J., Xia, Y., and Zhao, L. (2016). Improvement of Adsorbent Materials for CO₂ Capture by Amine Functionalized Mesoporous Silica with Worm-Hole Framework Structure. *Chem. Eng. J.* 306, 9–16. doi:10.1016/j.cej.2016.07.041
- Kierzkowska, A. M., Poulikakos, L. V., Broda, M., and Müller, C. R. (2013). Synthesis of Calcium-Based, Al₂O₃-Stabilized Sorbents for CO₂ Capture Using a Co-Precipitation Technique. *Int. J. Greenhouse Gas Control* 15, 48–54. doi:10.1016/j.jggc.2013.01.046
- Kishor, R., and Ghoshal, A. K. (2016). Polyethylenimine Functionalized As-Synthesized KIT-6 Adsorbent for Highly CO₂/N₂ Selective Separation. *Energy Fuels* 30 (11), 9635–9644. doi:10.1021/acs.energyfuels.6b02082
- Krishna, R., and van Baten, J. M. (2012). A Comparison of the CO₂ Capture Characteristics of Zeolites and Metal-Organic Frameworks. *Separat. Purif. Technol.* 87, 120–126. doi:10.1016/j.seppur.2011.11.031
- Liu, L., Xie, Z.-H., Deng, Q.-F., Hou, X.-X., and Yuan, Z.-Y. (2017). One-Pot Carbonization Enrichment of Nitrogen in Microporous Carbon Spheres for Efficient CO₂ Capture. *J. Mater. Chem. A* 5, 418–425. doi:10.1039/c6ta09782k
- Ozcan, D. C., Ahn, H., and Brandani, S. (2013). Process Integration of a Ca-Looping Carbon Capture Process in a Cement Plant. *Int. J. Greenhouse Gas Control* 19, 530–540. doi:10.1016/j.jggc.2013.10.009
- Plasynski, S. I., Litynski, J. T., McIlvried, H. G., and Srivastava, R. D. (2009). Progress and New Developments in Carbon Capture and Storage. *Crit. Rev. Plant Sci.* 28 (3), 123–138. doi:10.1080/07352680902776440
- Plaza, M. G., Pevida, C., Martín, C. F., Famoso, J., Pis, J. J., and Rubiera, F. (2010). Developing almond Shell-Derived Activated Carbons as CO₂ Adsorbents. *Separat. Purif. Technol.* 71, 102–106. doi:10.1016/j.seppur.2009.11.008
- Samanta, A., Zhao, A., Shimizu, G. K. H., Sarkar, P., and Gupta, R. (2012). Post-Combustion CO₂ Capture Using Solid Sorbents: A Review. *Ind. Eng. Chem. Res.* 51 (4), 1438–1463. doi:10.1021/ie200686q
- Sanz-Pérez, E. S., Dantas, T. C. M., Arencibia, A., Calleja, G., Guedes, A. P. M. A., Araujo, A. S., et al. (2017). Reuse and Recycling of Amine-Functionalized Silica Materials for CO₂ Adsorption. *Chem. Eng. J.* 308, 1021–1033. doi:10.1016/j.cej.2016.09.109
- Shi, Q., Li, A., Zhu, Z., and Liu, B. (2013). Adsorption of Naphthalene onto a High-Surface-Area Carbon from Waste Ion Exchange Resin. *J. Environ. Sci.* 25 (1), 188–194. doi:10.1016/s1001-0742(12)60017-5
- Sing, K. S. W., Everett, D. H., Haul, R. A. W., Moscou, L., Pierotti, R. A., Rouquerol, J., et al. (1985). Reporting Physisorption Data for Gas Solid Systems with Special Reference to the Determination of Surface Area and Porosity. *Pure Appl. Chem.* 54, 603–619.
- Wang, D., Ma, X., Sentorun-Shalaby, C., and Song, C. (2012). Development of Carbon-Based "Molecular Basket" Sorbent for CO₂ Capture. *Ind. Eng. Chem. Res.* 51 (7), 3048–3057. doi:10.1021/ie2022543
- Wang, M., Yao, L., Wang, J., Zhang, Z., Qiao, W., Long, D., et al. (2016). Adsorption and Regeneration Study of Polyethylenimine-Impregnated Millimeter-Sized Mesoporous Carbon Spheres for Post-combustion CO₂ Capture. *Appl. Energ.* 168, 282–290. doi:10.1016/j.apenergy.2016.01.085
- Wang, Q., Luo, J., Zhong, Z., and Borgna, A. (2011). CO₂ Capture by Solid Adsorbents and Their Applications: Current Status and New Trends. *Energy Environ. Sci.* 4 (1), 42–55. doi:10.1039/c0ee00064g
- Watabe, T., and Yogo, K. (2013). Isotherms and Isosteric Heats of Adsorption for CO₂ in Amine-Functionalized Mesoporous Silicas. *Separat. Purif. Technol.* 120, 20–23. doi:10.1016/j.seppur.2013.09.011
- Wee, J.-H. (2013). A Review on Carbon Dioxide Capture and Storage Technology Using Coal Fly Ash. *Appl. Energ.* 106, 143–151. doi:10.1016/j.apenergy.2013.01.062
- Wei, M., Yu, Q., Duan, W., Zuo, Z., Hou, L., and Dai, J. (2018). CO₂ adsorption and Desorption Performance of Waste Ion-Exchange Resin-Based Activated Carbon. *Environ. Prog. Sustain. Energ.* 37 (2), 703–711. doi:10.1002/ep.12743
- Wei, M., Yu, Q., Mu, T., Hou, L., Zuo, Z., and Peng, J. (2016). Preparation and Characterization of Waste Ion-Exchange Resin-Based Activated Carbon for CO₂ Capture. *Adsorption* 22 (3), 385–396. doi:10.1007/s10450-016-9787-8
- Yang, H., Yuan, Y., and Tsang, S. C. E. (2012). Nitrogen-enriched Carbonaceous Materials with Hierarchical Micro-Mesopore Structures for Efficient CO₂ Capture. *Chem. Eng. J.* 185–186, 374–379. doi:10.1016/j.cej.2012.01.083
- Zhang, D., Cheng, W., Ma, J., and Li, R. (2016). Influence of Activated Carbon in Zeolite X/Activated Carbon Composites on CH₄/N₂ Adsorption Separation Ability. *Adsorption* 22 (8), 1129–1135. doi:10.1007/s10450-016-9836-3
- Zhang, Z. J., Cui, P., Chen, X. Y., and Liu, J. W. (2013). The Production of Activated Carbon from Cation Exchange Resin for High-Performance Supercapacitor. *J. Solid State. Electrochem.* 17 (6), 1749–1758. doi:10.1007/s10008-013-2039-x

Conflict of Interest: The authors declare that the research was conducted in the absence of any commercial or financial relationships that could be construed as a potential conflict of interest.

Publisher's Note: All claims expressed in this article are solely those of the authors and do not necessarily represent those of their affiliated organizations, or those of the publisher, the editors, and the reviewers. Any product that may be evaluated in this article, or claim that may be made by its manufacturer, is not guaranteed or endorsed by the publisher.

Copyright © 2021 Wei and Zhao. This is an open-access article distributed under the terms of the Creative Commons Attribution License (CC BY). The use, distribution or reproduction in other forums is permitted, provided the original author(s) and the copyright owner(s) are credited and that the original publication in this journal is cited, in accordance with accepted academic practice. No use, distribution or reproduction is permitted which does not comply with these terms.



Flow Regimes and Transitions for Two-Phase Flow of R152a During Condensation in a Circular Minichannel

Na Liu*, Qian Zhao and Zhixiang Lan

School of Environmental and Municipal Engineering, Qingdao University of Technology, Qingdao, China

OPEN ACCESS

Edited by:

Huaqing Xie,
Northeastern University, China

Reviewed by:

Shan Hu,
Institute of Engineering
Thermophysics (CAS), China
Ji Wang,
China University of Petroleum, China
Wenhao Wang,
Guizhou University, China

*Correspondence:

Na Liu
liuna@qut.edu.cn

Specialty section:

This article was submitted to
Advanced Clean Fuel Technologies,
a section of the journal
Frontiers in Energy Research

Received: 10 October 2021

Accepted: 28 October 2021

Published: 12 November 2021

Citation:

Liu N, Zhao Q and Lan Z (2021) Flow
Regimes and Transitions for Two-
Phase Flow of R152a During
Condensation in a
Circular Minichannel.
Front. Energy Res. 9:792586.
doi: 10.3389/fenrg.2021.792586

Two-phase flow regimes were experimentally investigated during the entire condensation process of refrigerant R152a in a circular glass minichannel. The inner and outer diameters of the test minichannel were 0.75 and 1.50 mm. The channel was 500 mm long to allow observation of all the two-phase flow regimes during the condensation process. The experiments used saturation temperatures from 30 to 50°C, a mass flux of 150 kg/(m²·s) and vapor qualities from 0 to 1. The annular, intermittent and bubbly flow regimes were observed for the experimental conditions in the study. The absence of the stratified flow regime shows that the gravitational effect is no longer dominant in the minichannel for these conditions. Vapor-liquid interfacial waves, liquid bridge formation and vapor core breakage were observed in the minichannel. Quantitative measurements of flow regime transition locations were carried out in the present study. The experiments also showed the effects of the saturation temperature and the cooling water mass flow rate on flow regime transitions. The results show that the annular flow range decreases and the intermittent and bubbly flow ranges change little with increasing saturation temperature. The cooling water mass flow rate ranging from 38.3 kg/h to 113.8 kg/h had little effect on the flow regime transitions.

Keywords: two-phase flow, condensation, flow regime, minichannel, R152a

INTRODUCTION

Mini/Microchannels are widely used in many fields due to the advantages of enhanced heat transfer. The minichannels improve the system efficiency by reducing the air-side pressure drop and increasing the in-tube heat transfer coefficients. The minichannel heat exchangers also have the advantages of a smaller refrigerant charge, which leads to lower greenhouse gas emissions. Channels with hydraulic diameters ranging from 0.2 to 3 mm are defined as minichannels by Kandlikar and Grande (2003) for single-phase and two-phase fluid flows. Therefore, the test channel used in this study with a hydraulic diameter of 0.75 mm is classified as a minichannel. The flow regimes in

Abbreviations: D , tube diameter, mm; D_h , hydraulic diameter, mm; h_{lv} , latent heat, J/kg; t_s , saturation temperature, °C; p_s , saturation pressure, MPa; Z , flow regime coordinate, cm; Z_c , length of the entire condensation process, cm Greek symbols; α , aspect ratio; λ , thermal conductivity, W/(m·K); μ , viscosity, Pa·s; σ , surface tension, N/m.

minichannels differ from those in conventional channels because of the relative influences of gravity, shear stresses and surface tension.

Previous researchers, such as Alves (1954), Baker (1954) and Govier and Omer (1962), have given flow regime mappings for relatively large channels using air-water or air-oil mixtures. Suo and Griffith (1964) and Barnea et al. (1983) gave flow regime maps of air-water mixtures in small diameter circular channels. Investigations by several researchers (Damianides and Westwater (1988); Fukano et al. (1990)) showed that the flow regime maps of Mandhane et al. (1974), Taitel and Dukler (1976) and Weisman et al. (1979) in conventional channels failed to predict the flow regimes in small channels with hydraulic diameters ranging from 1 to 5 mm. Kawaji and Chung (2003) reviewed the previous research on adiabatic two-phase flows in narrow channels and performed new experiments. They concluded that the reduction of the tube diameter had a great influence on the flow regimes. Coleman and Garimella (1999) studied the effects of tube diameter and geometry on flow regimes and transitions of air-water flows in tubes with hydraulic diameters ranging from 1.3 to 5.5 mm. Then, Coleman and Garimella (2003) also conducted an experimental investigation of the two-phase flow mechanisms during condensation of refrigerant R134a in six round, square and rectangular tubes. Flow regimes of n-pentane during condensation in tubes with diameters of 10, 1.1 and 0.56 mm were experimentally investigated by Médéric et al. (2004). They found that the effect of gravity and capillary forces on the flow regimes were quite different for inner diameters less than 1 mm.

Two-phase flow regimes during condensation of FC-72 in 1 mm parallel, square micro-channels were experimentally observed by Kim et al. (2012). Five flow regimes were divided as smooth-annular, wavy-annular, transition, slug and bubbly flow. The smooth-annular flow and the wavy-annular flow were most prevalent among all flow regimes. Al-Zaidi et al. (2018) carried out flow visualization of HFE-7100 in a 0.57 mm rectangular multi-microchannel. Wang et al. (2017), Wang and Li (2018) studied two-phase flow regimes of R134a in 301.6 μm oval parallel microchannels. Nasrfard et al. (2019) experimentally studied the condensation heat transfer of R141b in intermittent flow regime within a smooth horizontal tube. Lei and Chen (2019) conducted numerical research on flow regimes of R134a based on the VOF approach. Jige et al. (2018) experimentally observed the two-phase flow characteristics of R32 in horizontal multiport rectangular minichannels with hydraulic diameters of 0.5 and 1.0 mm. A new prediction method of flow regimes for multiport minichannels, considering channel size, was developed based on the experimental results. Keniar and Garimella (2021) studied the intermittent flow of R134a during condensation in circular microchannels. Li et al. (2021) experimentally studied the flow pattern change in horizontal minichannels under electric field force. The results showed that the bubble behavior was suppressed by the electric field force.

Recent increased attention to environmental issues has brought substantially more stringent requirements for refrigerants in air-conditioning and refrigeration applications. The transition from CFCs to HCFCs and to HFCs has reduced the

environmental impact of refrigeration systems. Since R22 is widely used in domestic air conditioners in China, the substitution is quite urgent. Although HFCs have zero ozone depletion potential (ODP), many have high global warming potentials (GWP). Therefore, much effort is being focused on finding alternative refrigerants to conventional HFCs.

Table 1 listed the thermophysical and environmental characteristics of R22, R134a and R152a. The GWP of R152a is an order of magnitude smaller than that of R22 and R134a. The thermal conductivity, latent heat of vaporization and surface tension of R22 and R134a are lower than R152a. The heat transfer performance of R22, R134a and R152a during condensation was theoretically investigated by Wang and Rose (2011). The results showed that R152a had better heat transfer performance than R22 and R134a. The experimental research of Liu and Li (2015) also showed that the heat transfer coefficients during condensation of R152a were greater than those of R22. Although R152a is a potential substitute for R22, no experimental study has been carried out on the flow regimes during the entire condensation process in minichannels.

EXPERIMENTAL METHODS

Experimental Rig

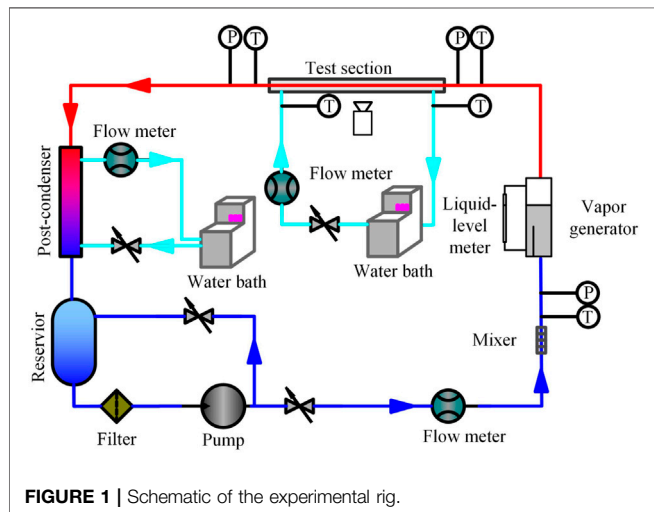
Figure 1 shows a schematic of the experimental rig established for flow regime observation. The rig consists of one refrigerant and two cooling water loops. The experimental apparatus consists of a refrigerant and two cooling water circuits. The subcooled refrigerant in the reservoir is filtered, circulates through the magnetic-driven gear pump that can be adjusted by the frequency converter, and then flows through the Coriolis effect mass flowmeter. The mass flow rate is controlled by a bypass loop. The refrigerant in the vapor generator is heated to saturation by adjusting the electric heating power. The liquid-level meter is used to monitor the liquid phase level and keep it steady in the vapor generator. The saturated fluid then flows into the circular glass channel in the test section. The vapor refrigerant is fully condensed by the cooling water in the test section. After the test section, the refrigerant flows to the post-condenser, where it is further subcooled, and finally returns to the reservoir. The operating pressure in the refrigerant circuit is controlled by adjusting the electric heating power of the heater installed in the reservoir.

The purity of the refrigerant R152a provided by the manufacturer is larger than 99.9%. The measures are taken to ensure that the vapor contains no incondensable gas: the experimental system is vacuumed for half an hour to remove the air; some R152a is filled into the system; vacuum the system again. The filling and evacuating measures were repeated several times to ensure that the system contained as little incondensable gas as possible. After the above measures, R152a was filled into the system.

The refrigerant and cooling water temperatures are measured using PT100 resistance thermometers. All PT100 resistance thermometers are calibrated using a 6,020 Series high precision calibration bath before the experiments. Trafag 8,251

TABLE 1 | Thermophysical and environmental properties of R22, R134a and R152a.

Fluids	$t_s/^\circ\text{C}$	p_s/MPa	$h_{lv}/\text{kJ/kg}$	$\mu/\mu\text{Pa}\cdot\text{s}$	$\lambda/\text{W}/(\text{m}\cdot\text{K})$	$\sigma/\text{N/m}$	ODP	GWP
R22	50	1.943	154.2	123.0	0.0719	0.00474	0.05	1700
R134a		1.318	151.8	141.8	0.0704	0.00489	0	1,300
R152a		1.177	245.4	122.2	0.0875	0.00648	0	120

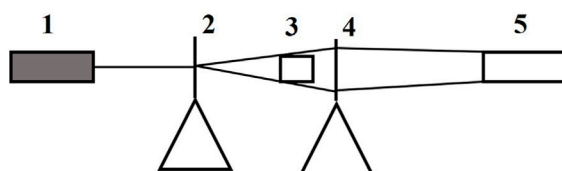
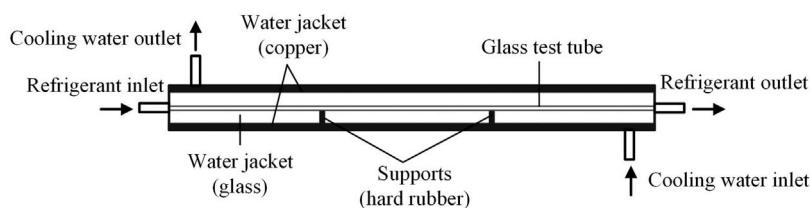
**FIGURE 1** | Schematic of the experimental rig.

pressure sensors are used to measure the refrigerant pressures through 1.0 mm pressure taps. Two Coriolis mass flowmeters are used to measure the mass flow rates of the refrigerant and the cooling water in the test section, respectively. The flow regimes during condensation are observed by an imaging system as shown in **Figure 2**. A MV-VS078FC industrial CCD camera is used with a resolution of $1,024 \times 768$ pixels, a light sensitivity of 0.01 LUX

and a shutter speed of 1×10^{-4} s. Experimental data are collected by an Agilent 34970A acquisition system.

Test Section

The test section was a counter flow tube-in-tube condenser as shown in **Figure 3**. The refrigerant was condensed inside the glass test tube by the cooling water flowing in the cooling water jacket. The test tube was a circular glass minichannel with inner and outer diameters of 0.75 and 1.50 mm. The test tube was 500 mm long to allow observation of all the flow regimes during the condensation process in the test section. A special external structure is required to bear the stress generated during the installation of the test section to ensure that the glass tube is not damaged. Copper joints with internal and external treads are connected to both ends of the glass tube in order to provide a labyrinth seal for the glass tube. Raw tape is wrapped on the ends of the glass tube and the adhesive is evenly covered on the raw tape to ensure the tightness and pressure resistance of the connection. The nuts filling with the mixture of raw tape and adhesive are installed under small squeeze force to avoid putting lateral stress on the glass tube. Two copper plates are installed outside the glass tube to transfer the torsion and bending stress generated during the installation process of the test section. Two glass sheets are installed on the front and back of the test section to offer the visual observation of the flow regimes. The cooling water jacket was rectangular, 500 mm long with the hydraulic diameter of 16 mm. The top and bottom materials of the cooling

**1. Light source, 2. Beam expander, 3. Test section, 4. Magnifying glass, 5. CCD camera****FIGURE 2** | Imaging system.**FIGURE 3** | Test section schematic.

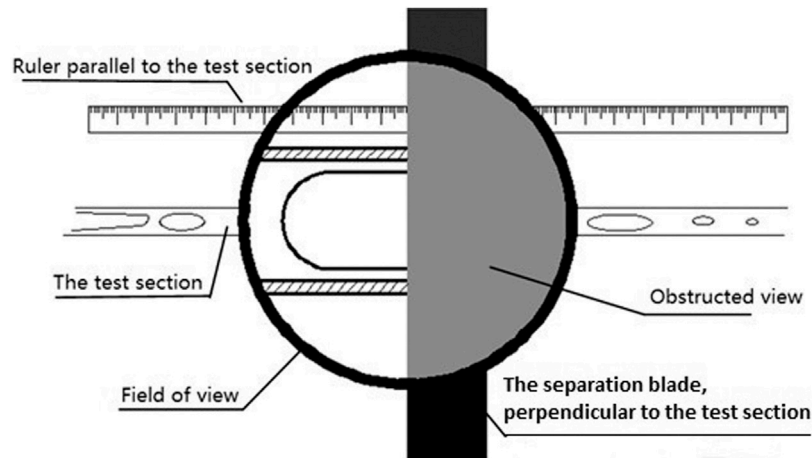


FIGURE 4 | Determination of the flow regime transition locations.

TABLE 2 | Uncertainties of the measured parameters.

Parameter	Uncertainty
Local coordinate (Z)	± 0.5 mm
Temperature (RTD)	$\pm 0.1^\circ\text{C}$
Refrigerant mass flow rate	$\pm 0.2\%$ (5 kg/h)
Cooling water mass flow rate	$\pm 0.2\%$ (5 kg/h)
Pressure	$\pm 0.3\%$ (6 MPa)

water jacket were copper, while the front and rear materials were glass for the observations. Two hard rubber supports were installed in the cooling water jacket to support the long glass tube. During the experiments, the cooling water jacket was exposed to the atmosphere which was around 18°C .

The locations of the flow regime transitions during the entire condensation process were recorded to investigate the effects of the experimental conditions on the flow regime transitions. The location determination method is shown in **Figure 4**. The coordinate measurement device consisted of a ruler placed parallel to the test section, the viewing device and the separation blade perpendicular to the test section. The ruler reading at the blade's left side was regarded as the local coordinate of the observed flow regime element.

Uncertainty Analysis

The experimental uncertainties of the parameters are listed in **Table 2**. The thermophysical properties of R152a are obtained through the REFPROP 9.0 software (Lemmon et al., 2010).

RESULTS AND DISCUSSION

In order to verify the reliability of the experimental system, single-phase heat transfer experiments were carried out in a 1.09 mm circular tube by Zhang et al. (2012). Experimental pressure drops agree well with the predicted results of

equation Blasius (1908), and the average deviation and root mean square deviation are within 1.7 and 8.8%, respectively. Experimental heat transfer coefficients agree well with the predicted results of correlation Gnielinski (1976), and the average deviation and root mean square deviation are within 4.1 and 12.8%. The deviation of the heat transfer rate between the refrigerant and the cooling water is within $\pm 5\%$. The heat loss in the test section was within ± 0.25 W. Single-phase verification experiments show that the experimental apparatus is reliable and can be used for two-phase flow and condensation heat transfer experiments.

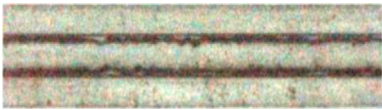
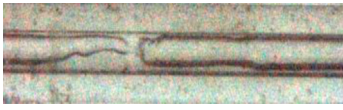
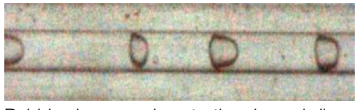
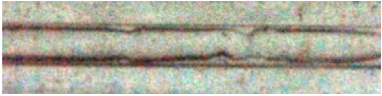


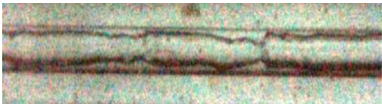


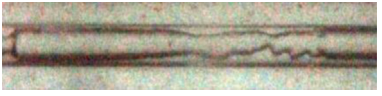
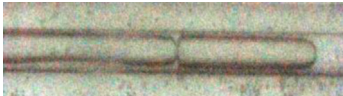
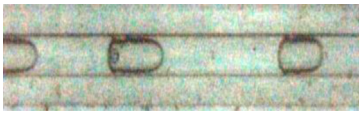
Flow Regimes During Condensation

The test section for the flow regime experiments was long enough to observe the entire condensation process. The annular, intermittent and bubbly flow regimes were observed in the present study as listed in **Table 3** as the vapor quality was reduced, which differs from the results of Coleman and Garimella (2003). In Coleman and Garimella's study, the flow regimes were categorized into four different flow regimes as intermittent flow, wavy flow, annular flow and dispersed flow. The relative importance of gravity, surface tension and interfacial shear stress differs for different flow regimes and transitions. In the present study, the interfacial shear stress is not large enough to entrain liquid droplets into the vapor core for $G = 150$ kg/(m²·s); therefore, the mist flow regime is not observed. In addition, the absence of the stratified flow regime suggested that gravity was no longer dominant for the 0.75 mm diameter tube. At low vapor qualities, the dispersed flow regime with bubbles dispersed across the tube cross section was also not observed in the study.

Annular Flow Regime

The annular flow regime occurred at the very beginning of the condensation process with the vapor flowing in the channel core and a uniform thin liquid film flowing along the channel periphery. Vapor-liquid interfacial waves were

TABLE 3 | Flow regimes during condensation of R152a in a 0.75 mm circular minichannel.

Annular	Intermittent	Bubbly
 Annular flow with a very thin liquid film	 Liquid bridge formation	 Bubble sizes are close to the channel diameter
 Quasi-symmetric waves at the top and bottom channels	 Vapor core breakage	 Buoyancy effect on the bubbles
 Vapor core deformation caused by waves	 Intermittent flow with a smooth vapor-liquid interface	 Decrease of the bubble size until completely condensed
 The vapor core being locally very thin	 Coalescence between slugs	
	 Intermittent flow dominated by short slugs	

caused by the shear stress between the two phases flowing with different velocities. There was no distinct difference between the top and bottom channel wave strengths because the liquid film was quite thin. The interfacial shear stress dominants at this stage.

The liquid film became thicker as the condensation proceeded. Gravity caused the liquid film to be thicker at the bottom of the channel than at the top. Therefore, the interfacial waves were no longer uniform around the channel periphery. The wave frequency decreased while the wave amplitude increased. According to Barnea et al. (1983), the current flow pattern can be subdivided as the wavy-annular flow regime which still belongs to the annular flow regime.

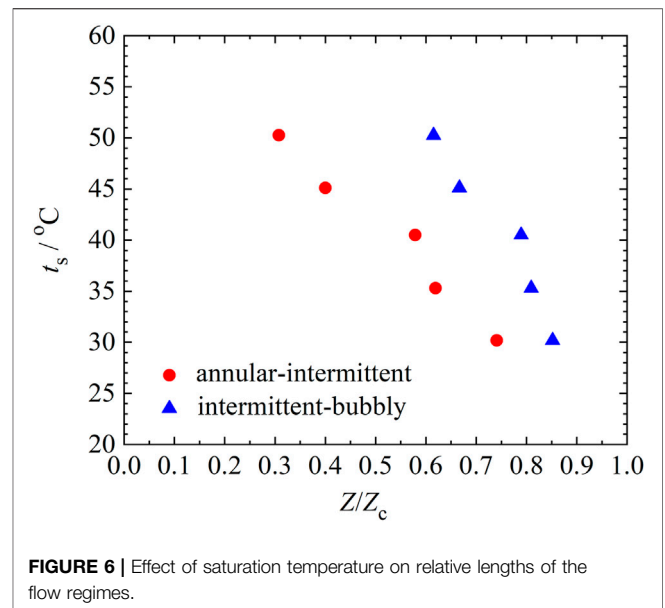
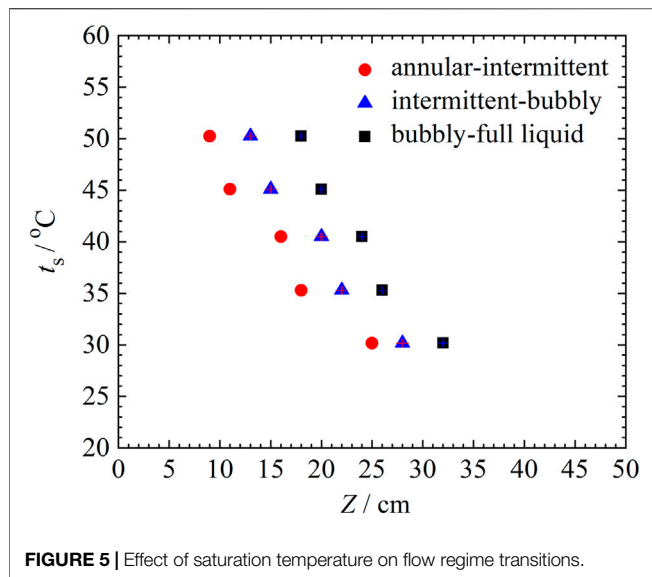
The interfacial waves then caused the vapor core to deform with the deformation becoming stronger as the liquid film became thicker. Two kinds of interfacial waves were observed during the wavy-annular flow regime. One occurred when the wave crests at the top and bottom channels locally reduced the vapor core size. The other occurred when the wave crests at the top and bottom channels were not at the same location and deformed the vapor core channel.

Three kinds of vapor core deformations were frequently observed during the wavy-annular flow regime as the vapor quality was reduced for the same refrigerant saturation temperature, cooling water mass flow rate and inlet cooling water temperature. Any vapor core deformations often led to the formation of liquid bridges and finally

vapor core breakage. The liquid film thickness at the top and bottom channels both increased causing vapor core deformation. The liquid film thickness at the bottom channel increased faster than that at the top channel. Strong interfacial waves caused several vapor core deformations in a short channel. Vapor core deformations indicate the occurrence of the surface tension effect. The combination of interfacial shear stress and surface tension will cause the transition from annular flow to intermittent flow with the increase of the liquid film thickness.

Intermittent Flow Regime

The flow regime transitioned from wavy-annular flow to intermittent flow as the liquid film became thicker and the interfacial waves were strong enough to form liquid bridges across the vapor core which broke the vapor core. The intermittent flow regime consisted of vapor slugs in the channel core with a liquid film coating the channel wall around the vapor slugs. Three types of liquid bridge formations and vapor core breakages corresponding to the vapor core deformations were observed during the intermittent flow regime with decreasing vapor quality for the same refrigerant saturation temperature, cooling water mass flow rate and inlet cooling water temperature. 1) Liquid films at the top and bottom of the channel become thicker which reduces the vapor core cross-sectional area. The top and bottom liquid films eventually join and the vapor core is broken into two parts. 2) The

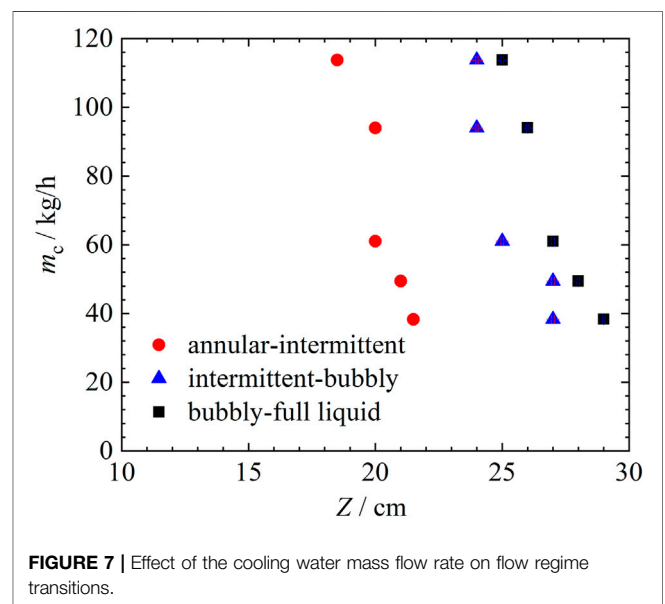


liquid bridge is caused by the liquid film thickness increasing at the bottom of the channel. The liquid bridge forms when the bottom liquid film is thick enough to reach the top liquid film. The resulting slug end is close to the top wall which creates a small thermal conduction resistance through the liquid film there and a high condensation rate. The slug end then condenses quickly and the liquid bridge forms. 3) Two liquid bridges forming in a short channel due to frequent strong waves. The vapor core is broken into several slugs. The short slug flows and condenses, which implies that short slugs also occur during the early period of the intermittent flow regime in addition to later on. Since short slugs appear for only a short time due to the high condensation rate, the intermittent flow regime is dominated by long slugs during the early period.

During the intermittent flow regime, the slug length decreases and the liquid bridge width increases due to condensation. Surface tension dominates among the three forces for the intermittent flow. However, slug coalescence due to the flow velocity difference was also observed. The coalescence frequency between slugs is much smaller than the breakage frequency of the slugs. Slug coalescence has little effect on the condensation heat transfer. In general, the slug lengths decrease as the condensation continues during the intermittent flow regime. The slug surface becomes very smooth implying the surface tension effect.

Bubbly Flow Regime

The flow regime transits to the bubbly flow regime when the bubble sizes are almost equivalent to the channel diameter. Gravity, surface tension and interfacial shear stress work simultaneously at this stage. The liquid film thickness around the channel increases and the condensation rate decreases with the decrease in the vapor quality. Bubbles rise to the top channel due to buoyancy as the bubbles become smaller. The movement of bubbles is mainly affected by gravity. The liquid films are thin



near the top channel so the conduction thermal resistance is small as the bubbles rise to the top channel. Therefore, the bubbly flow regime does not last for long and the flow finally transits to all liquid.

Effects of the Experimental Conditions on the Flow Regime Transitions

Effect of Saturation Temperature

Thermophysical properties especially the vapor-liquid density difference were directly influenced by the refrigerant saturation temperature. On the one hand, the vapor-liquid density difference decreases with increasing saturation temperature

resulting in smaller vapor core shear stress and weaker waves for which condition liquid bridges are not easy to form. On the other hand, the heat transfer temperature difference between the refrigerant and the cooling water increases with increasing the refrigerant saturation temperature for constant inlet cooling water temperature and mass flow rate resulting in faster condensate film growth for which condition liquid bridges are easy to form. The saturation temperature effect on the flow regime transitions depends on the relative size of the above two factors.

The flow regime transitions were identified as the annular-intermittent flow regime transition which occurs when liquid bridges form, the intermittent-bubbly flow regime transition which occurs when most bubble sizes are equivalent to the channel diameter and the bubbly-full liquid flow regime transition which occurs when the small bubbles disappear completely. **Figure 5** shows the effect of saturation temperature on the flow regime transitions for a constant cooling water mass flow rate of 61.0 kg/h with an inlet cooling water temperature of 15°C. Z represents the appearance of the flow regime along the test section. Z_c represents the length needed for the entire condensation process for each experimental condition.

Figure 5 show that flow regime transitions advance with increasing saturation temperature. The length for the entire condensation process decreases from 32.0 to 18.0 cm with saturation temperatures increasing from 30 to 50°C. The range of the annular flow regime decreases while the ranges of the intermittent and bubbly flow regimes change little with increasing saturation temperature or the temperature difference between the saturation temperature and the wall temperature. Thus, these results indicate that the heat transfer during condensation mainly occurs during the annular flow regime. The condensation process becomes faster and the condensation length needed for the same refrigerant mass flow rate becomes shorter with increasing the refrigerant and cooling water temperature difference. However, the saturation temperature has little effect on the heat transfer rates during the intermittent and bubbly flow regimes for constant cooling water mass flow rate and inlet cooling water temperature.

Figure 6 shows the effect of saturation temperature on the relative lengths of the flow regimes. The results show that the annular flow regime is dominant accounting for 75% for the total condensation range with the intermittent and bubbly flow regimes accounting for 11 and 14% for the saturation temperature of 30°C. The proportions of the annular, intermittent and bubbly flow regimes are 31, 30 and 39% for the saturation temperature of 50°C. Therefore, the actual ranges and the proportions of the annular flow regime both decrease with increasing saturation temperature. However, the actual ranges of the intermittent and bubbly flow regimes change little and the proportions increase with increasing saturation temperature.

Effect of the Cooling Water Mass Flow Rate

Figure 7 shows the effect of the cooling water mass flow rate (ranging from 38.3 kg/h to 113.8 kg/h) on the flow regime transitions for a saturation temperature of 45°C and an inlet cooling water temperature of 20°C. The results show that flow regime transitions advance slightly with increasing the cooling

water mass flow rate. For the mass flux of 150 kg/(m²·s), the flow regimes and transitions are significantly affected by the temperature difference between the saturation temperature of the refrigerant and the cooling water. However, the cooling water mass flow rate of 38.3 kg/h is high enough for the condensation heat transfer and further increasing the cooling water mass flow rate has little effect on flow regime transitions in the present study. In further research, different mass fluxes of the refrigerant should be experimentally studied to analyzed the effect of the cooling water mass flow rate.

CONCLUSION

The flow regimes during condensation of R152a were investigated experimentally in a 0.75 mm circular glass minichannel. The experiments used saturation temperatures from 30 to 50°C, a mass flux of 150 kg/(m²·s) and vapor qualities from 0 to 1. The results show that:

The annular, intermittent and bubbly flow regimes were observed during the condensation process. The absence of the stratified flow regime shows that the gravity effect is no longer dominant in the minichannel. The observations show the importance of the vapor-liquid interfacial waves, the vapor core deformations and the liquid bridge formations. The effects of the saturation temperature and the cooling water mass flow rate on the flow regime transitions were also investigated. Quantitative measurements of flow regime transition locations were carried out. The results show that the actual ranges and the proportions of the annular flow regime both decrease with increasing saturation temperature. However, the actual ranges of the intermittent and bubbly flow regimes change little and the proportions increase with increasing saturation temperature. The cooling water mass flow rate is significantly high and has little effect on the flow regime transitions in the present study.

DATA AVAILABILITY STATEMENT

The raw data supporting the conclusions of this article will be made available by the authors, without undue reservation.

AUTHOR CONTRIBUTIONS

NL established the experimental system, carried out the experiments and wrote the first submission of the paper. QZ and ZL gave a lot of help during the experiments. All authors contributed to the article and approved the submitted version.

FUNDING

This work is supported by the National Natural Science Foundation of China (Grant No. 51904325).

REFERENCES

- Alves, G. E. (1954). Cocurrent Liquid-Gas Flow in a Pipe-Line Contactor. *Chem. Eng. Process* 50, 449–456.
- Al-Zaidi, A. H., Mahmoud, M. M., and Karayiannis, T. G. (2018). Condensation Flow Patterns and Heat Transfer in Horizontal Microchannels. *Exp. Therm. Fluid Sci.* 90, 153–173. doi:10.1016/j.expthermflusci.2017.09.009
- Baker, O. (1954). Simultaneous Flow of Oil and Gas. *Oil Gas J.* 53, 185–195.
- Barnea, D., Luninski, Y., and Taitel, Y. (1983). Flow Pattern in Horizontal and Vertical Two Phase Flow in Small Diameter Pipes. *Can. J. Chem. Eng.* 61 (5), 617–620. doi:10.1002/cjce.5450610501
- Blasius, H. (1908). Grenzschichten in flüssigkeiten mit kleiner reibung. *z.math.u.phys* 56, 1–37.
- Coleman, J. W., and Garimella, S. (1999). Characterization of Two-phase Flow Patterns in Small Diameter Round and Rectangular Tubes. *Int. J. Heat Mass Transfer* 42 (15), 2869–2881. doi:10.1016/s0017-9310(98)00362-7
- Coleman, J. W., and Garimella, S. (2003). Two-phase Flow Regimes in Round, Square and Rectangular Tubes during Condensation of Refrigerant R134a. *Int. J. Refrig.* 26 (1), 117–128. doi:10.1016/s0140-7007(02)00013-0
- Damianides, C. A., and Westwater, J. W. (1988). “Two Phase Flow Patterns in a Compact Heat Exchanger and in Small Tubes,” in Second UK National Conference on Heat Transfer, Glasgow, September 14–16, 1988 (London: Mechanical Engineering Publications), 1257–1268.
- Fukano, T., Kariyasaki, A., and Kagawa, M. (1990). Flow Patterns and Pressure Drop in Isothermal Gas-Liquid Concurrent Flow in a Horizontal Capillary Tube. *Trans. Jpn. Soc. Mech. Eng. B* 4 (528), 153–161. doi:10.1299/kikaib.56.2318
- Gnielinski, V. (1976). New Equation for Heat and Mass Transfer in Turbulent Pipe and Channel Flow. *Int. Chem. Eng.* 16 (2), 359–368.
- Govier, G. W., and Omer, M. M. (1962). The Horizontal Pipeline Flow of Air-Water Mixtures. *Can. J. Chem. Eng.* 40 (3), 93–104. doi:10.1002/cjce.5450400303
- Jige, D., Kikuchi, S., Eda, H., Inoue, N., and Koyama, S. (2018). Two-phase Flow Characteristics of R32 in Horizontal Multiport Minichannels: Flow Visualization and Development of Flow Regime Map. *Int. J. Refrig.* 95, 156–164. doi:10.1016/j.ijrefrig.2018.09.005
- Kandlikar, S. G., and Grande, W. J. (2003). Evolution of Microchannel Flow Passages—Thermohydraulic Performance and Fabrication Technology. *Heat Transfer Eng.* 24, 3–17. doi:10.1080/0145763039011607710.1080/01457630304040
- Kawaji, M., and Chung, M. Y. (2003). “Unique Characteristics of Adiabatic Gas-Liquid Flows in Microchannels: Diameter and Shape Effects on Flow Patterns, Void Fraction and Pressure Drop,” in ASME International Conference on Microchannels & Minichannels, Rochester, NY, April 24, 25, 2003, 115–127. doi:10.1115/icmm2003-1013
- Keniar, K., and Garimella, S. (2021). Lagrangian Modeling of Intermittent Flow Condensation in Circular Micro- and Mini-Channels. *Int. J. Heat Mass Transfer* 164 (5), 120586. doi:10.1016/j.ijheatmasstransfer.2020.120586
- Kim, S.-M., Kim, J., and Mudawar, I. (2012). Flow Condensation in Parallel Microchannels - Part 1: Experimental Results and Assessment of Pressure Drop Correlations. *Int. J. Heat Mass Transfer* 55 (4), 971–983. doi:10.1016/j.ijheatmasstransfer.2011.10.013
- Lei, Y., and Chen, Z. (2019). Numerical Study of Condensation Flow Regimes in Presence of Non-condensable Gas in Minichannels. *Int. Commun. Heat Mass Transfer* 106, 1–8. doi:10.1016/j.icheatmasstransfer.2019.04.001
- Lemmon, E. W., Huber, M. L., and McLinden, M. O. (2010). *NIST Standard Referencedatabase 23: Reference Fluid Thermodynamic and Transport Properties-Refprop*. 9.0.
- Li, H.-W., Wang, Y.-C., Du, C.-H., and Hong, W.-P. (2021). Analysis of Flow Pattern Change in Horizontal Mini-Channel under Electric Field Force. *Int. Commun. Heat Mass Transfer* 121, 105081. doi:10.1016/j.icheatmasstransfer.2020.105081
- Liu, N., and Li, J. (2015). Experimental Study on Condensation Heat Transfer of R32, R152a and R22 in Horizontal Minichannels. *Appl. Therm. Eng.* 90, 763–773. doi:10.1016/j.applthermaleng.2015.07.062
- Mandhane, J. M., Gregory, G. A., and Aziz, K. (1974). A Flow Pattern Map for Gas-Liquid Flow in Horizontal Pipes. *Int. J. Multiphase Flow* 1 (4), 537–553. doi:10.1016/0301-9322(74)90006-8
- Médéric, B., Miscevic, M., Platel, V., Lavielle, P., and Joly, J.-L. (2004). Experimental Study of Flow Characteristics during Condensation in Narrow Channels: the Influence of the Diameter Channel on Structure Patterns. *Superlattices Microstruct.* 35 (3–6), 573–586. doi:10.1016/j.spmi.2003.11.008
- Nasrard, H., Rahimzadeh, H., Ahmadpour, A., and Naderan, H. (2019). Experimental Study of Condensation Heat Transfer for R141b in Intermittent Flow Regime within a Smooth Horizontal Tube. *Exp. Therm. Fluid Sci.* 105, 109–122. doi:10.1016/j.expthermflusci.2019.03.019
- Suo, M., and Griffith, P. (1964). Two-Phase Flow in Capillary Tubes. *J. Basic Eng.* 86 (3), 576–582. doi:10.1115/1.3653176
- Taitel, Y., and Dukler, A. E. (1976). A Model for Predicting Flow Regime Transitions in Horizontal and Near Horizontal Gas-Liquid Flow. *Aiche J.* 22 (1), 47–55. doi:10.1002/aic.690220105
- Wang, J., and Li, J. M. (2018). Pressure Drop of R134a and R1234ze(e) during Condensation in Horizontal Microchannel Arrays Cooled Symmetrically and asymmetrically. *Exp. Therm. Fluid Sci.* 96, 266–283. S0894177718304126. doi:10.1016/j.expthermflusci.2018.03.016
- Wang, H. S., and Rose, J. W. (2011). Theory of Heat Transfer during Condensation in Microchannels. *Int. J. Heat Mass Transfer* 54 (11–12), 2525–2534. doi:10.1016/j.ijheatmasstransfer.2011.02.009
- Wang, J., Wang, J., and Li, J. M. (2017). R134a Condensation Flow Regime and Pressure Drop in Horizontal Microchannels Cooled Symmetrically and Asymmetrically. *Int. J. Heat Mass Transfer* 115, 1091–1102. doi:10.1016/j.ijheatmasstransfer.2017.08.003
- Weisman, J., Duncan, D., Gibson, J., and Crawford, T. (1979). Effects of Fluid Properties and Pipe Diameter on Two-phase Flow Patterns in Horizontal Lines. *Int. J. Multiphase Flow* 5 (6), 437–462. doi:10.1016/0301-9322(79)90031-4
- Zhang, H.-Y., Li, J.-M., Liu, N., and Wang, B.-X. (2012). Experimental Investigation of Condensation Heat Transfer and Pressure Drop of R22, R410A and R407C in Mini-Tubes. *Int. J. Heat Mass Transfer* 55 (13–14), 3522–3532. doi:10.1016/j.ijheatmasstransfer.2012.03.012

Conflict of Interest: The authors declare that the research was conducted in the absence of any commercial or financial relationships that could be construed as a potential conflict of interest.

Publisher's Note: All claims expressed in this article are solely those of the authors and do not necessarily represent those of their affiliated organizations, or those of the publisher, the editors and the reviewers. Any product that may be evaluated in this article, or claim that may be made by its manufacturer, is not guaranteed or endorsed by the publisher.

Copyright © 2021 Liu, Zhao and Lan. This is an open-access article distributed under the terms of the Creative Commons Attribution License (CC BY). The use, distribution or reproduction in other forums is permitted, provided the original author(s) and the copyright owner(s) are credited and that the original publication in this journal is cited, in accordance with accepted academic practice. No use, distribution or reproduction is permitted which does not comply with these terms.



Effect of Tube Expansion on Heat Transfer and Pressure Drop Characteristics During Condensation in Micro-Fin Tubes

Na Liu*, Qian Zhao and Zhixiang Lan

School of Environmental and Municipal Engineering, Qingdao University of Technology, Qingdao, China

OPEN ACCESS

Edited by:

Huaqing Xie,
Northeastern University, China

Reviewed by:

Jie Sun,
Beijing University of Technology,
China

Hui Han,
China University of Petroleum
(Huadong), China

Qiang Li,
Heilongjiang Bayi Agricultural
University, China

*Correspondence:

Na Liu
liuna@qut.edu.cn

Specialty section:

This article was submitted to
Advanced Clean Fuel Technologies,
a section of the journal
Frontiers in Energy Research

Received: 08 November 2021

Accepted: 19 November 2021

Published: 02 December 2021

Citation:

Liu N, Zhao Q and Lan Z (2021) Effect
of Tube Expansion on Heat Transfer
and Pressure Drop Characteristics
During Condensation in Micro-
Fin Tubes.
Front. Energy Res. 9:811054.
doi: 10.3389/fenrg.2021.811054

Despite of the large number of research dedicated to condensation heat transfer and pressure drop characteristics in pristine micro-fin tubes, experimental investigation on effects of tube expansion have not been reported in the open literature. The paper reports measured cross-sectional dimensions, condensation heat transfer and pressure drop data of R1234ze(E) in pristine (5.10 mm OD) and expanded (5.26 mm OD) micro-fin tubes with mass fluxes from 100 to 300 kg/(m²·s). Effects of mass flux, vapor quality and tube expansion on the heat transfer coefficients and friction pressure gradients were investigated in the study. When the mass flux is 100 kg/(m²·s), the heat transfer coefficient and pressure drop of R1234ze(E) decrease after tube expansion. However, when the mass fluxes are 200 and 300 kg/(m²·s), tube expansion effects on the heat transfer coefficient and pressure drop are not notable. In addition, the experimental results are analyzed based on the existing condensation heat transfer and pressure drop correlations.

Keywords: micro-fin tube, tube expansion, condensation, heat transfer, pressure drop

INTRODUCTION

Since the invention of Fujie et al. (1977), micro-fin tubes have been widely used in refrigeration and air-conditioning systems for high heat transfer and relatively low pressure drop performance. For finned tube heat exchangers, micro-fin tubes and the external fins must have a metal-to-metal interference fit to decrease the contact thermal resistance. Mechanical tube expansion process is used to expand the tube outside diameter which is forced against the external fin collar leading to an interference fit. The tube internal enhancements will be deformed or crushed to varying degrees for the mechanical expanding effect. The internal surface area of the micro-fin tube will also be affected by tube expansion. Therefore, tube expansion may cause the negative effect on the thermal-hydraulic performance of finned tube heat exchangers.

Many investigations on the thermal-hydraulic performance during condensation of different refrigerants in pristine micro-fin tubes with a variety of enhancements have been conducted by various researchers (Cavallini et al., 2009; Colombo et al., 2012; Dalkilic and Wongwises, 2009; Doretti et al., 2013; Lee et al., 2014; Liebenberg and Meyer, 2008; Wu and Sundén, 2016; Wu et al., 2014; Wu et al., 2015). The direct use of the condensation heat transfer and pressure drop results based on the pristine micro-fin tubes without any modification may cause deviation for the actual thermal-hydraulic performance of the heat exchangers. Therefore, the tube expansion effect on the micro-fin tube internal surface, heat transfer coefficient and pressure drop are of great significance to be investigated.

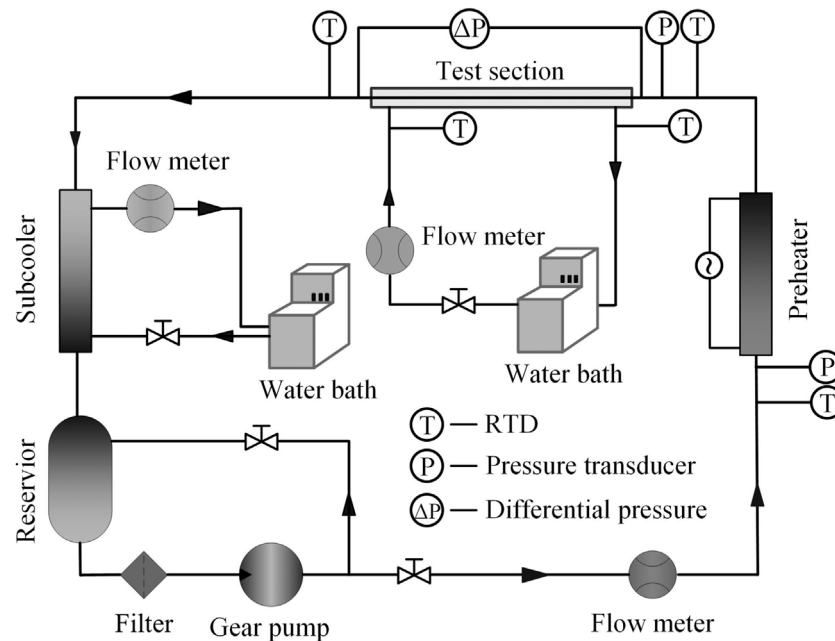


FIGURE 1 | Schematic diagram of the experimental apparatus.

Among the few investigations referring to tube expansion in the existing literature, Tang et al. (2009) studied the expansion forming of inner grooved tubes and effects of the geometrical parameters of the groove geometry on forming quality. Experiments using different fin type tubes were conducted in their study. A finite element model of the forming process was established in the study. The results showed that the fin height reduced by approximately 5–9%. The fin geometric parameter effects on the fin height reduction were studied. The study showed that the helix angle had an important influence on the fin height reduction and the fin height ratio played a significant role in affecting the deformation resistant force. However, the effect of the fin deformation on the inner wall area was not investigated.

Mehendale (2013) analyzed the tube expansion effect on the inner wall area changes and evaluated the existing in-tube heat transfer correlations during condensation. A method for estimating the effect of tube expansion on the in-tube heat transfer performance during condensation was reported. The results showed that the in-tube heat transfer performance of copper and aluminum tubes reduced by 9–36% after the tube expansion. The fin number and the fin apex angle effects on in-tube thermal performance during condensation were also analyzed for expanded micro-fin tubes. Moreover, Mehendale (2014) also numerically investigated the fin deformation influence on the refrigerant side thermal-hydraulic performance of R410A during boiling in micro-fin tubes.

To the author's knowledge, experimental studies on the effect of tube expansion on the heat transfer and pressure drop characteristics during condensation in micro-fin tubes are not available in the public literature. Therefore, the effects of tube

expansion on thermal-hydraulic performance during condensation of R1234ze(E) in pristine and expanded micro-fin tubes were experimentally studied in the present study.

EXPERIMENTAL APPARATUS AND PROCEDURES

Experimental Apparatus

Figure 1 shows the schematic diagram of the experimental apparatus established for two-phase flow and heat transfer experiments in micro-fin tubes. The experimental apparatus consists of a refrigerant and two cooling water circuits. The subcooled refrigerant in the reservoir is filtered, circulates through the magnetic-driven gear pump that can be adjusted by the frequency converter, and then flows through the Coriolis effect mass flowmeter. By adjusting the power of the preheater, the subcooled refrigerant is heated to the required inlet mass quality and temperature. The electric insulation heating wire is wound on the surface of the stainless-steel tube in the preheater. Glass fiber insulation and rubber foam insulation is used in the preheater. The mass quality of the refrigerant flowing into the test section is known. The refrigerant is condensed by the countercurrent cooling water in the test section. The refrigerant is fully condensed and subcooled by the cooling water in the sub-cooler. The sub-cooler is a shell-and-tube heat exchanger. The refrigerant flows on the tube side, and the water flows on the shell side. Afterwards, the refrigerant goes into the reservoir.

The cooling water circuit of the test section is composed of a constant temperature water bath, a Coriolis mass flowmeter and a

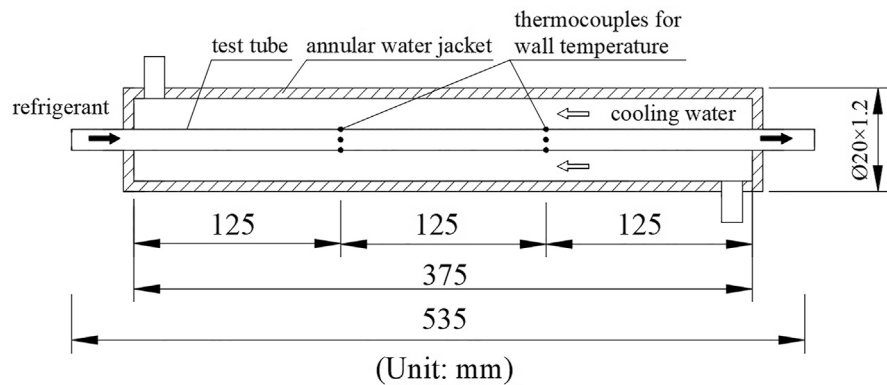


FIGURE 2 | Schematic diagram of the test section.

regulating valve. The cooling water flows in the annular area of the test section to condensate the refrigerant. The mass flow of the cooling water is controlled by the regulating valve and measured by the mass flowmeter. The inlet temperature of the cooling water in the test section is kept at 20°C. The cooling water flow rate was adjusted to ensure the inlet and outlet cooling water temperature difference in the test section larger than 1 K and the experimental uncertainty of the heat transfer rate lower than $\pm 10\%$.

Experimental Method and Condition

The refrigerant and cooling water temperatures are measured using PT100 resistance thermometers. Outer wall temperatures of the micro-fin tube are measured by eight copper-constantan thermocouples installed at two locations as shown in **Figure 2**. Thermocouples are evenly arranged on the upper, lower, and left and right sides of the outer wall of the micro-fin tube. Small slits are prepared carefully on the micro-fin tubes. Thermocouples are first welded to the surface and then surrounded with epoxy resin to avoid the effect of the cooling water in the test section. All the thermocouples and RTDs were calibrated before the experiments. Mixers were set before each fluid temperature measurement point to ensure that the fluids were fully mixed. The saturation states at the test section inlet and outlet were checked using the measured temperature and pressure. The average saturation temperature between the test section inlet and outlet was used to calculate the heat transfer coefficients. Trafag 8,251 pressure sensors are used to measure the refrigerant pressures through 1.0 mm pressure taps. The pressure drop of the refrigerant in the test section is measured through an EJA110A differential pressure sensor. Two Coriolis mass flowmeters are used to measure the mass flow rates of the refrigerant and the cooling water in the test section, respectively. The refrigerant temperature and pressure are used to ensure the saturation state at the entrance and exit of the test section. When all the temperatures, pressures and mass flow rates of the refrigerant and the cooling water keep constant for half an hour, the system is considered to reach a steady state. Experimental data are monitored and collected by an Agilent 34970A acquisition system with three 34901A cards at steady state. **Table 1** listed the experimental conditions in the study.

TABLE 1 | Experimental conditions.

Experimental parameter	Range
Refrigerant	R1234ze(E)
Refrigerant mass flux, [kg/(m ² ·s)]	100, 200, and 300
Cooling water mass flow rate, [kg/h]	4.6–19.0
Refrigerant saturation temperature, [°C]	40, 50
Cooling water inlet temperature, [°C]	20
Inlet vapor quality, [–]	0.25–0.96
Heat transfer rate, [W]	52.0–120.8

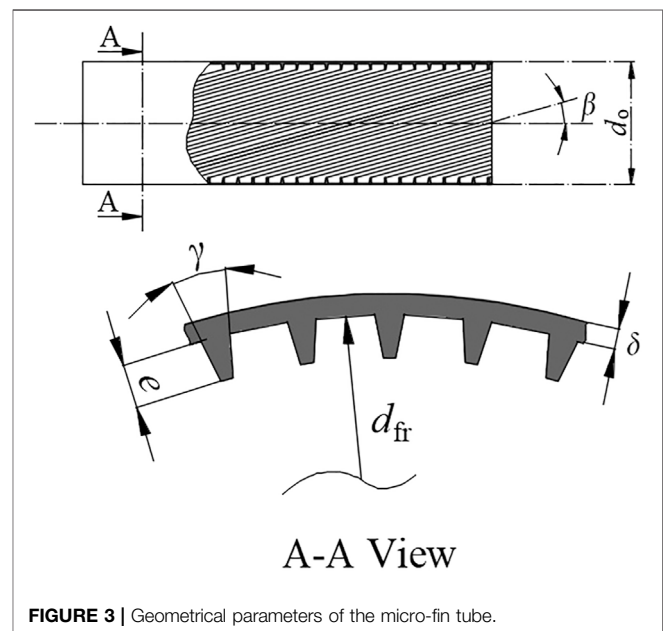


FIGURE 3 | Geometrical parameters of the micro-fin tube.

Test Section

The test section is a counter-flow tube-in-tube heat exchanger as illustrated in **Figure 2**. The refrigerant flows in the micro-fin tube, and the cooling water flows in the annular space. The length of the micro-fin tube is 535 mm and the length of the heat exchange

TABLE 2 | Micro-fin tube dimensions.

Geometrical feature	Pristine D_{Pri}	Expanded D_{Exp}	Relative change $(D_{Exp}-D_{Pri})/D_{Pri} \times 100\%$
Outside diameter d_o , [mm]	5.10	5.26	3.14%
Fin root diameter d_{fr} , [mm]	4.64	4.84	4.31%
Fin apex angle γ , [°]	40°	79°	97.50%
Wall thickness δ , [mm]	0.23	0.21	-8.70%
Fin height e , [mm]	0.11	0.10	-9.09%
Number of fins n , [-]	40	40	—
Helix angle β , [°]	18°	18°	—
Tube cross-sectional area A_c , [mm ²]	16.75	18.07	7.92%
Area enhancement ratio A/A_{fr} , [-]	1.44	1.26	-12.79%

section is 375 mm. The outer tube of the test section is a stainless-steel tube with outer diameter of 20 mm and wall thickness of 1.2 mm. Through considering the critical thermal insulation layer thickness, the insulation layer was set thick enough to weaken the heat loss in the test section. Besides, the aluminum foil was also used to reduce the radiation heat transfer between the outside wall of the test section and the external environment. In order to reduce the heat loss to the environment, 45 mm thick rubber foam insulation is used to wrap the entire experimental apparatus.

The test tubes are two micro-fin tubes in the pristine and expanded states respectively. Before the mechanical tube expansion process, they are from the same production batch with the same diameter. The pristine micro-fin tube is the raw material for residential air-conditioners. The expanded micro-fin tube is torn down from a residential air-conditioner which was mechanically expanded by a mandrel. **Figure 3** shows geometrical parameters of the micro-fin tubes. The outer diameters of the micro-fin tubes are measured by a vernier caliper and the micro-fin geometrical parameters are measured by Hitachi SU8010 scanning electron microscope with a resolution of 1.3 nm. The outer diameter and micro-fin geometrical parameters were measured several times in three various positions of the test tubes and average values were obtained as listed in **Table 2**. The outer diameter, the fin root diameter, the fin apex angle and the tube cross-sectional area increased by 3.14, 4.31, 97.50, and 7.92% after the tube expansion process, while the wall thickness, the fin height and the area enhancement ratio (the total surface area of the micro-fin tube (A) relative to the nominal inner area (A_{fr}) based on the fin root diameter (d_{fr})) decreased by 8.7, 9.09, and 12.79%.

Data Reduction and Uncertainty

The area enhancement ratio A/A_{fr} can be expressed as (Webb and Kim, 2005)

$$A/A_{fr} = 1 + 2[\sec(\gamma/2) - \tan(\gamma/2)] \times e/p_f \quad (1)$$

Based on the heat balance between the refrigerant side and the cooling water side, the heat transfer rate in the test section is calculated as

$$Q = c_{p,c} m_c (t_{out} - t_{in}) \quad (2)$$

The vapor quality of the refrigerant at the entrance of the test section, x_{in} , can be calculated as

$$x_{in} = \frac{UI - m_r (i_l - i_{in})}{m_r i_{lv}} \quad (3)$$

The vapor quality change, Δx , is calculated as

$$\Delta x = \frac{Q}{m_r i_{lv}} \quad (4)$$

The average vapor quality of the refrigerant in the test section, x_{ave} , is calculated as

$$x_{ave} = x_{in} - \frac{\Delta x}{2} \quad (5)$$

The outer wall temperature of the micro-fin tube is calculated as

$$t_{w,o} = \sum_{i=1}^8 t_{w,i}/8 \quad (6)$$

The temperature difference between the inner and outer walls of the micro-fin tube is calculated as

$$\Delta t_w = Q \frac{\ln(d_o/d_{fr})}{2\pi\lambda l} \quad (7)$$

The heat transfer coefficient at the refrigerant side, h , can be calculated as

$$h = \frac{Q}{A[(t_{s,in} + t_{s,out})/2 - (t_{w,out} + \Delta t_w)]} \quad (8)$$

Since the micro-fin tube is placed horizontally, the contribution of gravity is not considered. Therefore, the total pressure drop Δp_{total} of the refrigerant in the test section is calculated as

$$\Delta p_{total} = \Delta p_f + \Delta p_a \quad (9)$$

The accelerated pressure drop, Δp_a , is calculated using the model recommended by Carey (2020).

$$\Delta p_a = G^2 \left\{ \left[\frac{x^2}{\rho_v \alpha} + \frac{(1-x)^2}{\rho_l (1-\alpha)} \right]_{out} - \left[\frac{x^2}{\rho_v \alpha} + \frac{(1-x)^2}{\rho_l (1-\alpha)} \right]_{in} \right\} \quad (10)$$

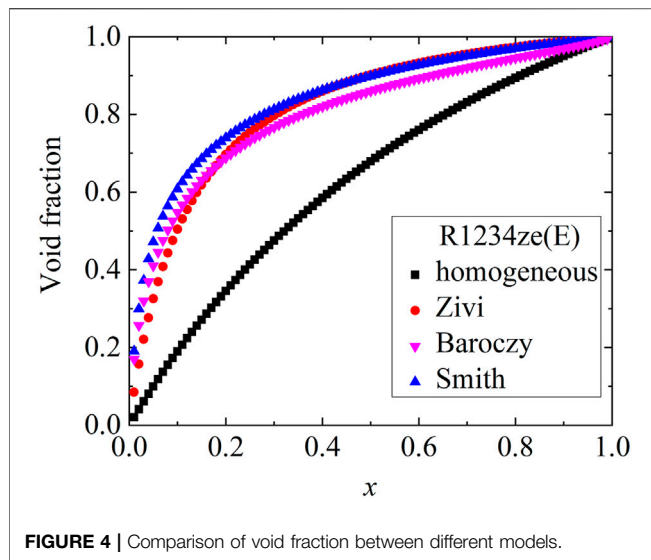


FIGURE 4 | Comparison of void fraction between different models.

TABLE 3 | Experimental uncertainties.

Parameter	Range	Maximum uncertainty
Diameter	—	±0.01 mm
Length	—	±0.5 mm
Temperature (thermocouple)	—	±0.5°C
Temperature (RTDs)	—	±0.1°C
Voltage	—	±0.1 V
Current	—	±0.1 A
Refrigerant mass flow rate	0–100 kg/h	±0.2% FS
Cooling water mass flow rate	0–30 kg/h	±0.2% FS
Pressure	0–6 MPa	±0.3% FS
Pressure difference	0–10 kPa	±0.075% FS
Mass flux	—	±3.6%
Average vapor quality	—	±4.2%
Pressure gradient	—	±3.8%
Heat transfer coefficient	—	±10.3%

The friction pressure drop gradient is expressed as

$$\left(\frac{dp}{dz} \right)_f = \frac{\Delta p_f}{L} \quad (11)$$

There are various void fraction models for smooth tubes in the public literature. However, there is no void fraction model specifically for micro-fin tubes. The void fraction model of smooth tubes is generally used for the micro-fin tube. The experimental study by Newell and Shah (2001) showed that void fraction of two micro-fin tubes differed little from that of the smooth tube. **Figure 4** shows the void fraction comparison among the homogeneous model, the Zivi (1964) model, the Baroczy (1966) model, and the Smith (1969) model for R1234ze(E) at 40°C. The void fraction of the homogeneous model is less than the void fraction of the three separated flow models. The maximum mean absolute deviations between the separated models for R1234ze(E) are 0.037. The small difference in the void fraction has little effect on the accelerated pressure

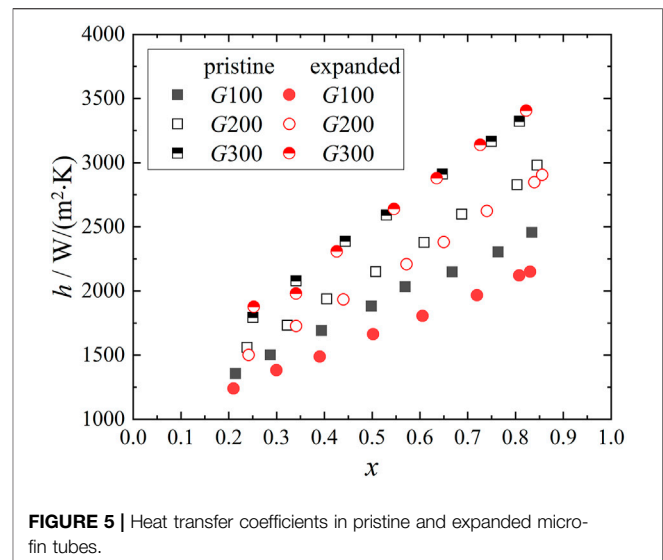


FIGURE 5 | Heat transfer coefficients in pristine and expanded micro-fin tubes.

drop. The Zivi (1964) model is used to calculate the accelerated pressure drop in the study.

The thermophysical properties of R1234ze(E) are obtained through the REFPROP software (Lemmon et al., 2010). The experimental uncertainties of the parameters listed in **Table 3** are analyzed using the method of Kline and McClintock (1953).

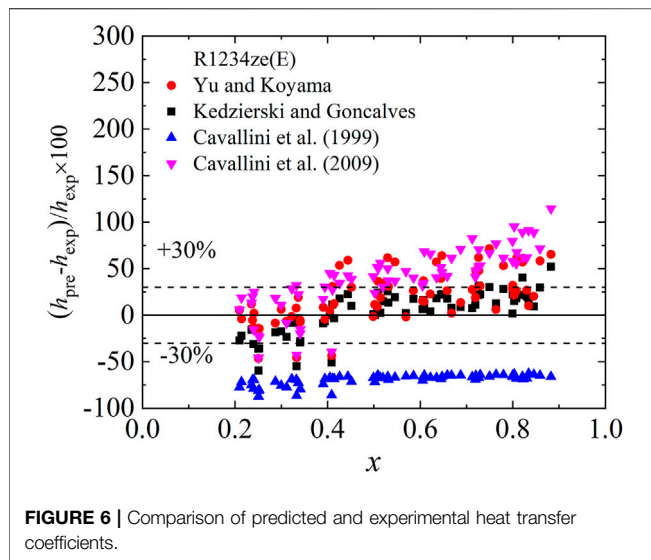
RESULTS AND DISCUSSION

In order to verify the reliability of the experimental system, single-phase heat transfer experiment of R1234ze(E) was conducted in 5.10 mm OD micro-fin tube. The Reynolds number ranges from 2.8×10^3 to 1.2×10^4 , and the inlet temperature of R1234ze(E) ranges from 35 to 39°C. The inlet temperature and flow rate of the cooling water in the test section are 15°C and 9.5 kg/h respectively. The deviation of the heat exchange between the refrigerant side and the cooling water side of the experimental section is within 5%.

The experimental results of single-phase heat transfer are in good agreement with the prediction results of Ravigururajanh (1986) with the absolute average deviation of 10.6%. Single-phase verification experiments show that the experimental apparatus is reliable and can be used for two-phase flow and condensation heat transfer experiments.

Heat Transfer Coefficient

In refrigeration and air conditioning systems, the mass flux of the refrigerant usually ranges from 100 to 500 kg/(m²·s). The mass flux of the refrigerant is taken as 100, 200 and 300 kg/(m²·s) in this study. **Figure 5** shows the heat transfer coefficients of R1234ze(E) in pristine and expanded micro-fin tubes. The results show that the heat transfer coefficient increases with the increase of mass flux and vapor quality. The influence of vapor quality on the heat transfer coefficient increases with the increase of mass flux.



The convection heat transfer between the refrigerant and the inner wall of the micro-fin tube is enhanced with the increase of mass flux resulting in larger heat transfer coefficients. Since the heat conduction resistance of the liquid film plays a leading role in the condensation heat transfer, the thickness and heat conduction resistance of the liquid film decrease with the increase of vapor quality resulting in larger heat transfer coefficients.

The heat transfer coefficients of the pristine micro-fin tube and the expanded micro-fin tube are compared to study the influence of tube expansion. When the mass flux is $100 \text{ kg}/(\text{m}^2 \cdot \text{s})$, the heat transfer coefficients in the pristine micro-fin tube are greater than those in the expanded micro-fin tube. When the mass flux is 200 and $300 \text{ kg}/(\text{m}^2 \cdot \text{s})$, tube expansion has little effect on the heat transfer coefficient.

Micro-fins are used to redistribute the condensate film and maintain a thin film along the tube wall, thereby increasing the heat transfer coefficient. The redistribution effect will be weakened after the expansion process. During the expansion process, the internal fins of the tube underwent an amount of deformation, i.e., the fin apex angle increased while the fin height and the inner surface heat exchange area decreased as listed in **Table 2**, which degraded the fluid turbulence, surface tension induced drainage and the in-tube thermal performance during condensation. It is well known that micro-fins are effective at low mass fluxes, in which the stratified flow dominates, and which can be responsible for the tube expansion effect. Therefore, the tube expansion process degraded the in-tube thermal performance during condensation of R1234ze(E) at low mass flux ($G = 100 \text{ kg}/(\text{m}^2 \cdot \text{s})$) in the present study.

The prediction deviations of the existing correlations (Yu and Koyama, 1998; Kedzierski and Goncalves, 1999; Cavallini et al., 1999; Cavallini et al., 2009) for the present heat transfer coefficients are analyzed in the study, and the results are shown in **Figure 6**. The performance of each correlation is evaluated according to the arithmetic mean deviation of relative residuals of heat transfer coefficient, a.m., and the root

mean square deviation of the relative residuals of heat transfer coefficient, r.m.s, which is defined as follows:

$$\text{a.m.} = \frac{1}{N} \sum \frac{a_{\text{pre}} - a_{\text{exp}}}{a_{\text{exp}}} \times 100\% \quad (12)$$

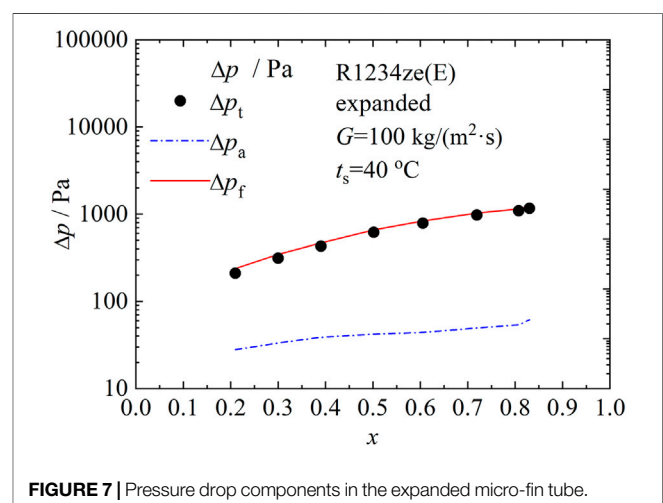
$$\text{r.m.s} = \sqrt{\frac{1}{N} \sum \left(\frac{a_{\text{pre}} - a_{\text{exp}}}{a_{\text{exp}}} \right)^2} \times 100\% \quad (13)$$

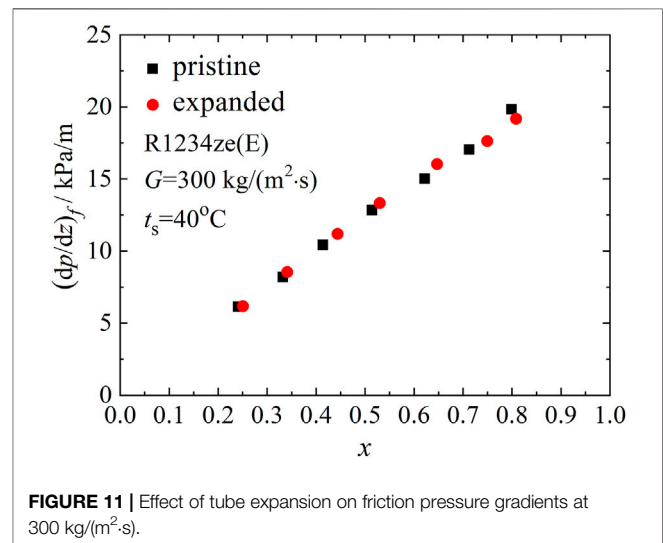
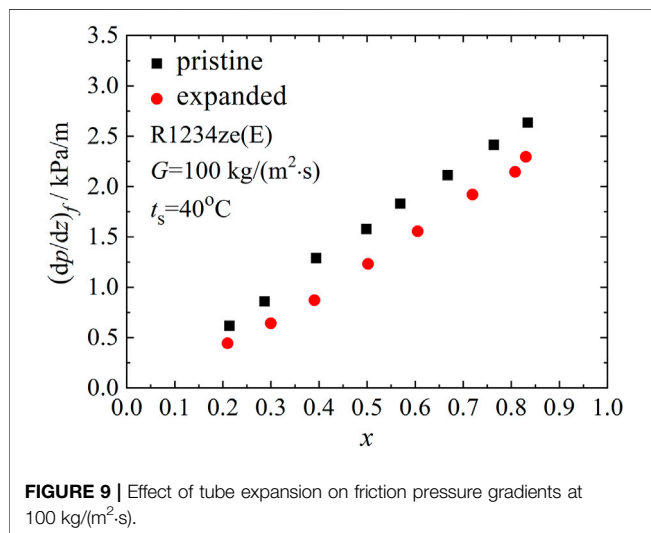
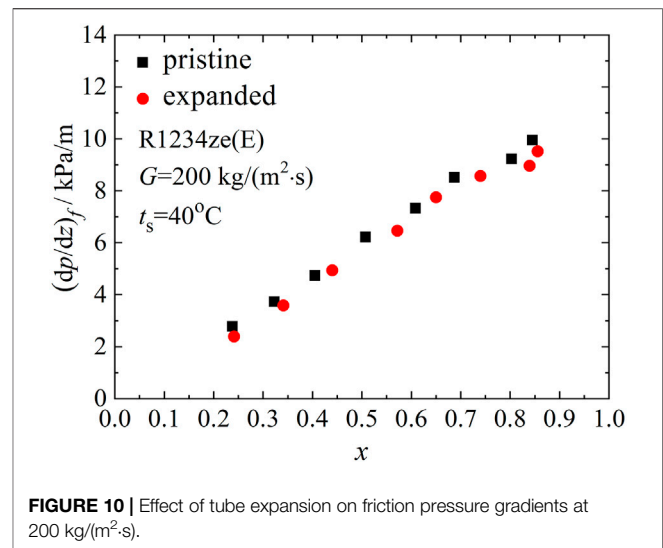
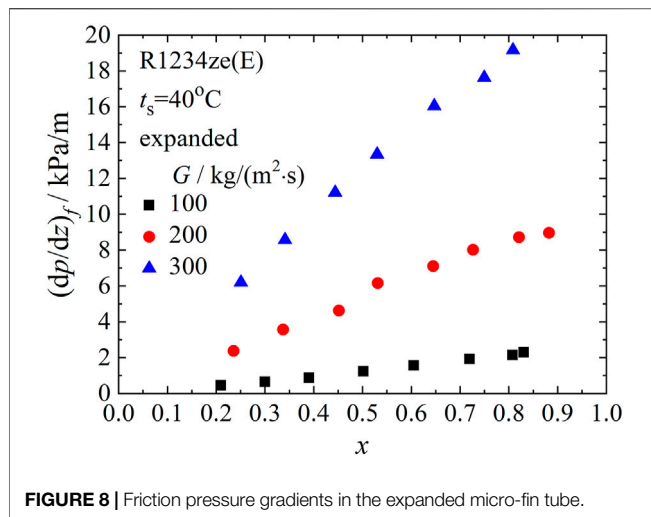
where a represents to the heat transfer coefficient h or friction pressure gradient $(dp/dz)_f$ and N is the number of experimental data. **Figure 6** indicates that (Kedzierski and Goncalves, 1999 correlation can predict the data well with 22.8% r.m.s errors for R1234ze(E). Prediction deviation of Yu and Koyama (1998) correlation for R1234ze(E) is 20.9%, while that of Cavallini et al. (2009) correlation is 39.2%. Though Cavallini et al. (1999) could predict the trend of the present heat transfer coefficients well, the predictions are lower than the data of R1234ze(E) by 69.4%. Prediction deviations for the present data by Cavallini et al. (1999) correlation may be due to the low fin height (0.11 mm) and the small tube outer diameter (5.10 mm) of the micro-fin tube. According to Cavallini et al. (2009), the height of the micro-fin of the previous micro-fin tube is 0.2–0.25 mm, and the outer diameter of the tube is generally greater than 9.5 mm. Cavallini et al. (1999) correlation, which was established based on those configurations as database, may therefore be limited.

Friction Pressure Drop

Figure 7 shows all the pressure drop components of R1234ze(E) at mass flux of $100 \text{ kg}/(\text{m}^2 \cdot \text{s})$ in the expanded micro-fin tube. The measured total pressure drop, the acceleration pressure drop and the friction pressure drop all increase with the increase of vapor quality. The acceleration pressure drops for all the experimental conditions are within 14.1% for R1234ze(E) of the total pressure drops in the present study. In this study, the friction pressure gradient was analysed.

Figure 8 shows the friction pressure gradients of R1234ze(E) in the expanded micro-fin tube. The mass fluxes are 100, 200 and



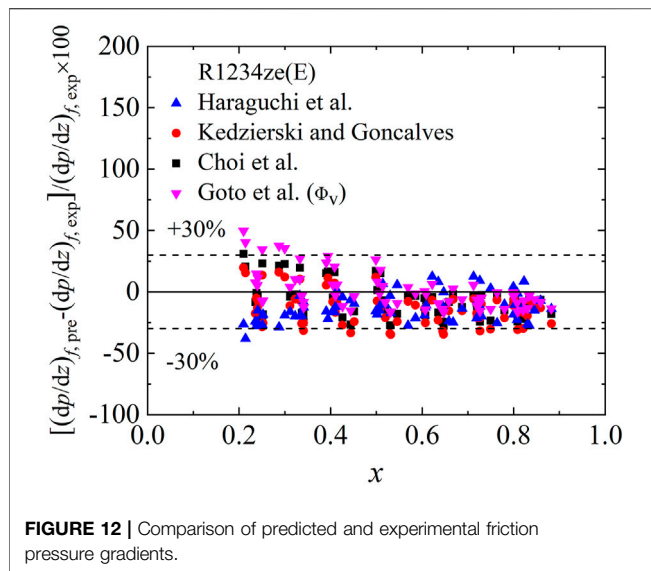


300 kg/(m²·s) with the saturation temperature of 40°C. The experimental data shows that the friction pressure gradient increases with the increase of mass flux and vapor quality, which is the general trend of the friction pressure gradient (Collier and Thome, 1994). As the mass flux increases, the vapor quality dependence of the heat transfer coefficient also becomes stronger. The shear stress at the two-phase interface and the shear stress between the liquid film and the inner wall of the tube both increase with the increase of mass flow and vapor quality, resulting in a greater friction pressure gradient.

In **Figures 9, 10, 11**, friction pressure gradients of the pristine micro-fin tube along with those of the expanded micro-fin tube for R1234ze(E) are compared to show effects of tube expansion for a given mass flux. At low mass flux [$G = 100 \text{ kg}/(\text{m}^2 \cdot \text{s})$] shown in **Figure 9**, friction pressure gradients of R1234ze(E) in the expanded micro-fin tube decreased after the expansion process. The expansion effect was not notable at mass fluxes of 200 and 300 kg/(m²·s).

During the expansion process, the internal fins of the tube underwent an amount of deformation as listed in **Table 2**, which degraded the fluid turbulence and friction pressure gradients. The stratified flow was dominant at low mass flux, where tube expansion was effective in reducing the friction pressure gradient.

The experimental pressure gradients are compared with available correlations (Haraguchi et al. (1993); Kedzierski and Gonclaves, (1999); Choi et al. (1999); Goto et al., 2001), and the comparison are shown in **Figure 12**. Goto et al. (2001) correlation based on vapor-phase two-phase multiplier (Φ_v) is applied in the study. The comparison shows that Haraguchi et al. (1993), Kedzierski and Gonclaves (1999), Choi et al. (1999) and Goto et al. (2001) correlations predict the pressure gradients well.



CONCLUSION

This paper reports experimental data during condensation of R1234ze(E) in pristine (5.10 mm OD) and expanded (5.26 mm OD) micro-fin tubes. In the study, the cross-sectional dimensions of the pristine and expanded micro-fin tubes are microscopically measured. The mass fluxes of the experiment are 100, 200, and 300 kg/(m²·s), the saturation temperature is 40°C, and the vapor qualities are from 0.1 to 0.9. Based on the research in this study, the following conclusions are obtained:

- 1 The outer diameter, the fin root diameter and the tube cross-sectional area of the micro-fin tube increased by 3.14, 4.31, and 7.92% after the tube expansion process, while the wall thickness, the fin height and the area enhancement ratio decreased by 8.70, 9.09, and 12.79%.

REFERENCES

- Baroczy, C. J. (1966). A Systematic Correlation for Two-phase Pressure Drop. *Atoms Int.* 62 (64), 232–249.
- Carey, V. P. (2020). *Liquid-vapor Phase-Change Phenomena: An Introduction to the Thermophysics of Vaporization and Condensation Processes in Heat Transfer Equipment*. Boca Raton: CRC Press. doi:10.1201/9780429082221
- Cavallini, A., Del Col, D., Mancin, S., and Rossetto, L. (2009). Condensation of Pure and Near-Azeotropic Refrigerants in Microfin Tubes: A New Computational Procedure. *Int. J. Refrigeration* 32 (1), 162–174. doi:10.1016/j.ijrefrig.2008.08.004
- Choi, J. Y., Kedzierski, M. A., and Domanski, P. (1999). *A Generalized Pressure Drop Correlation for Evaporation and Condensation of Alternative Refrigerants in Smooth and Micro-fin Tubes*. Gaithersburg, USA: US Department of Commerce, Technology Administration, National Institute of Standards and Technology, Building and Fire Research Laboratory.
- Collier, J. G., and Thome, J. R. (1994). Convective Boiling and Condensation. *Chem. Eng. Sci.* 28, 132–138.
- Colombo, L. P. M., Lucchini, A., and Muzzio, A. (2012). Flow Patterns, Heat Transfer and Pressure Drop for Evaporation and Condensation of R134A in microfin Tubes. *Int. J. refrigeration* 35 (8), 2150–2165. doi:10.1016/j.ijrefrig.2012.08.019

- 2 The heat transfer coefficients and friction pressure gradients increase with the increase of mass flux and vapor quality. The influence of vapor quality on the heat transfer coefficients and friction pressure gradients increases with the increase of mass flux.
- 3 At mass flux of 100 kg/(m²·s), the heat transfer coefficients and friction pressure gradients of R1234ze(E) decrease after the expansion process. At mass fluxes of 200 and 300 kg/(m²·s), tube expansion effects on the data are not notable for R1234ze(E).
- 4 The Kedzierski and Goncalves (1999) correlation predicts the heat transfer coefficients reasonably well of R1234ze(E). The pressure gradient data for R1234ze(E) is well predicted by Haraguchi et al. (1993), Kedzierski and Goncalves (1999), Choi et al. (1999) and Goto et al. (2001) correlations.

DATA AVAILABILITY STATEMENT

The original contributions presented in the study are included in the article/Supplementary Material, further inquiries can be directed to the corresponding author.

AUTHOR CONTRIBUTIONS

NL established the experimental system, carried out the experiments and wrote the first submission of the paper. QZ and ZXL gave a lot of help during the experiments. All authors contributed to the article and approved the submitted version.

FUNDING

This work is supported by the National Natural Science Foundation of China (Grant No. 51904325).

- Dalkilic, A. S., and Wongwises, S. (2009). Intensive Literature Review of Condensation inside Smooth and Enhanced Tubes. *Int. J. Heat Mass Transfer* 52 (15–16), 3409–3426. doi:10.1016/j.ijheatmasstransfer.2009.01.011
- Doretti, L., Rossetto, L., Longo, G. A., Cavallini, A., and Del Col, D. (1999). A New Computational Procedure for Heat Transfer and Pressure Drop during Refrigerant Condensation inside Enhanced Tubes. *J. Enh Heat Transf* 6 (6), 441–456. doi:10.1615/JEnhHeatTransf.v6.i6.50
- Doretti, L., Zilio, C., Mancin, S., and Cavallini, A. (2013). Condensation Flow Patterns inside plain and Microfin Tubes: A Review. *Int. J. Refrigeration* 36 (2), 567–587. doi:10.1016/j.ijrefrig.2012.10.021
- Fujie, K., Itoh, M., Innami, T., Kimura, H., Nakayama, W., and Yanagida, T. (1977). *Heat Transfer Pipe (No. US 4044797)*.
- Goto, M., Inoue, N., and Ishiwatari, N. (2001). Condensation and Evaporation Heat Transfer of R410A inside Internally Grooved Horizontal Tubes. *Int. J. Refrigeration* 24 (7), 628–638. doi:10.1016/S0140-7007(00)00087-6
- Haraguchi, H., Koyama, S., Esaki, J., and Fujii, T. (1993). “Condensation Heat Transfer of Refrigerants HCFC134a, HCFC123 and HCFC22 in a Horizontal Smooth Tube and a Horizontal Micro-fin Tube,” Proceedings of the 30th National Symposium of Japan, Yokohama, Japan. 343–345.
- Kedzierski, M. A., and Goncalves, J. M. (1999). Horizontal Convective Condensation of Alternative Refrigerants within a Micro-fin Tube. *J. Enh Heat Transf* 6 (2–4), 161–178. doi:10.1615/JEnhHeatTransf.v6.i2-4.90

- Kline, S. J., and McClintock, F. A. (1953). Describing Uncertainties in Single-Sample Experiments. *Mech. Eng.* 75 (1), 3–8.
- Lee, E. J., Kim, N. H., and Byun, H. W. (2014). Condensation Heat Transfer and Pressure Drop in Flattened Microfin Tubes Having Different Aspect Ratios. *Int. J. refrigeration* 38, 236–249. doi:10.1016/j.ijrefrig.2013.09.035
- Lemmon, E. W., Huber, M. L., and McLinden, M. O. (2010). NIST Reference Fluid Thermodynamic and Transport Properties–REFPROP. *NIST Stand. reference database* 23, v9.
- Liebenberg, L., and Meyer, J. P. (2008). A Review of Flow Pattern-Based Predictive Correlations during Refrigerant Condensation in Horizontally Smooth and Enhanced Tubes. *Heat Transfer Eng.* 29 (1), 3–19. doi:10.1080/01457630701677049
- Mehendale, S. S. (2014). “The Impact of Fin Deformation on Boiling Heat Transfer and Pressure Drop in Internally Grooved Tubes,” in International Heat Transfer Conference Digital Library, Kyoto, Japan, August 10–15, 2014 (Begel House Inc). doi:10.1615/ihtc15.fbl.008800
- Mehendale, S. (2013). “The Impact of Fin Deformation on Condensation Heat Transfer Coefficients in Internally Grooved Tubes,” in Heat Transfer Summer Conference, Minneapolis, Minnesota, USA, July 14–19, 2013 (American Society of Mechanical Engineers (ASME)), 55485, V002T07A002. doi:10.1115/HT2013-17111
- Newell, T. A., and Shah, R. K. (2001). An Assessment of Refrigerant Heat Transfer, Pressure Drop, and Void Fraction Effects in Microfin Tubes. *Hvac&R Res.* 7 (2), 125–153. doi:10.1080/10789669.2001.10391267
- Ravigururajan, T. S. (1986). General Correlations for Pressure Drop and Heat Transfer for Single-Phase Turbulent Flows in Ribbed Tubes. *Doctoral dissertation. Iowa State University*
- Smith, S. L. (1969). Void Fractions in Two-phase Flow: a Correlation Based upon an Equal Velocity Head Model. *Proc. Inst. Mech. Eng.* 184 (1), 647–664. doi:10.1243/PIME_PROC_1969_184_051_02
- Tang, D., Peng, Y., and Li, D. (2009). Numerical and Experimental Study on Expansion Forming of Inner Grooved Tube. *J. Mater. Process. Tech.* 209 (10), 4668–4674. doi:10.1016/j.jmatprotec.2008.11.037
- Webb, R. L., and Kim, N. Y. (2005). *Enhanced Heat Transfer*. New York: Taylor & Francis.
- Wu, Z., and Sundén, B. (2016). Frictional Pressure Drop Correlations for Single-phase Flow, Condensation, and Evaporation in Microfin Tubes. *J. Heat Transfer* 138 (2), 022901. doi:10.1115/1.4031268
- Wu, Z., Sundén, B., Wadekar, V. V., and Li, W. (2015). Heat Transfer Correlations for Single-phase Flow, Condensation, and Boiling in Microfin Tubes. *Heat Transfer Eng.* 36 (6), 582–595. doi:10.1080/01457632.2014.939531
- Wu, Z., Sundén, B., Wang, L., and Li, W. (2014). Convective Condensation inside Horizontal Smooth and Microfin Tubes. *J. Heat transfer* 136 (5), 051504. doi:10.1115/1.4026370
- Yu, J., and Koyama, S. (1998). Condensation Heat Transfer of Pure Refrigerants in Microfin Tubes. *International Refrigeration and Air Conditioning Conference*. 431.
- Zivi, S. M. (1964). Estimation of Steady-State Steam Void-Fraction by Means of the Principle of Minimum Entropy Production. *J. Heat Transfer* 86 (2), 247–251. doi:10.1115/1.3687113

Conflict of Interest: The authors declare that the research was conducted in the absence of any commercial or financial relationships that could be construed as a potential conflict of interest.

Publisher’s Note: All claims expressed in this article are solely those of the authors and do not necessarily represent those of their affiliated organizations, or those of the publisher, the editors and the reviewers. Any product that may be evaluated in this article, or claim that may be made by its manufacturer, is not guaranteed or endorsed by the publisher.

Copyright © 2021 Liu, Zhao and Lan. This is an open-access article distributed under the terms of the Creative Commons Attribution License (CC BY). The use, distribution or reproduction in other forums is permitted, provided the original author(s) and the copyright owner(s) are credited and that the original publication in this journal is cited, in accordance with accepted academic practice. No use, distribution or reproduction is permitted which does not comply with these terms.

GLOSSARY

A refrigerant side surface area, m^2
 A_c channel cross-sectional area, m^2
 A_{fr} channel surface area based on the fin root diameter, m^2
 d_{fr} fin root diameter, m
 d_o outside diameter, m
 e fin height, m
 G mass flux, $\text{kg}/(\text{m}^2 \cdot \text{s})$
 h heat transfer coefficient, $\text{W}/(\text{m}^2 \cdot \text{K})$
 i specific enthalpy, J/kg
 i_v latent heat of vaporization, J/kg
 I electric current, A
 l effective heat transfer length, m
 L micro-fin tube length, m
 m mass flow rate, kg/s
 n number of fins
 U electric voltage, V
 p pressure, Pa
 p_f rib pitch normal to the fins, m
 Q heat transfer rate, W
 t temperature, $^{\circ}\text{C}$
 x vapor quality

Greek symbols

α void fraction
 β helix angle
 γ apex angle
 δ wall thickness, m
 λ thermal conductivity, $\text{W}/(\text{m} \cdot \text{K})$
 ρ density, kg/m^3

Subscripts

ave average
c cooling water
exp expanded or experimental
f friction
i inner
l liquid
in inlet
o outer
out outlet
pri pristine
pre predicted
r refrigerant
v vapor
w wall



Element Distribution and Migration Behavior in the Copper Slag Reduction and Separation Process

Zongliang Zuo^{1,2}, Yan Feng¹, Siyi Luo^{1*}, Xinjiang Dong¹, Xiaoteng Li¹, Dongdong Ren¹, Qingbo Yu³ and Jianxiang Guo¹

¹School of Environmental and Municipal Engineering, Qingdao University of Technology, Qingdao, China, ²Shanghai Engineering Research Center of Solid Waste Treatment and Resource Recovery, Shanghai Jiao Tong University, Shanghai, China, ³School of Metallurgy, Northeastern University, Shenyang, China

OPEN ACCESS

Edited by:

Kaiqiang Zhang,
Imperial College London,
United Kingdom

Reviewed by:

Sang-Sup Lee,
Chungbuk National University, South
Korea
B. C. Meikap,
Indian Institute of Technology
Kharagpur, India

*Correspondence:

Siyi Luo
luosiyi666@126.com

Specialty section:

This article was submitted to
Advanced Clean Fuel Technologies,
a section of the journal
Frontiers in Energy Research

Received: 18 August 2021

Accepted: 23 November 2021

Published: 09 December 2021

Citation:

Zuo Z, Feng Y, Luo S, Dong X, Li X,
Ren D, Yu Q and Guo J (2021) Element
Distribution and Migration Behavior in
the Copper Slag Reduction and
Separation Process.
Front. Energy Res. 9:760312.
doi: 10.3389/fenrg.2021.760312

Copper slag is a solid pollutant with high recyclability. Reduction and separation are regarded as effective disposal methods. However, during the melting process, the separation and migration behavior of elements in the copper slag is complicated. Thus, the formation of pollutants cannot be controlled merely by optimizing the operation parameters. The elemental distribution and migration behavior are discussed in this work. In reduction experiments, the copper slag smelting liquid was divided into three layers: a reduction slag layer, a reactive boundary layer, and an iron ingot layer. Reduction slag and ingot iron were on the top and bottom of the liquid, respectively. Residual carbon oozed at the interface. C can react with reducible "O" atoms, which exist in $2\text{FeO}\cdot\text{SiO}_2$, Fe_3O_4 , and CuO . Meanwhile, CO was generated and overflowed from the liquid layer. After reduction by C or CO, metallic iron and copper were produced and migrated to the iron ingot layer. In the liquid, S gradually diffused into the upper layer. Some of the ZnO and CuS spilled from the liquid into the flume. After reduction, $\text{CaO}\cdot\text{SiO}_2$ was generated and moved to the upper layer.

Keywords: copper slag, element migration, reduction, pollutants, element separation

1 INTRODUCTION

Metallurgical solid waste residue is produced after the extraction of valuable metals. Copper slag is a type of nonferrous metal smelting slag produced in pyrometallurgy. Copper slag is the melt of various oxides and mainly comes from slag-forming components in flux, ore, ash, and reducing agent (fuel) as part of the smelting, converting, and refining three processes in the copper pyrometallurgical procedure (Moskalyk and Alfantazi, 2003).

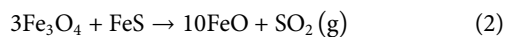
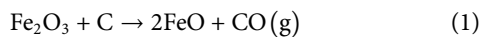
Depending on the pyrometallurgical process used, copper slag can be divided into smelting slag, blowing slag, refining slag, and dilution slag. The growth rate in recent years would predict that the output of copper slag will exceed 24 million tons by 2020 (Fuentes et al., 2020).

According to the research of typical copper companies in China, the iron and copper grades of copper slag are approximately 40 and 1%, respectively, which are higher than the current grade of iron and copper. Copper slag is a type of secondary resource with a large quantity and high quality. The typical composition of copper slag is Cu 0.42–4.6%; Fe 29–40%; SiO_2 30–40%; $\text{CaO} \leq 11\%$; $\text{Al}_2\text{O}_3 \leq 10\%$ (Piatak et al., 2015). The copper phase in copper smelting slag is mainly copper sulfide, accounting for more than 60% of the total copper, and followed by copper oxide and copper metal. The iron phase is mainly composed of fayalite and magnetite, the sum of which accounts for more

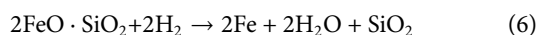
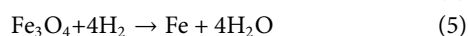
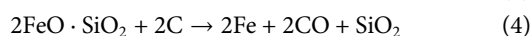
than 80% of the total iron distribution rate, in which the distribution rate of fayalite is 8–65%, and that of magnetite is 33–45%.

The development of new technology, comprehensive utilization of copper slag resources, and extraction of valuable metals, such as iron, and can promote the sustainable development of the metallurgical industry. These technologies are conducive to the rational utilization of secondary resources, which have the dual significance of economic and environmental protection. In the 1970s, China began to study the comprehensive utilization of copper slag, mainly applied to the cement and construction industry, and with various production uses. In the cement industry, it is used as a raw material for cement clinker, cement concrete mixed material, and used as an iron correction agent to produce Portland cement clinker (Shi et al., 2008; Feng et al., 2019; Wang et al., 2020). In the construction industry, it is used in brick making and various cutting blocks and is an alternative to sand for concrete preparation (Kalusuraman et al., 2019; Lan et al., 2020). At home and abroad, research on the recovery of single metal copper from copper slag has been more in-depth and has achieved fruitful results (Zhang et al., 2015; Heo et al., 2016; Liao et al., 2016; Guo et al., 2017; Li et al., 2017). In summary, the current technology mainly includes pyrometallurgy, mineral processing, and the wet method.

The principle of the fire dilution method is that a large amount of Fe_3O_4 in copper slag leads to an increase in slag viscosity and the loss of copper (Zhang et al., 2005). By reducing the content of magnetic Fe_3O_4 in slag, the inclusion of copper can be reduced, and the recovery of copper can be achieved (Sun et al., 2020). The common method is to reduce the content of Fe_3O_4 by adding a reducing agent (carbon powder, broken coal; Eq. 1) and sulfide (FeS, pyrite; Eq. 2).



The technology of reduction modification refers to the technology in which ferroolivine and magnetite in copper slag are reduced to metal iron (MFe) by a reducing agent at a temperature lower than the temperature required to produce liquid iron. With reduction, iron grains continuously precipitate and grow, and the symbiotic relationship with the slag phase changes into a dissemination relationship. Iron is dissociated by grinding and iron is recovered by magnetic separation (Zhang et al., 2015). At present, lignite, coke, hydrogen, and a reducing gas mixture (Zhang et al., 2021) are commonly used as reducing agents. Some scholars have used biomass (Zuo et al., 2016; Zuo et al., 2018), biochar (Zuo et al., 2020a), and plastic coke (Zuo et al., 2021a) as novel cheap reducing agents.



Extraction of a single element from copper slag has been comprehensively studied, but the research focus is limited to a

single index of metal recovery. During iron extraction from copper slag, the removal of impurity elements is negligible. Only a few scholars have conducted preliminary research on Fe, Cu, S, As, and P in the process of iron extraction (Cheng et al., 2015; Deegan and Peters, 2017; Meng et al., 2019; Sun et al., 2019; Ming et al., 2020; Zhang et al., 2020).

However, the process of melting separation is commonly used after the reduction of iron and copper. Owing to the lack of understanding of the separation and migration of the main elements in copper slag during melting separation, operation parameters cannot be optimized to control the formation of pollutants to reduce pollution to the environment. The burden of flue gas post-treatment is aggravated after flue gas emission (Bal et al., 2019). For example, people usually use spray washing to remove particulate matter or harmful substances in the flue gas. The design of scrubber structure is closely related to the state of solid particles in flue gas. Understanding the migration of elements is also the basic basis of flue gas treatment (Raj Mohan and Meikap, 2009).

In this study, after the direct reduction reaction of carbon-bearing pellets, chemical composition, XRF, and SEM-EDS analyses were conducted on copper slag, reduction slag, and ingot iron. The migration and transformation behaviors of the elements were studied during the process of melting separation.

2 EXPERIMENTS AND METHODS

2.1 Samples

2.1.1 Sample source

The raw materials used in the experiment were copper slag, coal, and limestone. Copper slag was obtained from a flash smelting furnace in Gansu Province, China. The type of coal used in the experiment was lignite and was obtained from a coal mine plant in Liaoning Province. Limestone was ordered online from the Sinopharm Group.

2.1.2 Sample pretreatment

Copper slag and lignite were mechanically crushed into small particles with diameters less than 200 mesh. Limestone was calcined at 1,000°C in a high-temperature vacuum tube furnace for 2 h and then cooled in N_2 atmosphere. CaO was obtained by the calcination of limestone. The samples were dried at 105°C for 24 h and then placed in a rapid glass dryer.

2.1.3 Sample components

The chemical component and mineral phase results of copper slag were obtained from our previous work (Zuo et al., 2020b; Zuo et al., 2020a). The chemical components of copper slag are FeO 37.50%; Fe_3O_4 18.90%; CaO 0.23%; Al_2O_3 0.98%; MFe 1.24%; SiO_2 31.99%; Cu 0.74%; MgO 0.42%; S 0.39%; Zn 2.78%; others 4.87% (Zuo et al., 2020b). The phase of the copper slag is mainly fayalite and magnetite, based on the XRD results. The proximate analysis results of lignite are moisture (3.13%), volatile matter (32.78%), ash (14.3%), and fixed carbon (49.79%) (Zuo et al., 2020a). The purity of CaO was above 99.9%.

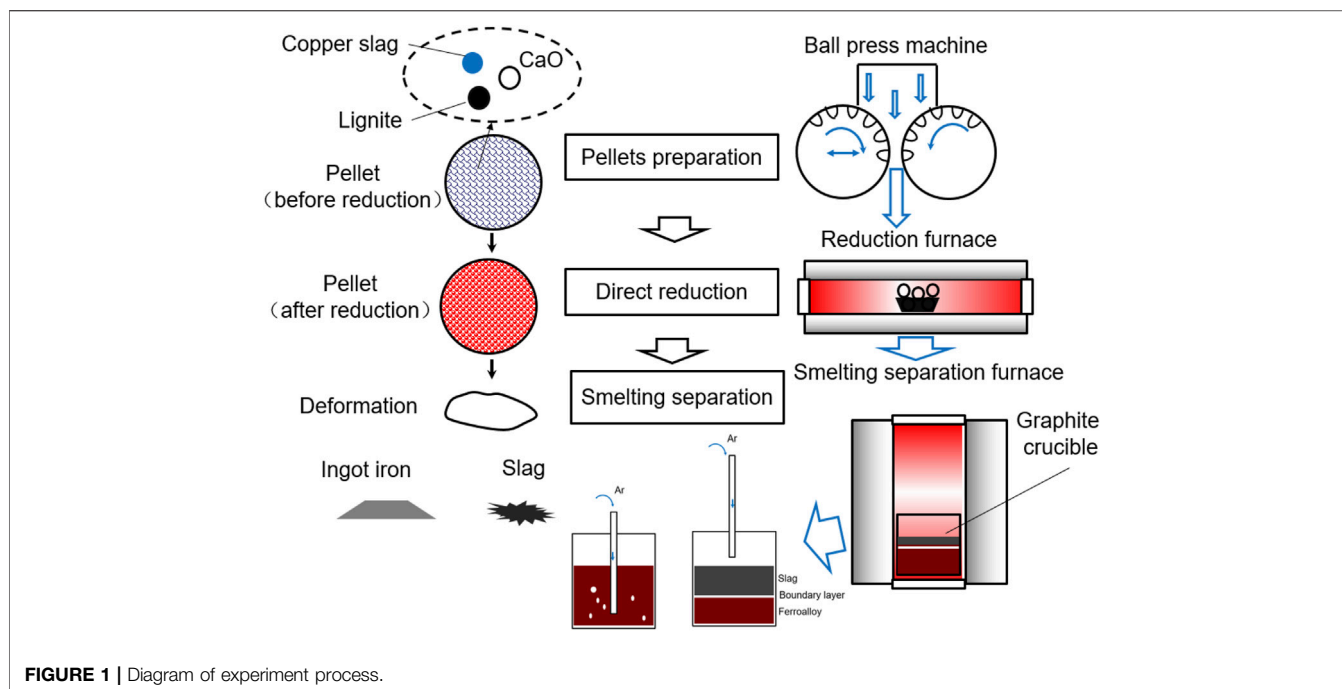


FIGURE 1 | Diagram of experiment process.

2.2 Direct Reduction and Smelting Separation

The process of sample treatment, direct reduction, and smelting separation are shown in **Figure 1**. First, copper slag, lignite, and CaO were thoroughly blended. The mass ratio of copper slag and lignite is based on the molar ratio of “O” and “C”. The mass ratio of the copper slag to CaO is based on the molar ratio of SiO₂ and CaO. In this experiment, the molar ratios of C/O and CaO/SiO₂, regarded as the optimum reaction conditions, were all 1.0, and based on previous experimental results (Zuo et al., 2017; Zuo et al., 2020b). The masses of lignite and CaO were calculated based on Eqs 7, 8. A carbonaceous pellet with copper slag and CaO was prepared in a spherical shape using a ball-press machine. The maximum diameter of the pellets was 21 mm. The mass of each pellet was approximately 10 g. The pressure setting of the briquetting machine was set to 30 MPa.

$$m_{\text{lignite}} = \text{FeO}\% / 100 \times m_{\text{copper slag}} \times 12/72 + \text{Fe}_3\text{O}_4\% / 100 \times m_{\text{copper slag}} \times 48/232 \quad (7)$$

$$m_{\text{CaO}} = \text{SiO}_2\% / 100 \times m_{\text{copper slag}} \times 56/60 \quad (8)$$

where m_{lignite} is the mass of lignite, g; $m_{\text{copper slag}}$ is the mass of copper slag, g; m_{CaO} is the mass of CaO, g; $\text{Fe}_3\text{O}_4\%$ is the mass percentage of Fe₃O₄ in copper slag, and %; $\text{FeO}\%$ is the mass percentage of FeO in the copper slag, %.

The pellets were then placed in a corundum crucible in a reduction furnace. The temperature was programmed to heat and kept at 1,150°C for 30 min to achieve the reduction reaction of the copper slag.

Finally, the pellets were placed in a graphite crucible in a smelting-separation furnace with a mass of 460 g. Ar was blown into the melting copper slag using a crucible tube, as shown in **Figure 1**. Pellets were heated to 1,350°C and held for 15 min. The

sample was then cooled in a furnace. The Ar crucible tube was removed from the liquid level and allowed to flow until the temperature of the furnace reached 100°C.

To analyze the feasibility of this technology, economic estimation was calculated based on experimental data and energy consumption of each industrial scale process (Zuo et al., 2021b; Gu, 2021). The calculation results are based on the current price of raw materials and converted into United States dollars. For this three steps, the energy consumption is in the form of electricity. In this paper, the energy consumption is transformed into mass of standard coal. By calculation, we can see that this method has great economic benefits. On average, United States \$ 25.056 can be obtained for each treatment of 100 kg copper slag.

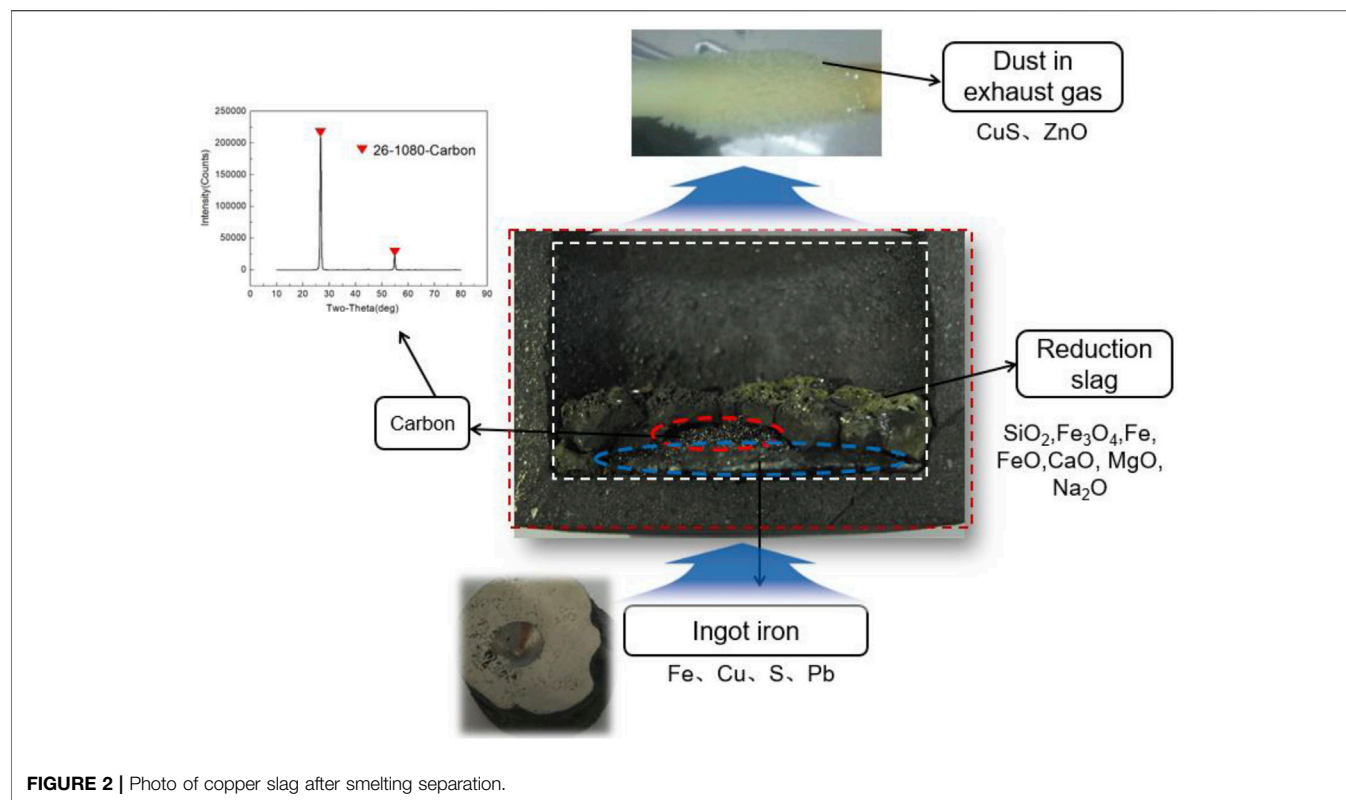
2.3 Analysis Method

Graphite crucible was cut by a chainsaw to obtain slag and ingot iron. The mass of slag, ingot iron, and carburizing powder was then tested. Then, chemical composition, mineral phase, element distribution, and crystal structure of slag, collected dust or iron ingot were analyzed by XRD, and SEM metallurgical microscope.

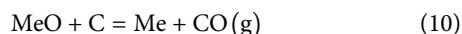
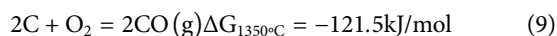
3 RESULTS AND DISCUSSION

3.1 Sample Material Distribution

When cooled to room temperature, the copper slag was stratified and solidified. By cutting, the original characteristics of the slag after stratification were retained. A photograph of the copper slag after the layering process is shown in **Figure 2**. It was eroded to varying degrees inside and outside of the graphite crucible. On the outside of the graphite crucible, oxygen in the air contacted the graphite crucible and carried out oxidation erosion on the outside

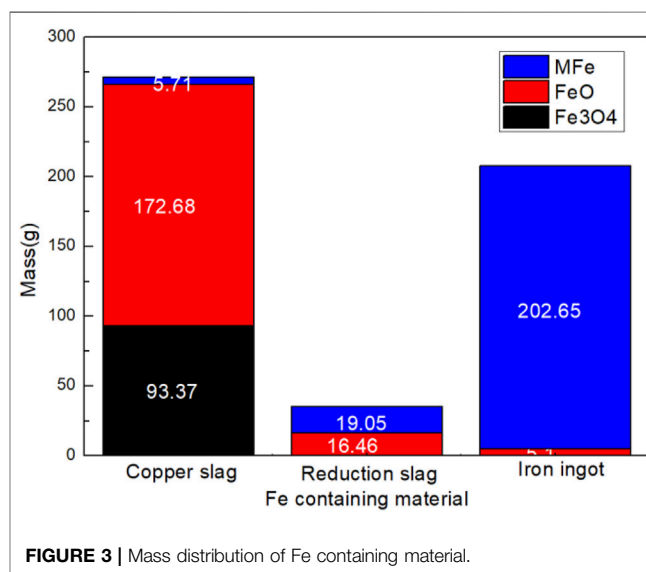


surface. As shown in **Eq. 9**, the oxidation erosion of graphite proceeds at the separation temperature. On the inside of the graphite crucible, Ar gas was protected from the surface of the crucible to some extent. However, erosion occurred mainly because of the reaction of metal oxides with graphite on the crucible surface, as shown in **Eq. 10**. “MeO” represents any metal oxide. The inside erosion phenomenon occurs only when they are in contact with one another.

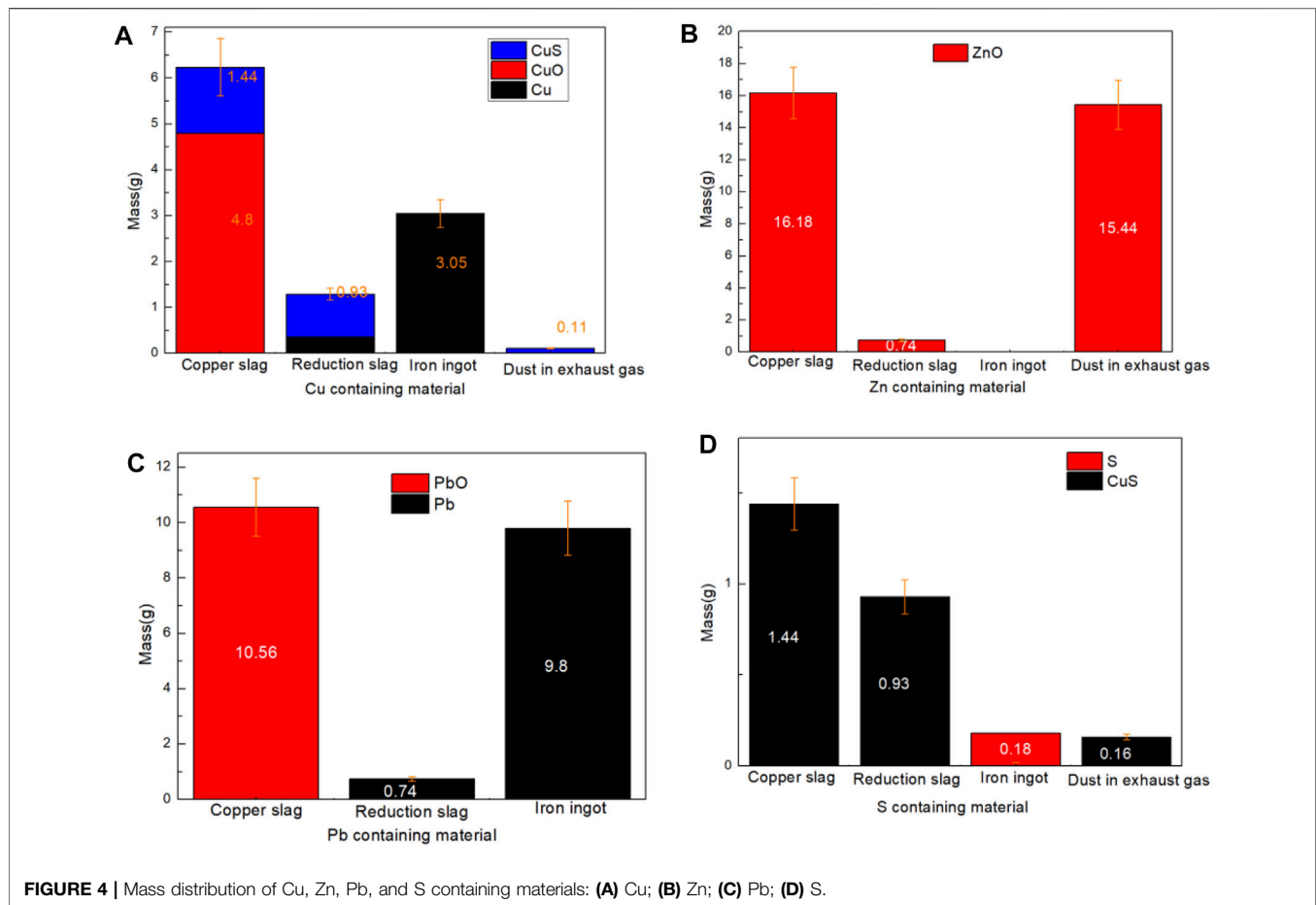


After reduction and solidification, there was a distinct stratification in the copper slag. The reduction slag is on the top of the solid copper slag, and ingot iron is on the bottom of the solid copper slag. The reduction slag is black brown in color, and tiny pores are present inside the sample. This means that the gas was produced by the reduction reaction, and volatiles were generated.

In addition, on the surface of the reduction slag, there appeared a slightly yellow material. This is due to the release of sulfur from the copper slag, which is removed by the gas. At the bottom, the iron ingot is shaped like a flying saucer. There is an interfacial exudate at the top of the flying saucer, which was analyzed to be residual carbon by XRD, and as shown in **Figure 2**. The residual carbon oozed at the interface between the iron ingot and the reducing slag. This reveals the direction of material diffusion in the smelting reduction process to some extent.



During the melting separation process, volatile substances are produced as gas dust in the molten pool. These volatiles were deposited on a corundum tube, as shown in **Figure 2**. Analyzed by XRD, the main components of some dusts are CuS and ZnO. Therefore, it is very important to collect soot volatilized from the copper slag in the molten state to reduce environmental pollution. The mass of the reduction slag, ingot iron, carbon, and volatiles



were obtained. The mass percentages of copper slag, lignite, and CaO before reduction were 314.60, 52.61, and 93.92 g, respectively. Mass percentage of reduction slag, ingot iron, carbon, and volatiles (carried dust in gas: CuS, ZnO; gas: CO, CO₂) after reduction were 238.5, 222.6, 1.12, and 1.88 g, respectively.

3.2 Reaction Analysis in Copper Slag

Reactions in the copper slag reduction process were analyzed based on chemical composition tests. Based on the results, we determined the element type and mass content in the sample. The reactions of iron oxide containing a typical reduction reaction are shown in Eq. 10. Mass distribution of Fe, Cu, Zn, S, Pb, as typical elements, and were analyzed as shown in Figures 3, 4. In copper slag, the phases of Fe element are FeO, Fe₃O₄, and MFe. 86.71% of Fe element moved into iron ingot in the phase of MFe as shown in Figures 3, 4. Some FeO still entered into the reduction slag and ingot respectively. The results confirmed the reduction reaction sequence of iron oxides (Fe₃O₄-FeO-Fe) to a certain extent.

In copper slag, the phases of Cu element are Cu, CuO, and CuS. 10.17, 86.70, and 3.13% of Cu element moved into reduction slag, iron ingot and some in the phase of (CuS, Cu), (Cu), and (CuS) respectively, as shown in Figures 4A,D. Although only a small part of CuS enters the flue gas, its polluting characteristics

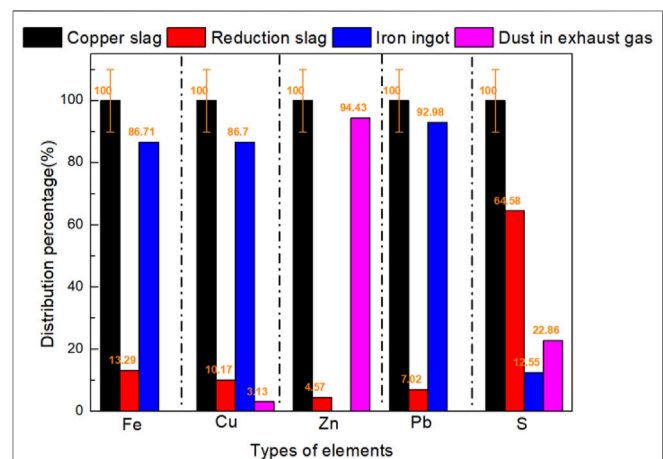


FIGURE 5 | Typical elements distribution percentage in copper slag, reduction slag, iron ingot, and dust in exhaust gas.

should be paid more attention on recovery study. In the reducing atmosphere, CuO phase has been transformed into Cu phase completely. This is because that, copper is preferentially reduced in the reduction process compared with FeO or Fe₃O₄.

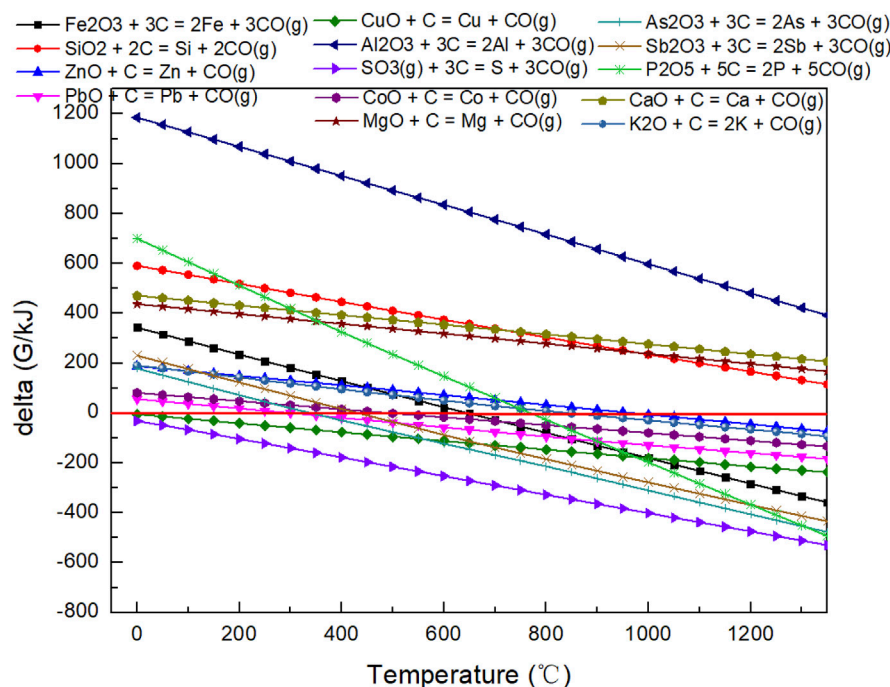


FIGURE 6 | Gibbs free energy of reduction reactions of the oxide that may exist in copper slag.

In copper slag, the phase of Zn element is merely ZnO. As shown in **Figures 4B, 5**, due to the volatile characteristics of ZnO at high temperature, 94.43% of ZnO entered into the flue gas. Due to the simple element migration, the recovery purity of ZnO powder in flue gas will be relatively high.

In copper slag, the phases of S element are S and CuS. As shown in **Figures 4D, 5**, the distribution of S was obvious. 64.58% of S existed in reduction slag in the phase of CuS and 22.86% of S existed in smoke in the phase of CuS. To capture such volatile solid pollutants, spray soot or spray is usually used to collect such soot, and such as Venturi tube (Bal and Meikap, 2017). However, it should be noted that due to the entry of sulfur-containing substances in copper slag, the corrosion of scrubber needs attention (Sarkar et al., 2007).

In copper slag, the phases of Pb element are Pb and PbO. As shown in **Figures 4C, 5**, the distribution of Pb was derived by its gravity. 92.98% of Pb element went into iron ingot.

The Gibbs free energy of the reaction of C with oxide materials in copper slag varies with temperature, as shown in **Figure 6**. We should declare that not all elements in the slag exist in the oxidation state; we only discuss the possible reduction situation as far as possible. As for SiO₂, Al₂O₃, CaO, and MgO, reactions of C with these oxide materials cannot occur when the temperature is higher than 1,150°C. The other reaction of oxide materials with C can take place at this temperature. In other words, during the direct reduction and smelting separation process, Si, Al, Ca, and Mg elements exist in the oxide state, while the other elements cannot stably exist in that state.

3.3 Element Transformation Analysis

Metallographic microscope photos of the copper slag, reduction slag, and ingot are shown in **Figure 7**. Because of the corrosive effect that occurs during the sample making process, we can find the boundary profile of the metal oxide phase and matrix in the copper slag. At different magnifications, we found that the phases in the copper slag were embedded into the matrix like jelly. After reduction, the metal oxides are stripped from the matrix, and the boundary contour becomes clearer. They are a mixture of iron oxide and slag. As shown in **Table 1**, in the obtained iron ingot, the black matrix material is mainly fayalite, and which is not fully reacted and is distributed in the iron metal. Some black matrix materials are dots, and some are lines.

A typical circular area element analysis of the iron ingot is shown in **Figure 8A**, based on SEM-EDS. In the reduction process, the matrix of fayalite shrinks continuously. As circular areas 1# and 2#, two typical circular fayalite matrices, the radius of the circle is small. The reduction degree of 2# was higher than that of 1#. Chemical analysis of the points was shown in **Table 2**. The Fe atoms acquired were 54.54 and 50.83% for 2# and 1#, respectively. Through the element distribution and the changes in the size of the circles in these two areas, we can determine the migration rule of elements (O, Al, Si, Fe, and S) inside the circle. Fe and O are mainly present in the matrix of the black circle in the form of FeO. The small holes in the circle matrix are caused by the release of O atoms and migrate to the produced gas. The Fe atom migrates from the inside to the outside of the circle matrix continuously. Al and Si are all present in the slag phase. The S element exists in the circle matrix at the initial

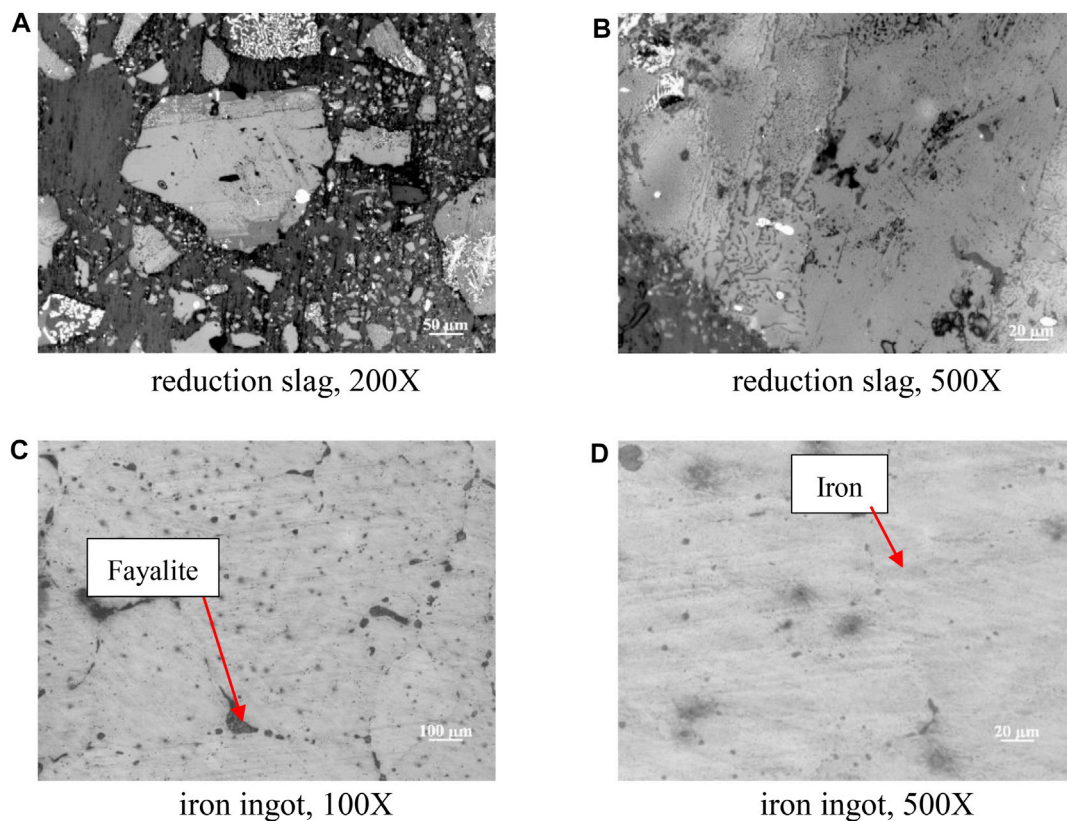


FIGURE 7 | Metallographic microscope photos of copper slag and reduction slag: **(A)** reduction slag, 200X; **(B)** reduction slag 500X; **(C)** iron ingot, 100X; **(D)** iron ingot, 500X.

TABLE 1 | Economic estimation of direct reduction and smelting separation running process.

Indicators	Item	Pellets preparation, direct reduction and smelting separation process		
		Mass/(kg/100 kg copper slag)	Energy/(kJ/100 kg copper slag)	Cost/(\$/100 kg copper slag)
Energy consumption: 0.08415 \$/kgce	Standard coal consumption of pellets preparation	0.26	7,630	-0.044
	Standard coal consumption of direct reduction	14.56	4,25,910	-2.445
	Standard coal consumption of smelting separation	7.96	2,32,940	-1.340
Resource consumption	Copper slag (high temperature)	100	1,21,000	0
	Coal	16.72	2,65,580	-2.614
	Limestone	29.85	—	-1.680
Emissions	Ferroalloy	70.76	—	33.179
	Slag (cooled)	75.81	8339.1	0
Total income				25.056

stage of reduction, and the concentration of S decreases at the later reduction stage. Another typical circle matrix region, such as 3#, is shown in **Figure 8B**. Atom percentages of Fe is 44.22%. The results further confirmed the migration order of Fe and O and confirmed the regional variation relationship of the matrix. It should be noted that the proportions of Cu and S atoms were significantly higher than elsewhere in 1#, 2#, and 3#. This indicates that during the reduction process, Cu and S are in

the CuS phase, and part of the CuS will migrate to the produced gas.

3.4 Element Migration Mechanism of Smelting Copper Slag

The element migration behavior during the separation process is accompanied by a partial reduction reaction. During melting

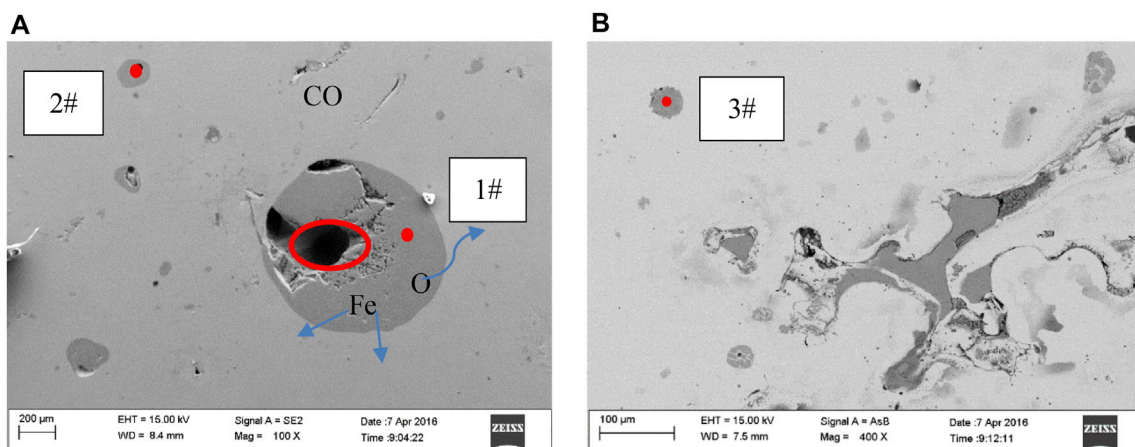


FIGURE 8 | SEM photo of iron ingot and location of analysis points (A) 1# and 2#; (B) 3#.

TABLE 2 | Element composition of point 1#–3#.

Element	1# Atomic%	2# Atomic%	3# Atomic%
O	42.06	40.50	51.76
Al	4.62	2.81	1.87
Si	1.27	1.29	1.45
S	1.22	0.86	0.7
Fe	50.83	54.54	44.22
Total	100	100	100

separation, the liquid is divided into three layers: a reduction slag layer, a reactive boundary layer, and an iron ingot layer. The element migration process and mechanism follow the rules described below. A diagram of the element migration mechanism of smelting copper slag in a reducing atmosphere is shown in **Figure 9**.

Because melting separation is carried out in a graphite crucible, C powder participates in a secondary reduction reaction during the separation process. C reacts with reducible “O” atoms, which exist in $2\text{FeO}\cdot\text{SiO}_2$, Fe_3O_4 , CuO forms, and CO is generated and overflows the liquid layer.

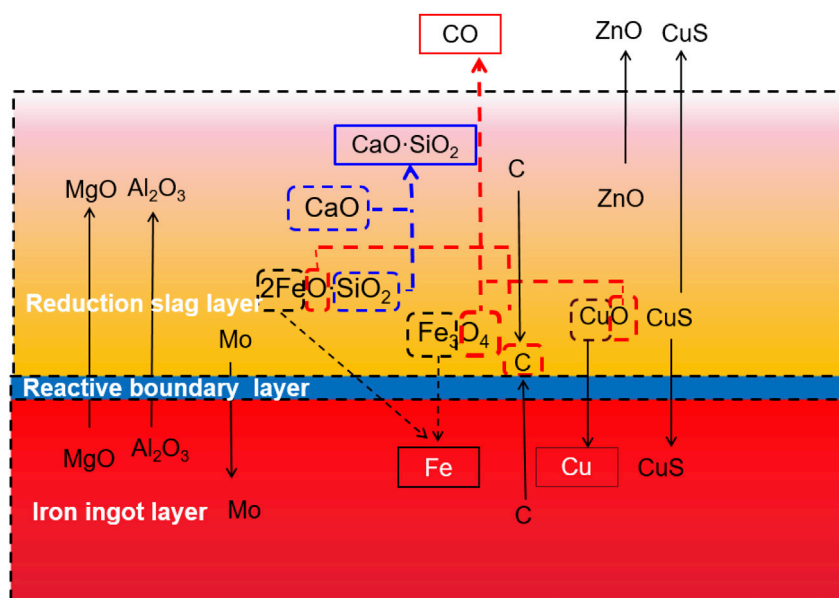
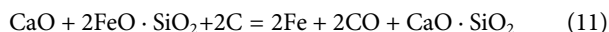


FIGURE 9 | Diagram of element migration mechanism of smelting copper slag in reducing atmosphere.

According to the analysis of the chemical composition and phase in the slag, it can be found that the Fe atom in the copper slag mainly exists in the $2\text{FeO}\cdot\text{SiO}_2$ and Fe_3O_4 phases. After reduction by C or CO, metallic iron is produced and migrates downward to the iron ingot layer because of its higher density. The Cu in the melting liquid is in the form of CuO and CuS. Like Fe, CuO is reduced by C, and metallic copper is produced and migrates downward to the iron ingot layer because of its higher density. The reduction reaction is more likely to occur than the iron oxide reduction reaction.

S exists mainly in the form of CuS. Based on the chemical composition analysis, the weight percentages of S in the copper slag, reduction slag, and iron ingot were 0.84, 1.20, and 0.051%, respectively. This indicates that the migration of S in the liquid gradually moves from diffusion to the upper reduction slag layer. Through the chemical composition analysis of the upper layer reduction slag and the phase analysis of the products in the flue gas, it was found that there was a large amount of ZnO and CuS dust in the smoke. Thus, much of the ZnO and CuS spilled from the liquid into the smoke.

As for Si, it exists mainly in the form of $2\text{FeO}\cdot\text{SiO}_2$. When CaO is in contact with $2\text{FeO}\cdot\text{SiO}_2$, desilication and slagging reactions occurred, as shown in Eq. 11. After the reaction, $\text{CaO}\cdot\text{SiO}_2$ is generated and ascends to the upper reduction slag layer because of its lower density.



4 CONCLUSION

Pellet direct reduction and metal separation is regarded as an efficient way to dispose copper slag. The element distribution and migration step during the copper slag reduction and smelting separation processes are obtained in this paper.

- 1) During melting separation, the copper slag liquid is divided into three layers. The residual carbon oozed at the interface between the iron ingot later and the reducing slag layer.

REFERENCES

- Bal, M., and Meikap, B. C. (2017). Prediction of Hydrodynamic Characteristics of a Venturi Scrubber by Using CFD Simulation. *South Afr. J. Chem. Eng.* 24, 222–231. doi:10.1016/j.sajce.2017.10.006
- Bal, M., Siddiqi, H., Mukherjee, S., and Meikap, B. C. (2019). Design of Self Priming Venturi Scrubber for the Simultaneous Abatement of HCl Gas and Particulate Matter from the Flue Gas. *Chem. Eng. Res. Des.* 150, 311–319. doi:10.1016/j.cherd.2019.08.005
- Cheng, C., Xue, Q., Wang, G., Zhang, Y., and Wang, J. (2015). Phosphorus Migration during Direct Reduction of Coal Composite High-Phosphorus Iron Ore Pellets. *Metall. Mater. Trans. B* 47 (1), 154–163. doi:10.1007/s11663-015-0479-7
- Deegan, M. M., and Peters, J. C. (2017). CO Reduction to $\text{CH}_3\text{OSiMe}_3$: Electrophile-Promoted Hydride Migration at a Single Fe Site. *J. Am. Chem. Soc.* 139 (7), 2561–2564. doi:10.1021/jacs.6b12444

- 2) Based on the SEM-EDS analysis, Fe and O mainly existed in the matrix and in the form of FeO. The small holes in the matrix were caused by the release of O atoms. The Fe atoms migrated continuously from the inside to the outside of the circle matrix. Cu and S were present in the CuS phase.
- 3) As typical elements, Fe, Cu, Zn, S, and Pb's distribution were analyzed based on element chemical analysis in three layers. As the main migration route, 86.71% of Fe element moved into iron ingot in the phase of MFe; 86.70% of Cu element moved into iron ingot; 94.43% of ZnO entered into the flue gas; 64.58% of S existed in reduction slag in the phase of CuS; 92.98% of Pb element went into iron ingot.
- 4) C reacted with reducible "O" atoms, which exist in $2\text{FeO}\cdot\text{SiO}_2$, Fe_3O_4 , and CuO. CO is generated and overflowed from the liquid layer. Metallic iron and copper were produced and migrated to the iron ingot layer. S migrates in the liquid gradually to the upper reduction slag layer. $\text{CaO}\cdot\text{SiO}_2$ was generated, which went up to the upper layer.

DATA AVAILABILITY STATEMENT

The original contributions presented in the study are included in the article/Supplementary Material, further inquiries can be directed to the corresponding author.

AUTHOR CONTRIBUTIONS

ZZ wrote the article and organized the experiments. SL and QY provided the experiment equipment. The other authors analyzed the datas.

FUNDING

This research has been supported by the Natural Science Foundation of Shandong Province (ZR2020QE150 and ZR2019MEE015), the key research and development plan of Shandong Province (2018GSF117042).

- Feng, Y., Yang, Q., Chen, Q., Kero, J., Andersson, A., Ahmed, H., et al. (2019). Characterization and Evaluation of the Pozzolanic Activity of Granulated Copper Slag Modified with CaO. *J. Clean. Prod.* 232, 1112–1120. doi:10.1016/j.jclepro.2019.06.062
- Fuentes, I., Ulloa, C., Jimenez, R., and Garcia, X. (2020). The Reduction of Fe-Bearing Copper Slag for its Use as a Catalyst in Carbon Oxide Hydrogenation to Methane. A Contribution to Sustainable Catalysis. *J. Hazard. Mater.* 387, 121693. doi:10.1016/j.jhazmat.2019.121693
- Gu, J. (2021). *Experiment and Energy Consumption Analysis of Direct Reduction & Melting Separation Process for Low-Grade Composite Iron Ore*. Beijing: Beijing University of Technology.
- Guo, Z., Zhu, D., Pan, J., Zhang, F., and Yang, C. (2017). Industrial Tests to Modify Molten Copper Slag for Improvement of Copper Recovery. *JOM* 70 (4), 533–538. doi:10.1007/s11837-017-2671-5
- Heo, J. H., Chung, Y., and Park, J. H. (2016). Recovery of Iron and Removal of Hazardous Elements from Waste Copper Slag via a Novel Aluminothermic

- Smelting Reduction (ASR) Process. *J. Clean. Prod.* 137, 777–787. doi:10.1016/j.jclepro.2016.07.154
- Kalusuraman, G., Thirumalai Kumaran, S., Aslan, M., Küçükömeroğlu, T., and Siva, I. (2019). Use of Waste Copper Slag Filled Jute Fiber Reinforced Composites for Effective Erosion Prevention. *Measurement* 148, 106950. doi:10.1016/j.measurement.2019.106950
- Lan, W., Wu, A., and Yu, P. (2020). Development of a New Controlled Low Strength Filling Material from the Activation of Copper Slag: Influencing Factors and Mechanism Analysis. *J. Clean. Prod.* 246, 119060. doi:10.1016/j.jclepro.2019.119060
- Li, B., Wang, X., Wang, H., Wei, Y., and Hu, J. (2017). Smelting Reduction and Kinetics Analysis of Magnetic Iron in Copper Slag Using Waste Cooking Oil. *Sci. Rep.* 7 (1), 2406. doi:10.1038/s41598-017-02696-y
- Liao, Y., Zhou, J., and Huang, F. (2016). Separating and Recycling of Fe, Cu, Zn from Dumped Copper Slag by Microwave Irradiation Assisted Carbothermic Method. *J. Residuals Sci. Technol.* 13 (S1), S155–S160. doi:10.12783/issn.1544-8053/13/S1/22
- Meng, D.-L., Chen, C.-H., Yi, J.-D., Wu, Q., Liang, J., Huang, Y.-B., et al. (2019). Migration-Prevention Strategy to Fabricate Single-Atom Fe Implanted N-Doped Porous Carbons for Efficient Oxygen Reduction. *Research* 2019, 1768595. doi:10.34133/2019/1768595
- Ming, J., Xin, S., Yongmei, H., Bo, L., Fangdong, Z., Tianguo, L., et al. (2020). Migration and Transformation Behavior of Heavy Metal Elements during the Calcination Process of Copper Slag. *Appl. Chem. Industry* 49 (7), 1703–1705. doi:10.16581/j.cnki.issn1671-3206.20200416.007
- Moskalyk, R. R., and Alfantazi, A. M. (2003). Review of Copper Pyrometallurgical Practice: Today and Tomorrow. *Minerals Eng.* 16 (10), 893–919. doi:10.1016/j.mineng.2003.08.002
- Piatak, N. M., Parsons, M. B., and Seal, R. R. (2015). Characteristics and Environmental Aspects of Slag: A Review. *Appl. Geochem.* 57, 236–266. doi:10.1016/j.apgeochem.2014.04.009
- Raj Mohan, B., and Meikap, B. C. (2009). Performance Characteristics of the Particulate Removal in a Novel Spray-Cum-Bubble Column Scrubber. *Chem. Eng. Res. Des.* 87, 109–118. doi:10.1016/j.cherd.2008.05.011
- Sarkar, S., Meikap, B. C., and Chatterjee, S. G. (2007). Modeling of Removal of Sulfur Dioxide from Flue Gases in a Horizontal Cocurrent Gas-Liquid Scrubber. *Chem. Eng. J.* 131, 263–271. doi:10.1016/j.cej.2006.12.013
- Shi, C., Meyer, C., and Behnood, A. (2008). Utilization of Copper Slag in Cement and concrete. *Resour. Conservation Recycling* 52 (10), 1115–1120. doi:10.1016/j.resconrec.2008.06.008
- Sun, Y.-S., Li, Y.-F., Han, Y.-X., and Li, Y.-J. (2019). Migration Behaviors and Kinetics of Phosphorus during Coal-Based Reduction of High-Phosphorus Oolitic Iron Ore. *Int. J. Miner. Metall. Mater.* 26 (8), 938–945. doi:10.1007/s12613-019-1810-0
- Sun, Y., Chen, M., Cui, Z., Contreras, L., and Zhao, B. (2020). Equilibria of Iron Silicate Slags for Continuous Converting Copper-Making Process Based on Phase Transformations. *Metall. Mater. Trans. B* 51 (5), 2039–2045. doi:10.1007/s11663-020-01901-0
- Wang, Q., Li, Z., Li, D., Tian, Q., Guo, X., Yuan, Z., et al. (2020). A Method of High-Quality Silica Preparation from Copper Smelting Slag. *JOM* 72 (7), 2676–2685. doi:10.1007/s11837-020-04196-3
- Zhang, L., Zhang, L., and Mingyu, W. (2005). Oxidization Mechanism in CaO-FeO_x-SiO₂ Slag with High Iron Content. *Trans. Nonferrous Met. Soc. China* 15 (4), 938–943.
- Zhang, J., Qi, Y.-h., Yan, D.-L., and Xu, H.-c. (2015). A New Technology for Copper Slag Reduction to Get Molten Iron and Copper Matte. *J. Iron Steel Res. Int.* 22 (5), 396–401. doi:10.1016/s1006-706x(15)30018-2
- Zhang, J., Luo, G., Chen, Y., Xin, W., and Zhu, J. (2020). Phosphorus Migration Behavior of Medium-Phosphorus Magnetite Ore during Carbothermic Reduction. *ISIJ Int.* 60 (3), 442–450. doi:10.2355/isijinternational.ISIJINT-2019-214
- Zhang, H., Bao, L., Chen, Y., Xuan, W., and Yuan, Y. (2021). Efficiency Improvements of the CO-H₂ Mixed Gas Utilization Related to the Molten Copper Slag Reducing Modification. *Process Saf. Environ. Prot.* 146, 292–299. doi:10.1016/j.psep.2020.09.011
- Zuo, Z., Yu, Q., Wei, M., Xie, H., Duan, W., Wang, K., et al. (2016). Thermogravimetric Study of the Reduction of Copper Slag by Biomass. *J. Therm. Anal. Calorim.* 126 (2), 481–491. doi:10.1007/s10973-016-5570-z
- Zuo, Z., Yu, Q., Liu, J., Qin, Q., Xie, H., Yang, F., et al. (2017). Effects of CaO on Reduction of Copper Slag by Biomass Based on Ion and Molecule Coexistence Theory and Thermogravimetric Experiments. *ISIJ Int.* 57 (2), 220–227. doi:10.2355/isijinternational.ISIJINT-2016-402
- Zuo, Z., Yu, Q., Xie, H., Wang, K., Liu, S., Yang, F., et al. (2018). Mechanical and Reduction Characteristics of Cold-Pressed Copper Slag Pellets Compositized within Biomass and lignite. *Renew. Energ.* 125, 206–224. doi:10.1016/j.renene.2018.02.057
- Zuo, Z., Yu, Q., Xie, H., Yang, F., Han, Z., and Qin, Q. (2020a). Direct Reduction of Copper Slag-Carbon Composite Pellets by Coal and Biochar. *Environ. Technol.* 41 (17), 2240–2252. doi:10.1080/09593330.2018.1561757
- Zuo, Z., Yu, Q., Luo, S., Zhang, J., and Zhou, E. (2020b). Effects of CaO on Two-step Reduction Characteristics of Copper Slag Using Biochar as Reducer: Thermodynamic and Kinetics. *Energy Fuels* 34 (1), 491–500. doi:10.1021/acs.energyfuels.9b03274
- Zuo, Z., Feng, Y., Li, X., Luo, S., Ma, J., Sun, H., et al. (2021a). Thermal-Chemical Conversion of Sewage Sludge Based on Waste Heat cascade Recovery of Copper Slag: Mass and Energy Analysis. *Energy* 235 (15), 121327. doi:10.1016/j.energy.2021.121327
- Zuo, Z., Luo, S., Liu, S., Zhang, J., Yu, Q., and Bi, X. (2021b). Thermokinetics of Mass-Loss Behavior on Direct Reduction of Copper Slag by Waste Plastic Char. *Chem. Eng. J.* 405, 126671. doi:10.1016/j.cej.2020.126671

Conflict of Interest: The authors declare that the research was conducted in the absence of any commercial or financial relationships that could be construed as a potential conflict of interest.

Publisher's Note: All claims expressed in this article are solely those of the authors and do not necessarily represent those of their affiliated organizations, or those of the publisher, the editors and the reviewers. Any product that may be evaluated in this article, or claim that may be made by its manufacturer, is not guaranteed or endorsed by the publisher.

Copyright © 2021 Zuo, Feng, Luo, Dong, Li, Ren, Yu and Guo. This is an open-access article distributed under the terms of the Creative Commons Attribution License (CC BY). The use, distribution or reproduction in other forums is permitted, provided the original author(s) and the copyright owner(s) are credited and that the original publication in this journal is cited, in accordance with accepted academic practice. No use, distribution or reproduction is permitted which does not comply with these terms.



Preparation of Adsorbents by Pyrolysis of Sludge Mixed With Steel Slag and Study on Adsorption of Chromium Ions in Water

Xiaowen Qi, Enze Zhou*, Xuefei Wu, Siyi Luo* and Yanggang Song

College of Environmental and Municipal Engineering, Qingdao University of Technology, Qingdao, China

OPEN ACCESS

Edited by:

Xuezhong He,
Guangdong Technion-Israel Institute
of Technology, China

Reviewed by:

Jiuyang Lin,
Fuzhou University, China
Sathish Sanjeevi,
National Energy Technology
Laboratory (DOE), United States

*Correspondence:

Enze Zhou
zhouenze@126.com
Siyi Luo
luosiyi666@126.com

Specialty section:

This article was submitted to
Advanced Clean Fuel Technologies,
a section of the journal
Frontiers in Energy Research

Received: 06 September 2021

Accepted: 06 December 2021

Published: 05 January 2022

Citation:

Qi X, Zhou E, Wu X, Luo S and Song Y
(2022) Preparation of Adsorbents by
Pyrolysis of Sludge Mixed With Steel
Slag and Study on Adsorption of
Chromium Ions in Water.
Front. Energy Res. 9:771603.
doi: 10.3389/fenrg.2021.771603

In this study, the dewatered sludge from the sewage plant and the open-hearth steel slag of the steel plant are used as raw materials. As two wastes, they were mixed and pyrolyzed to prepare a composite adsorbent. Further, the adsorption mechanism of the adsorbent to chromium ions in the sewage is explored. The pyrolysis reaction behavior of sludge mixed with steel slag was studied by the thermogravimetric analysis technology. SEM, BET, and XPS were used to analyze the specific surface area, pore size distribution, and pore structure characteristics of pyrolysis products, respectively. Moreover, a comprehensive analysis of the adsorbent was carried out for the adsorption mechanism of hexavalent chromium ions. The results show that the addition of steel slag promotes the pyrolysis of the sludge in each stage. When the content of steel slag is 80%, the increases of reaction rate are the most obvious with the largest increase of weight loss rate in each stage. The SEM results show that the enrichment of sludge on metal oxides is enhanced in the high-temperature range (600–700°C). Besides, when the content of steel slag is 40–60%, the mixture's growth rate of the specific surface area can reach 600% and the growth rate of total pore volume can reach 350% (the situations of sludge as the baseline). Regarding the measurement of Cr(VI), the adsorption rate of the steel-slag solution is 50.93% and that of the sludge solution is 69%. However, the adsorption rate can be increased to 95% when the steel slag and sludge were mixed as an adsorption solution. In conclusion, the adsorption mechanism of Cr(VI) by additives is controlled by both physical and chemical processes. The present study provides a theoretical basis and technical support for the scientific and reasonable utilization of sludge and steel slag.

Keywords: sewage sludge, steel slag, adsorbent, pyrolysis kinetics, Cr(VI) adsorption

INTRODUCTION

Sewage sludge is one of the main byproducts after sewage treatment. As a kind of high-wet-base biomass, it contains not only organic residues, inorganic particles, and colloids (Wei et al., 2011) but also a large amount of toxic and harmful substances such as pathogenic bacteria (Fernando and Fedorak, 2005), dioxins (Raheem et al., 2018), and heavy metal ions (Fang et al., 2016). If it is discharged without treatment, it is very easy to cause secondary pollution to groundwater and soil, endangering human health directly (Bondarczuk et al., 2015). Most of the domestic and foreign sludge treatment technologies and equipment are mainly aimed at the safe disposal of sludge

digestion. The disposal methods mainly include anaerobic digestion, sanitary landfill, incineration treatment, and water body disposal (Raheem et al., 2018; Stunda-Zujeva et al., 2018), which have not produced actual economic benefits and formed valuable commodities. Steel slag is the main byproduct of the iron and steel production process, which is composed of various oxides oxidized by impurities such as silicon, manganese, phosphorus, and sulfur in pig iron in the smelting process and salts generated by the reaction of these oxides and solvents (Piatak et al., 2015). At present, the utilization of steel slag is mainly consumed in the direction of building materials (Liu et al., 2020; Sridhar and Sastri, 2021), and the efficient development and utilization of steel slag resources has been the focus of attention of the metallurgical industries around the world for many years (Diao et al., 2016).

Due to the high content of carbon, hydrogen, nitrogen, phosphorus, and other resource elements, sludge has become a key resource, which can be used as a raw material. It is possibly a valuable strategy to convert it into biochar through the heat treatment technology (Bora et al., 2020). Pyrolysis, a typical heat treatment technology (Barry et al., 2019), which can reduce the volume of sludge, kill microorganisms, and parasite eggs and transform heavy metals from a weakly bound state to a stable state, ensures the security of applications (Jin et al., 2016). The bio-oil and pyrolysis gas produced by pyrolysis are potentially for reusing (Cao and Pawlowski, 2012). The biological carbon can be used as a fertilizer or made into an adsorbent, the whole process of which has higher resource utilization and better environmental protection.

In recent years, pyrolysis of sludge into an adsorbent has attracted the attention of many scholars. However, the porosity, specific surface area, and adsorption capacity of the adsorbents produced by pyrolysis of sewage sludge are far behind those of commercial activated carbon adsorbents. In order to improve the adsorption performance of sludge adsorbents, some scholars used other biomass for co-pyrolysis such as cotton stalks (Wang et al., 2019), rice husks (Yang et al., 2010), and bagasse (Lin et al., 2017). Some scholars have tried to add chemical agents for activation during the pyrolysis process. Li et al. used ZnCl_2 and KOH to activate the sludge to prepare desulfurizing adsorbents (Li et al., 2014); the capacity of sulfur is 7.7 mg/cm^3 , the maximum value of iodine is 409.95 mg/g , and the desulfurization activity is better than that of industrial activated carbon. The co-pyrolysis technology was applied to municipal sewage sludge and hazelnut shells with the alkaline activating agent K_2CO_3 by Zhao et al. (2018), and they found that after co-pyrolysis at 850°C , the specific surface area reached $1990.23 \text{ m}^2/\text{g}$ and the iodine adsorption number was 1068.22 mg/g . Luo et al. (2020) activated the sludge with KOH and H_2SO_4 and found that both KOH and H_2SO_4 can reduce the pyrolysis activation energy and promote the release of volatiles. However, from the perspective of literature review, there is no mention of adding steel slag in the pyrolysis process of sludge.

The metal oxides such as CaO , Al_2O_3 , Fe_2O_3 , and MgO and a large amount of Fe contained in the steel slag all have certain catalytic activity. During the pyrolysis of pine wood chips, Lee added steel slag as an adsorbent, which significantly accelerated

the reaction rate and promoted the generation of CH_4 and H_2 (Lee et al., 2020). About 40% of the open-hearth steel slag is CaO . Zuo found that in the study of the reduction characteristics of copper slag using biochar as a reducing agent, CaO can improve the reduction reaction of $2\text{FeO}\cdot\text{SiO}_2$ in copper slag and significantly reduce Gibbs free energy (Zuo et al., 2019). As a catalyst, the performance of steel slag is acceptable to improve the adsorption. Meanwhile, the application of steel slag is an environmental-friendly method for addressing the waste pollution.

In this study, steel slag mixed with sewage sludge was used for pyrolysis preparation of the adsorbent to adsorb Cr(VI) , which is extremely harmful to the human body in sewage. The steel slag helps the sludge base to produce a larger adsorption surface area. At the same time, certain components contained in the steel slag undergo oxidation–reduction reactions with Cr(VI) , which helps the adsorption of Cr(VI) . The pyrolysis behavior of the sludge mixed with steel slag was investigated by the thermogravimetric analysis technology, combined with the e-sports scanning technology, the specific surface area analysis technology, X-ray photoelectron spectroscopy (XPS), and other means to analyze the adsorption mechanism of sludge-based adsorbents. The concept of “treating waste with waste” has been a successful realization and has provided a feasible path for the development and utilization of sludge and steel slag.

MATERIALS AND METHODS

Materials Preparation

In this study, sewage sludge with a moisture content of 78% was obtained from a sewage treatment plant in Qingdao, China. The sewage sludge was dried at 105°C for 24 h and then ground into a powder ($<80 \mu\text{m}$). The industrial analysis and elemental analysis of the sample are shown in **Table 1**. The steel slag was taken from a steel plant in Qingdao, China, and ground into a powder ($<80 \mu\text{m}$). The composition of steel slag measured by X-ray fluorescence spectroscopy (XRF) is shown in **Table 2**. The main chemicals used in the research are potassium dichromate ($\text{K}_2\text{Cr}_2\text{O}_7$, AR), diphenylcarbazide ($\text{C}_{13}\text{H}_{14}\text{N}_4\text{O}$, AR), sulfuric acid (H_2SO_4 , AR), and phosphoric acid (H_3PO_4 , AR), which are produced by Tianjin Guangcheng Chemical Reagent Co., Ltd.

GA Experiments and Kinetic Analysis

TG Experiment

We used a thermogravimetric analyzer (METTLER TGA/DSC1) to pyrolyze sludge and steel slag. The accuracy of the thermometer is $\pm 0.2 \text{ K}$, and the sensitivity of the microbalance is less than $\pm 0.1 \mu\text{g}$. The pyrolysis process is carried out under a nitrogen atmosphere with a purity of 99% and a flow rate of 20 ml/min . Each sample is kept at $10 \pm 0.1 \text{ mg}$ to alleviate heat- and mass-transfer limitations. The initial temperature is room temperature, the end temperature is 900°C , and the heating rate is set to 15°C/min . Pyrolysis was carried out with pure sludge (DS) and sludge steel slag with ratios of 1:4 (SS 20%), 2:3 (SS 40%), 3:2 (SS 60%), and 4:1 (SS 80%).

TABLE 1 | Characteristics of bagasse and sludge on a dry basis.

Samples	Ultimate analysis (wt%) ^a			Proximate analysis (wt%)				
	Volatile	Ash	Fixed carbon	C	H	N	S	O
Sewage sludge	52.03	39.94	8.03	25.44	4.29	4.37	1.30	26.47

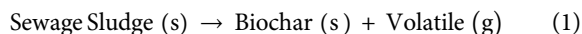
^aAccording to the method of coal industry analysis in China (Chinese standard methods, GB/T 212-2008).

TABLE 2 | Chemical composition of steel slag.

Samples	Chemical composition							
	CaO	SiO ₂	Fe ₂ O ₃	Al ₂ O ₃	MgO	MnO	SO ₃	Others
Steel slag	38.59	34.50	12.18	2.45	7.03	2.97	1.45	0.83

The kinetic parameters obtained from thermogravimetric analysis are often used to evaluate the thermal behavior of materials under isothermal or non-isothermal conditions. Under the non-isothermal boundary conditions, the degradation of the sludge may also be understood as comprising a heterogeneous solid-phase reaction with a complex reaction mechanism. In order to understand the mechanism of kinetics, the kinetic equation of the solid reaction was first established, and then, the effective kinetic parameters were solved by the nonlinear optimization method.

The solid-state degradation of sewage sludge as a single reaction can be represented as (Naqvi et al., 2018)



The rate equation of the solid reaction can be described by the following formula:

$$\frac{d\alpha}{dt} = kf(\alpha) \quad (2)$$

where k is the rate constant, $f(\alpha)$ is the kinetic model, t is the reaction time, and α is the extent of conversion. Also, α is defined in terms of mass loss as

$$\alpha = \frac{w_0 - w}{w_0 - w_\infty} \quad (3)$$

where w_0 is the initial mass of the precursor, w is the instantaneous mass, and w_∞ is the remaining mass of the material.

$f(\alpha)$ is a function related only to the reaction mechanism. If the effect of temperature on the activation energy is ignored, then $f(\alpha) = (1 - \alpha)^n$, where n is the reaction order of the reaction. From the Arrhenius equation that expresses the relationship between chemical reaction rate and temperature, the formula can be obtained

$$k = Ae^{-\frac{E}{RT}} \quad (4)$$

where A is the frequency factor, E is the activation energy, R is the ideal gas constant, and T is the absolute temperature.

Bringing Eq. 4 to Eq. 2, Eq. 2 becomes

$$\frac{d\alpha}{dt} = Ae^{-\frac{E}{RT}}(1 - \alpha)^n \quad (5)$$

According to the Coats-Redfern equation (Zaker et al., 2021), the heating rate $\beta = \frac{dT}{dt}$ is a fixed value, which can be put into Eq. 4 and sorted out to get

$$\int_0^\alpha \frac{d\alpha}{f(\alpha)} = \frac{A}{\beta} \int_{T_0}^T e^{-\frac{E}{RT}} dT \quad (6)$$

According to the method of Friedman (Friedman, 1964), the logarithm form is adopted for Eq. 6

$$\ln \left[\frac{1 - (1 - \alpha)^{1-n}}{(1 - n)T^2} \right] = \ln \left[\left(\frac{AR}{\beta E} \right) \left(1 - \frac{2RT}{E} \right) \right] - \frac{E}{RT} \quad (7)$$

For the general reaction temperature range and most E values, $\frac{E}{RT} > 1$, therefore, $1 - \frac{2RT}{E} \approx 1$, then

$$n \neq 1 \quad \ln \left(\frac{1 - (1 - \alpha)^{1-n}}{(1 - n)T^2} \right) = \ln \left(\frac{AR}{\beta E} \right) - \frac{E}{RT} \quad (8)$$

$$n = 1 \quad \ln \left(-\frac{\ln(1 - \alpha)}{T^2} \right) = \ln \left(\frac{AR}{\beta E} \right) - \frac{E}{RT} \quad (9)$$

Equations 8, 9 can be written as a straight line ($y = ax + b$). $1/T$ equals X , $\ln \left(\frac{1 - (1 - \alpha)^{1-n}}{(1 - n)T^2} \right)$ and $\ln \left(-\frac{\ln(1 - \alpha)}{T^2} \right)$ are considered as y . Thus, the activation energy E can be obtained from the slope of the straight line, and the pre-exponential factor a can be obtained from its intercept. In this paper, the step size of n is 0.5, and the reaction order n is determined in the interval of 0–3 according to the principle of large absolute values of the correlation coefficient.

Pyrolysis Experiment

The pyrolysis experiment was carried out in a tube furnace (skgl-1200-II). The length of the quartz tube in the tube furnace was 1500 mm, and the inner diameter was 73 mm. About 5.000 ± 0.005 g of the raw material loaded into the quartz vessel is placed in the quartz tube. In order to form an oxygen-free atmosphere before pyrolysis, 0.5 L/min N_2 was added into the system as a carrier gas for 10 min. N_2 was added in the whole pyrolysis process to maintain an inert atmosphere. Under the heating rate of 15 C/min, the initial temperature was room temperature, the final temperature was 700°C, and the temperature was kept for 30 min. DS, SS 20%, SS 40%, SS 60, and SS 80% were made into adsorbents for standby. Then, the raw materials mixed with sludge and steel slag in the same ratio were prepared into adsorbents under the same conditions, but the final temperatures were 300°C, 400°C, 500°C, 600°C, and 700°C, respectively.

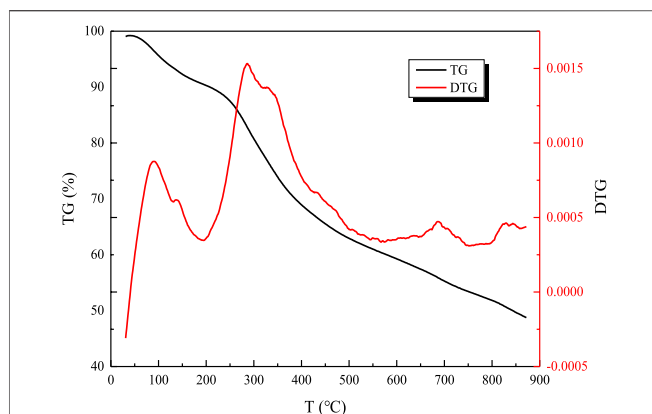


FIGURE 1 | TG-DTG curve of sewage sludge.

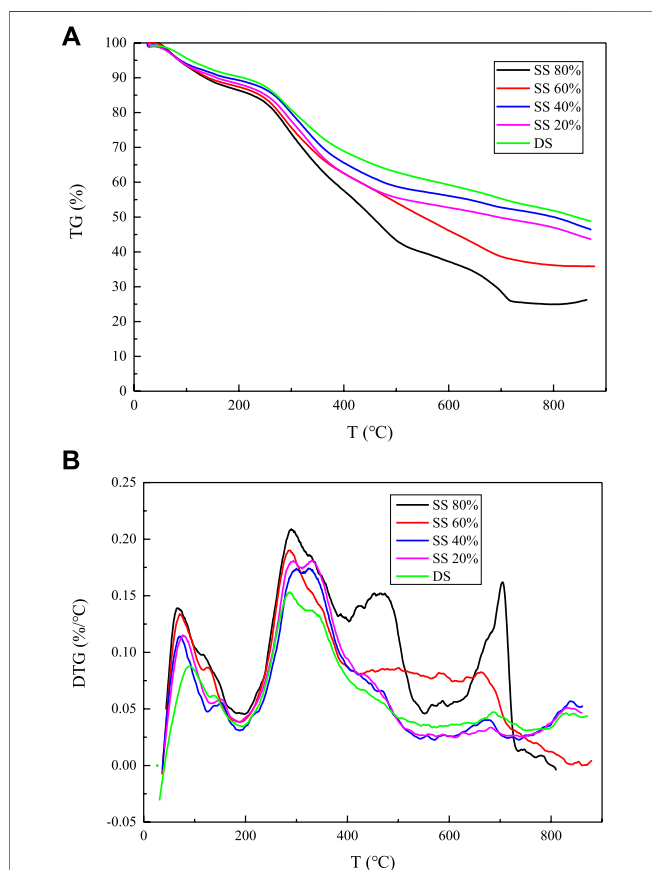


FIGURE 2 | Thermogravimetric analysis of sludge and steel slag with different mixing ratios: (A) TG curve and (B) DTG curve.

Adsorption Experiment

0.2829 g of potassium dichromate ($K_2Cr_2O_7$; AR) was dissolved in a beaker with distilled water and poured into a 1L volumetric flask to make $0.1 \text{ mg} \cdot \text{ml}^{-1}$ Cr(VI) standard solution. We used a dilute ($K_2Cr_2O_7$; AR) standard solution with distilled water to prepare 5 mg/L simulated wastewater. All adsorption experiments were

carried out in a 250 ml conical flask at room temperature. The conical flask contained 100 ml of simulated wastewater. 500 mg of adsorbents of different components was added. After labeling, they were placed at a 160 r/min rotating speed. On the centrifuge, the centrifugation time is 12 h. The sample was filtered through a filter paper and a funnel, and the absorbance was measured by diphenylcarbazide spectrophotometry, and then, the concentration of chromium ions in the filtrate was analyzed. All adsorption experiments are repeated. Also, the adsorption rate of chromium ions Φ (%; removal efficiency) is as follows:

$$\Phi = \frac{C_0 - C}{C_0} \times 100\% \quad (10)$$

where Φ is the removal efficiency, c_0 is the initial concentration of Cr(VI) in the solution ($\text{mg} \cdot \text{L}^{-1}$), and C is the concentration of Cr(VI) at time t of adsorption ($\text{mg} \cdot \text{L}^{-1}$).

Characteristic Description

The specific surface areas of sludge with different blending ratios and slag were made by N_2 adsorption (at 77K) were determined using a surface analyzer (Micromeritics, ASAP 2460). Before the desorption procedure, the adsorbent was degassed at 320°C for 4 h under vacuum. The SEM images of the samples with different pyrolysis temperatures were obtained using a German Merlin high-resolution field emission scanning electron microscope. X-ray photoelectron spectroscopy (XPS; 250XI) was used to analyze the surface valence state and structure of the SS60% adsorbent before and after adsorption and explore its adsorption mechanism for Cr(VI).

RESULTS AND DISCUSSION

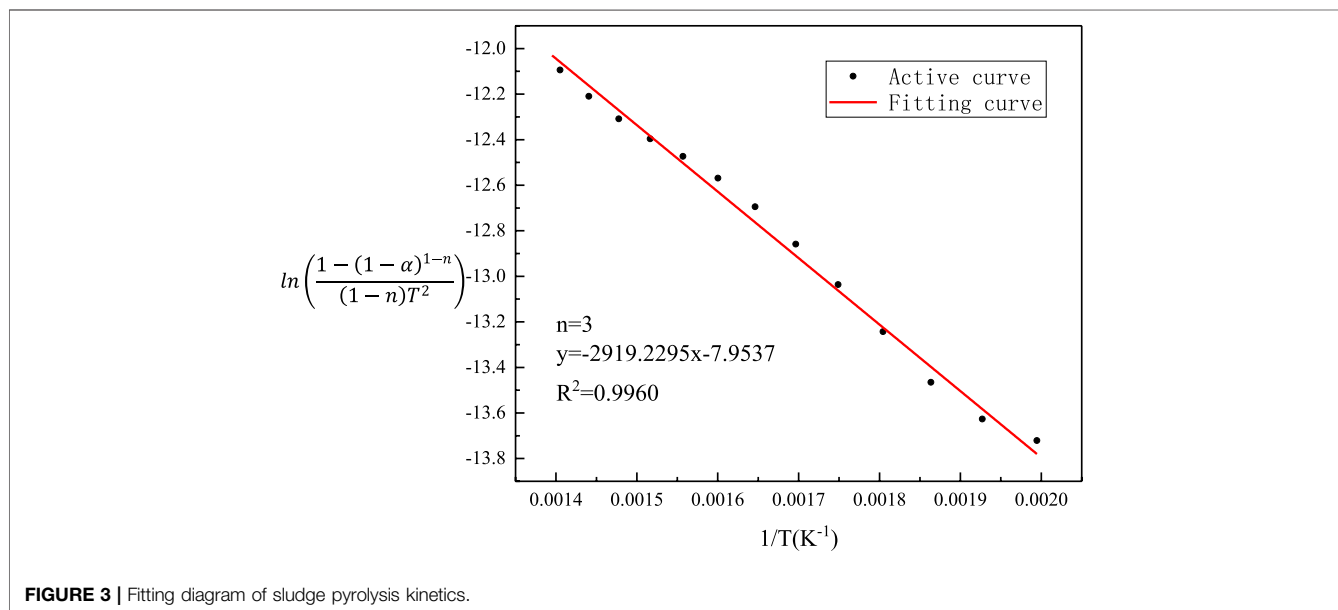
Thermogravimetric Analysis

As can be seen from Figure 1, there are three weight loss peaks during the pyrolysis reaction of simple sludge components, that is, pyrolysis is divided into three parts. The first stage of the weight loss peak starts at about 60°C , and the weight loss process is short and the rate is low until about 200°C , which is a process of water evaporation and separation in the sludge. In the second stage, the weightlessness begins at 200°C , and the weight loss process is longer and the rate is faster until about 550°C . This is caused by the transformation reaction of aliphatic compounds, protein, and carbohydrate compounds in the sludge, the breaking of peptide bonds and branched chains, and the release of a large number of volatiles (Magdziarz and Wilk, 2013). The third stage of weightlessness is between 550°C and 750°C , which is caused by the decomposition of residual organic salts in the sludge components.

It can be seen from the TG curve in Figure 2 that the curve of pure sludge is the flattest, and after mixing with steel slag, as the mixing ratio increases, the curve gradually becomes steeper and the end point of the curve becomes lower and lower. It shows that the degree of pyrolysis of sludge has also increased, and the maximum increase is about 20%. From the DTG curve, we compared with pure sludge in the first stage, second stage, and third stage of the pyrolysis reaction. In the first stage, the peaks

TABLE 3 | Calculation results of the sludge cracking mechanism model.

Order of reaction	Slope	Intercept	Correlation coefficient	Frequency factor	Activation energy
n	a	b	R ²	A	E/(KJ/mol)
0.5	-1053.8805	-11.8384	0.8923	0.1142	8.7619
1	-1366.1729	-11.1790	0.9381	0.2864	11.3583
1.5	-1709.4628	-10.4610	0.9639	0.7349	14.2124
2	-2083.4348	-9.6822	0.9787	1.9514	17.3216
2.5	-2487.1711	-8.8471	0.9873	5.3696	20.6783
3	-2919.2295	-7.9537	0.9960	15.3972	24.2704

**FIGURE 3** | Fitting diagram of sludge pyrolysis kinetics.**TABLE 4** | Calculation results of different ratios of sludge and steel slag cracking mechanism models.

Steel slag content	Slope	Intercept	Correlation coefficient	Frequency factor	Activation energy
%	a	b	R ²	A	E/(KJ/mol)
20	-3159.2788	-7.5204	0.9944	25.7009	26.2662
40	-3345.5029	-7.2140	0.9933	36.9701	27.8145
60	-3534.1110	-6.8288	0.9960	57.4046	29.3825
80	-3701.8138	-6.5491	0.9971	79.5302	30.7768

are all increased, the peaks are sharper, and the peak area becomes larger. The first stage does not increase in proportion, and the increase is about 26% of the pure sludge. This indicates that the internal sludge is contained in the sludge after adding steel slag. The rate of water release has increased and is more obvious. From the point of view of weight loss rate, the mixing of steel slag increases the evaporation of internal water. When the content of steel slag is 80%, the change is the largest, increasing from 9.5 to 16.1%; In the second stage of the pyrolysis process, the maximum weight loss rate is increased, reaching the maximum when the steel slag content is 80%, and the rate is increased by about one-

third. When the content is 60%, the rate is slightly lower, but the weight loss rate reaches the maximum value, which is increased from 29%. As much as 41%, the maximum rate and weight loss rate in the third stage change positively with the content of steel slag. When the content of steel slag is 80%, both reach the maximum, increasing by 245 and 80%, respectively.

In fact, the above-mentioned changes are caused because the steel slag contains a large amount of metal oxides such as CaO and Fe₂O₃. CaO itself can react with free water molecules and release heat, and it has a very high melting point. In the low-temperature stage of sludge pyrolysis, the H₂O released as the temperature rises

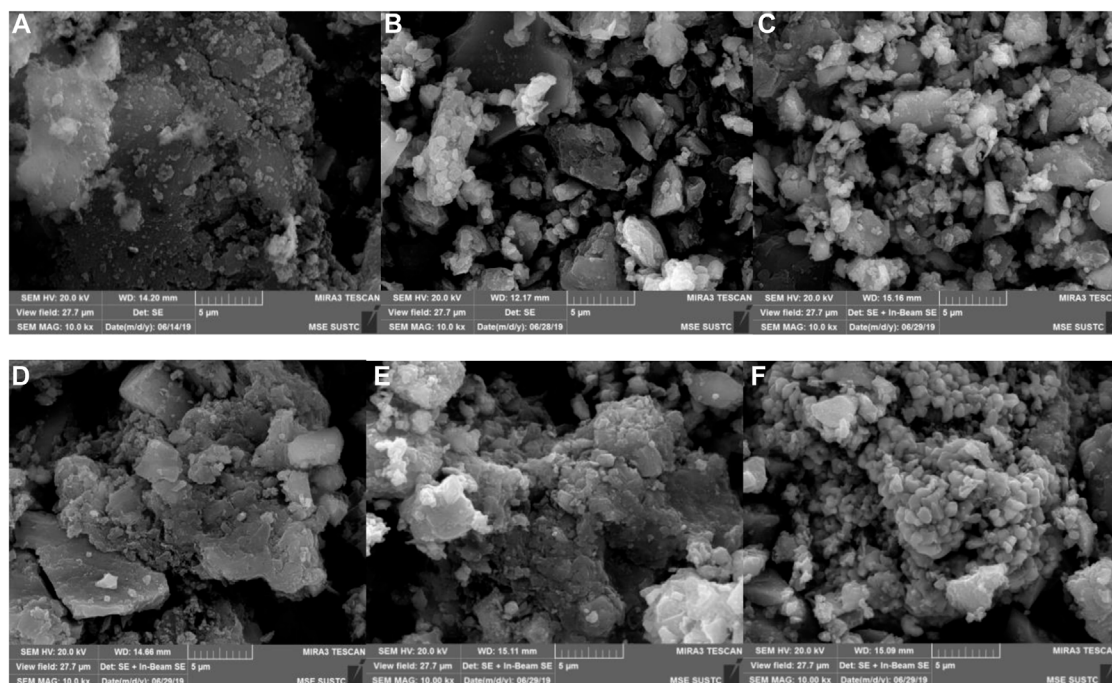


FIGURE 4 | SEM images of various stages of pyrolysis of sludge and steel slag: (A) DS, (B) 300°C SS, (C) 400°C SS, (D) 500°C SS, (E) 600°C SS, and (F) 700°C SS.

is released from the sludge and is converted from the bound state. It is a free state, and then, after contact with CaO, a chemical reaction occurs and energy is released, and it also provides a part of energy for the pyrolysis of sludge so that the reaction rate and weight loss rate of the first stage are increased. At the same time, when the pyrolysis temperature reaches 650 ~ 750°C, a large amount of CO₂ is generated and precipitated. This part of the gas is absorbed by CaO, thereby increasing the weight loss rate and the reaction rate. CaO may react as follows during pyrolysis: (CaO + H₂O → Ca(OH)₂; Ca(OH)₂ + CO₂ → CaCO₃ + H₂O). Fe₂O₃ is oxidizing and may react with H₂ and CO from sludge pyrolysis under high-temperature conditions (Fe₂O₃ + 3H₂ → 2Fe + 3H₂O; Fe₂O₃ + 3CO → 2Fe + 3CO₂), and part of H₂ and CO were absorbed, which accelerated the reaction rate and weight loss rate to a certain extent.

Pyrolysis Kinetic Analysis

It can be seen from Table 3 that when $n = 3$, the fitted linear correlation coefficient $R^2 = 0.9960$ is the highest, and the frequency factor $A = 15.3972$ is the largest. Therefore, the kinetic model function of sludge pyrolysis is $f(\alpha) = (1 - \alpha)^3$. The regression equation is $y = 2919.2295x - 7.9537$. Also, the fitted image is shown in Figure 3.

Using the same mathematical model and calculation method, $n = 3$, the kinetic calculation of the pyrolysis process of the sludge steel slag mixture mixed with different proportions of steel slag is carried out. The obtained kinetic parameters and activation energy are shown in Table 4.

It can be seen from Table 4 that the activation energy of the main reaction stage increases after mixing steel slag, and the

activation energy increases from 24.2704 kJ/mol to 30.7768 kJ/mol with the increase of steel slag content. The maximum increase is up to 26.8 %, and this increase gradually increases with the change of steel slag content. It can be seen from Table 2 that CaO accounts for 38.59% of the total composition of steel slag and SiO accounts for 34.50% of the total composition of steel slag. According to the conclusion of thermogravimetric analysis, the existence of CaO can promote the decomposition and release of organic matter such as CH₄ in the main stage of pyrolysis. The role of CaO in the activation energy is reduced, and there are metal oxides in steel slag. However, a high content of SiO₂ does not have catalytic performance, and to a certain extent, it hinders the heat and mass transfer inside the sludge particles, hinders the pyrolysis reaction, and increases the activation energy. It can be deduced that SiO₂ will play a certain inhibitory effect in the main stage of sludge pyrolysis. This effect increases gradually with the increase of SiO₂ content, and the final activation energy increases or decreases are the results of multiple factors. Here, the incorporation of steel slag increases the activation energy of sludge and inhibits pyrolysis.

Micromorphology and Specific Surface Areas of the Adsorbent

It can be seen from Figure 4 from the surface morphology diagrams of each stage of pyrolysis that the surface of the sludge itself is relatively dense, and the particles are very rare. After being mixed with steel slag and pyrolyzed together, as the pyrolysis temperature increased, there was a very obvious change that a lot of particles appeared on the surface of the residue, and

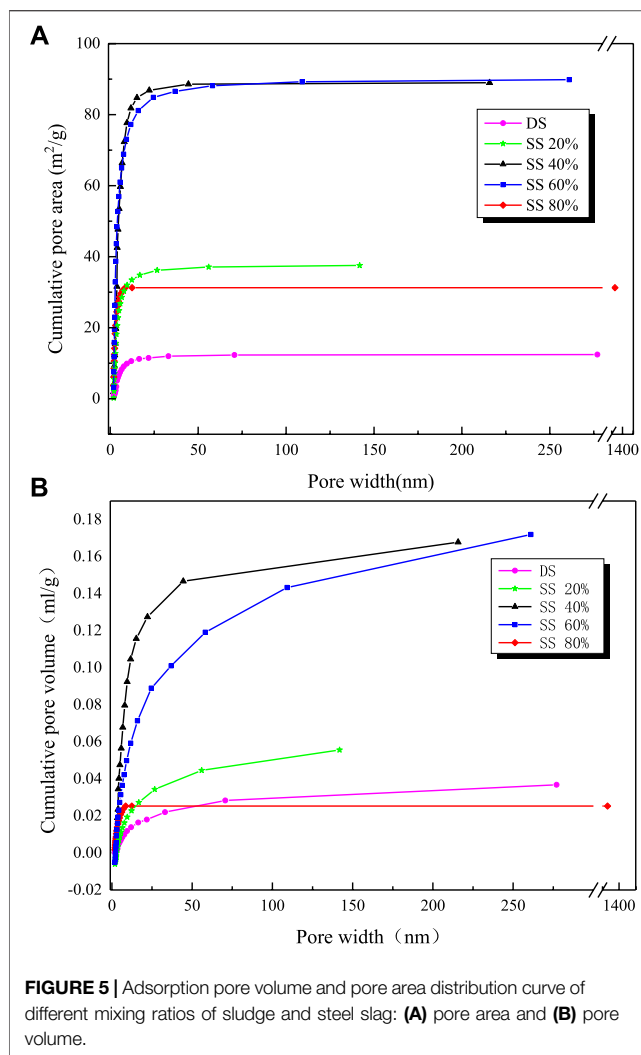


FIGURE 5 | Adsorption pore volume and pore area distribution curve of different mixing ratios of sludge and steel slag: **(A)** pore area and **(B)** pore volume.

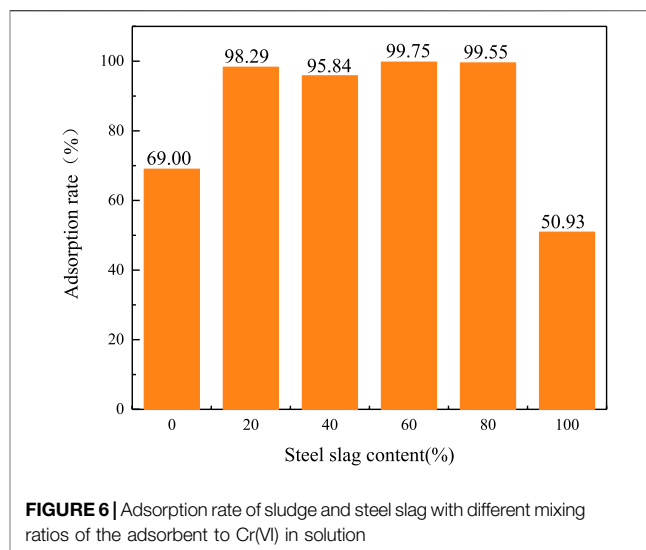


FIGURE 6 | Adsorption rate of sludge and steel slag with different mixing ratios of the adsorbent to Cr(VI) in solution

of metal oxide groups and forms clusters with certain morphological characteristics.

Specific Surface Area and Pore Structure of the Adsorbent

It can be seen in **Figure 5** that the curve grows most rapidly within 0–50 nm after pyrolysis of pure sludge, the curve basically tends to be flat after 75 nm, and most of the points are concentrated between 0 ~ 75 nm, which shows that most of the average pore size of the pyrolysis residue is below 75 nm and the maximum pore size is about 275 nm. After adding steel slag, the slope of the adsorption pore volume curve increases compared with pure sludge, and the curve trend is closer to the Y-axis. It can be judged that the pore size of the mixed residue is

TABLE 5 | Pore size distribution parameters of adsorbents with different contents of steel slag.

Steel slag content	0	20%	40%	60%	80%
BET: m²/g	12.4400	36.3528	88.7830	87.6663	31.8990
Total pore volume: m³/g	0.0368	0.0563	0.1643	0.1748	0.02764
Average hole diameter: nm	11.8300	7.500	7.6872	8.7100	4.1500
Most probable aperture: nm	3.8800	3.8100	4.1300	4.0000	1.8900
D10 pore diameter: nm	3.6900	2.9400	3.4982	3.7200	1.8200
D90 pore diameter: nm	99.2700	34.1100	24.0678	25.100	23.7300

the dense surface became fluffy. After 500°C, the pores became larger and larger, which can be explained by that the pyrolysis reaction of the sludge progresses, and a large amount of volatiles are released after the temperature rises. The dense surface collapses and a large number of ravines are produced, which provides considerable adsorption possibilities for the adsorbent. However, the steel slag reacts with the sludge, and the pyrolysis temperature of 600–700°C strengthens the enrichment of heavy metals in the sludge. The concentration causes the precipitation

relatively reduced. It can be seen from **Table 5** that the total pore volume of the mixture is larger than that of pure sludge, and it increases first and then decreases with the increase of steel slag content. When the steel slag content is 40 and 60 %, the maximum is about 5 times of pure sludge, and the average pore diameter decreases. When the steel slag content was 80 %, it reached the minimum value of 4.1500 nm, which reduced about 60 % of the pure sludge, while the average pore diameter of the other three groups had little difference. The most probable

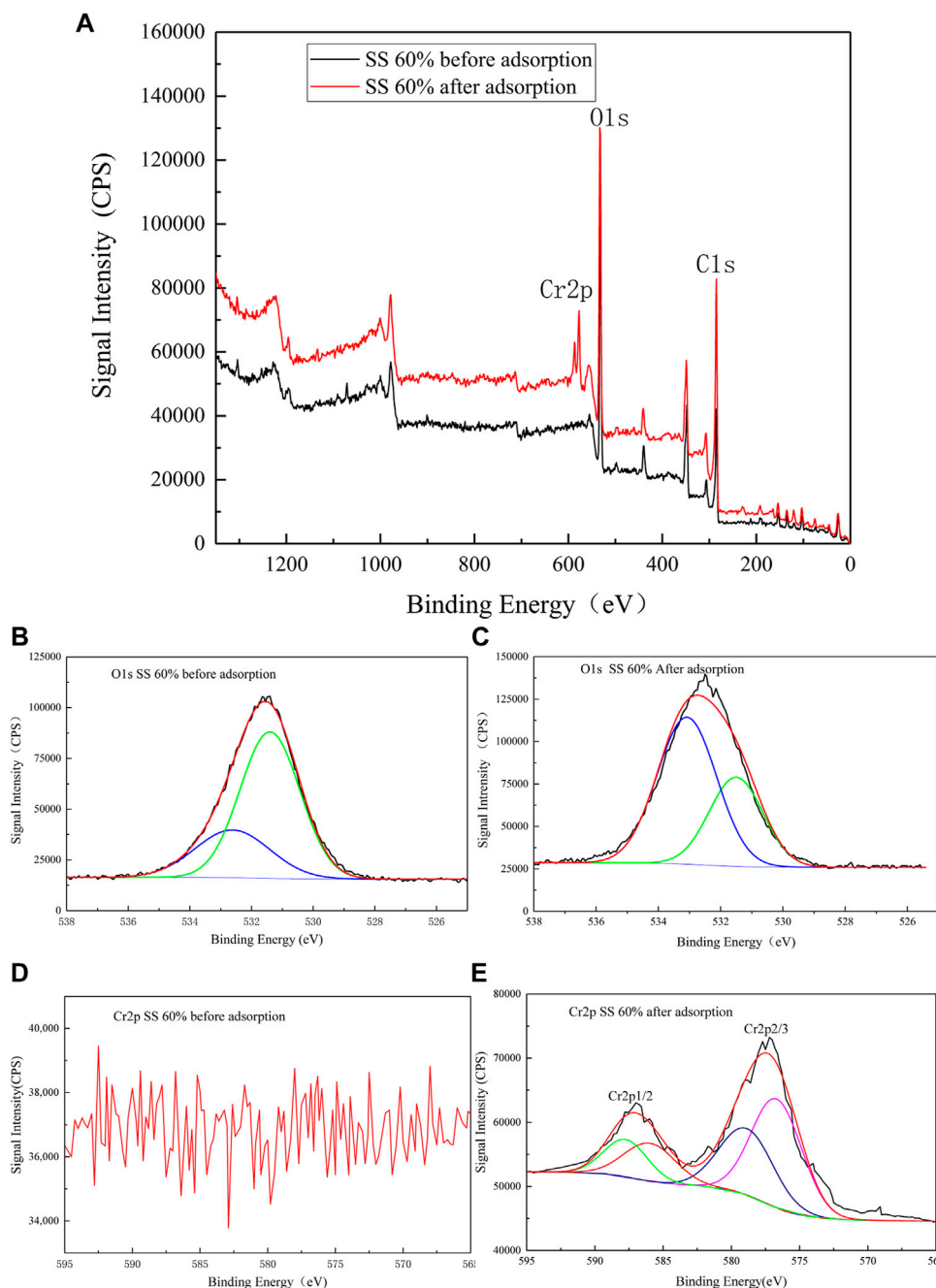


FIGURE 7 | XPS spectra (A) SS 60% before and after adsorption of Cr(VI). (B) O1s SS 60% before adsorption. (C) O1s SS 60% after adsorption. (D) Cr2p SS 60% before adsorption. (E) Cr2p SS 60% after adsorption.

diameter is basically unchanged. From the point of view of the diameter of the D90 hole, the change after mixing is large. The diameter of the D90 hole of the pure sludge is 99.2700 nm. As the amount of steel slag mixed increases, the diameter of the D90 hole decreases to between 23 ~ 34 nm. The rate is 66 ~ 77%. The change of the specific surface area is also very obvious, and its change trend is consistent with the total pore volume. It first

increases and then decreases. When the steel slag content is 80%, the minimum is 31.8990 m²/g, and the growth rate is 158%. At 40%, the maximum is 88.7830 m²/g, and the growth rate is 616%.

Combined with the analysis results of the pictures obtained by scanning electron microscopy, after the sludge and steel slag are mixed, the steel slag powder is dispersed and attached to the surface of the sludge, causing a lot of irregular protrusions on the

surface of the mixture, and then undergoes high-temperature pyrolysis. Analyzing the moisture and volatilization contained in the sludge, the inside and surface of the sludge collapsed, and many macroporous structures appeared. At the same time, the enhancement of the enrichment of metal oxides by the sludge at high temperature makes this part of the material fill the sludge itself and the newly formed macroporous structure and disperse it into a number of relatively small mesopores. These changes also made the originally dense surface and became fluffy and porous, thus increasing the specific surface area of the mixture. However, as the steel slag content becomes larger and larger and the proportion reaches 80%, a large amount of steel slag filling makes the surface ravines of the sludge and the macroporous structure produced by pyrolysis gradually fill up and disappear, and the increase in the specific surface area of the product gradually decreases. It is even smaller than when it is not added. Therefore, in terms of specific surface area, it is not that the larger the amount of steel slag blended, the better the adsorption performance of the obtained adsorbent. A proper amount of steel slag blending will increase the specific surface area of the mixture and reduce its pore size range. The best blending amount is between 40 and 60%.

Adsorption Experiment

The results of adsorption experiments (Figure 6) exhibited that the sludge and steel slag after pyrolysis alone have a certain adsorption capacity for chromium ions, but the adsorption rate is not high. The adsorption rates of the steel slag and sludge for Cr(VI) are 50.93 and 69%, respectively. Nevertheless, the Cr(VI) adsorption rate of the product obtained from pyrolysis of the mixture of steel slag and sludge improves greatly, and the adsorption rate increases above 95%. When the steel slag content is 60%, the adsorption rate is the highest up to 99.75%. In fact, the adsorption rate of steel slag on Cr(III) is very high and the adsorption capacity of Cr(VI) is weak. The method in this paper can directly adsorb Cr(VI) with the blended pyrolysis residue and can also achieve an adsorption rate equivalent to Cr(III). On the one hand, the increase in specific surface area and surface wrinkles after blending pyrolysis greatly enhances its adsorption effect; on the other hand, the increase of metal oxides and the reducing groups generated after sludge pyrolysis are conducive to the affinity adsorption and reduction of Cr(VI) under a neutral pH environment.

X-Ray Photoelectron Spectra Before and After SS 60% Adsorption

Figure 7A shows that the residues before and after adsorption contain the C and O elements. The adsorption peak of the O element changes significantly after adsorption, and the Cr peak appears in the full spectrum after adsorption. Figures 7B,C are the energy spectra of O 1s before and after adsorption. Before adsorption, 532.5 and 531.4 eV are the binding energies of non-metal oxide (SiO_2) and carbonate (CaCO_3), respectively. The binding energy after adsorption is converted to 533.1 and 531.5 eV, which are the binding energies of non-metal oxide

(SiO_2) and metal oxide (Cr_2O_3), respectively, indicating that the O element participates in the adsorption process. Figure 7D is the Cr 2p energy spectrum before adsorption. It can be seen that there are all miscellaneous peaks and no Cr 2p peaks. Figure 7E is the Cr 2p energy spectrum after adsorption. The binding energies of Cr 2p_{3/2} and Cr 2p_{1/2} are respectively 577.2 and 587 eV. Cr 2p_{3/2} can be peaked to fit Cr(VI) and Cr(III), and its binding energy is 578.4 and 576.6 eV, respectively; Cr 2p_{1/2} can be peaked to fit Cr(VI) and Cr(III) and its combination. The energy is 587.5 and 586.1 eV, respectively (Ai et al., 2008). This may be due to the presence of some highly reducing components (such as zero-valent iron) in the adsorbent, which reduces a part of Cr(VI) to Cr(III) through an oxidation–reduction reaction. This shows that the adsorption mechanism of the adsorbent to Cr(VI) is controlled by both physical and chemical processes.

CONCLUSION

The sludge-based adsorbent was prepared by blending pyrolysis of sludge with steel slag. It was found that the adsorbent had a good adsorption effect on Cr(VI). When steel slag accounted for 60%, the removal capacity of Cr(VI) in the solution reached 99.75%. Some metal oxides (CaO , Fe_2O_3) in steel slag can react with the gases (H_2 , CO) generated by sludge pyrolysis to promote sludge pyrolysis, while the high content of SiO_2 in steel slag can increase the activation energy of sludge and inhibit sludge pyrolysis. At the same time, with the addition of steel slag, the pore structure of the sludge-based adsorbent becomes developed and the specific surface area doubles, and the optimal addition is when the steel slag ratio is 40–60%. In addition, XPS analysis shows that the adsorption mechanism of Cr(VI) by the additive is controlled by both physics and chemistry.

DATA AVAILABILITY STATEMENT

The original contributions presented in the study are included in the article/Supplementary Material; further inquiries can be directed to the corresponding authors.

AUTHOR CONTRIBUTIONS

XQ designed the experiment and wrote the manuscript. EZ reviewed and revised the manuscript. XW processed the data and figures. SL developed the concept. YS revised the manuscript.

FUNDING

This work was supported by the Natural Science Foundation of Shandong Province, China (No. ZR2019MEE015) and 2020 science and technology project of Qingdao West Coast New Area (Science and technology benefiting the people) (No. 2020-99).

REFERENCES

- Ai, Z., Cheng, Y., Zhang, L., and Qiu, J. (2008). Efficient Removal of Cr(VI) from Aqueous Solution with Fe@Fe₂O₃ Core-Shell Nanowires. *Environ. Sci. Technol.* 42 (18), 6955–6960. doi:10.1021/es800962m
- Barry, D., Barbiero, C., Briens, C., and Berruti, F. (2019). Pyrolysis as an Economical and Ecological Treatment Option for Municipal Sewage Sludge, *Biomass and Bioenergy* 122, 472–480. doi:10.1016/j.biombioe.2019.01.041
- Bondarczuk, K., Markowicz, A., and Piotrowska-Seget, Z. (2015). The Urgent Need for Risk Assessment on the Antibiotic Resistance Spread via Sewage Sludge Land Application. *Environment International* 87, 49–55. doi:10.1016/j.envint.2015.11.011
- Bora, A. P., Gupta, D. P., and Durbha, K. S. (2020). Sewage Sludge to Bio-Fuel: A Review on the Sustainable Approach of Transforming Sewage Waste to Alternative Fuel. *Fuel* 259, 116262. doi:10.1016/j.fuel.2019.116262
- Cao, Y., and Pawłowski, A. (2012). Sewage Sludge-To-Energy Approaches Based on Anaerobic Digestion and Pyrolysis: Brief Overview and Energy Efficiency Assessment. *Renewable and Sustainable Energy Reviews* 16 (3), 1657–1665. doi:10.1016/j.rser.2011.12.014
- Diao, J., Zhou, W., Ke, Z., Qiao, Y., Zhang, T., Liu, X., et al. (2016). System Assessment of Recycling of Steel Slag in Converter Steelmaking. *Journal of Cleaner Production* 125, 159–167. doi:10.1016/j.jclepro.2016.03.040
- Fang, W., Wei, Y., and Liu, J. (2016). Comparative Characterization of Sewage Sludge Compost and Soil: Heavy Metal Leaching Characteristics. *Journal of Hazardous Materials* 310, 1–10. doi:10.1016/j.jhazmat.2016.02.025
- Fernando, N. L., and Fedorak, P. M. (2005). Changes at an Activated Sludge Sewage Treatment Plant Alter the Numbers of Airborne Aerobic Microorganisms. *Water Research* 39 (19), 4597–4608. doi:10.1016/j.watres.2005.08.010
- Friedman, H. L. (1964). Kinetics of thermal Degradation of Char-Forming Plastics from Thermogravimetry. Application to a Phenolic Plastic. *J. Polym. sci., C Polym. Symp.* 6 (1), 183–195. doi:10.1002/polc.5070060121
- Jin, J., Li, Y., Zhang, J., Wu, S., Cao, Y., Liang, P., et al. (2016). Influence of Pyrolysis Temperature on Properties and Environmental Safety of Heavy Metals in Biochars Derived from Municipal Sewage Sludge. *Journal of Hazardous Materials* 320, 417–426. doi:10.1016/j.jhazmat.2016.08.050
- Lee, S., Kim, S.-H., Jung, S., Park, Y.-K., Tsang, Y. F., and Kwon, E. E. (2020). Use of Steel Slag as a Catalyst in CO₂-cofeeding Pyrolysis of pine Sawdust. *Journal of Hazardous Materials* 392, 122275. doi:10.1016/j.jhazmat.2020.122275
- Li, F., Yan, B., Zhang, Y., Zhang, L., and Lei, T. (2014). Effect of Activator on the Structure and Desulphurization Efficiency of Sludge-Activated Carbon. *Environmental Technology* 35 (20), 2575–2581. doi:10.1080/21622515.2014.913689
- Lin, Y., Liao, Y., Yu, Z., Fang, S., and Ma, X. (2017). A Study on Co-pyrolysis of Bagasse and Sewage Sludge Using TG-FTIR and Py-GC/MS. *Energy Conversion and Management* 151, 190–198. doi:10.1016/j.enconman.2017.08.062
- Liu, J., Yu, B., and Wang, Q. (2020). Application of Steel Slag in Cement Treated Aggregate Base Course. *Journal of Cleaner Production* 269, 121733. doi:10.1016/j.jclepro.2020.121733
- Luo, S., Liu, L., Song, Y., Fang, L., Wang, J., Zuo, Z., et al. (2020). Effect of Activation Pretreatment on the Pyrolysis Behavior of Sludge. *J. biobased mat bioenergy* 14 (4), 461–466. doi:10.1166/jbmb.2020.1989
- Magdziarz, A., and Wilk, M. (2013). Thermogravimetric Study of Biomass, Sewage Sludge and Coal Combustion. *Energy Conversion and Management* 75, 425–430. doi:10.1016/j.enconman.2013.06.016
- Naqvi, S. R., Tariq, R., Hameed, Z., Ali, I., Taqvi, S. A., Naqvi, M., et al. (2018). Pyrolysis of High-Ash Sewage Sludge: Thermo-Kinetic Study Using TGA and Artificial Neural Networks. *Fuel* 233, 529–538. doi:10.1016/j.fuel.2018.06.089
- Piatak, N. M., Parsons, M. B., and Seal, R. R. (2015). Characteristics and Environmental Aspects of Slag: A Review. *Applied Geochemistry* 57, 236–266. doi:10.1016/j.apgeochem.2014.04.009
- Raheem, A., Sikarwar, V. S., He, J., Dastyar, W., Dionysiou, D. D., Wang, W., et al. (2018). Opportunities and Challenges in Sustainable Treatment and Resource Reuse of Sewage Sludge: A Review. *Chemical Engineering Journal* 337, 616–641. doi:10.1016/j.cej.2017.12.149
- Sridhar, B., and Sastri, M. V. S. S. (2021). Studies on Strength and Behaviour of Hot Mix Asphalt Using Steel Slag Aggregates in Pavements. [J]. *Key Engineering Materials* 6211, 254–262. doi:10.4028/www.scientific.net/kem.882.254
- Stunda-Zujeva, A., Kreicbergs, I., and Medne, O. (2018). Sustainable Utilization of Sewage Sludge: Review of Technologies. *Kem* 762, 121–125. doi:10.4028/www.scientific.net/kem.762.121
- Wang, Z., Liu, K., Xie, L., Zhu, H., Ji, S., and Shu, X. (2019). Effects of Residence Time on Characteristics of Biochars Prepared via Co-pyrolysis of Sewage Sludge and Cotton Stalks. *Journal of Analytical and Applied Pyrolysis* 142, 104659. doi:10.1016/j.jaap.2019.104659
- Wei, L.-L., Zhao, Q.-L., Hu, K., Lee, D.-J., Xie, C.-M., and Jiang, J.-Q. (2011). Extracellular Biological Organic Matters in Sewage Sludge during Mesophilic Digestion at Reduced Hydraulic Retention Time. *Water Research* 45 (3), 1472–1480. doi:10.1016/j.watres.2010.11.003
- Yang, Y.-Q., Cui, M.-H., Guo, J.-C., Du, J.-J., Zheng, Z.-Y., and Liu, H. (2010). Effects of Co-pyrolysis of rice Husk and Sewage Sludge on the Bioavailability and Environmental Risks of Pb and Cd. *Environmental technology* 42, 2304–2312. doi:10.1080/09593330.2019.1701562
- Zaker, A., Chen, Z., Zaheer-Uddin, M., and Guo, J. (2021). Co-pyrolysis of Sewage Sludge and Low-Density Polyethylene - A Thermogravimetric Study of Thermo-Kinetics and Thermodynamic Parameters. *Journal of Environmental Chemical Engineering* 9, 104554. doi:10.1016/J.JECE.2020.104554
- Zhao, B., Xu, X., Zeng, F., Li, H., and Chen, X. (2018). The Hierarchical Porous Structure Bio-Char Assessments Produced by Co-pyrolysis of Municipal Sewage Sludge and Hazelnut Shell and Cu(II) Adsorption Kinetics. *Environ Sci Pollut Res* 25 (20), 19423–19435. doi:10.1007/s11356-018-2079-y
- Zuo, Z., Yu, Q., Luo, S., Zhang, J., and Zhou, E. (2019). Effects of CaO on Two-step Reduction Characteristics of Copper Slag Using Biochar as Reducer: Thermodynamic and Kinetics. *Energy Fuels* 34 (1), 491–500. doi:10.1021/acs.energyfuels.9b03274

Conflict of Interest: The authors declare that the research was conducted in the absence of any commercial or financial relationships that could be construed as a potential conflict of interest.

Publisher's Note: All claims expressed in this article are solely those of the authors and do not necessarily represent those of their affiliated organizations or those of the publisher, the editors, and the reviewers. Any product that may be evaluated in this article or claim that may be made by its manufacturer is not guaranteed or endorsed by the publisher.

Copyright © 2022 Qi, Zhou, Wu, Luo and Song. This is an open-access article distributed under the terms of the Creative Commons Attribution License (CC BY). The use, distribution or reproduction in other forums is permitted, provided the original author(s) and the copyright owner(s) are credited and that the original publication in this journal is cited, in accordance with accepted academic practice. No use, distribution or reproduction is permitted which does not comply with these terms.



AHP-Based Evaluation of the Suitability of Shallow Geothermal Energy Utilization in GSHP System

Jie Dong^{1,2}, Peng He^{1,2}, Honghua Liu^{1,2*}, Yong Guan^{1,2}, Haisong Liu^{1,2}, Weiqiang Xia^{1,2} and Jierui Dong³

¹Key Laboratory of Geological Safety of Coastal Urban Underground Space, Ministry of Natural Resources, Qingdao, China,

²Qingdao Geo-Engineering Surveying Institute (Qingdao Geological Exploration Development Bureau), Qingdao, China, ³School of Environment and Municipal Engineering, Qingdao University of Technology, Qingdao, China

OPEN ACCESS

Edited by:

Huaqing Xie,
Northeastern University, China

Reviewed by:

Bo Han,
Heriot-Watt University,
United Kingdom
Fujiao Tang,
Harbin Institute of Technology, China
Wei Song,
North China University of Technology,
China

*Correspondence:

Honghua Liu
majorhp0207@163.com

Specialty section:

This article was submitted to
Advanced Clean Fuel Technologies,
a section of the journal
Frontiers in Energy Research

Received: 21 January 2022

Accepted: 08 February 2022

Published: 03 March 2022

Citation:

Dong J, He P, Liu H, Guan Y, Liu H,
Xia W and Dong J (2022) AHP-Based
Evaluation of the Suitability of Shallow
Geothermal Energy Utilization in
GSHP System.
Front. Energy Res. 10:859454.
doi: 10.3389/fenrg.2022.859454

Shallow geothermal energy (SGE) is a part of geothermal resources and is mainly used through ground source heat pumps (GSHP). However, the potential of SGE varies from region to region due to different geological conditions. There is a lack of regulations and codes for assessing SGE, which makes the design and planning of GSHP restricted. In this study, an evaluation system of the suitability of GSHP in a region of Qingdao by using Analytic Hierarchy Process (AHP) is proposed, and the test area is divided into three suitability levels based on suitability scores. The evaluation system contains property indicators, elemental indicators, and their weights. The result shows that the highly suitable area for the application of GSHP in the test area is 110.04 km², accounting for 41.8% of the whole test area. The area of moderately suitable area is 65.02 km², accounting for 24.7%, and GSHP should be developed and utilized on the basis of full demonstration in this level. The unsuitable area for GSHP is 88.19 km², accounting for 33.5%. The indicator weights in this article may only be applicable to the Qingdao area and cities with similar geological conditions to Qingdao. However, the indicators within this evaluation system can be applied to the vast majority of locations where GSHP are to be developed, as it provides a method of assessment in terms of geological conditions, groundwater conditions, construction conditions, and ecological aspects.

Keywords: shallow geothermal energy (SGE), ground source heat pump (GSHP), Analytic Hierarchy Process (AHP), evaluation system, suitability zoning

1 INTRODUCTION

Shallow geothermal energy (SGE) is a part of geothermal resources, which generally refers to the thermal energy resources in the interior of the earth with a temperature of less than 25°C from the thermostatic zone to 200 m burial depth, and has the value of development and utilization at present. In China, it has been proven that the SGE resources available within 1.69×10^5 km² are equivalent to 7×10^{12} kg of coal (Xu et al., 2020). In 2021, 58.8% of geothermal energy resources was extracted through ground source heat pumps (GSHP) (Lund et al., 2021), which provide energy by the borehole heat exchanger (BHE) (Sarbu et al., 2014). According to the current GSHP code in China

Abbreviations: AHP, Analytic Hierarchy Process; BHE, borehole heat exchanger; GSHP, ground source heat pumps; SGE, shallow geothermal energy; A, judgement matrix; a_{ij} , ratio of the impact of x_j to x_i ; CR, consistency ratio; CI, consistency indicator; n , the number of indicators; RI, random consistency index; w_i , number of hidden layer neurons; x_i, x_j , elemental indicators; λ_{max} , the main eigenvalue of the matrix.

(GB 50366-2009, 2009), the ground temperature and thermal conductivity obtained from thermal response tests are essential parameters. However, these two parameters cannot represent the development potential of SGE and efficiency of GSHP in detail (Luo et al., 2016). Moreover, BHE is usually deeper than 100 m, which means the initial investment is costly. Therefore, before designing GSHP, the local geological environment, thermophysical properties of the soil, groundwater conditions, and construction costs need to be evaluated to ensure the efficiency of GSHP (Casasso et al., 2017).

However, these influencing factors do not have a clear description of their contribution. Firstly, the geological, climatic, and hydrological conditions vary from region to region and are difficult to generalize by the same criteria. Secondly, the factors are not independent of each other but interact with each other. For example, lithology will largely determine the ability of heat transfer (He et al., 2017; Kai-Qi et al., 2020), as well as the microscopic particle shape (Wang et al., 2019), porosity (Dong et al., 2015), saturation (Tong et al., 2009), and groundwater conditions (Chen, 2008; Zhang et al., 2015) of the rock can also contribute to changes in thermal conductivity (Dong et al., 2021). In engineering, lithology and rock thickness can also affect construction difficulty and drilling costs. In fact, one of the most important factors of concern for engineering is construction costs. Construction methods vary in different geological conditions, which lead to the differences in construction costs. Thirdly, the safety and sustainability of GSHP also need to be considered, which makes the evaluation of SGE a task that requires multidisciplinary and multisectoral cooperation. At present, the development of SGE is still in the exploration stage, and there is a lack of systematic technical codes for evaluation and calculation methods of SGE (Wang et al., 2020).

The Analytic Hierarchy Process (AHP), developed by Saaty (1988), quantifies the empirical judgment of decision makers and is suitable for problems that are difficult to analyze completely quantitatively, such as evaluating SGE. AHP uses various types of indicators to form an evaluation system (Tinti et al., 2018). This system generally includes the influencing factors from the above literature, but the contribution of each indicator will be different. Therefore, the evaluation system cannot be applied to every region due to the different geological conditions. This article establishes an evaluation system applicable to the Qingdao area based on the geographic conditions, urban characteristics, and geological conditions. The evaluation system consists of four attribute indicators and 11 element indicators, and their weights are analyzed and calculated. Finally, this article uses the geographic information system (GIS) to classify the evaluation area and obtain an effective SGE suitability index. The research results can provide guidance to the development of GSHP.

2 MATERIALS AND METHODS

2.1 Analytic Hierarchy Process

AHP is essentially the formalization of our intuitive understanding of a complex problem using a hierarchical structure (Saaty, 1994). The AHP is a systematic analysis

TABLE 1 | Random consistency indexes for different matrix sizes.

n	1	2	3	4
<i>RI</i>	0.00	0.00	0.52	0.89

method that integrates qualitative and quantitative analyses. It quantifies the empirical decision of policymakers and is applicable to problems that are difficult to analyze completely quantitatively. It is applied to multiple fields (Vaidya et al., 2006). The structure at least has three levels: the focus or the overall goal of the problem on the top level, multiple criteria that define alternatives in the middle level, and competing alternatives in the bottom level. The main application of SGE is GSHP, thus the AHP system in this study will be built on all factors that affect GSHP. In this article, there are three steps in AHP modelling:

- 1) The influencing factors are analyzed and a hierarchy is created. The details are shown in **Section 2.2**.
- 2) The judgment matrices for each level are constructed. The property indicators in the second layer are compared pairwise, and then the elemental indicators under each property indicator are also compared pairwise. Two indicators, x_i and x_j , are taken at a time, and a_{ij} represents the ratio of the impact of x_i and x_j on the target (GSHP system). The result of the comparison is represented by the judgement matrix $A = (a_{ij})_{n \times n}$. If the ratio of the impact of x_i to x_j on the target is a_{ij} , then the ratio of the impact of x_j to x_i should be $a_{ji} = \frac{1}{a_{ij}}$. The weight of each indicator w_i can be calculated by **Eq. 1**:

$$w_i = \frac{\sum_{j=1}^n \frac{a_{ij}}{\sum_{i=1}^n a_{ij}}}{n} \quad (1)$$

where n is the number of indicators.

- 3) The consistency of each judgment matrix is checked. First, the consistency indicator CI is calculated:

$$CI = \frac{\lambda_{max} - n}{n - 1} \quad (2)$$

where λ_{max} is the main eigenvalue of the matrix. The CI values represent the variance of the error incurred in estimating a_{ij} . Second, the value of the AHP conducted is checked, and CI is compared with the appropriate values of the random consistency index RI . Saaty (1990) provided values for RI , which are shown in **Table 1**.

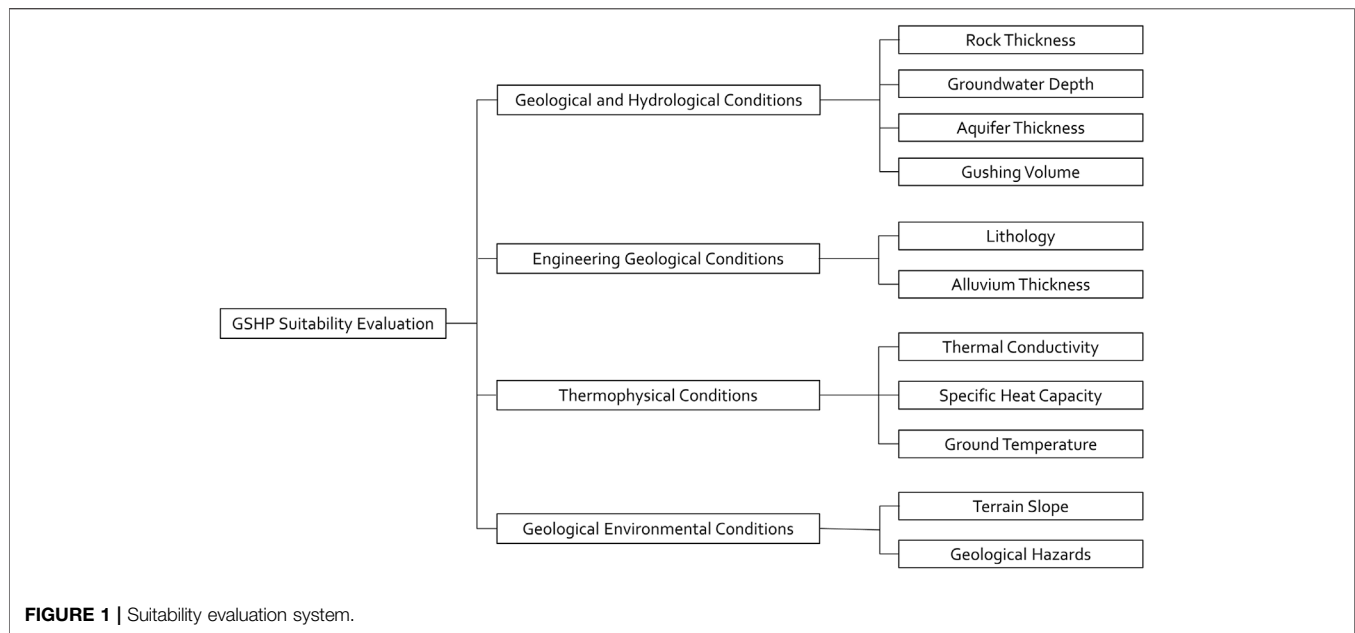
Third, when the consistency ratio $CR < 0.10$, the results of the analysis are acceptable, otherwise the judgement matrix is amended appropriately.

$$CR = \frac{CI}{RI} \quad (3)$$

2.2 Establishing the Evaluation System

2.2.1 Evaluation Indicators

In the AHP, the evaluation indicators are divided into two levels. The first level of indicators is property indicators, which provides



a general description of all the indicators that affect the decision. In this study, since the water quality and quantity in the test area are not suitable for hybrid GSHP, the closed-loop GSHP with vertical borehole is the subject. According to the code for the evaluation of SGE in Shandong Province (DB37/T 4308-2021, 2021), the selection of property indicators includes geological and hydrogeological conditions, engineering geological conditions, thermophysical conditions, and geological environmental conditions. The second level of indicators is the elemental indicators, which are elements that can describe property indicators. These elemental indicators may be interacting (DZ/T 0225-2009, 2009), for example, lithology and groundwater conditions will affect thermal conductivity and specific heat capacity. The hierarchical analysis can effectively resolve these ambiguities.

The evaluation system shown in **Figure 1** is established. In order to ensure the long-term operational efficiency of GSHP and to protect the local ecology (Hähnlein et al., 2013), the ecological protection area and the metro line are used as the restricted area in this study, which are directly labeled as poor suitability areas.

1) Geological and hydrogeological conditions

This index includes rock thickness, groundwater depth, aquifer thickness, and gushing volume. Underground rock thickness affects the difficulty of BHE construction and the initial investment of engineering. During the construction of BHE, if there is a lot of gravel and sand, a casing will be required when drilling. The best drilling conditions are achieved when the thickness of the rock is greater than the length of the BHE. In addition, the more complex the underground stratification, the higher the difficulty and cost during the construction of the BHE.

The groundwater depth affects the heat transfer of the BHE. The heat and cold load released by the BHE are carried away by the groundwater and then energy transfers quickly between the groundwater and soil (Zhang et al., 2020). This makes the accumulation of underground cold and heat loads less likely to form, thus enabling a more durable and stable provision of energy. The aquifer thickness and gushing volume determine the effect of underground heat transfer and heat exchange conditions of the soil. Although the permeability coefficient is a representative of groundwater transport, there are strips of aquifer rock structure in the test area (**Figure 2C**). The aquifer thickness and gushing volume would be more representative of the groundwater conditions in the test area.

2) Engineering geological conditions

This index includes the lithology and the alluvial thickness. The lithology affects the heat transfer capacity of BHE. Generally, bedrock such as granite has higher thermal conductivity and higher heat transfer efficiency (VDI 4640/1, 2010). The alluvial thickness mainly considers the difficulty of hole formation during the drilling operation. If the thickness of alluvial is too large, it is not only difficult to drill but also prone to collapse after lifting the drill, which makes it difficult to build a borehole.

3) Thermophysical conditions

This index includes thermal conductivity, specific heat capacity, and ground temperature. Thermal conductivity reflects energy transfer, which directly determines the level of heat transfer capacity of the BHE. The specific heat capacity represents the heat absorbed or released when the temperature of the soil changes and can indicate the amount of SGE contained in the soil. The ground temperature indicates the gradient of the

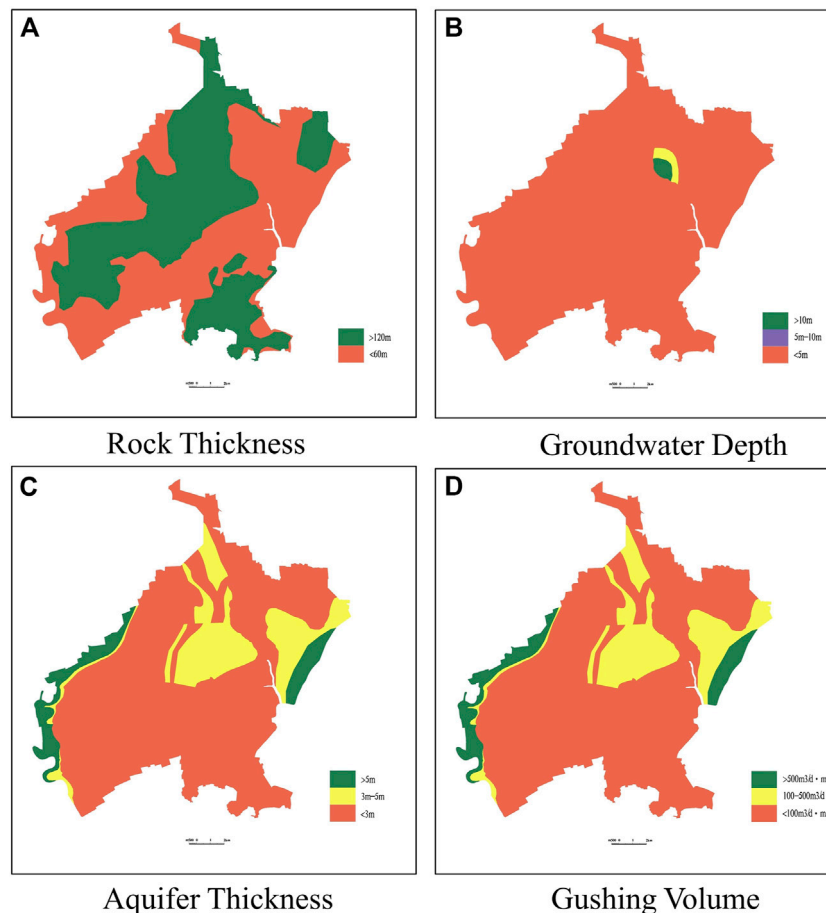


FIGURE 2 | The map of geological and hydrological conditions. (A) Rock thickness, (B) groundwater depth, (C) aquifer thickness, and (D) gushing volume.

earth's temperature and the earth's heat flow; the higher the temperature, the more abundant the SGE (Zhang et al., 2019).

4) Geological environmental conditions

Geological environmental conditions include topography and geological hazards, which are mainly concerned on the construction and operation of GSHP. The smoother the topography and lesser the geological hazards, the better it is for organizing the construction and later the operation.

2.2.2 Quantification of Indicators

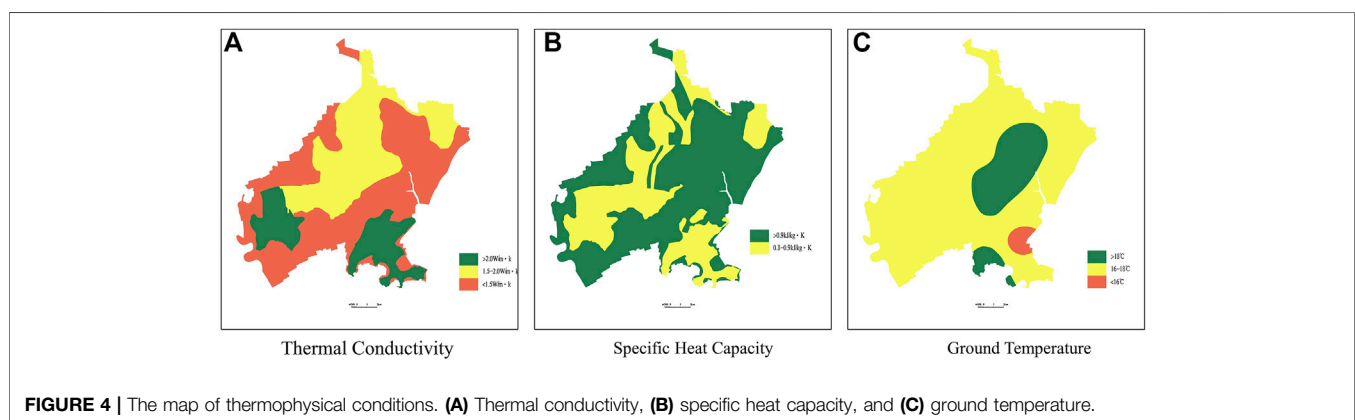
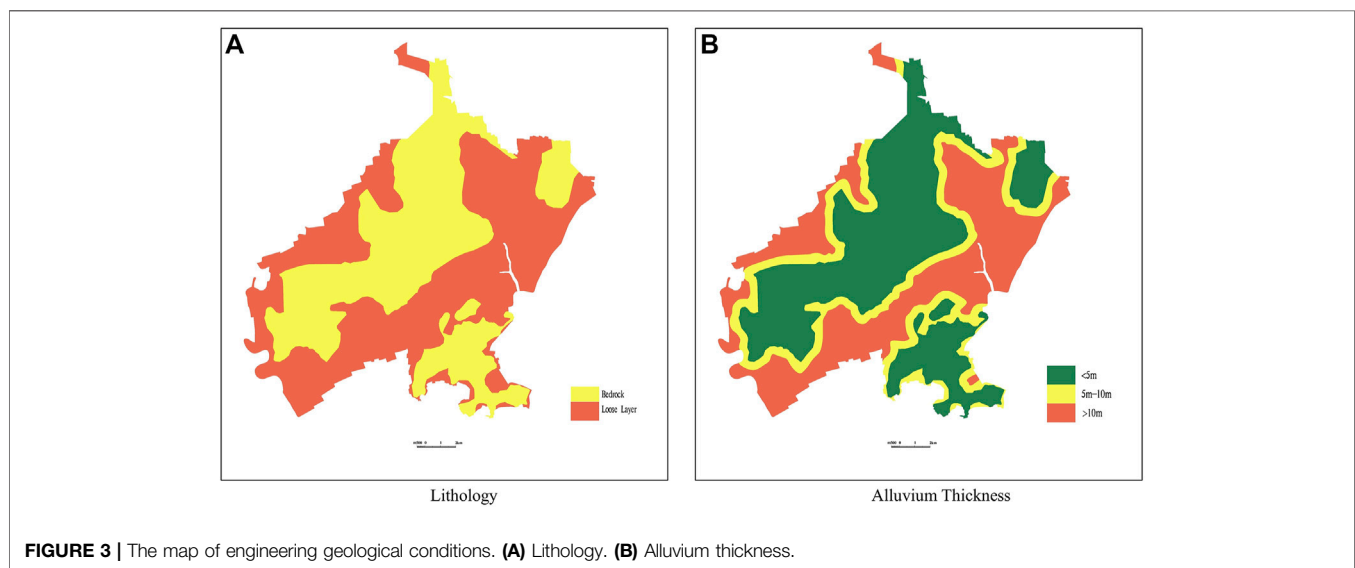
The indicators mentioned above use different forms and scales of data. In order to compare and calculate different data within the same evaluation system, it is necessary to standardize the data before evaluation. In this study, the standardization of data is done by dividing the range of each element into three levels of criteria, i.e., 9, 5, and 1, based on whether the GSHP is suitable for construction. In **Table 2**, the scoring used here is shown, i.e., 1~9 intended to increase the variation in the final score. Due to the large number of elemental indicators, the weights do not differ significantly in value. If smaller scores are used, the range of the

final scores would be so small that it would be difficult to assign a suitability level. The more favorable the GSHP, the higher the score obtained, thus transforming all data into dimensionless values that can be compared with each other. The quantitative grading of each indicator is based on both the geological environment conditions and the operability of the system in the process of quantification. The quantification of each indicator is shown in **Table 2**. After quantification, the maps of each indicator are drawn in the GIS, and the results are shown in **Figures 2–5**.

The classification of the range of each indicator is based on the Chinese code (DZ/T 0225-2009, 2009; DB37/T 4308-2021, 2021) and on real GSHP applications. It is important to emphasize that the lithology of the strata in the test area can be divided into two categories: bedrock zone and loose layer. In the bedrock zone, the rock thickness is all greater than 120 m, which is the usual length of the buried pipe. In the loose layers, where the rock thickness is less than 60 m, gravel and sandy soils lead to increased construction costs and therefore score lower. In addition, the groundwater in the test area is barren and unsuitable for hybrid GSHP. However, the transport of groundwater will significantly enhance the heat transfer capacity of the BHE. In order to

TABLE 2 | The quantification of indicators.

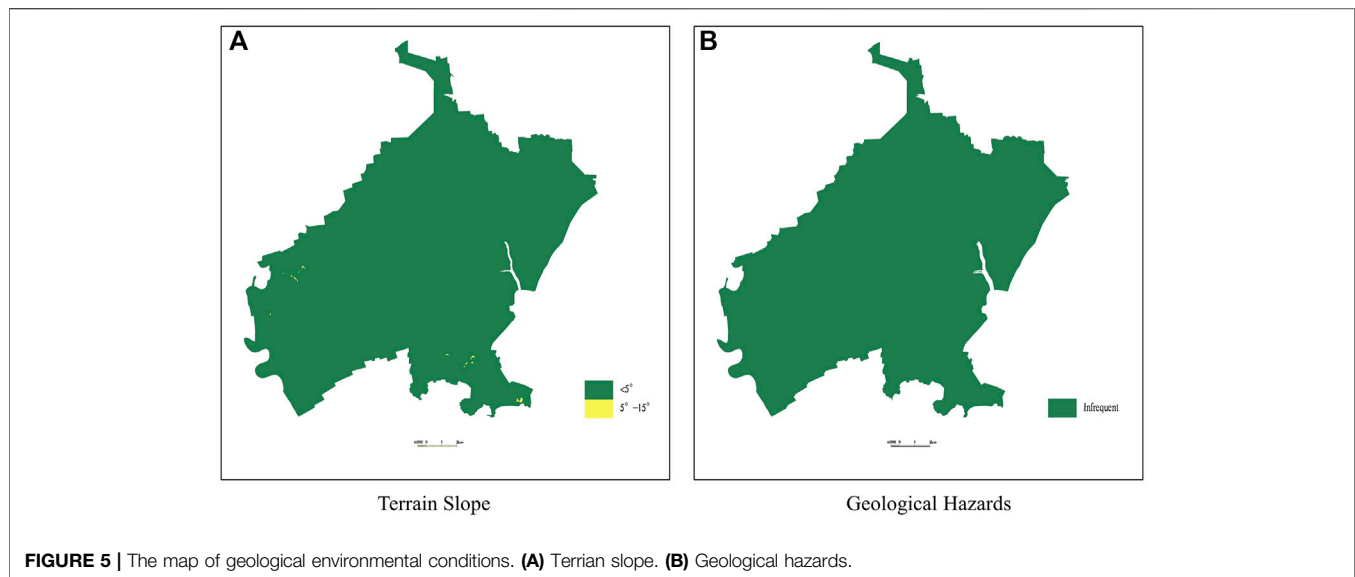
Property indicators	Elemental indicators	Scores			Data source
		9	5	1	
Geological and hydrological conditions	Rock thickness (m)	>120	60–120	<60	Geological survey
	Groundwater depth (m)	>9	6–9	<6	Hydrogeological survey
	Aquifer thickness (m)	>5	3–5	<3	Hydrogeological survey
	Gushing volume (m ³ /d·m)	>500	100–500	<100	Hydrogeological survey
Engineering geological conditions	Lithology	Intrusive rock	Bedrock	Loose Layer	Geological survey
	Alluvium thickness (m)	<5	5–10	>10	Geological survey
Thermophysical conditions	Thermal conductivity (W/m·K)	>2.0	1.5–2.0	<1.5	Thermal response test
	Specific heat capacity (kJ/kg·K)	>0.9	0.8–0.9	<0.8	Thermal response test
	Ground temperature (°C)	>18	16–18	<16	Thermal response test
Geological environmental conditions	Terrain slope (°)	<5	5–15	>15	Geological survey
	Geological hazards	Infrequent	Moderate	Prone area	Geological survey



demonstrate the influence of groundwater, three groundwater-related indicators, namely, the groundwater depth, aquifer thickness, and gushing volume, are partitioned according to the results of the recharge experiment.

2.2.3 The Weights of Indicator

In this study, the AHP was used to determine the indicators' weights. On the basis of the hierarchical relationship of the evaluation system, the importance of each indicator in the property layer and the element

**TABLE 3 |** Calculation and results of the weights of the property indicators.

Property indicators	Geological and hydrogeological conditions	Engineering geological conditions	Thermophysical condition	Geological environmental conditions	Weight
Geological and hydrogeological conditions	1	2	1	4	0.3504
Engineering geological conditions	0.5	1	0.333	2	0.1679
Thermophysical condition	1	3	1	4	0.3942
Geological environmental conditions	0.25	0.5	0.25	1	0.0876

TABLE 4 | Calculation and results of the weights of geological and hydrogeological conditions.

Geological and hydrogeological conditions	Rock thickness	Groundwater depth	Gushing volume	Aquifer thickness	Weight
Rock thickness	1	2	3	4	0.4461
Groundwater depth	0.5	1	2	3	0.2900
Gushing volume	0.3333	0.5	1	2	0.1710
Aquifer thickness	0.25	0.3333	0.5	1	0.0929

TABLE 5 | Calculation and results of the weights of engineering geological conditions.

Engineering geological conditions	Lithology	Alluvial thickness	Weight
Lithology	1	3	0.75
Alluvial thickness	0.3333	1	0.25

layer is compared separately using the 1–9 scale method to form a comparison matrix. The consistency of the comparison matrix is checked by calculation. If necessary, the comparison matrix is modified to finally reach an acceptable consistency and finally the weights of each indicator is determined.

The calculation and results of the weights of the property indicators are presented in **Table 3** and are analyzed by

consistency analysis. Among the four property indicators, the thermophysical condition is the most important because it reflects the heat exchange capacity of the GSHP. The geological and hydrogeological conditions reflect the SGE and the main factors affecting heat exchange.

Among the four indicators of geological and hydrogeological conditions, the rock thickness has the greatest weight and aquifer thickness has the least weight. The aquifer thickness is related to the type of geology in the test area, which is less water-rich (**Figure 2**). Therefore, the aquifer thickness has little influence. The two hydrogeological indicators, groundwater depth and gushing volume, mainly represent their influence on the heat transfer, both of which are slightly more important than the aquifer thickness. The calculation and results of the weights of geological and hydrogeological conditions are presented in **Table 4**.

TABLE 6 | Calculation and results of the weights of thermophysical condition.

Thermophysical condition	Thermal conductivity	Specific heat capacity	Ground temperature	Weight
Thermal conductivity	1	3	2	0.5538
Specific heat capacity	0.3333	1	1	0.2154
Ground temperature	0.5	1	1	0.2308

TABLE 7 | Calculation and results of the weights of geological environment conditions condition.

Geological environment conditions	Terrain slope	Geological hazards	Weight
Terrain slope	1	0.5	0.3333
Geological hazards	2	1	0.6667

The engineering geological conditions include two indicators: lithology and alluvial thickness, with lithology being given more weight than alluvial thickness. The lithology represents the difference of the physical and thermal physical characteristics of the soil, which has an important influence on the suitability zoning and resource calculation. The lithology is more important than the alluvial thickness because the distribution of the floodplain is less and is not representative (**Figure 3**). The calculation and results of the weights of engineering geological conditions are presented in **Table 5**.

In the design and utilization of GSHP, the thermophysical properties, as an extremely important aspect, influence the calculation of suitability zoning and resource volume (**Figure 4**). Among them, the thermal conductivity is directly involved in the calculation of heat transfer as an indicator. Therefore, the thermal conductivity is the most important indicator. The specific heat capacity and ground temperature represent the magnitude of the SGE and also have an influence on the suitability zoning. The calculation and results of the weights of thermophysical conditions are presented in **Table 6**.

Geological environment conditions include two indicators: terrain slope and geological hazards (**Figure 5**). The terrain slope affects the difficulty of GSHP construction, while geological hazards

are directly responsible for whether GSHP can be implemented. Therefore, the weight of the geological hazards is higher than the terrain slope. The calculation and results of the weights of the thermophysical conditions are presented in **Table 7**.

The weights of all indicators are presented in **Table 8**. The thermophysical conditions are the property indicators with the highest weight, which lead to the thermal conductivity becoming the highest elementary indicator. The importance of the geological and hydrogeological conditions is also high.

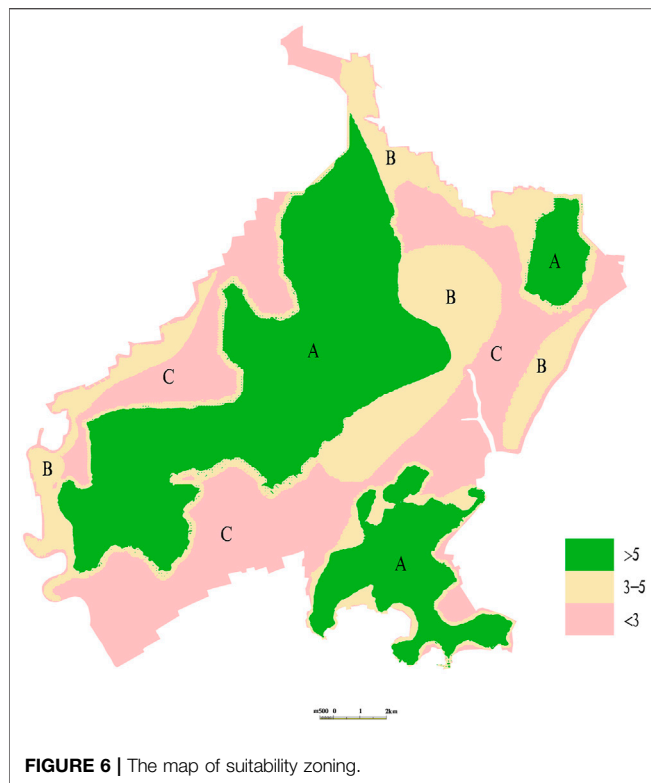
3 RESULT AND DISCUSSION

According to the above weights, each indicator is assigned a value in the GIS multiplied by its corresponding weight, and then summed up to derive the score on each point. In this article, according to the scores, the areas with scores greater than 5 are set as high suitability areas (A), 3–5 as medium suitability areas (B), and less than 3 as low suitability areas (C). The results are shown in **Figure 6**.

In **Figure 6**, area A covers an area of 110.04 km², accounting for 41.8% of the test area. It is mainly distributed in the northeast, central, southwest, and southeast of the working area. Area A is a bedrock area (**Figure 3A**), and the lithology is mainly basalt, coarse andesite, andesite, breccia, etc. The thickness of the rock is greater than 120 m (**Figure 2A**), and the construction conditions are moderate. The thermal conductivity is greater than 2.0 w/(mK) in the southwestern region and the south-eastern region (**Figure 4A**), with good heat transfer conditions. The lithology of the central region is basalt, and the thickness of the aquifer is moderate. The specific heat capacity is greater than 0.9 kJ/(kgK) (**Figure 4B**), which means that the heat transfer capacity is strong. It is suitable for the development and utilization of GSHP in area A.

TABLE 8 | The weights of indicators.

Property indicators	Weighting of property indicators	Elementary indicators	Weighting of elementary indicators	Integrated weights
Geological and hydrological conditions	0.3504	Rock thickness	0.4461	0.1563
		Groundwater depth	0.2900	0.1016
		Aquifer thickness	0.1710	0.0599
		Gushing volume	0.0929	0.0326
Engineering geological conditions	0.1679	Lithology	0.75	0.1259
		Alluvium thickness	0.25	0.0420
Thermophysical conditions	0.3942	Thermal conductivity	0.5538	0.2283
		Specific heat capacity	0.2154	0.0849
		Ground temperature	0.2308	0.0910
Geological environmental conditions	0.0876	Terrain slope	0.3333	0.0292
		Geological hazards	0.6667	0.0584



Area B covers 65.02 km², accounting for 24.7%. It is mainly located in the central and north-eastern bedrock areas, and the lithology is mainly basalt, coarse andesite, andesite, breccia, etc. (Figure 3A). The thickness of the rock is more than 120 m (Figure 2A), which means the drilling conditions are suitable. The thermal conductivity of the central and north-eastern part is 1.5–2.0 w/(mK) (Figure 4A). Thus, the comprehensive heat transfer capacity of the geotechnical layer is strong. In addition, the ground temperature conditions are good. The GSHP should be developed and utilized on the basis of full demonstration in area B.

Area C covers 88.19 km², accounting for 33.5%. Area C is not only the area with a score less than 3 but also that which includes the ecological protection zone and metro area. It is mainly located in the loose layer (Figure 3A) with rock thickness less than 60 m (Figure 2A). The thermal conductivity is less than 1.5 w/(mK) (Figure 4A), and the heat transfer capacity is poor. It is not suitable for the development of GSHP.

REFERENCES

- Casasso, A., and Sethi, R. (2017). Assessment and Mapping of the Shallow Geothermal Potential in the Province of Cuneo (Piedmont, NW Italy). *Renew. Energ.* 102, 306–315. doi:10.1016/j.renene.2016.10.045
- Chen, S. X. (2008). Thermal Conductivity of Sands. *Heat Mass. Transfer* 44 (10), 1241–1246. doi:10.1007/s00231-007-0357-1

4 CONCLUSION

This study establishes an evaluation system based on the geographic conditions, urban characteristics, and geological conditions in Qingdao. After the analysis and calculation of AHP, the weights of the elemental indicators are calculated. Then, the suitability zones are mapped through GIS. The following conclusions are drawn:

- 1) In the evaluation system, although the thermal conductivity is the most important indicator, geological conditions and hydrogeological conditions are also of high importance. The thermal conductivity alone cannot be considered when designing GSHP.
- 2) The AHP-based evaluation system can provide an effective solution of suitability evaluation for SGE exploration in the GSHP application in the Qingdao region. This system can be extended to places with similar geological conditions in Qingdao and provide a reference for evaluation of SGE in other regions.
- 3) In the test area, the area of high suitability (area A) is 110.04 km², accounting for 41.8%. The area of medium suitability (area B) covers 65.02 km², accounting for 24.7%. The area of low suitability (area C) covers 88.19 km², accounting for 33.5%.
- 4) Due to geological differences, the weights used in this article may not be applicable to all regions. In addition, although the AHP is already a very mature evaluation method, its subjectivity is inevitable. It is recommended that a more objective evaluation method be used for subsequent use as a basis for development.

DATA AVAILABILITY STATEMENT

The original contributions presented in the study are included in the article/Supplementary Material, further inquiries can be directed to the corresponding author.

AUTHOR CONTRIBUTIONS

JD conducted the experiments and wrote the manuscript. PH and HoL have corrected and edited the manuscript. YG and HaL supported the project technically. WX and JrD were responsible for software data curation.

- DB37/T 4308-2021 (2021). *Specification for Investigation and Evaluation of Regional Shallow Geothermal Energy*. Beijing, China: Shandong Administration for Market Regulation.
- Dong, J., Li, X., Han, B., Tian, R., and Yu, H. (2022). A Regional Study of In-Situ thermal Conductivity of Soil Based on Artificial Neural Network Model. *Energy and Buildings* 257, 111785. doi:10.1016/j.enbuild.2021.111785
- Dong, Y., McCartney, J. S., and Lu, N. (2015). Critical Review of Thermal Conductivity Models for Unsaturated Soils. *Geotech Geol. Eng.* 33, 207–221. doi:10.1007/s10706-015-9843-2

- DZ/T 0225-2009 (2009). *Specification for Shallow Geothermal Energy Investigation and Evaluation*. Beijing, China: Ministry of Land and Resources of the People's Republic of China.
- GB 50366-2009 (2009). *Technical Code for Ground-Source Heat Pump System*. Ministry of Construction.
- Hähnlein, S., Bayer, P., Ferguson, G., and Blum, P. (2013). Sustainability and Policy for the thermal Use of Shallow Geothermal Energy. *Energy Policy* 59, 914–925. doi:10.1016/j.enpol.2013.04.040
- He, H., Zhao, Y., Dyck, M. F., Si, B., Jin, H., Lv, J., et al. (2017). A Modified Normalized Model for Predicting Effective Soil thermal Conductivity. *Acta Geotech.* 12, 1281–1300. doi:10.1007/s11440-017-0563-z
- Li, K.-Q., Li, D.-Q., and Liu, Y. (2020). Meso-scale Investigations on the Effective thermal Conductivity of Multi-phase Materials Using the Finite Element Method. *Int. J. Heat Mass Transfer* 151, 119383. doi:10.1016/j.jheatmasstransfer.2020.119383
- Lund, J. W., and Toth, A. N. (2021). Direct Utilization of Geothermal Energy 2020 Worldwide Review. *Geothermics* 90, 101915. doi:10.1016/j.geothermics.2020.101915
- Luo, J., Rohn, J., Xiang, W., Bertermann, D., and Blum, P. (2016). A Review of Ground Investigations for Ground Source Heat Pump (GSHP) Systems. *Energy and Buildings* 117, 160–175. doi:10.1016/j.enbuild.2016.02.038
- Saaty, T. L. (1994). How to Make a Decision: the Analytic Hierarchy Process. *Interfaces* 24 (6), 19–43. doi:10.1287/inte.24.6.19
- Saaty, T. L. (1988). “What Is the Analytic Hierarchy Process,” in *Mathematical Models for Decision Support* (Berlin, Heidelberg: Springer), 109–121. doi:10.1007/978-3-642-83555-1_5
- Saaty, T. L. (1990). *Decision Making for Leaders: The Analytic Hierarchy Process for Decisions in a Complex World* (RWS Publications).
- Sarbu, I., and Sebarchievici, C. (2014). General Review of Ground-Source Heat Pump Systems for Heating and Cooling of Buildings. *Energy and buildings* 70, 441–454. doi:10.1016/j.enbuild.2013.11.068
- Tinti, F., Kasmaee, S., Elkarmoty, M., Bonduà, S., and Bortolotti, V. (2018). Suitability Evaluation of Specific Shallow Geothermal Technologies Using a GIS-Based Multi Criteria Decision Analysis Implementing the Analytic Hierarchic Process. *Energies* 11 (2), 457. doi:10.3390/en11020457
- Tong, F., Jing, L., and Zimmerman, R. W. (2009). An Effective thermal Conductivity Model of Geological Porous media for Coupled Thermo-Hydro-Mechanical Systems with Multiphase Flow. *Int. J. Rock Mech. Mining Sci.* 46 (8), 1358–1369. doi:10.1016/j.jrmms.2009.04.010
- Vaidya, O. S., and Kumar, S. (2006). Analytic Hierarchy Process: An Overview of Applications. *Eur. J. Oper. Res.* 169 (1), 1–29. doi:10.1016/j.ejor.2004.04.028
- VDI 4640/1 (2010). *VDI 4640 Blatt 1: 2010-06: Thermal Use of the Underground*.
- Wang, C., Lai, Y., Zhang, M., and Li, S. (2019). A Generalized thermal Conductivity Model of Geomaterials Based on Micro-structures. *Acta Geotech.* 14, 1423–1436. doi:10.1007/s11440-018-0728-4
- Wang, G., Liu, Y., Zhu, X., and Zhang, W. (2020). The Status and Development Trend of Geothermal Resources in China. *EARTH SCIENCE FRONTIERS* 27 (01), 312–321. doi:10.13745/j.esf.2020.1.1
- Xu, Y.-S., Wang, X.-W., Shen, S.-L., and Zhou, A. (2020). Distribution Characteristics and Utilization of Shallow Geothermal Energy in China. *Energy and Buildings* 229, 110479. doi:10.1016/j.enbuild.2020.110479
- Zhang, B., Gu, K., Shi, B., Liu, C., Bayer, P., Wei, G., et al. (2020). Actively Heated Fiber Optics Based thermal Response Test: A Field Demonstration. *Renew. Sustain. Energ. Rev.* 134, 110336. doi:10.1016/j.rser.2020.110336
- Zhang, C., Song, W., Liu, Y., Kong, X., and Wang, Q. (2019). Effect of Vertical Ground Temperature Distribution on Parameter Estimation of *In-Situ* thermal Response Test with Unstable Heat Rate. *Renew. Energ.* 136, 264–274. doi:10.1016/j.renene.2018.12.112
- Zhang, N., Yu, X., Pradhan, A., and Puppala, A. J. (2015). Thermal Conductivity of Quartz Sands by Thermo-Time Domain Reflectometry Probe and Model Prediction. *J. Mater. Civ. Eng.* 27 (12), 04015059. doi:10.1061/(asce)mt.1943-5533.0001332

Conflict of Interest: The authors declare that the research was conducted in the absence of any commercial or financial relationships that could be construed as a potential conflict of interest.

Publisher's Note: All claims expressed in this article are solely those of the authors and do not necessarily represent those of their affiliated organizations, or those of the publisher, the editors, and the reviewers. Any product that may be evaluated in this article, or claim that may be made by its manufacturer, is not guaranteed or endorsed by the publisher.

Copyright © 2022 Dong, He, Liu, Guan, Liu, Xia and Dong. This is an open-access article distributed under the terms of the Creative Commons Attribution License (CC BY). The use, distribution or reproduction in other forums is permitted, provided the original author(s) and the copyright owner(s) are credited and that the original publication in this journal is cited, in accordance with accepted academic practice. No use, distribution or reproduction is permitted which does not comply with these terms.



Heat Transfer Characteristics and Pressure Drop of U-type Channel in Vacuum Distillation Process for Titanium Sponge

Kangquan Yang, Chengqi Zhang, Hui Yuan and Fuzhong Wu*

School of Materials and Metallurgy, Guizhou University, Guiyang, China

OPEN ACCESS

Edited by:

Zongliang Zuo,
Qingdao University of Technology,
China

Reviewed by:

Kaijie Liu,
Ganjiang Innovation Academy, (CAS),
China

Xianglong Li,

Soochow University, China

Limin Hou,

Inner Mongolia University of Science
and Technology, China

*Correspondence:

Fuzhong Wu
gutwzf@163.com

Specialty section:

This article was submitted to
Advanced Clean Fuel Technologies,
a section of the journal
Frontiers in Energy Research

Received: 07 January 2022

Accepted: 14 February 2022

Published: 18 March 2022

Citation:

Yang K, Zhang C, Yuan H and Wu F
(2022) Heat Transfer Characteristics
and Pressure Drop of U-type Channel
in Vacuum Distillation Process for
Titanium Sponge.
Front. Energy Res. 10:850431.
doi: 10.3389/fenrg.2022.850431

Blockage of the U-type channel exacerbates the intermittency of production, and clarifying the channel heat transfer characteristics and pressure drop is an effective way to address this problem. The channel heat transfer and flow characteristics of the fluid in the channel are experimentally investigated in this study. According to the experiments, the heat transfer coefficient is between 59.95 and 200.29 W/m²·K and increases with the flow velocity and fluid temperature. Because the pressure drop is usually accompanied by a change in the energy loss of the fluid, the energy loss is evaluated experimentally. The results demonstrate that the friction loss in the straight tube section accounts for 80% of the energy loss. A bent tube of 90° is recommended instead of a right-angle tube to reduce the pressure drop. A dimensionless relation regarding the Nusselt number is presented to predict the heat transfer characteristics. We provided proposals to address the problem of blockage of the U-type channel, this is helpful to reduce production energy consumption and improve the quality of titanium sponge.

Keywords: convective heat transfer, energy loss, heat transfer coefficient, nusselt number, pressure drop

INTRODUCTION

The Kroll process is a unique existing industrial process for titanium sponge, the primary industrial choice in titanium chains, and this process has played a significant role in the titanium industry over the past decades (Nagesh et al., 2008; Zhang et al., 2011; Wang and Wu., 2021). The Kroll process is costly, energy-intensive, and intermittent (Wang et al., 2017; Takeda and Okabe, 2019). After the reduction process, the remaining magnesium and magnesium chloride were separated via vacuum distillation to obtain a titanium sponge (Nagesh et al., 2004; Cui et al., 2011). The fluid was distilled from the reduction reactor to the condenser, and the channel was easily blocked in the production process because of the unreasonable heating system of the heater and the energy loss of the fluid. This further exacerbated the intermittency of production, leading to a long production period. Titanium sponge pores were easy to sinter and other problems (Li et al., 2015; Liang et al., 2018) affected the distillation period, further increasing the energy consumption. However, this difficulty has not yet been effectively addressed. To address this blockage, it is necessary to clarify the channel heat transfer characteristics and pressure drop.

Currently, there is no research on the heat transfer characteristics and pressure drop of U-type channels in the vacuum distillation processes for titanium sponges. Therefore, this experiment referred to the literature on the heat transfer of fluids in a tube (Gorman et al., 2015; Moghadam et al., 2020; Qi et al., 2019; Baik et al., 2019). Hekmatipour et al. (2017) experimentally studied the

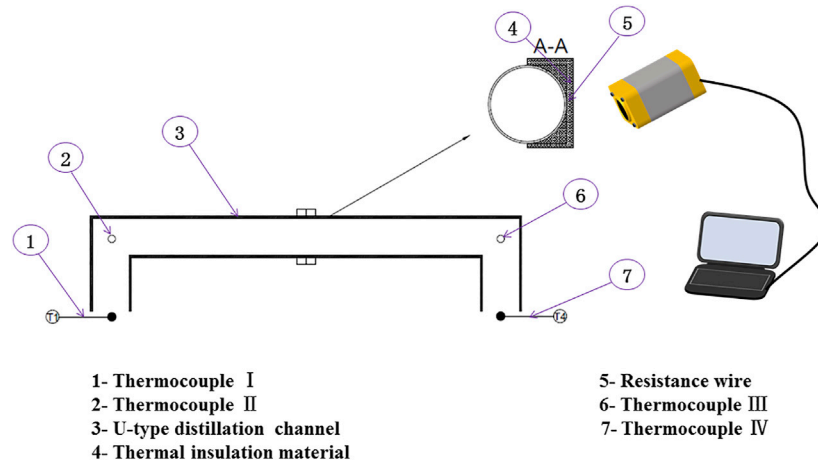


FIGURE 1 | Schematic of the experimental apparatus.

TABLE 1 | Detailed parameters of heater.

Power (kW)	Thermal insulation material	Thickness (m)
15.00	Aluminum silicate fiber	0.08

convective heat transfer of nanofluids in a tube. In this study, we present a correlation relation for the nanofluid to predict the Nusselt number. Wen et al. (2019) experimentally investigated the air flowing through helical tube bundles and obtained the flow and convective heat transfer characteristics. We propose two empirical relations to describe the convective heat transfer coefficient and friction factor. Sarmadian et al. (2020) investigated the heat transfer characteristics in a heat exchanger and discussed the heat transfer improved by twisted tapes. The channel heat transfer performance and pressure drop improved with the installation of the twisted tapes. The friction and heat transfer characteristics of a fluid influenced by a circular ring turbulator in a tube were experimentally studied (Kongkaitpaiboon et al., 2010), and the heat transfer rates increased from approximately 57–195% when the CRTs were installed. Baba et al. (2018) studied the convective heat transfer of an Fe_3O_4 -water nanofluid in a heat exchanger. The heat transfer and pressure drop of different heat exchangers are also discussed. We propose a correlation for the Nusselt number. Similarly, the aforementioned studies provide theoretical support for this experiment.

The heat transfer and flow characteristics of a mixed system of nitrogen, gaseous magnesium, and gaseous magnesium chloride in the channel were investigated experimentally. The Nusselt number dimensionless correlation relation was obtained based on experimental data.

METHODS

Experimental Apparatus

Figure 1 shows the apparatus used in this experiment. The distillation channel is 1Cr18Ni9Ti stainless steel tube, length

TABLE 2 | Components of the typical industrial vacuum distillation mixture.

Component	Molar fraction (%)	Temperature range (K)
Nitrogen	96.00–98.00	913.00–1023.00
Gaseous magnesium	1.00–2.50	
Gaseous magnesium chloride	1.00–1.50	

of the horizontal section is 3.62 m, vertical section is 0.40 m, inner diameter is 0.129 m, and outer diameter is 0.159 m. A heater with constant power was used to heat the distillation tube to maintain the fluid temperature, and the parameters are listed in Table 1.

To measure the temperature of the outer wall of the heater, an RSE300 infrared thermal imager was used. Two K-type thermocouples were installed on the tube to obtain the temperature of its outer wall. In addition, the fluid temperature was measured using two other K-type thermocouples at the inlet and outlet. By pumping a vacuum with nitrogen, the pressure drop can be obtained based on the vacuum degree.

In this study, the fluid consisted of a mixed system of nitrogen, gaseous magnesium, and gaseous magnesium chloride (listed in Table 2). As the temperature increased from 913.00 to 1023.00 K.

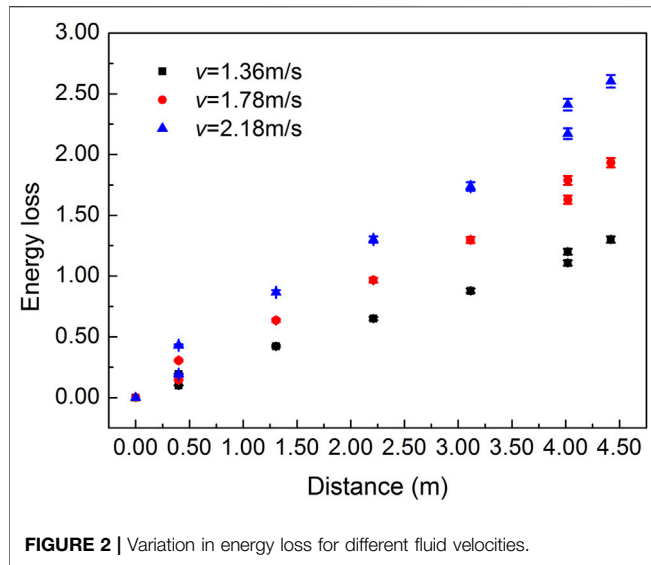
Theoretical Background

Pressure Drop

Clearly, as the fluid is distilled from the reduction reactor to the condenser in the straight tube section, the energy loss is caused by the viscous force of the fluid. There was a local loss because the flow direction changed dramatically at the right angle of the channel.

Taking the horizontal line of the channel inlet and outlet as a benchmark, the inlet velocity was considered as zero. The Bernoulli equation of the fluid is as follows:

$$\frac{\Delta p}{\rho g} = \frac{av^2}{2g} + L \quad (1)$$



Furthermore, the energy loss of the fluid is as follows:

$$L = \gamma \frac{l}{d} \frac{v^2}{2g} + \xi \frac{v^2}{2g} \quad (2)$$

Clearly, the local loss coefficient is 1.97. The coefficient of frictional loss was calculated using formula (3) to (5) (Demirkir and Erturk, 2021) and verified according to the range of the Reynolds number.

$$\gamma = \frac{64}{Re} \quad (Re < 2320) \quad (3)$$

$$\gamma = \frac{0.3164}{Re^{0.25}} \quad (4 \times 10^3 < Re < 10^5) \quad (4)$$

$$\gamma = 0.0032 + 0.221Re^{-0.237} \quad (10^5 < Re < 3 \times 10^6) \quad (5)$$

Hence, the flow velocity can be solved by Eq. (1)–(5).

Heat Conduction

In the distillation process, the channel is isothermal, and the axial heat transfer can be ignored and regarded as a one-dimensional heat conduction with an internal heat source.

The resistance wire conducts heat through the channel and insulation layer, and the power is obtained as follows:

$$P = P_{lo} + P_{ef} \quad (6)$$

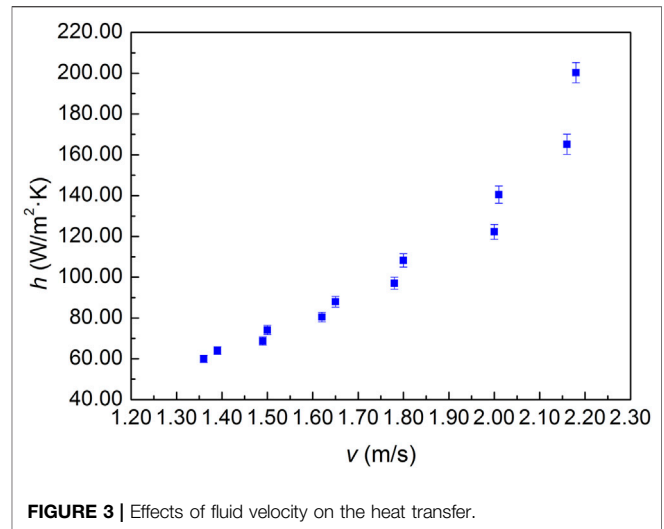
Mathematical formulation of heat conduction in thermal insulation layer is expressed as follows:

$$\frac{d^2t}{dx^2} + \frac{\Phi}{\lambda_a} = 0 \quad (7)$$

$$x = 0, \quad \frac{dt}{dx} = 0 \quad (8)$$

$$x = \delta, \quad t = t_h \quad (9)$$

Heat transfer process with the channel is analyzed as follows:



$$t_o - t_i = \frac{\Phi_{ef}}{2\pi l \lambda_t} \ln \frac{d_i}{d_o} \quad (10)$$

$$t_i - t_f = \frac{\Phi_{ef}}{h \pi l d_i} \quad (11)$$

The heat transfer coefficient is complex heat transfer coefficient, and the heat transfer coefficient is obtained as follows:

$$h = \frac{2\lambda_t \Phi_{ef}}{2\pi l d_i \lambda_t (t_o - t_f) - d_i \Phi_{ef} \ln \frac{d_i}{d_o}} \quad (12)$$

Furthermore, the Nusselt, Reynolds, and Prandtl numbers are obtained as follows, respectively:

$$Nu = \frac{h d_i}{\lambda_f} \quad (13)$$

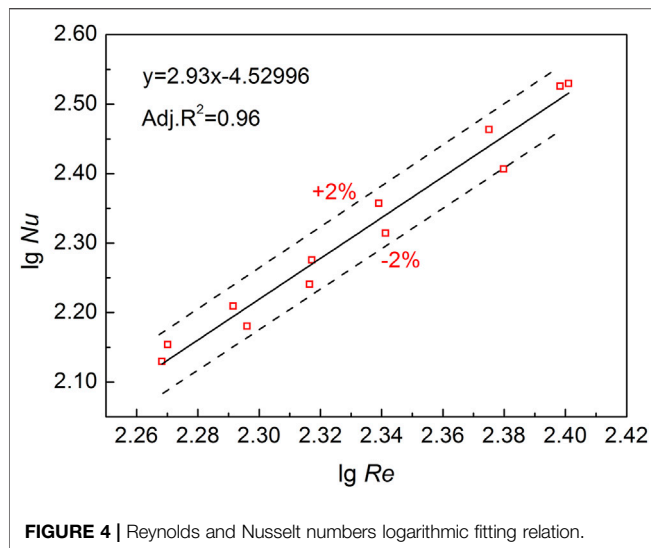
$$Re = \frac{\rho v d_i}{\mu} \quad (14)$$

$$Pr = \frac{\mu C_p}{\lambda_f} \quad (15)$$

RESULTS AND DISCUSSIONS

Energy Loss

The pressure drop is usually accompanied with change in the energy loss of the fluid. **Figure 2** shows the energy loss of the fluid inside the channel under various flow velocities. It is observed that the energy loss increases with distance and reaches a maximum as the fluid reaches the condenser. The energy loss doubled when the flow velocity increased from 1.36 to 2.18 m/s. Furthermore, the friction loss in the straight tube section accounted for 80% of the energy loss, which was proportional to the square of the flow velocity. Therefore, the pressure drop can be controlled at a reasonable level by pumping the vacuum in the production process to reduce energy loss.



As shown in **Figure 2**, the energy loss increases suddenly owing to the local loss at the right angle of the channel. As observed in the theoretical background sections, the pressure drop increases because of the increase in fluid energy loss to a great extent. Improving the channel structure to reduce the local loss coefficient may be an effective way to reduce pressure drop. The local loss coefficient of the bent tube with 90° was several times smaller than that of the right-angle tube, and under similar conditions, the fluid energy loss in the bent tube with 90° decreased by 13% compared with that in the right-angle tube. Therefore, a bent tube of 90° is recommended instead of a right-angle tube.

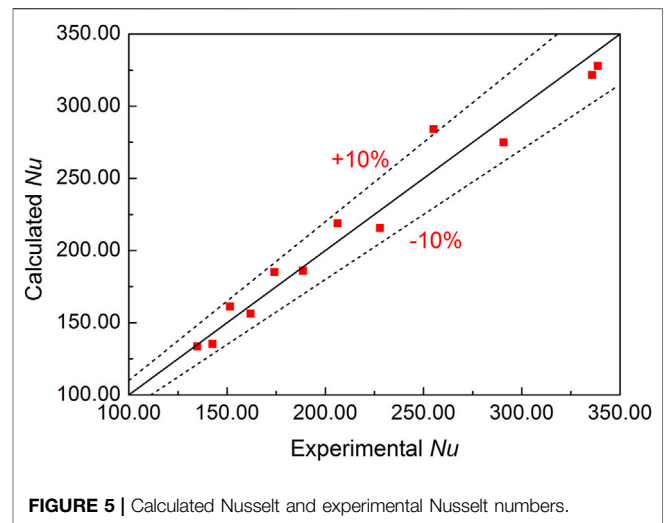
Heat Transfer Coefficient

The heat transfer coefficient inside the whole channel is not constant, and the heat transfer coefficient in this study is mean heat transfer coefficient. **Figure 3** shows the variation in the heat transfer coefficient with fluid velocity. The heat transfer coefficient increased as the Reynolds number increased because the flow velocity increased, resulting in an increase in the intensity of convective heat transfer. The extent of the increase in the heat-transfer coefficient also increased with a further increase in the flow velocity. Furthermore, as observed in **Figure 3**, the heat transfer coefficient is between 59.95 and 200.29 W/m²·K.

In addition, the effect of the fluid temperature on heat transfer was investigated. The temperature difference decreases as the fluid temperature increases. An increase in the fluid temperature increases the thermal conductivity and reduces the dynamic viscosity of the fluid. Therefore, the heat transfer coefficient increases and boosts the intensity of the convective heat transfer.

Heat Transfer Characteristics

The temperature ranges from 913.00 to 1023.00 K, fluid thermo-physical properties have no significant change, and the Prandtl number is between 0.0204 and 0.0208, which is approximately 0.0205 in this study. Therefore, the dimensionless relation is determined by the Nusselt and Reynolds numbers, as expressed in **Eq. 16** as follows:



$$Nu = CRe^n \quad (16)$$

Constants C and n were determined from the experimental data. **Figure 4** shows the Reynolds and Nusselt numbers logarithmic fitting relation, and the relational formula is expressed as follows:

$$Nu = 2.95 \times 10^{-5} Re^{2.93} (Adj.R^2 = 0.96) \quad (17)$$

Furthermore, **Figure 5** shows a comparison of the Nusselt numbers calculated from **Eq. 17** using the experimental Nusselt number, that is, the convective heat transfer characteristics for $185.45 < Re < 250.18$, $Pr = 0.0205$ could be predicted using **Eq. 17** and with no significant errors.

CONCLUSION

The channel heat transfer and flow characteristics of the fluid in the channel were investigated experimentally. The energy loss of the fluid was also analyzed. The impact of the flow velocity and temperature on the heat transfer coefficient was discussed. The conclusions are as follows:

- 1) The pressure drop increased with the energy loss. The energy loss of the fluid in the channel consists of the friction loss in the straight tube section and local loss at the right angle of the channel. The friction loss in the straight-tube section accounted for 80% of the energy loss. A bent tube of 90° is recommended to minimize the local loss to lower the pressure drop.
- 2) The heat transfer coefficient is between 59.95 and 200.29 W/m²·K. Moreover, the heat transfer coefficient increases with fluid velocity and fluid temperature.
- 3) A dimensionless relation regarding the Nusselt number is presented to predict the heat transfer characteristics.

DATA AVAILABILITY STATEMENT

The original contributions presented in the study are included in the article/Supplementary Material, further inquiries can be directed to the corresponding author.

AUTHOR CONTRIBUTIONS

KY, CZ, HY, and FW conceived and designed the study. KY, CZ, and HY were responsible for the experimental operation, and KY analyzed the experimental data. KY wrote the manuscript, and FW revised it.

FUNDING

The author acknowledges the financial support received from the National Natural Science Foundation of China (grant number

51874108), the Science and Technology Foundation of Guizhou Province (grant number QKHJC 2019-1406, and QKHJC-ZK 2021-YB261), and the Talent Projects of Guizhou University and the Education Department of Guizhou Province (grant number GDPY 2019-20, and QJHKYZ 2021-097).

ACKNOWLEDGMENTS

The authors thank Qiang Liang and Lvguo Zhang of Zunyi Titanium Co., Ltd. for providing experimental batches in this work.

REFERENCES

- Baba, M. S., Raju, A. V. S. R., and Rao, M. B. (2018). Heat Transfer Enhancement and Pressure Drop of Fe₃O₄-water Nanofluid in a Double Tube Counter Flow Heat Exchanger with Internal Longitudinal Fins. *Case Stud. Therm. Eng.* 12, 600–607. doi:10.1016/j.csite.2018.08.001
- Baik, W., Lee, W., and Yun, R. (2019). Heat Transfer and Pressure Drop Characteristics of CO₂ Mixtures in a Pipeline under the Seawater Condition. *Int. J. Heat Mass Transfer* 136, 627–634. doi:10.1016/j.ijheatmasstransfer.2019.03.026
- Bera, T. K., Biswas, S. K., Rajan, K., and Nagaraju, J. (2014). Projection Error Propagation-Based Regularization (PEPR) Method for Resistivity Reconstruction in Electrical Impedance Tomography (EIT). *Measurement* 49, 329–350. doi:10.1016/j.measurement.2013.11.003
- Cui, C., Hu, B., Zhao, L., and Liu, S. (2011). Titanium alloy Production Technology, Market Prospects and Industry Development. *Mater. Des.* 32, 1684–1691. doi:10.1016/j.matdes.2010.09.011
- Demirkır, Ç., and Ertürk, H. (2021). Convective Heat Transfer and Pressure Drop Characteristics of Graphene-Water Nanofluids in Transitional Flow. *Int. Commun. Heat Mass Transfer* 121, 105092. doi:10.1016/j.icheatmasstransfer.2020.105092
- Gorman, J. M., Carideo, M., Sparrow, E. M., and Abraham, J. P. (2015). Heat Transfer and Pressure Drop Comparison of Louver- and plain-finned Heat Exchangers where One Fluid Passes through Flattened Tubes. *Case Stud. Therm. Eng.* 5, 122–126. doi:10.1016/j.csite.2015.03.002
- Hekmatipour, F., Akhavan-Behabadi, M. A., Sajadi, B., and Fakoor-Pakdaman, M. (2017). Mixed Convection Heat Transfer and Pressure Drop Characteristics of the Copper Oxide-Heat Transfer Oil (CuO-HTO) Nanofluid in Vertical Tube. *Case Stud. Therm. Eng.* 10, 532–540. doi:10.1016/j.csite.2017.09.009
- Kongkaitpaiboon, V., Nanan, K., and Eiamsa-ard, S. (2010). Experimental Investigation of Convective Heat Transfer and Pressure Loss in a Round Tube Fitted with Circular-Ring Turbulators. *Int. Commun. Heat Mass Transfer* 37, 568–574. doi:10.1016/j.icheatmasstransfer.2009.12.016
- Liang, L., Dachun, L., Heli, W., Kaihua, L., Juhai, D., and Wenlong, J. (2018). Removal of Chloride Impurities from Titanium Sponge by Vacuum Distillation. *Vacuum* 152, 166–172. doi:10.1016/j.vacuum.2018.02.030
- Liang, L., Kaihua, L., Qingdong, M., and Cong, W. (2015). “Research on Quality Improvement of Titanium Sponge by Process Optimization,” in *Rare Metal Technology 2015*. Editors N. R. Neelameggham, S. Alam, H. Oosterhof, A. Jha, D. Dreisinger, and S. Wang (Switzerland, FL: Springer, Cham Press), 231–237. doi:10.1007/978-3-319-48188-3_26
- Moghadam, M. T., Behabadi, M. A., Sajadi, B., Razi, P., and Zakaria, M. I. (2020). Experimental Study of Heat Transfer Coefficient, Pressure Drop and Flow Pattern of R1234yf Condensing Flow in Inclined plain Tubes. *Int. J. Heat Mass Transfer* 160, 120199. doi:10.1016/j.ijheatmasstransfer.2020.120199
- Nagesh, C. R. V. S., Ramachandran, C. S., and Subramanyam, R. B. (2008). Methods of Titanium Sponge Production. *Trans. Indian Inst. Met.* 61, 341–348. doi:10.1007/s12666-008-0065-7
- Nagesh, C. R. V. S., Rao, C. S., Ballal, N. B., and Rao, P. K. (2004). Mechanism of Titanium Sponge Formation in the Kroll Reduction Reactor. *Metall. Mater. Trans. B* 35, 65–74. doi:10.1007/s11663-004-0097-2
- Qi, C., Chen, X., Wang, W., Miao, J., and Zhang, H. (2019). Experimental Investigation on Flow Condensation Heat Transfer and Pressure Drop of Nitrogen in Horizontal Tubes. *Int. J. Heat Mass Transfer* 132, 985–996. doi:10.1016/j.ijheatmasstransfer.2018.11.092
- Sarmadian, A., Moghaddam, H. A., Asnaashari, A., Joushani, H. A. N., Moosavi, M., Islam, M. S., et al. (2020). Flow Boiling Heat Transfer and Pressure Drop Characteristics of Isobutane in Horizontal Channels with Twisted tapes. *Int. J. Heat Mass Transfer* 162, 120345. doi:10.1016/j.ijheatmasstransfer.2020.120345
- Takeda, O., and Okabe, T. H. (2019). Current Status of Titanium Recycling and Related Technologies. *JOM* 71, 1981–1990. doi:10.1007/s11837-018-3278-1
- Wang, W., Wu, F., and Jin, H. (2017). Enhancement and Performance Evaluation for Heat Transfer of Air Cooling Zone for Reduction System of Sponge Titanium. *Heat Mass. Transfer* 53, 465–473. doi:10.1007/s00231-016-1836-z
- Wang, W., and Wu, F. (2021). Quantifying Heat Transfer Characteristics of the Kroll Reactor in Titanium Sponge Production. *Front. Energ. Res.* 9, 759781. doi:10.3389/fenrg.2021.759781
- Wen, J., Fu, Y., Bao, X., Liu, Y., and Xu, G. (2019). Flow Resistance and Convective Heat Transfer Performances of Airflow through Helical-Tube Bundles. *Int. J. Heat Mass Transfer* 130, 778–786. doi:10.1016/j.ijheatmasstransfer.2018.10.129
- Zhang, W., Zhu, Z., and Cheng, C. Y. (2011). A Literature Review of Titanium Metallurgical Processes. *Hydrometallurgy* 108, 177–188. doi:10.1016/j.hydromet.2011.04.005

Conflict of Interest: The authors declare that the research was conducted in the absence of any commercial or financial relationships that could be construed as a potential conflict of interest.

Publisher’s Note: All claims expressed in this article are solely those of the authors and do not necessarily represent those of their affiliated organizations, or those of the publisher, the editors, and the reviewers. Any product that may be evaluated in this article, or claim that may be made by its manufacturer, is not guaranteed or endorsed by the publisher.

Copyright © 2022 Yang, Zhang, Yuan and Wu. This is an open-access article distributed under the terms of the Creative Commons Attribution License (CC BY). The use, distribution or reproduction in other forums is permitted, provided the original author(s) and the copyright owner(s) are credited and that the original publication in this journal is cited, in accordance with accepted academic practice. No use, distribution or reproduction is permitted which does not comply with these terms.

NOMENCLATURE

c_p Specific heat capacity of the fluid, J/mol·K

d Diameter, m

g Acceleration of gravity (9.81 m/s²)

h Heat transfer coefficient, W/m²·K

L Energy losses

l Tube length, m

M Relative molecular mass

Nu Nusselt number

Pr Prandtl number

P Power

Re Reynolds number

t Temperature, K

U Uncertainty

v Fluid velocity, m/s

Δp Pressure drop, kPa

α Kinetic energy correction factor

γ Frictional loss coefficient

δ Thickness, m

λ Thermal conductivity, W/m·K

ξ Local loss coefficient

ω Molar fraction

ρ Density, Kg/m³

μ Dynamic viscosity, Pa·s

$\dot{\Phi}$ Inner heat source, W/m³

Φ Heat flux, W

Subscripts

a Aluminum silicate fiber

ef Effective

h Outer wall of heater

lo Loss

i Inner

o Outer

t Tube

x Component

Frontiers in Energy Research

Advances and innovation in sustainable, reliable
and affordable energy

Explores sustainable and environmental
developments in energy. It focuses on
technological advances supporting Sustainable
Development Goal 7: access to affordable,
reliable, sustainable and modern energy for all.

Discover the latest Research Topics

[See more →](#)

Frontiers

Avenue du Tribunal-Fédéral 34
1005 Lausanne, Switzerland
frontiersin.org

Contact us

+41 (0)21 510 17 00
frontiersin.org/about/contact



Frontiers in Energy Research

